



UvA-DARE (Digital Academic Repository)

Essays in stochastic modeling with applications to economics

Lin, X.

Publication date

2026

Document Version

Final published version

[Link to publication](#)

Citation for published version (APA):

Lin, X. (2026). *Essays in stochastic modeling with applications to economics*. [Thesis, fully internal, Universiteit van Amsterdam].

General rights

It is not permitted to download or to forward/distribute the text or part of it without the consent of the author(s) and/or copyright holder(s), other than for strictly personal, individual use, unless the work is under an open content license (like Creative Commons).

Disclaimer/Complaints regulations

If you believe that digital publication of certain material infringes any of your rights or (privacy) interests, please let the Library know, stating your reasons. In case of a legitimate complaint, the Library will make the material inaccessible and/or remove it from the website. Please Ask the Library: <https://uba.uva.nl/en/contact>, or a letter to: Library of the University of Amsterdam, Secretariat, P.O. Box 19185, 1000 GD Amsterdam, The Netherlands. You will be contacted as soon as possible.



tinbergen
institute

GRADUATE PROGRAM



VU

Essays in Stochastic Modeling with Applications to Economics

Xu Lin

This dissertation examines how stochastic dynamics shape economic outcomes and policy under uncertainty, focusing on the COVID-19 pandemic and climate change. Using stochastic differential equations, it captures randomness in epidemiological, climate, and economic processes that deterministic models miss. The first part develops a stochastic behavioral epidemiological model to evaluate COVID-19 lockdowns, incorporating behavioral adaptation and learning about mortality risk to better replicate observed infection patterns. It shows that lockdowns create significant real option value by delaying infections until vaccines are available, a mechanism largely absent in standard deterministic analyses. The second part uses Dynamic Stochastic Integrated Assessment Models (DSICE) to study climate policy, demonstrating that stochastic climate damages and tipping risks substantially increase the Social Cost of Carbon and justify stronger abatement policies.

Xu Lin studied Mathematics at Renmin University of China, Statistics at Columbia University, and Financial Mathematics at Vrije Universiteit Amsterdam. From 2019 to 2021, she completed the Research Master in Economics at the Tinbergen Institute. In 2021, she joined the Department of Economics at the University of Amsterdam as a PhD student under the supervision of Professor Rick van der Ploeg and Professor Sweder van Wijnbergen. Her research focuses on macro-finance, stochastic modeling, and climate economics.

Essays in Stochastic Modeling with Applications to Economics

Xu Lin



Essays in Stochastic Modeling with Applications to Economics

Xu Lin

ISBN: 978 90 361 0843 0

Cover: Wassily Kandinsky, *Several Circles (1926)*, Solomon R. Guggenheim Museum, New York City

Tinbergen cover design: *Crasborn Graphic Designers bno, Valkenburg a.d. Geul*

This book is no. **889** of the Tinbergen Institute Research Series, established through cooperation between Rozenberg Publishers and the Tinbergen Institute. A list of books which already appeared in the series can be found in the back.

Essays in Stochastic Modeling with Applications to Economics

ACADEMISCH PROEFSCHRIFT

ter verkrijging van de graad van doctor
aan de Universiteit van Amsterdam
op gezag van de Rector Magnificus
prof. dr. ir. P.P.C.C. Verbeek

ten overstaan van een door het College voor Promoties ingestelde commissie,
in het openbaar te verdedigen in de Agnietenkapel
op maandag 26 januari 2026, te 16.00 uur

door Xu Lin
geboren te Liaoning

Promotiecommissie

<i>Promotor:</i>	prof. dr. F. van der Ploeg	Universiteit van Amsterdam
<i>Copromotor:</i>	prof. dr. S.J.G. van Wijnbergen	Universiteit van Amsterdam
<i>Overige leden:</i>	prof. dr. R.J.A. Laeven	Universiteit van Amsterdam
	dr. S. Jensen	Oslo Business School
	prof. dr. A.H.E. Koolman	Vrije Universiteit Amsterdam
	prof. dr. T.S. van den Bremer	TU Delft
	dr. T.R.G.R. Douenne	Universiteit van Amsterdam
	dr. S.W.J. Olijslagers	Centraal Planbureau
	prof. dr. E.C. Perotti	Universiteit van Amsterdam

Faculteit Economie en Bedrijfskunde

Acknowledgements

I would like to express my sincere gratitude to my supervisor, Sweder van Wijnbergen, for his invaluable guidance and support throughout my PhD journey. This thesis would not have been possible without your mentorship. I am truly grateful for the countless hours you have spent reviewing my work, offering insightful feedback, and guiding me in the right direction. I feel very fortunate to have had the opportunity to work with and learn from you. Your guidance has profoundly shaped my academic growth and will continue to influence my future endeavors.

I am also deeply thankful to my supervisor, Rick van der Ploeg. Our meetings were always intellectually stimulating and inspiring, and I greatly appreciated the clarity, depth, and enthusiasm you brought to every discussion. Your deep knowledge and passion for the field have been invaluable in refining this thesis. I am very grateful for the constructive advice and encouragement you provided, which helped me persevere and grow as a researcher.

I would like to thank my friends and colleagues at the Tinbergen Institute and MInt for their camaraderie and stimulating discussions along the way. Each conversation, suggestion, and act of support has contributed to this journey, and I am grateful to all of you.

Finally, I owe my deepest gratitude to my parents for their unwavering love, encouragement, and support throughout my life and this PhD journey. Your belief in me has been a constant source of strength, and I could not have achieved this without your sacrifices, guidance, and steadfast faith in me. This accomplishment is as much yours as it is mine, and I will always be grateful for everything you have done to make it possible.

List of Authors

On Lockdowns, Laissez Faire Strategies and Pandemics

This chapter is co-authored with Sweder van Wijnbergen.

The Social Cost of Carbon Under Climate Volatility Risk

This chapter is co-authored with Sweder van Wijnbergen.

Carbon Price and Tipping Risk: the Case of the Greenland Ice Sheet and Thawing Permafrost

This chapter is single-authored.

Contents

1	Introduction	1
2	On Lockdowns, Laissez-Faire Strategies and Pandemics	5
2.1	Introduction	6
2.2	The Behavioral SEIRS Model: BSEIRS	9
2.2.1	Fear of Contagion	10
2.2.2	A Behavioral Theory of Fear of Contagion	11
2.2.3	Heterogeneous Preferences and Fear of Contagion	13
2.2.4	Belief Updating on COVID-19 Mortality Rate	14
2.2.5	The BSEIRS Model	15
2.3	Vaccines as Options and the Health Benefits of Lockdown Strategies	18
2.3.1	Total Health Benefits of Lockdown Strategies	18
2.3.2	The Option Value of Lockdowns	20
2.3.3	The Maximum Upfront Payment for Vaccines	20
2.4	Calibration	21
2.5	Simulation Results	26
2.5.1	Pandemic Simulations	26
2.5.2	Option Values of Lockdown	29
2.6	Conclusion	34
	Appendix 2.A Parameters of the BSEIRS Model	37
	Appendix 2.B Lockdown Severity	39
	Appendix 2.C Alternative Models with Different Vaccine Effects	40
	Appendix 2.D Computational Procedures for the Value Functions	43
3	The Social Cost of Carbon Under Climate Volatility Risk	47
3.1	Introduction	47
3.2	The Model	53
3.2.1	The Climate Model	53
3.2.2	The Economic Model	54

3.2.3	The Social Cost of Carbon	56
3.3	Calibration	56
3.4	The SCC and Climate Volatility Risk: Numerical Results	57
3.4.1	The New Climate Regime (A): Higher Disaster Frequency	58
3.4.2	The New Climate Regime (B): Higher Disaster Intensity	77
3.4.3	Arrival Rates of Climate Regime Shift	83
3.5	Endogenous Carbon Emissions	88
3.5.1	Endogenous Emissions and Changing Disaster Frequency	89
3.5.2	Endogenous Emissions and Changing Disaster Intensity	91
3.6	An alternative Model of Climate Volatility Risk: Gradually Unfolding Tipping Points	92
3.7	Conclusion	95
	Appendix 3.A Solution to the Optimization Problem and SCC	97
	Appendix 3.B Numerical Results for the New Climate Regime (B)	104
3.B.1	Risk-Free Rate	104
3.B.2	Risk Premium	105
4	Carbon Price and Tipping Risk	109
4.1	Introduction	109
4.2	Model	116
4.3	Calibration	125
4.4	Numerical Results	129
4.4.1	The Business-As-Usual scenario	129
4.4.2	Optimal Abatement	132
4.4.3	The Warming Effect of Permafrost Methane	135
4.4.4	The Tipping of GIS Under Different Equilibria	136
4.5	Conclusion	142
	Appendix 4.A The Hamilton-Jacobi-Bellman (HJB) Equation of the Optimization Problem and SCC	144
	Appendix 4.B Summary of Model Parameters	145
	Bibliography	147
	Summary	157
	Nederlandse Samenvatting (Summary in Dutch)	159

Chapter 1

Introduction

This dissertation investigates stochastic dynamic systems in two areas that have drawn increasing attention from economists: the COVID-19 pandemic and climate change. Both represent complex, high-impact phenomena characterized by deep uncertainty, non-linear dynamics, and significant long-term consequences for human welfare. The central theme is how stochastic processes, represented by stochastic differential equations, shape economic uncertainty and influence policy design under uncertainty.

Uncertainty is inherently embedded in all economic systems. Accurately modeling the stochastic elements is crucial for understanding economic dynamics, assessing risk, and informing policies that balance trade-offs between current costs and future benefits. Stochastic models provide a richer representation of randomness than deterministic frameworks, and allow researchers to incorporate uncertainty in key parameters and state variables, account for behavioral adaptation, and evaluate policy interventions across multiple plausible scenarios. This dissertation contributes to this literature by applying stochastic modeling to two global challenges – public health crises and climate change – where uncertainty is not only pervasive but also plays a central role in policy making.

COVID-19 Pandemic: Stochastic Modeling and Policy Analysis Chapter 2 focuses on the COVID-19 pandemic, with a particular emphasis on the economic evaluation of lockdown policies under uncertainty. On 30 January 2020, the World Health Organization (WHO) declared COVID-19 a Public Health Emergency of International Concern (PHEIC). By April 2024, over 450 million cases has been reported worldwide within the first two years, with more than seven million fatalities. Due to the rapid transmission of the virus, COVID-19 quickly escalated into a global health crisis, which consequently affected the global economy especially during the first two waves of the pandemic. In response to this unprecedented health and economic crises, governments worldwide implemented different lockdown policies in hope of slowing down the spread of coronavirus. However, opinions diverged on how stringent the lockdown

policy should be, especially given the uncertainty over vaccine development and the evolution of the coronavirus at the early stage of the pandemic.

One of the primary challenges in making effective policies was that standard epidemiological models often failed to accurately simulate future pandemic trajectories, thereby limiting their usefulness as references for policy discussions. These models generally neglected critical factors for the pandemic trajectory, including vaccine development timelines, the emergence of new variants, reinfections, and behavioral responses to perceived mortality risk. Many models assumed permanent immunity or static transmission parameters, which generated pandemic simulations that are inconsistent with the observed dynamics of the virus. Such simplifications limited the ability of policymakers to assess the potential benefits and costs of various interventions.

To address these gaps, this dissertation develops a stochastic behavioral SEIRS (Susceptible-Exposed-Infectious-Recovered-Susceptible) model. The model explicitly incorporates individual behavioral adaptation and a learning process in which people gradually adjust their social behavior based on information about mortality risk. This allows for a realistic representation of how fear of contagion, information diffusion, and evolving epidemiological knowledge interact to shape pandemic trajectories. The model is calibrated using data from the Netherlands and demonstrates better performance in reproducing observed infection patterns during the first two waves of COVID-19 compared to earlier models.

Using this framework, we analyze the value of different lockdown policies, focusing on both lives saved and the additional “real option value” that lockdowns provide. Lockdowns delay infections until vaccines become available, which effectively gives individuals the option to avoid infection and gain protection. Our simulations indicate that this real option effect accounts for nearly 70% of the total value of statistical lives saved under intermittent and rollover lockdown policies, highlighting an important mechanism overlooked in conventional analyses. The model also clarifies the interaction between lockdown stringency, vaccine timing, and health benefits. Although extended waiting for vaccines increases the real option value, early vaccine availability maximizes the total lives saved.

This chapter contributes methodologically by demonstrating how stochastic modeling can capture behavioral responses and learning. From a policy perspective, it provides guidance on lockdown assessment that accounts for uncertainty. Beyond COVID-19, these insights are relevant for managing future pandemics or other public health crises with similar characteristics of uncertainty and irreversibility.

Climate Change: Stochastic Dynamics and the Social Cost of Carbon Chapter 3 and 4 apply stochastic modeling to climate economics. Climate change represents a long-term, systemic risk characterized by deep uncertainty, non-linear dynamics, and the possibility of

catastrophic outcomes. Early research has largely relied on Integrated Assessment Models (IAMs) based on deterministic assumptions and exogenously set discount rates, which often understate risk and fail to capture rare disastrous events.

This dissertation uses Dynamic Stochastic IAMs (DSICE), which endogenize discount rates by linking them to the covariance between assets and consumption. This enables a more realistic assessment of the Social Cost of Carbon (SCC) and the design of optimal abatement strategies over time. By modeling both the economic system and the climate system as stochastic and interdependent, the framework provides a richer understanding of risk, welfare impacts, and policy trade-offs.

Chapter 3 focuses on stochastic volatility of climate damages, a higher-order uncertainty that has received little attention in the literature. Extreme weather events are becoming increasingly frequent and severe, and the volatility of their economic impacts evolves stochastically over time. By modeling both the frequency and intensity of climate disasters as stochastic processes, we show that stochastic volatility substantially increases the SCC by more than 30% in certain scenarios, relative to models that are deterministic or only consider first-order uncertainty. Our analysis further distinguishes between stochastic shocks to disaster frequency and intensity, showing that shocks to intensity have a disproportionately larger effect on the SCC for risk-averse agents due to the non-linear amplification of damages under extreme events. This demonstrates that higher-order stochastic uncertainty is critical for climate policy analysis and should be explicitly incorporated in long-term planning and carbon pricing decisions.

Chapter 4 examines climate tipping points, focusing on the thawing of permafrost and the melting of the Greenland Ice Sheet (GIS). Tipping points are critical thresholds in the climate system. Crossing tipping thresholds can induce abrupt and potentially irreversible changes. These processes differ in both mechanism and economic impact. Permafrost thaw releases large quantities of methane, substantially accelerating global warming and increasing the frequency and severity of extreme weather events, whereas GIS melting mainly contributes to sea-level rise, threatening coastal infrastructures and human settlements. Using a continuous-time DSICE model with dynamic tipping blocks, we quantify the economic and policy implications of tipping risks.

Our results show that incorporating tipping points increases the SCC and encourage aggressive emission abatement. The thawing permafrost exerts a larger influence on optimal policies than GIS melting due to its direct effect on warming through methane emission, while these two tipping processes can amplify each other through positive feedback. Optimal abatement policies considering both tipping points could reduce warming by 0.7°C and climate-induced damages by over 30% relative to a business-as-usual scenario by 2100. These findings highlight the importance of distinguishing between different types of tipping elements, as well as integrating mitigation and adaptation strategies to manage climate risk effectively.

Roadmap of the Dissertation The dissertation is structured as follows. Chapter 2 develops and applies a stochastic behavioral SEIRS model to evaluate COVID-19 lockdown policies and quantify the real option value of delaying infections until vaccines are available. Chapters 3 and 4 focus on climate change. Chapter 3 introduces stochastic volatility in climate damages and examines its impact on the SCC and optimal abatement strategies. Chapter 4 extends this framework to include climate tipping points, analyzing their effects on the SCC and the stringency of optimal abatement policy. The final chapter synthesizes the findings, and discusses broader implications for policy and economic modeling.

Overall, this dissertation demonstrates that uncertainty is not merely a complication to be minimized but a central feature of complex economic and environmental systems. By explicitly modeling stochastic processes, this work provides a framework for understanding how uncertainty shape optimal policy interventions and long-term welfare outcomes.

Chapter 2

On Lockdowns, Laissez Faire Strategies and Pandemics

Abstract

We construct a behavioral SEIRS epidemic model to simulate the COVID-19 pandemic, and evaluate the effectiveness of different lockdown policies under uncertainty about vaccines. The model has three new features: (i) a micro-founded theory of people's behavioral response to fear of contagion, (ii) learning about the COVID-19 mortality rate, and (iii) the possibility of reinfection, all contributing to a better fit of the pandemic data. We highlight that lockdowns confer a real option with uncertain exercise timing in the presence of uncertainty about vaccine arrival date and effectiveness. Before an effective vaccine becomes available, a lockdown will slow down the spread of virus leaving more people alive when the vaccine arrives. Thus stricter lockdown policies grant more people access to this real option of getting vaccinated before being infected once the vaccine arrives, and thus lead to a lower mortality rate.

2.1 Introduction

The COVID-19 pandemic has caused waves of health and economic crises worldwide that are unprecedented in modern times. To contain and mitigate the pandemic's negative impact, great effort has been made in vaccine development, and many governments across the globe have imposed different lockdown policies in hope of slowing down the spread of coronavirus.

It is widely acknowledged that lockdowns mitigate the risk of ICU overload by slowing down virus transmission, thereby ensuring access to care for critically ill patients and saving lives. We highlight another often overlooked advantage of lockdowns: they curb COVID-19 infections before vaccines become available, allowing more individuals to acquire immunity through vaccination rather than through infection. This reduces the number of infections needed to reach herd immunity and enhances the protective impact of ongoing vaccine research, ultimately lowering overall COVID-19 mortality. Importantly, both vaccine research outcomes and eventual effectiveness are stochastic and can be modeled as binary options. Lockdowns increase the number of people who survive to potentially benefit from these compound binary options, whose exercise is further complicated by the uncertainty of vaccine arrival. In this sense, lockdowns possess real option value (Dixit and Pindyck (1994), van Wijnbergen (2022)), as they provide the population with access to future health gains contingent on the uncertain development and timing of effective vaccines.

In order to assess the effectiveness and real option value of lockdown policies, we first construct an enriched epidemiological model (Behavioral SEIRS model, or BSEIRS) based on the standard SEIRS (Susceptible – Exposed – Infectious – Recovered – Susceptible) framework. Then we simulate the pandemic using this model under alternative lockdown strategies to assess the effectiveness of lockdown policies based on the total lifetime saved throughout the pandemic.

Our epidemiological model incorporates several critical extensions to more accurately simulate the COVID-19 pandemic. It accounts for the seasonality of virus transmission and the impact of lockdown policies on the timing of infection prevalence, under uncertainty regarding both the arrival date and the effectiveness of vaccines. The model outperforms existing models in matching observed pandemic data due to three key innovations. First, we integrate a fully micro-founded model of endogenous behavioral response to the pandemic driven by fear of contagion. While fear of contagion has appeared in the literature, it is typically implemented in an ad hoc, reduced-form manner in epidemiological models. In contrast, we adopt an explicit decision-theoretic framework in which individual fear levels are linked to endogenously updated public beliefs about COVID-19 mortality. Individuals who perceive higher mortality risk voluntarily reduce social interactions and stay indoors, while those with lower fear levels do not. The proportion of individuals with high versus low fear generates an aggregate effect of fear on virus transmission.

Second, we explicitly model the belief-updating process regarding the current COVID-19 mortality rate. Society updates its belief about mortality risk over time through Bayesian learning from observed pandemic data. Since public perception of mortality risk determines the overall level of fear and consequently the behavioral responses to the pandemic, the belief-updating process is crucial for accurate pandemic simulations. The integration of learning dynamics with a fully micro-founded behavioral response to contagion risk is a novel contribution to the literature. It is not merely innovative for its own sake: fully endogenizing public attitudes is essential for explaining the multiple pandemic waves observed in the data.

Third, our model incorporate the possibility of reinfection and waning immunity following vaccination. Individuals who have recovered COVID-19 or been vaccinated can still become infected as their antibodies diminish over time. Accounting for reinfection and fading immunity helps explain the resurgence of infections even after a large portion of the population has been vaccinated. In this context, herd immunity cannot be sustained unless vaccinations are repeated at sufficiently short time intervals, presenting a clear challenge for policymakers.

Based on the simulated pandemic trajectories generated by our BSEIRS model described above, we assess the total health benefits of lockdowns, including both the real option value and the gains in lifetime from flattening the infection curve. The overall health benefits are measured using the value of a statistical life year (VSL), which quantifies an individual's willingness to trade wealth for a reduction in mortality risk and thus provides a consistent metric for assessing the benefits of lockdown policies. We focus on three types of lockdown strategies under vaccine uncertainty: (i) Laissez-Faire (LF), in which no lockdown is imposed; (ii) Intermittent Lockdown (LD), similar to measures implemented in the Netherlands; and (iii) Rollover-Infection Lockdown (RO), designed to flatten the infection curve by maintaining the effective reproduction number at one.

Our simulations show that uncertainty regarding vaccine arrival and effectiveness causes the real option value of lockdowns to account for roughly 70% of the total health benefits, measured in VSL, for both intermittent and rollover lockdown policies. Therefore, the real option dimension of lockdowns is an essential consideration in evaluating pandemic policies. Perhaps somewhat counterintuitively, the option value is larger when vaccines take longer to become available or are less effective. This is because these situations correspond to an extended waiting time for vaccination. Given that the real option value of lockdown reflects the health benefit of individuals remaining at home while awaiting vaccine availability, a longer waiting period enables lockdowns to prevent more infections before vaccines are administered, thereby increasing the option value. However, this does not imply that delayed or ineffective vaccination is desirable. Across all lockdown policies, the total health benefit from vaccination is higher when an effective vaccination program begins earlier, even if immunity from vaccination wanes over time. Across all lockdown policies, the total health benefit from vaccination is higher

when an effective vaccination program begins earlier, even if immunity from vaccination wanes over time. Finally, we find that the total health benefits of lockdown increase with lockdown stringency, vaccine arrival rate, and vaccine effectiveness.

Our paper contributes to the literature on epidemiological models for the COVID-19 pandemic. The canonical framework for modeling contagious diseases is the Susceptible – Infectious – Recovered (SIR) model of Kermack and McKendrick (1927). A key assumption in this model is that individuals who recover acquire permanent immunity. This assumption is also adopted by most of the early COVID-19 literature. Avery et al. (2020) provides a thorough overview of the application of SIR models during the early stage of the pandemic.

In the standard SIR model, each individual falls into one of three health states: Susceptible (S), Infectious (I), or Recovered (R). Susceptible and infectious individuals are assumed to behave in a similar manner and cannot be distinguished unless tested. New infections arise at a rate proportional to the interaction between susceptible and infectious individuals, which is typically approximated by the product of their respective group sizes. McCallum et al. (2001) discusses whether this formulation produces a good approximation of pathogen transmission and survey alternative specifications of pathogen transmission. More recent work extends the SIR model by introducing stochastic dynamics in epidemic evolution, as reviewed in Greenwood and Gordillo (2009).

This canonical SIR framework has been widely used in economic policy discussions on lockdowns and other interventions during the COVID-19 crisis. For example, Kaplan et al. (2020) couples an extended SIR model with a heterogeneous-agent incomplete-market general equilibrium framework to study the trade-off between health and economic outcomes under different lockdown policies. Acemoglu et al. (2021) constructs a multi-group SIR model heterogeneous vulnerability and show that group-targeted lockdowns can substantially outperform uniform policies in terms of both health and economic costs. van Wijnbergen (2022) is closest to our approach, which examines the real option aspect of lockdowns, but still within the canonical SIR setting.

While SIR models are useful for building intuition, they generate several counterfactual predictions, as we illustrate with data from the Netherlands. First, the standard SIR model predicts a single large infection peak under laissez-faire, while in reality, even countries without strict lockdowns (e.g. Sweden) went through multiple infection peaks¹. Second, standard SIR models imply that lockdowns only delay infections without reducing the cumulative infections reached by the end of the pandemic, and predict a surge in cases immediately upon reopening. In reality, however, post-lockdown waves have been smaller than predicted. Third, the canonical framework omits important features such as incubation periods, waning immunity, and vaccination effects. These shortcomings cast doubt on policy implications from SIR models.

¹See Swedish COVID-19 data. Data source: World Health Organization (2025)

Motivated by these limitations, we develop a more sophisticated model based on the recently developed Susceptible - Exposed - Infectious - Recovered (SEIR) model. As shown in He et al. (2020) and López and Rodo (2021), SEIR models improve the empirical fit of pandemic dynamics by introducing an exposed class (E) representing infected but not yet infectious individuals, and allowing for hospitalization (H) among severe cases. These additional compartments capture the incubation period and the hospitalization status after infection, both of which play a central role in shaping the time path of the pandemic.

We extend the SEIR framework in several important directions. First, we incorporate the empirically documented possibility of reinfection due to waning immunity, which significantly alters the pandemic trajectory. Reinfection has been widely observed around the world in the later stages of the pandemic (Dolgin et al. (2021); Prillaman (2022); Rahman et al. (2022)), and makes *herd immunity* hard to achieve. Second, we model behavioral responses to the fear of contagion within a decision-theoretic framework. A recent empirical study Goolsbee and Syverson (2021) shows that fear of contagion reduced U.S. economic activity more than the implemented lockdown policies. Existing literature has so far introduced such behavior in an arguably ad hoc, reduced-form aggregate manner (see for example Perra et al. (2011) and Epstein et al. (2021)). By contrast, our framework explicitly model the behavior change induced by fear of contagion through a decision-theoretic framework in an epidemiological model. This enables us to link fear-of-contagion behavior to both the utility of staying at home and the process of learning about mortality risk. It also allows us to incorporate heterogeneity in behavioral responses and to capture phenomena such as pandemic fatigue (see Atkeson (2021)).

Finally, We incorporate seasonality in contagion following Aron and Schwartz (1984), allow for the arrival of more contagious variants, and account for uncertainty regarding the timing and effectiveness of vaccines. We also analyze how different lockdown stringencies affect the predictive performance of the model with respect to observed pandemic dynamics.

The rest of the paper is structured as follows. Section 2.2 presents the behavioral SEIRS (BSEIRS) model. Section 2.3 introduces the theoretical framework for evaluating the option value of lockdown policies. Section 2.4 describes the calibration of model parameters based on existing evidence and Dutch pandemic data. Section 2.5 reports simulation results, highlighting the health benefits of lockdowns and quantifying option values. Section 2.6 concludes.

2.2 The Behavioral SEIRS Model: BSEIRS

In Subsection 2.2.1, we extend standard epidemiological models of COVID-19 by (A) accounting for endogenously generated fear of contagion, (B) incorporating a learning process under a time-varying mortality rate of COVID-19, and (C) allowing for the possibility of reinfection. To improve the accuracy of forecasts relative to the observed pandemic trajectory,

we further consider the emergence of new and more transmissible variants, the seasonality of virus transmission, lockdown strategies of varying severity, and uncertainties regarding vaccine arrival, roll-out timing and speed, and effectiveness.

We first develop a decision-theoretic framework to analyze fear of contagion and the learning process regarding mortality risk. These two behavioral sub-models are then incorporated into our extension of the SEIRS model, which we label the BSEIRS model (Behavioral SEIRS).

2.2.1 Fear of Contagion

Goolsbee and Syverson (2021) show that fear of contagion accounts for much of the reduction in economic activity in the United States, whereas the effect of legal shutdowns was comparatively moderate. These findings provide the empirical foundation for our epidemiological model.²

In the existing epidemic literature, susceptible individuals are divided into two groups based on their level fear of contagion. Individuals whose fear exceeds a certain threshold voluntarily reduce physical interactions with others and therefore face a lower probability of infection than those with weaker concerns. The joint behavior of both groups determines the overall transmission rate of the virus.

A limitation of existing fear-of-contagion models is that they link fear solely to the number of new infections, implicitly assuming that fear is driven by the transmission rate of the virus. This assumption contradicts the empirical finding of Goolsbee and Syverson (2021), who show that fear of contagion was driven primarily by reported deaths. This finding is consistent with the multiple high infection peaks observed during the second wave in the Netherlands and other countries. If fear of contagion were driven by the number of new infections, a slight increase in new infection cases would trigger greater fear across the population, which in turn would reduce social interactions and stabilize infection rates at a lower level. Such a mechanism would prevent the surges in daily cases that were in fact observed. By instead modeling fear of contagion as a function of perceived mortality risk, our framework explains why periods of lower death rates coincided with rising daily infections during the second and third waves of the pandemic.

This assumption also helps explain the emergence of subsequent waves. At the onset of the pandemic, the COVID-19 case fatality rate was high in several countries, including the US, UK, and the Netherlands. The high mortality risk increased fear of contagion, leading many individuals to reduce their social activities and stay at home, which in turn suppressed virus

²Another behavioral response related to fear of contagion is pandemic fatigue, as discussed in Atkeson (2021), which is defined as a declining sensitivity of individuals' behavior to the COVID-19 mortality rate over time. While increases in reported daily deaths initially raise awareness and encourage protective behavior, this sensitivity diminishes as people grow fatigued with lockdown restrictions. Since both pandemic fatigue and fear of contagion are driven by perceptions of mortality risk, we incorporate them into the BSEIR model through the same behavioral framework and do not distinguish between them further.

transmission. As the case fatality ratio declined over time – whether due to the emergence of less deadly variants, improved medical capacity, or shifts in the age distribution of infections as vulnerable elderly groups were increasingly vaccinated – fear of contagion diminished. Consequently, susceptible individuals became more socially active, raising transmission rates and driving new waves of infections.

We also address another shortcoming in the existing literature, where behavioral responses to disease prevalence are introduced in an ad hoc reduced form and individuals are typically assumed to share the same level of sensitivity to mortality risk (see, for example, Perra et al. (2011), Epstein et al. (2021), and Atkeson (2021)). In contrast, our model introduces heterogeneity in behavioral sensitivity, allowing for differences in how individuals perceive and respond to mortality risk.

2.2.2 A Behavioral Theory of Fear of Contagion

At any time t during the pandemic, an agent born at $t_0 < t$ can choose between staying at home ($\lambda = 0$) or going out to engage in social interactions ($\lambda = 1$). Here λ is an indicator representing the individual's behavior at time t . For notational simplicity, we suppress the time subscript of λ in what follows. The life-time welfare of an agent born at time t_0 , evaluated at time t given behavior λ , is defined as

$$W(t|t_0, \lambda) = \int_t^{t_0+T} sp(t'|t_0, \lambda) e^{-\rho t'} u(c_{t'}|\lambda) dt' \quad (2.1)$$

where T is the expected longevity of individuals who are never infected by COVID-19, and ρ is the time discount rate. The instantaneous utility $u(c_{t'}|\lambda)$ at time t' depends on consumption and is conditional on the behavioral choice λ . Specifically, staying at home ($\lambda = 0$) is associated with lower utility, reflecting the disutility of reduced social interactions.

We denote by $sp(t'|t_0, \lambda)$ the survival probability at time t' for an agent born at t_0 with behavior λ . This probability declines over time at a rate $p(t' | t_0, \lambda)$, which depends both on the agent's age at time t' ($t' - t_0$) and on their behavioral choice λ . Formally, we have

$$\begin{aligned} \frac{d [sp(t|t_0, \lambda)]}{dt} &= -p(t|t_0, \lambda), \quad \forall t \in (t_0, t_0 + T), \\ sp(t_0|t_0, \lambda) &= 1, \\ sp(t|t_0, \lambda) &= 0, \quad \forall t < t_0 \text{ or } t > t_0 + T, \end{aligned}$$

which implies

$$sp(t'|t_0, \lambda) = sp(t|t_0, \lambda) - \int_t^{t'} p(t''|t_0, \lambda) dt'' \quad (2.2)$$

Combining equations (2.1) and (2.2), the lifetime welfare of an agent born at t_0 with behavioral choice λ can be expressed as

$$W(t|t_0, \lambda) = sp(t|t_0, \lambda) \int_t^{t_0+T} e^{-\rho t'} u(c_{t'}|\lambda) dt' - \int_t^{t_0+T} \left[\int_t^{t'} p(t''|t_0, \lambda) dt'' \right] e^{-\rho t'} u(c_{t'}|\lambda) dt' \quad (2.3)$$

Let ΔW denote the difference in welfare between going out and staying at home for an agent born at t_0 . Using Equation (2.3), we then obtain

$$\begin{aligned} \Delta W &= W(t|t_0, \lambda = 1) - W(t|t_0, \lambda = 0) \quad (2.4) \\ &= \int_t^{t_0+T} sp(t'|t_0, \lambda = 1) e^{-\rho t'} u(c_{t'}|\lambda = 1) dt' - \int_t^{t_0+T} sp(t'|t_0, \lambda = 0) e^{-\rho t'} u(c_{t'}|\lambda = 0) dt' \quad (2.5) \end{aligned}$$

The pandemic begins unexpectedly at time t , so it is reasonable to assume that

1. The probability of survival before t is independent of behavioral choice λ , since this choice is only made after the onset of the pandemic, i.e.,

$$sp(t|t_0, \lambda = 0) = sp(t|t_0, \lambda = 1).$$

2. Agents' consumption prior to time t is independent of λ , i.e.

$$c_{t'}(\lambda = 1) = c_{t'}(\lambda = 0), \quad t' < t.$$

Using these assumptions, the welfare difference ΔW in Equation (2.4) can be rewritten as

$$\begin{aligned} \Delta W &= W(t|t_0, \lambda = 1) - W(t|t_0, \lambda = 0) \\ &= \int_t^{t_0+T} \left[\int_{t_0}^{t'} p(t''|t_0, \lambda = 0) dt'' \right] e^{-\rho t'} u(c_{t'}|\lambda = 0) dt' \\ &\quad - \int_t^{t_0+T} \left[\int_{t_0}^{t'} p(t''|t_0, \lambda = 1) dt'' \right] e^{-\rho t'} u(c_{t'}|\lambda = 1) dt'. \quad (2.6) \end{aligned}$$

The welfare difference under different behavioral choices λ depends on the mortality rate following infection. A higher mortality rate associated with going out makes social interactions

considerably more costly in terms of expected welfare. If the mortality rate for going out increases uniformly for all individuals, from $p(\cdot|t_0, \lambda = 1)$ to $\delta p(\cdot|t_0, \lambda = 1)$ (with $\delta > 1$), then the welfare difference for agents born at t_0 can be expressed as

$$\Delta W_\delta = \Delta W_{\delta=1} - (\delta - 1) \int_t^{t_0+T} \left[\int_{t_0}^{t'} p(t''|t_0, \lambda = 1) dt'' \right] e^{-\rho t'} u(c_{t'}|\lambda = 1) dt' \quad (2.7)$$

where the correction term, $(\delta - 1) \int_t^{t_0+T} \left[\int_{t_0}^{t'} p(t''|t_0, \lambda = 1) dt'' \right] e^{-\rho t'} u(c_{t'}|\lambda = 1) dt'$, is negative for all $\delta > 1$. Therefore,

$$\Delta W_\delta - \Delta W_{\delta=1} < 0 \quad (2.8)$$

In other words, engaging in more physical social activities reduces welfare to a greater extent when the virus is more deadly.

2.2.3 Heterogeneous Preferences and Fear of Contagion

A clearly counterfactual implication of the mechanism developed in Section 2.2.2 is that it yields an all-or-nothing outcome: if the welfare function W is defined as above, agents of the same age would make the same behavioral choices. This contradicts observed behavior, as in reality some individuals go out while others stay home. To address this, we introduce agent-specific preferences for going out.

We consider a continuum of agents indexed by $h \in [h, \bar{h}]$, with density function $g(h)$, where h represents the additional benefit that an agent derives from going out. Agents with lower h exhibit greater fear of contagion, whereas those with higher h are less concerned about infection and are less willing to sacrifice their social life, even under high exposure risk. Here h reflects individual preferences and is independent of the pandemic situation.

To incorporate heterogeneity in the preference parameter h , we generalize the welfare function for an agent of type h as

$$\tilde{W}(t|t_0, \lambda, h) = h\lambda + W(t|t_0, \lambda).$$

This formulation incorporates the additional benefit from going out, $h\lambda$, alongside the welfare from consumption as defined in Equation (2.1). Then, for any given $\delta > 1$, we can define a cutoff preference level $h_c(\delta)$ such that if the mortality rate for going out is $\delta p(\cdot|t_0, \lambda = 1)$, agents with $h > h_c(\delta)$ will choose to go out, while those with $h < h_c(\delta)$ will stay at home. Agents with $h = h_c(\delta)$ are indifferent between the two options. Formally, the cutoff $h_c(\delta)$ satisfies the

equation

$$\Delta\tilde{W}_{(\delta,h_c)} := h_c(\delta) + \Delta W_\delta = 0. \quad (2.9)$$

As the virus becomes more life-threatening (i.e. as δ increases), the welfare associated with going out declines, making the welfare difference ΔW_δ more negative. Consequently, the cutoff preference level $h_c(\delta)$ rises.

Let $\pi(\delta) := \int_{\underline{h}}^{h_c} g(h)dh$ be the fraction of agents staying at home, then

$$\frac{d\pi}{d\delta} = g(h_c) \frac{dh_c}{d\delta} > 0 \quad (2.10)$$

which implies that a higher probability of death from infection leads more individuals to choose to stay at home. In other words, the aggregate level of fear of contagion is positively correlated with the mortality risk of COVID-19.

The main purpose of this section is to provide intuition for how increasing mortality risk influences agents' behavior. For simplicity, we assumed that agents make behavioral decisions at a given point in time based on the belief that their current assessment of the COVID-19 death rate remains constant. While a fully dynamic decision-making model that accounts for potential future updates in mortality estimates would be more realistic, it would also substantially increase complexity without altering the fundamental relationship between fear of contagion and mortality beliefs that we aim to highlight.

2.2.4 Belief Updating on COVID-19 Mortality Rate

Individuals' behavior depends on their beliefs about the current excess mortality rate δ , which evolves over time and is only imperfectly observable. As new information arrives, individuals continuously update their beliefs. Because it takes time for people to fully learn the true mortality rate, there is a lag between their beliefs and the actual rate. To capture this dynamic in the model, we denote the population's belief about the excess mortality rate δ_t at time t , as θ_t , and use the following rules to approximate the belief-updating process over time:

$$d\theta_t = \xi(\delta_t - \theta_t)dt. \quad (2.11)$$

This provides a reduced-form approximation of the learning process. Intuitively, the belief θ converges to the actual mortality rate δ at a speed ξ .

It is important to emphasize that individuals' behavior is driven by their *beliefs* about the excess mortality risk, rather than by the true mortality rate. Consequently, it is crucial to distinguish between their belief, $\theta(t)$, and the actual COVID-19 mortality rate, $\delta(t)$. We will

show in Section 2.5.1 that explicitly accounting for this distinction improves the accuracy of pandemic forecasts.

2.2.5 The BSEIRS Model

We are now ready to present the behavior-augmented SEIRS model, which incorporates various lockdown policies, the influence of agents' behavior on the pandemic trajectory, uncertain and limited vaccine effectiveness, and the possibility of reinfection. Standard SEIRS models categorize individuals to four groups: S (Susceptible), E (Exposed), I (Infectious), and R (Recovered).

We expand this framework in several ways. In our model, the recovered group includes not only individuals who have recovered from infection, but also those who have been vaccinated and acquired immunity. As immunity wanes over time, individuals in the recovered group can transition back to the susceptible state, making them vulnerable to reinfection. Furthermore, the pandemic path depends heavily on the timing and effectiveness of vaccines. Let t_{vac} be the arrival time of vaccines, $100\% \alpha$ their effectiveness against infection, and κ the reinfection rate. Without much loss of generality, we assume that vaccines are equally effective against all circulating variants, thereby avoiding the need to introduce additional health states into the model.

To integrate behavioral responses and the possibility of reinfection into our model, we divide susceptible individuals into three subgroups: (i) those who have never been infected or vaccinated and fear infection (S_f), (ii) those who have never been infected or vaccinated but do not fear infection (S_{nf}), and (iii) those who become susceptible again after recovery or vaccination due to reinfection or waning immunity (S_m). Individuals in S_m believe they are immune to COVID-19 and thus behave without fear of contagion, regardless of the virus' mortality rate. Susceptible individuals in S_{nf} and S_f adjust their behavior over time according to the current mortality rate and the belief-updating rule described in Section 2.2.4. The definitions of the states S_{nf} , S_f , S_m , along with all other health states in the BSEIRS model (E , E_v , I , I_v , H , R and D) are summarized in Table 2.1.

Following Section 2.2.1, we define $\delta(t)$ as the excess mortality rate applicable to all infected individuals, regardless of whether they stay at home or go out. That is, once infected at t , every individual faces the same death rate, $\delta(t)$. When $\delta(t) = 1$, the mortality rate of COVID-19 equals the natural death rate, implying that the pandemic has no additional health effect. As $\delta(t)$ increases, individuals infected with the virus face a higher chance of death.

At time t , all susceptible individuals must decide whether to adjust their behavior based on their current belief, $\theta(t)$, about the excess mortality rate, $\delta(t)$. Let $\pi(\theta(t))$ be the proportion of susceptible individuals in state S_f relative to the total number of individuals in states S_{nf} and S_f .

Table 2.1: Health States in the Baseline Behavioral SEIR Model

Notation	Definition
S_{nf}	Susceptible individuals without fear of contagion
S_f	Susceptible individuals with fear of contagion
S_m	Individuals who becomes susceptible again after recovery and vaccination
E	Exposed to the original variant (but not yet infected)
E_v	Exposed to the new variant (but not yet infected)
I	Infected by the original variant
I_v	Infected by the new variant
H	Hospitalized (critically ill in ICUs)
R	Recovered from the disease or vaccinated (immune to the virus)
D	Death after the treatment in ICUs

Immediately before the pandemic progresses at time t , a behavioral shift occurs, redistributing individuals between states S_f and S_{nf} . Specifically, the number of individuals in state S_{nf} becomes

$$S_{nf}(t) \leftarrow (1 - \pi(\theta(t))) [S_{nf}(t) + S_f(t)],$$

and the number of individuals in state in S_f becomes

$$S_f(t) \leftarrow \pi(\theta(t)) [S_{nf}(t) + S_f(t)].$$

The dynamics of the BSEIRS model are described by the following system of equations:

$$\dot{S}_{nf}(t) = -[\beta(t)I(t) + \beta_v(t)I_v(t)]S_{nf}(t) - m_0(t) \quad (2.12a)$$

$$\dot{S}_f(t) = -[p\beta(t)I(t) + p\beta_v(t)I_v(t)]S_f(t) - m_f(t) \quad (2.12b)$$

$$\dot{S}_m(t) = -[\beta(t)I(t) + \beta_v(t)I_v(t)]S_m(t) + (1 - \alpha)(m_0(t) + m_f(t)) + \kappa R(t) \quad (2.12c)$$

$$\dot{E}(t) = \beta(t)I(t)S_{nf}(t) + p\beta(t)I(t)S_f(t) + \beta(t)I(t)S_m(t) - \sigma E(t) \quad (2.12d)$$

$$\dot{E}_v(t) = \beta_v(t)I_v(t)S_{nf}(t) + p\beta_v(t)I_v(t)S_f(t) + \beta_v(t)I_v(t)S_m(t) - \sigma E_v(t) + \bar{E}_v(t) \quad (2.12e)$$

$$\dot{I}(t) = \sigma E(t) - \gamma I(t) \quad (2.12f)$$

$$\dot{I}_v(t) = \sigma E_v(t) - \gamma I_v(t) \quad (2.12g)$$

$$\dot{H}(t) = \eta(t)\gamma(I(t) + I_v(t)) - \zeta H(t) \quad (2.12h)$$

$$\dot{R}(t) = (1 - \nu(t))\zeta H(t) + (1 - \eta(t))\gamma(I(t) + I_v(t)) + \alpha(m_0(t) + m_f(t)) - \bar{E}_v(t) - \kappa R(t) \quad (2.12i)$$

$$\dot{D}(t) = \nu(t)\zeta H(t) \quad (2.12j)$$

Individuals in states $S_{nf}(t)$ and $S_f(t)$ are susceptible but not yet exposed. They can either become exposed to the virus or receive vaccination. The exposure rate to the original variant

is proportional to the number of infections, $\beta(t)I(t)$, and for the new variant, $\beta_v(t)I_v(t)$. The parameter $p \in (0, 1)$ in Equation (2.12b) indicates that the probability of contagion for individuals in S_f is reduced to $100p\%$ of that for individuals in S_{nf} . Because individuals who fear contagion engage in fewer social interactions, they face a lower risk of infection compared to those who are less cautious. Vaccines are distributed randomly at a constant rate m . The vaccination rates for susceptible individuals are weighted by subgroup size: $m_{nf}(t) := m \frac{S_{nf}(t)}{S_{nf}(t)+S_f(t)}$ and $m_f(t) := m \frac{S_f(t)}{S_{nf}(t)+S_f(t)}$, respectively.³ Limited vaccine effectiveness ($\alpha < 1$) implies that vaccinated individuals either acquire immunity and transition to R with probability α , or fail to gain immunity and move to susceptible state S_m with probability $1 - \alpha$.

Individuals exposed to the virus become infected at a rate σ , which we assume to be the same for all variants (Equations 2.12f and 2.12g). Infected individuals leave states I or I_v at a constant rate γ , with a probability $\eta(t)$ of becoming critically ill and hospitalized⁴, and a probability of $(1 - \eta(t))$ of recovering from the disease. Equation (2.12h) indicates that critically ill individuals exit the hospital at rate ζ . Upon discharge, they either die with probability $\nu(t)$ (Equation 2.12j) or recover with probability $1 - \nu(t)$ (Equation 2.12i). Individuals in the recovered state R may become susceptible again and transition to state S_m at rate κ .

The transmission rates $\beta(t)$ for the original variant and $\beta_v(t)$ for the new variants are directly affected by lockdown policies in the following manner:

$$\beta(t) = \bar{\beta} (1 - ld(t)) (1 + \psi(t)) \quad (2.13)$$

$$\beta_v(t) = \bar{\beta}_v (1 - ld(t)) (1 + \psi(t)) \quad (2.14)$$

where $\bar{\beta}$ and $\bar{\beta}_v$ represent the natural transmission rates in the absence of seasonality effects or lockdown measures (later referred to as “Laissez Faire”). The parameter $ld(t)$ quantifies the stringency of lockdown policies, including the closure of public spaces and implementation of preventive measures such as social distancing and mask wearing, while $\psi(t)$ captures the seasonality factor.

Finally, in another extension of the standard SEIRS model, we account for the emergence of a new variant at a specific date t_v following the appearance of the original variant. To capture this, we introduce two additional health states: E_v representing individuals exposed to the new variant, and I_v representing those infected by it. The new variant is introduced via a shift factor $\bar{E}_v(t)$ in Equation (2.12e), where $\bar{E}_v(t) = 0$ for all $t \neq t_v$ and $\bar{E}_v(t_v) = 1$.⁵

³In this model, vaccination (partially) prevents infection. Appendix 2.C presents an alternative model in which vaccination does not reduce infection risk but lowers the probability of severe illness if infected.

⁴In reality, the rate of hospitalization varies across different age groups. Here, we do not explicitly model the age structure, and $\eta(t)$ represents the average hospitalization rate.

⁵In Equation (2.12i) this quantity is subtracted from the change in the recovered state R to maintain a constant total population. Because this shift involves only a single individual at t_v , its effect on the quantitative implications of the model for the entire population is negligible.

2.3 Vaccines as Options and the Health Benefits of Lockdown Strategies

In this section, we provide the theoretical framework for quantifying the option values associated with different lockdown strategies, which stem from the uncertainty in vaccine timing and effectiveness. Epidemiologists widely recommended lockdown measures during the COVID-19 pandemic to mitigate waves of contagion and reduce the peak of the infection curve. This perspective has also been a primary focus in the existing literature; see in particular Kaplan et al. (2020), where vaccines are assumed to arrive at a known date and to be fully effective upon arrival. In contrast, this paper adopts a different approach: we focus on the uncertainties surrounding vaccine arrival and effectiveness, and explore the implications of this uncertainty for the valuation of lockdown strategies.

A partially effective vaccine ($\alpha < 1$) can be viewed as a binary option: choosing to take the vaccine (exercising the option) may provide immunity or may not, whereas not taking it guarantees no protection. For a new disease or a new variant of an existing disease, this option is often unavailable initially, and both the timing and likelihood of vaccine availability are uncertain. This uncertainty significantly complicates the valuation of the binary option. Furthermore, it introduces an option value to lockdown strategies, as highlighted in van Wijnbergen (2022). Lockdowns flatten the infection curve and, while they may have limited impact on total mortality, they shift deaths backwards in time. This means that at any given moment, more people are alive than would have been without lockdowns, including at the time a new vaccine becomes available. Those additional individuals alive at the vaccine arrival date gain the opportunity to exercise the binary vaccine option, which they would have missed without the earlier implementation of lockdowns. The surplus value arising from this increased access constitutes the real-option value of lockdown strategies.

Of course, lockdowns may have intrinsic value independent of their effect on the number of people who gain access to future vaccines. Conversely, the value of vaccine development is directly influenced by lockdowns if they affect the population eligible to receive the vaccine. To capture this interaction, we solve the decision-making problem faced by a government that must simultaneously decide its lockdown strategy and how much to invest in securing early vaccine availability.

2.3.1 Total Health Benefits of Lockdown Strategies

At the onset of the pandemic ($t = 0$), the government must decide on

1. The lockdown policy to be implemented during the pandemic;
2. Whether to pay upfront for early access to vaccines once they become available.

Governments have many potential lockdown policies to choose from. We focus on three possible policy designs: (i) Laissez-faire (LF), in which no lockdown restrictions are imposed; (ii) Intermittent lockdowns (LD), as implemented in the Netherlands; and (iii) Rollover-infection lockdowns (RO), aimed at flattening the infection curve by maintaining the effective reproduction number at one. As in Section 2.2.5, we denote the time path of lockdown severity by $ld(t)_t$.

In addition to selecting a lockdown strategy, the government must also decide whether to allocate funding for vaccine development via an upfront payment, and if so, the amount to invest. Providing funding may lead to the development of a vaccine, though its arrival is uncertain and its effectiveness may be partial ($\alpha < 1$). Conversely, if the government chooses not to make an upfront payment, no vaccine will be available in the future. Let the indicator variable v equal 1 if the government makes the upfront payment and 0 otherwise. If the upfront payment is made ($v = 1$), the vaccine arrival is modeled as a Poisson process with a time-dependent arrival rate $\lambda(t)$. As vaccine development progresses, the probability of discovering a vaccine increases, which is modeled by a linear arrival rate, $\lambda(t) = \bar{\lambda}t$, with $\bar{\lambda} > 0$.

The health benefits of the government's decisions regarding lockdown strategy and vaccine development funding accrue through two channels. First, lockdowns slow the progression of the pandemic, and, if sufficiently stringent, help prevent ICU overload. The net effect is a flattening of the cumulative death curve. While delaying the mortality curve may or may not ultimately reduce total deaths, it clearly preserves life years. The health benefits arising from this first channel depend solely on the stringency and duration of lockdowns and are independent of the vaccine development process. Second, stringent lockdowns prevent or at least mitigate the likelihood of sharp surges of infections before vaccines become available. In effect, lockdowns buy additional time for susceptible individuals who might otherwise have died from COVID-19 prior to vaccine availability. The health benefits arising from this second channel stem from the interaction between lockdown measures and vaccine timing and effectiveness, and this interaction is the main focus of this paper.

Formally, let $V(\{ld(t)\}_t, v)$ be the total value of statistical life years (TVSLY) under government policy $(\{ld(t)\}_t, v)$. We define the health benefits of a lockdown strategy $\{ld(t)\}_t$ as

$$V^e(\{ld(t)\}_t, 1) := V(\{ld(t)\}_t, 1) - V(LF, 0)$$

that is, the TVSLY under policy $(\{ld(t)\}_t, 1)$ minus the TVSLY under the baseline strategy $(LF, 0)$ when the government neither imposes lockdown restrictions nor provides upfront funding for vaccine development. The value V^e can be further decomposed as follows:

$$\begin{aligned} V^e(\{ld(t)\}_t, 1) &= V(\{ld(t)\}_t, 1) - V(LF, 0) \\ &= [V(\{ld(t)\}_t, 1) - V(\{ld(t)\}_t, 0)] + [V(\{ld(t)\}_t, 0) - V(LF, 0)] \end{aligned} \tag{2.15}$$

where the two terms in the second line correspond to the health benefits from the second and the first channel mentioned in the previous paragraph. The government's decision to implement a specific policy $(ld(t)_t, v)$ depends on the value of $V^e(ld(t)_t, v)$ as well as the total cost of vaccines⁶, which includes both the upfront payment for vaccine development and the cost of vaccine doses once they become available.

2.3.2 The Option Value of Lockdowns

The option value of a lockdown period is defined as the health benefit associated with waiting for vaccines under a given lockdown strategy. In other words, it measures the additional lives and life-years saved by implementing a lockdown, compared to a laissez-faire approach in which no such waiting occurs. For susceptible individuals, lockdowns effectively buy time by delaying the COVID-19 mortality curve, increasing the probability that they are vaccinated before becoming infected. In this sense, a lockdown offers binary options with uncertain exercise timing to those who would not have been alive at the time of vaccine availability without the lockdown.

Formally, the option value of a lockdown policy $\{ld(t)\}_t$ can be expressed as

$$V(\{ld(t)\}_t, 1) - V(LF, 1)$$

where $V(\{ld(t)\}_t, 1)$ and $V(LF, 1)$ are the lives and life-years saved under stochastic arrival of vaccines for the lockdown strategy $\{ld(t)\}_t$ and for the laissez-faire scenario, respectively. Intuitively, the option value captures how much extra health benefit a lockdown policy brings under vaccine uncertainty compared with laissez-faire; it is the value of more people gaining access to life-saving vaccines once they become available. The option value differs from the total health benefits of vaccination, which were discussed in Section 2.3.1.

2.3.3 The Maximum Upfront Payment for Vaccines

To clarify the concept of the option value of a lockdown, we compare it with another metric: the maximum upfront payment for vaccines, which reflects the government's willingness to invest in vaccines in advance. It quantifies the lives and life-years saved by vaccination under a given lockdown policy. Unlike the option value of lockdown, which primarily captures the benefit of delaying infections until vaccines become available, the maximum upfront payment directly measures the value of vaccination itself.

⁶In practice, governments of smaller countries may invest less in vaccine development. For larger countries, financing vaccine research generates minimal international externalities, as a substantial portion of the benefits accrues domestically. For smaller countries, however, there is a significant externality, since foreign populations also benefit from vaccine development.

For a given lockdown policy, we calculate the maximum upfront payment for vaccines as the difference between the health benefits derived from vaccination and the cost of buying vaccines. Using the same notations as above, this can be expressed as

$$V(\{ld(t)\}_t, 1) - V(\{ld(t)\}_t, 0) - cN$$

where $V(\{ld(t)\}_t, 1) - V(\{ld(t)\}_t, 0)$ is the health benefits from vaccines, c is the price per vaccine dose, and N is the total population of the country.

2.4 Calibration

Epidemiological Model The basic reproduction number $R_0 := \frac{\bar{\beta}}{\gamma}$ of the original variant was time-varying with the initial value 2.5 according to Liu et al. (2020) which summarized 12 studies estimating the basic reproductive number of COVID-19 in China and overseas from 1 January and 7 February 2020. We also consider two World Health Organization (WHO)-designated variants of concern (VOCs) which prevailed in the Netherlands during our study period: Alpha (B.1.1.7) and Delta (B.1.617.2), see Figure 2.1. The figure shows that the most transmissible variant will gradually dominate the others when several variants coexist. Therefore, in the pandemic simulations, we assume that the joint impact of all circulating variants is determined by the most contagious variant, which becomes dominant around seven days after its emergence. This approach avoids the need to introduce additional health states, thereby reducing the associated computational complexity. More detailed information on the variants is provided in Table 2.2.

Figure 2.1: Percentage of variants detected in the Netherlands.

(Source: <https://coronadashboard.government.nl/landelijk/varianten>)

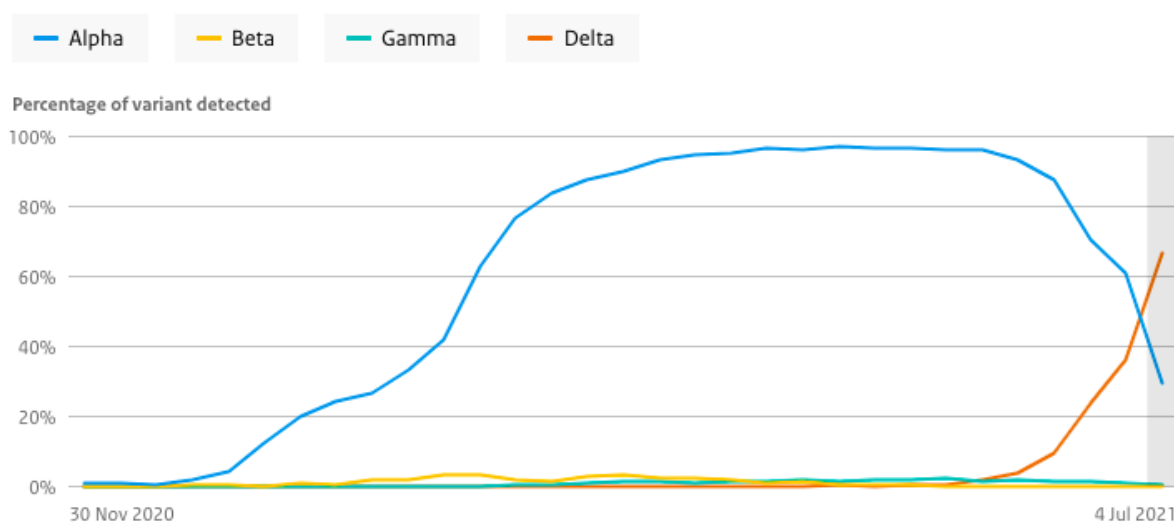


Table 2.2: Information on the dominating SARS-CoV-2 variants in the Netherlands in 2020 and 2021. The percentage of infections for each variant can be found in the RIVM Coronavirus Dashboard. Data are updated weekly so the arrival date of a new variant is set as the middle of the week when it was first reported. Basic reproduction numbers are provided by Davies et al. (2021) and Liu and Rocklöv (2021).

Label	Scientific Name	Reproduction No.	Arrival Date	Day
Alpha	B.1.1.7	3.9	3 Dec 2020	281
Delta	B.1.617.2	5.08	27 May 2021	456

The other parameter values of the BSEIRS model are summarized in Table 2.3. All except κ are determined according to the calibrations in Atkeson (2021) using CDC data⁷. The value of the reinfection rate κ matches the finding of reduced protection from infection in previously uninfected participants after 6 months (Doria-Rose et al. (2021)).

Table 2.3: Values of Epidemiological Parameters

Parameter	Value	Explanation
γ	0.4	Recovery rate
σ	0.425	Transfer rate from exposed to infected
ζ	$\frac{1}{10}$	Exit rate from hospital
κ	$\frac{1}{180}$	Reinfection rate
$\bar{\beta}$	γR_0	Baseline transmission rate of the original variant
$\bar{\beta}_v$	$\gamma R_{v,0}$	Baseline transmission rate of the new variant
<i>seasonalsize</i>	0.25	The scale of the seasonal fluctuation in virus transmissibility
<i>seasonalposition</i>	30	The location of the seasonal peak
p	0.25	The ratio of infection probabilities for S_f and S
δ_N	0.009	Natural mortality rate (Netherlands in 2019)

Contrary to Atkeson (2021), we do not assume a constant COVID-19 mortality rate. Pandemic data from the Netherlands⁸ show that both the percentage of hospitalized individuals with severe illness among the infected population (denoted $\eta(t)$) and the mortality rate for critically ill patients (denoted $\nu(t)$) vary over time. To ensure consistency with the Dutch pandemic data, we assign the values shown in Figure 2.2 to $\eta(t)$ and $\nu(t)$ correspondingly. The hospitalization rate $\eta(t)$ decreases over time, while the mortality rate $\nu(t)$ fluctuates. Notably, the mortality rate was higher during the first wave of the pandemic compared to subsequent waves. Overall, Figure 2.2 suggests that the virus becomes less deadly over time. This trend may be attributed to the prioritization of vaccination for the most vulnerable age groups, particularly older individuals. As a result, the unvaccinated population gradually shifts toward younger individuals, who are generally less susceptible to severe symptoms.

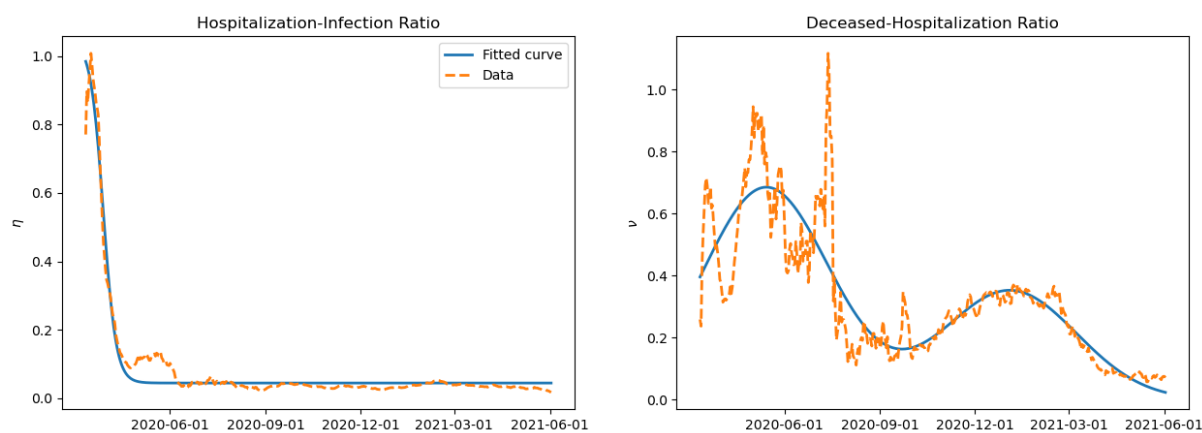
⁷See <https://COVID.cdc.gov/COVID-data-tracker/#datatracker-home>

⁸Raw data and explanations can be found on the Coronavirus Dashboard (see <https://coronadashboard.government.nl/>), which are provided by the National Institute for Public Health and the Environment (RIVM), municipal health services (GGDs) and hospitals in the Netherlands.

There are two issues with using the pandemic data-based estimates of η and ν (the blue lines in Figure 2.2). First, both the hospitalized-to-infected ratio η and the deceased-to-hospitalized ratio ν are fractions and should therefore stay below one. However, the values shown in Figure 2.2 sometimes exceed one. This arises from the time lag between infection and hospitalization, and between hospitalization and subsequent death. The ratios η and ν are calculated using *concurrent* variables, which means that the number of hospitalized patients at a given time can exceed the *current* number of infected individuals if infections are falling. The same issue affects the measurement of ν .

The second issue is that both series are highly volatile, especially during the early stage of the pandemic, while it is reasonable to expect that they would change only gradually over time. This spurious volatility is most likely caused by the use of concurrent data and possibly also by delays in reporting pandemic outcomes. Therefore, instead of using the raw values derived directly from the pandemic data, we apply a smoothing algorithm to both η and ν (see the blue lines in Figure 2.2). Details of the smoothing algorithm are provided in Appendix 2.A.

Figure 2.2: The hospitalization-infection ratio η and the deceased-hospitalization ratio ν . The dashed curves represent values calculated from the moving average data, while the solid curves show the fitted smooth curves.



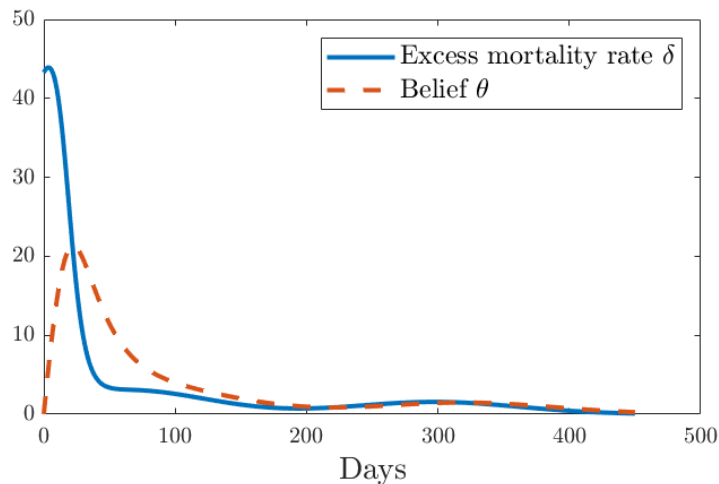
Using the smoothed values of $\eta(t)$ and $\nu(t)$, we can compute the excess mortality rate $\delta(t)$. As defined in Section 2.2.1, $\delta(t)$ represents the ratio of the probability of dying following a COVID-19 infection at time t to the natural death probability δ_N , so the probability of death from COVID-19 once infected is given by $\delta(t)\delta_N$. Since $\eta(t)$ is the conditional probability of hospitalization once infected, and $\nu(t)$ is the conditional probability of death given hospitalization, the probability of dying from COVID-19 once infected can be expressed as the product $\eta(t)\nu(t)$. Therefore, the excess mortality rate is given by

$$\delta(t) = \frac{\eta(t)\nu(t)}{\delta_N}.$$

Using the smoothed values of η and ν , we can then construct the time path of $\delta(t)$ for use in our simulations.

Individuals update their beliefs about the excess mortality rate based on the currently available pandemic data. Following the belief updating procedure outlined in Section 2.2.4, we set the initial belief on the excess mortality rate as the natural death rate $\delta_N = 0.009$, and calibrate the convergence rate ξ to 0.04. The temporal evolution of both the belief $\theta(t)$ and the actual excess mortality rate $\delta(t)$ is shown in Figure 2.3. Initially, individuals tend to underestimate the true excess mortality rate. However, as more pandemic data becomes available, their beliefs gradually adjust and eventually converge to the concurrent actual mortality rate.

Figure 2.3: The actual excess mortality rate $\delta(t)$ and the belief $\theta(t)$ in the first 450 days since the onset of the pandemic in the Netherlands.



The Dutch Vaccination Program The COVID-19 vaccination program in the Netherlands began in January 2021, with the rollout speed accelerating over time. As of 10 July 2021, a total of 17,960,133 doses have been administered, of which 11,693,749 are first doses and 6,228,245 are second doses. On average, around 0.4% of the population received their first dose each day. Four types of vaccines (BioNTech/Pfizer, Moderna, AstraZeneca, Janssen) are available in the Netherlands, with BioNTech/Pfizer and AstraZeneca being the most widely administered vaccines after accounting for differences in required doses. The corresponding effectiveness rates are around 80% for BioNTech/Pfizer and 60% for Astra/Zenica.⁹ Accordingly, we examine three scenarios for vaccine effectiveness in the simulations: 80%, 60% and full (100%) effectiveness. We abstract from the effect of the second dose, since the majority of vaccine-induced immunity comes from the first dose and the time interval between doses is relatively short.

⁹According to the Institute for Health Metrics and Evaluation (IHME), University of Washington. Data source: <https://www.healthdata.org/COVID/COVID-19-vaccine-efficacy-summary>

Lockdown Strategy Official announcements regarding COVID-19 measures in the Netherlands are archived on the government website¹⁰. Regulations have been frequently revised throughout the pandemic. We summarize the implemented policies in a stylized manner in Table 2.4. To justify the chosen values for lockdown stringency, we compare them with the stringency index data from the Oxford COVID-19 Government Response Tracker (OxCGRT). Appendix 2.B shows that our values reflect the timing of major policy changes while avoiding unnecessary disturbances to the simulated pandemic trajectory.

Table 2.4: Lockdown timeline

Lockdown dates	Severity	Explanation
Day 1 - 26	0	Before national-level lockdown policy.
Day 27 - 95	0.4	Stricter lockdown rules are announced at a press conference on 23 March 2020.
Day 96 - 230	0.2	Bar and restaurants reopened on 1 June 2020.
Day 231 - 292	0.5	Lockdown tightened in November 2020.
Day 293 - 490	0.64	Stricter lockdown from 15 December 2020 and curfew starting from 23 January 2021.

Value of Statistical Life (Years) and the Cost of Vaccines Following Kniesner et al. (2012), we set the value of a statistical life (VSL) at 7 million USD and the value of a statistical life year (VSLY) at 0.3 million USD.¹¹ The population of the Netherlands is approximately 17.5 million. Dyer (2021) provides the prices of each vaccine type in the Netherlands, which are summarized in Table 2.5 along with the percentage of each type administered by 10 July 2021¹². The prices reported were applicable in late January of 2021. We use the weighted average vaccine price (\approx \$13 per dose) for computation and assume each person receives two doses.¹³

Table 2.5: Price List of Vaccines for EU and the Percentage of Doses in the Netherlands

	BioNTech-Pfizer	Moderna	AstraZeneca	Janssen
Price per dose (\$)	14.7	18	2.15	8.5
Percentage	71.9%	8.4%	15.6%	4.1%

¹⁰<https://www.government.nl/topics/coronavirus-COVID-19/news>

¹¹We have not found VSL/VSLY estimates specific to the Netherlands. Kniesner et al. (2012)'s estimates are based on US data.

¹²Percentages are calculated based on the total number of doses and differ from the distribution of vaccines among the population, because the Janssen vaccine requires a single dose while the others requires two.

¹³This may overestimate the cost of purchasing vaccines slightly since Janssen is a single-shot vaccine. However, due to lack of information on the precise number of receivers of each vaccine and the fact that only a small fraction of the population received the Janssen vaccine, our computation provides a reasonable approximation.

2.5 Simulation Results

In this section, we present the simulated pandemic trajectories in the Netherlands using the BSEIRS model described in Section 2.2.5, compute the option value of lockdowns, and quantify the portion of the total health benefit of lockdown that is attributed to the option value of lockdown.

With the possibility of reinfection, herd immunity against COVID-19 may not be achievable in the long run. This complicates the evaluation of lockdown and vaccination policies due to uncertainties regarding new variants, vaccine development, and the duration of the pandemic. The goal of the numerical exercises in this section is to provide a quantitative comparison across different lockdown and vaccination strategies. To ensure consistency, we restrict the simulation period for all policies considered. Simulations begin on the date of the first reported case and span 500 days ($T = 500$), from 27 February 2020 to 10 July 2021.

2.5.1 Pandemic Simulations

Figure 2.4 presents the simulated trajectories of daily COVID-19 infections and deaths in the Netherlands, together with the corresponding empirical data. Three possible values of vaccine effectiveness are considered: full effectiveness ($\alpha = 1$), Pfizer ($\alpha = 0.8$) and AstraZeneca ($\alpha = 0.6$). The simulated infection curves with 80% of vaccine effectiveness closely match the empirical data, particularly capturing with the turning points observed in the infection trajectory.

The simulated trajectories diverge across different levels of vaccine effectiveness once vaccinations begin to take effect around Day 370. Higher vaccine effectiveness leads to a more pronounced decline in daily infections. A similar pattern is observed in the daily deaths curve, although differences across effectiveness levels are less pronounced, reflecting the gradual decrease in the virus' lethality over time. The sharp rise in infections around Day 470 is driven by the emergence of a more transmissible new variant, highlighting that infection rates increase more rapidly under lower vaccine effectiveness when a new variant emerges.

Figure 2.4: Data and simulations of daily infections and deaths under different vaccine efficacy.

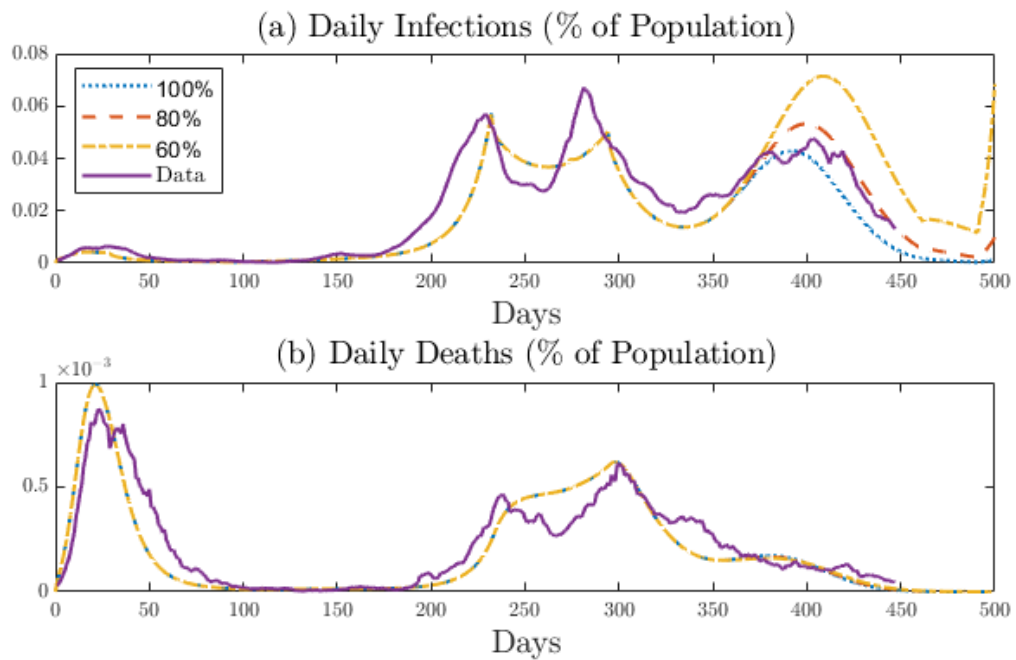
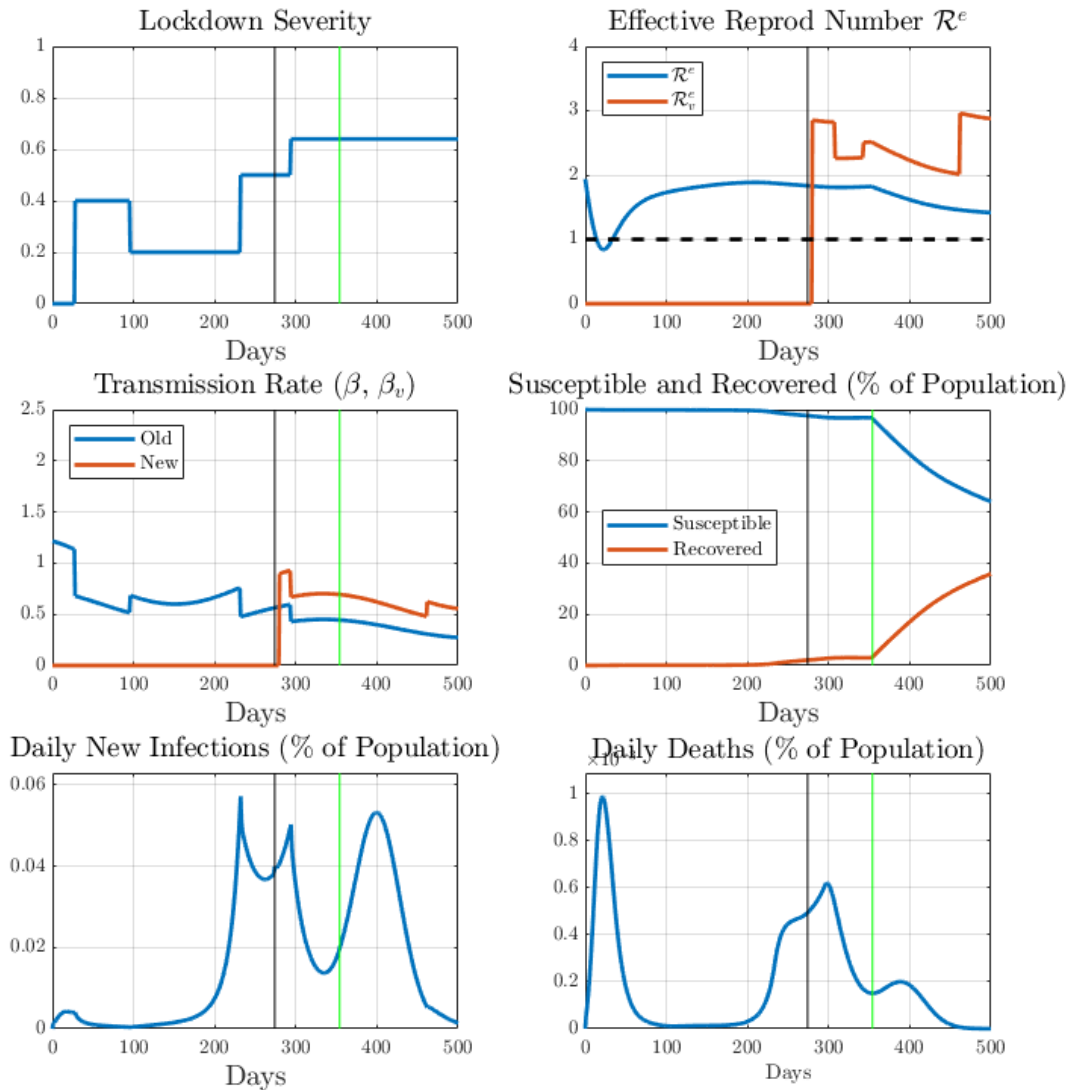


Figure 2.5 presents the simulated trajectories of additional pandemic-related variables, including lockdown severity, the effective reproductive number, the transmission rate, the proportion of individuals in susceptible and recovered states, and daily infections and deaths. The black and green vertical lines in each plot indicate the arrival of the first new variant and the vaccine, respectively. The emergence of a more transmissible variant results in an immediate surge in the transmission rate, infections and deaths. In contrast, the impact of the vaccine rollout unfolds more gradually, reflecting the time required to distribute the vaccines.

Figure 2.5: Simulated pandemic trajectories for the first 500 days of the pandemic in the Netherlands. The black and green vertical lines refer to the arrival time of the first new variant and the vaccine. Vaccine effectiveness is set at 80% and antibodies diminish at a rate of $\kappa = 1/180$.

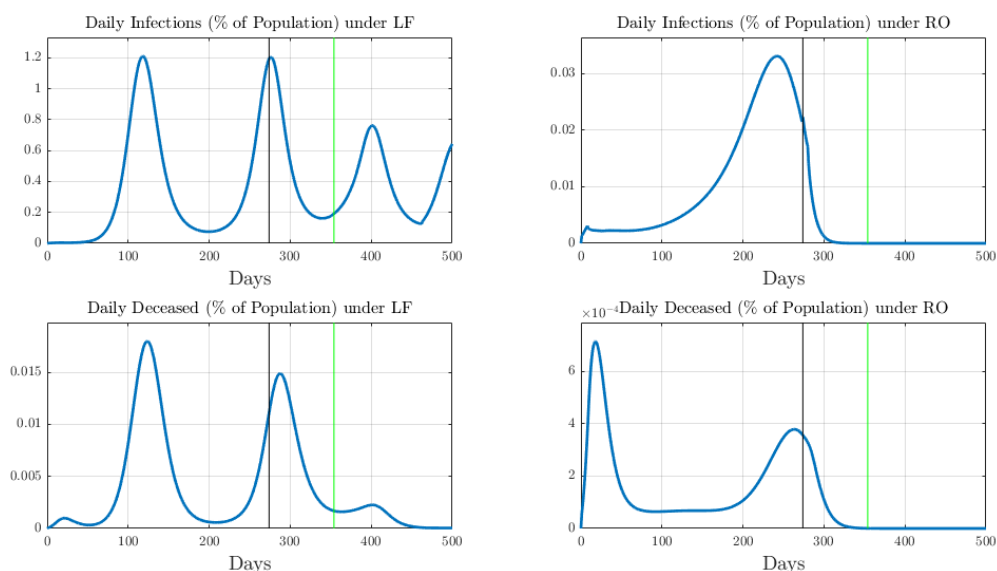


Simulations Under Other Lockdown Strategies To assess the impact of other lockdown strategies on virus transmission, we simulate the pandemic under two additional strategies: Laissez faire (LF) and rollover-infection lockdown (RO). We assume that the rollover strategy (RO) starts eight days after the first reported case, consistent with the timing of the Dutch-type intermittent lockdown (LD).

Figure 2.6 shows the simulations of daily infections and deaths under LF and RO strategies. Compared with the intermittent lockdown (LD) in the Netherlands, the peaks of infection and death curves are higher under LF and lower under RO. This implies that stricter lockdown

measures are effective in preventing sharp surges in infections and reducing COVID-related mortality.

Figure 2.6: Simulated daily infections and deaths under *laissez faire* (LF) and rollover lockdown (RO), where the vaccine effectiveness is $\alpha = 0.8$.



2.5.2 Option Values of Lockdown

In this subsection, we present the computational results for the option values of various lockdown strategies. In particular, we examine how the vaccine arrival rate, effectiveness, and roll-out speed affect the option values. Our numerical results indicate that under the stochastic arrival of vaccines, the option value represents the major component of the total health benefits associated with any given lockdown policy.

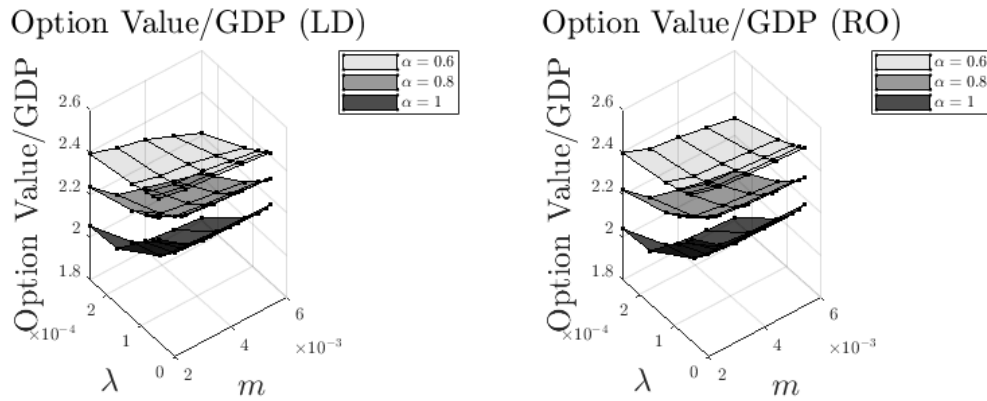
Moreover, we emphasize that the option value differs from the health benefit provided by vaccines. To illustrate this, we compute the maximum upfront payment the government would be willing to make for early access to vaccines. This maximum upfront payment reflects the government's expected health benefits from the vaccines. Our findings show that these expected benefits differ from the option value, thereby justifying the distinction between the two types of health benefits associated with lockdown measures.

We conduct a 500-day pandemic simulation under each lockdown policy. The numerical results capture the health benefit of government interventions over the first 500 days following the pandemic outbreak. Detailed computational procedures are provided in Appendix 2.D.

Option Values Figure 2.7 presents the option value of each lockdown policy, expressed as a multiple of the Netherlands' 2020 GDP (912 billion, World Bank). This value is affected not

only by the chosen lockdown policy but also by the vaccine arrival rate (λ), the vaccination roll-out speed (m), and vaccine effectiveness (α).

Figure 2.7: Ratios of option values and the Dutch GDP under lockdown policy LD and RO.



We provide a comprehensive overview of the option values under different scenarios in Table 2.6. For both the LD and the RO strategies, the option value decreases as the vaccine arrival rate λ , vaccine effectiveness α , and the roll-out speed m of vaccines increase. A high arrival rate λ implies that vaccines become available early, leaving little waiting time for the potential binary option holders under lockdown. For instance, consider an extreme scenario where vaccines were available within just a few days. In this case, only a small fraction of the total population would be infected prior to vaccination, even under the least stringent lockdowns. Therefore, the early availability of vaccines has a limited effect on the value of statistical lives saved.

Conversely, when vaccines are rolled out slowly (i.e., when m is small) or have low effectiveness (i.e., when α is small), immunity in the population accumulates more gradually. Under these conditions, lockdown measures prevent a larger number of infections before vaccination and slow virus transmission by restricting social activity among the susceptible. As a result, the option value of lockdowns is higher.

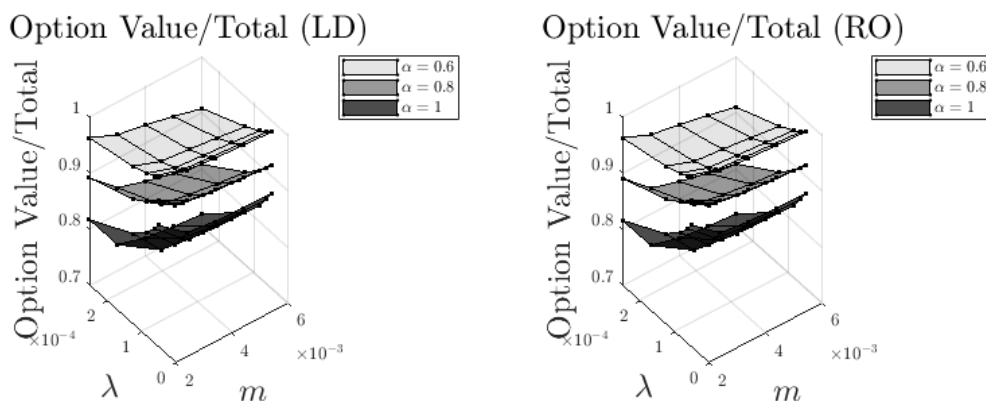
Comparing the option values under intermittent lockdown (LD) and roll-out (RO) lockdown policies, we find that more stringent lockdowns yield higher option values, given the same vaccine arrival rate, effectiveness and roll-out speed. Intuitively, stricter lockdowns provide better protection against the virus, and therefore effectively extend the time available for susceptible individuals to receive vaccines before exposure to the virus.

Figure 2.8 shows the proportion of option value in the total health benefits of government lockdown and vaccination policies. Under both LD and RO strategies, the option value makes up the majority of the total health benefit. In all scenarios considered in our simulations, the option value accounts for at least 70% of the total health benefits attributable to lockdown measures under stochastic vaccine arrival.

Table 2.6: Ratios of option values and the Dutch GDP (OV/GDP) under the Dutch intermittent lockdown (LD) and the roll-over infection lockdown (RO).

Effectiveness α	Arrival Rate $\bar{\lambda}$	LD			RO		
		0.003	0.004	0.005	0.003	0.004	0.005
100%	0.05	2.188	2.173	2.168	2.186	2.171	2.167
	0.08	2.100	2.085	2.079	2.090	2.076	2.072
	0.13	2.023	2.005	1.998	2.011	1.995	1.991
80%	0.05	2.325	2.309	2.298	2.325	2.308	2.298
	0.08	2.272	2.253	2.239	2.263	2.245	2.233
	0.13	2.223	2.201	2.181	2.211	2.191	2.175
60%	0.05	2.447	2.438	2.425	2.457	2.447	2.440
	0.08	2.425	2.414	2.393	2.426	2.417	2.408
	0.13	2.401	2.386	2.356	2.399	2.389	2.376

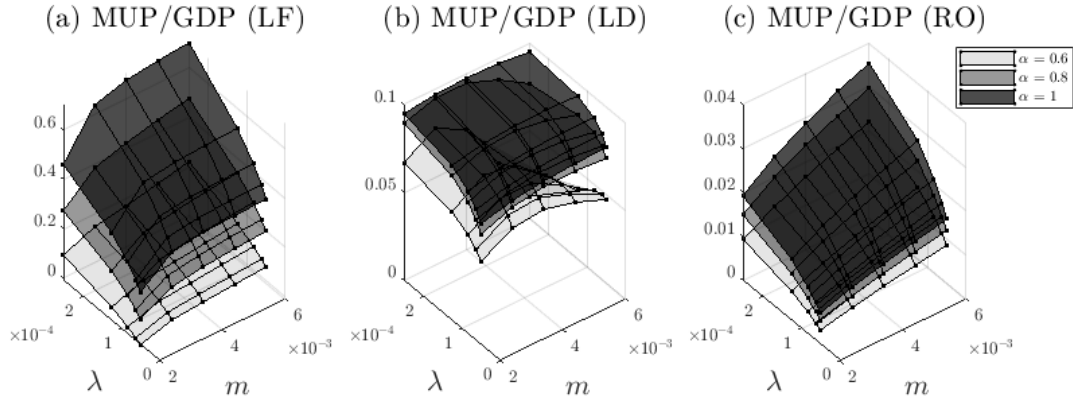
Figure 2.8: The proportion of option value in the total benefits from government lockdown and vaccination policies in different scenarios.



Maximum Upfront Payment for Vaccines Next, we calculate the government's willingness to pay for vaccines in advance, which is measured by the maximum upfront payment it is willing to make to secure access before vaccines become available. This maximum upfront payment measures the total health benefit derived from vaccination under a given lockdown policy, and is conceptually different from the option value of lockdown.

Figure 2.9 shows the maximum upfront payments as multiples of the Dutch GDP in 2020. Our results indicate that, overall, governments are less willing to pay for vaccines under more stringent lockdown policies. Intuitively, when strict lockdowns cannot be implemented, governments rely more heavily on vaccines to save lives, and are therefore willing to invest in early access to the vaccines. Conversely, when stringent lockdown measures are in place, individuals are already well protected, reducing the additional health benefit of vaccination. As a result, the government is less inclined to make substantial upfront payments for vaccines in this case.

Figure 2.9: Ratio of maximum upfront payments (MUP) and GDP under different lockdown policies.



To examine how the maximum upfront payment varies with vaccine characteristics, we present the results for each scenario in Table 2.7. Under both LF and RO policies, the maximum upfront payment increases monotonically with the vaccine arrival rate and roll-out speed. However, this pattern does not hold for LD strategies. Under LD, earlier and faster vaccination can lead to an earlier occurrence of reinfections. With a moderate lockdown stringency, more infections may arise in the near future if individuals do not receive booster shots. Therefore, in the presence of reinfection, a rapid vaccine roll-out does not necessarily translate into greater health benefits when the lockdown is not sufficiently stringent.

Table 2.7: Ratios of the maximum upfront payment and the Dutch GDP (MUP/GDP) under different lockdown policies.

α	$\bar{\lambda}$	LF			LD			RO		
		0.003	0.004	0.005	0.003	0.004	0.005	0.003	0.004	0.005
100%	0.05	0.304	0.320	0.326	0.073	0.075	0.077	0.010	0.011	0.013
	0.08	0.404	0.421	0.427	0.085	0.087	0.088	0.014	0.017	0.019
	0.13	0.487	0.506	0.514	0.092	0.093	0.094	0.018	0.021	0.024
80%	0.05	0.163	0.181	0.192	0.069	0.072	0.072	0.008	0.009	0.011
	0.08	0.228	0.249	0.262	0.082	0.084	0.083	0.011	0.014	0.016
	0.13	0.283	0.307	0.325	0.089	0.090	0.087	0.015	0.018	0.020
60%	0.05	0.028	0.039	0.048	0.057	0.059	0.055	0.005	0.006	0.008
	0.08	0.061	0.072	0.083	0.068	0.068	0.058	0.007	0.009	0.011
	0.13	0.091	0.103	0.118	0.074	0.071	0.056	0.010	0.012	0.014

Conversely, a rapid and efficient vaccination program is more effective under stringent lockdown policies, even when reinfection is possible. Under the RO strategy, the negative health effects of reinfection are minimal due to the heightened stringency of lockdown measures, which keeps daily infections low. Moreover, a fast vaccination roll-out allows individuals to

acquire immunity without becoming ill, thereby maximizing the health benefits associated with vaccination.

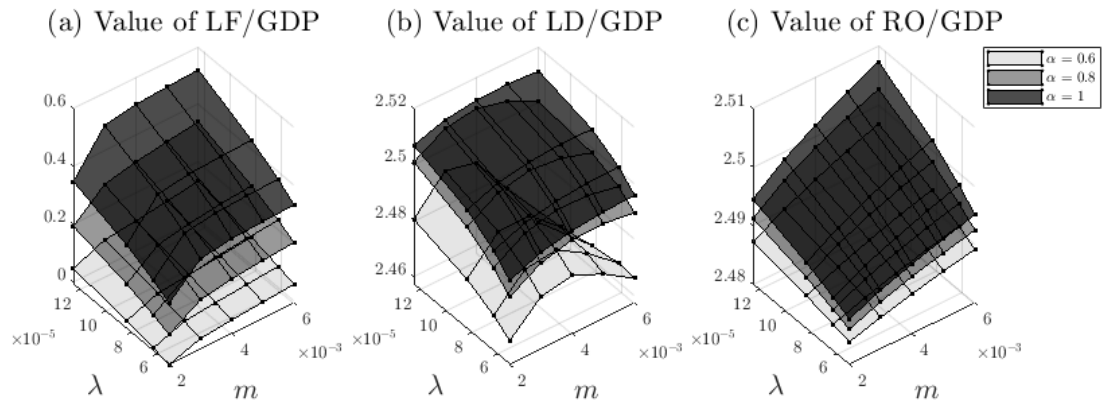
Under LF, the pandemic progresses at such a rapid pace that reinfection may occur before vaccines become available. In this case, early and effective vaccination primarily accelerates the acquisition of immunity without preventing infections. Consequently, the government is more inclined to invest in vaccines if they are expected to arrive sooner and be distributed more quickly.

It is important to note that the discussion above does not imply that vaccination is inherently less valuable under any intermittent lockdown policy. In reality, LD policies are adjusted over time in response to the evolving pandemic situation and vaccine development. In our simulations, however, we simply assume that the lockdown is fixed at the outset. This simplification explains why the health benefits from vaccination may decline with larger λ and m : the lockdown severity of LD is not dynamically adjusted over time to address the real-time pandemic evolution. The resulting non-monotonicity in the maximum upfront payment under LD implies that the total health benefit from vaccines is jointly determined by the reinfection rate, lockdown stringency, and vaccination roll-out.

Both the option value of lockdown and the maximum upfront payment are influenced by uncertainty regarding vaccines, but they capture different aspects of the health benefits associated with the government's lockdown and vaccination policies, and therefore respond differently to the lockdown severity and vaccine characteristics (see Figure 2.7 and Figure 2.9). Option values reflect the lives saved by lockdowns through providing more people the opportunity to receive vaccines in the future. A delayed vaccine arrival increases the time during which susceptible individuals are protected under lockdown, resulting in higher option values. However, this does not imply that delayed vaccine availability, lower vaccine effectiveness, or slower vaccine roll-out is desirable. In fact, governments are willing to make higher upfront payment for earlier access to vaccines to ensure that more people gain immunity without experiencing adverse health outcomes.

Finally, we compute the total health benefits under each lockdown policy with stochastic vaccine arrival, as shown in Figure 2.10. Our findings indicate that, in general, stricter lockdown measures yield higher total health benefits. These benefits are also influenced by factors such as the vaccine arrival rate, vaccine effectiveness, and the reinfection rate. Earlier and faster vaccination can sometimes accelerate the occurrence of reinfections. Consequently, under less stringent lockdown policies, more infections may occur in the future, despite a substantial portion of the population being vaccinated. In contrast, when lockdown measures are strict, a rapid and efficient vaccination program can save more lives, even in the presence of potential reinfection.

Figure 2.10: Total value of each policy as multiple of GDP in 2020 in the Netherlands.



2.6 Conclusion

In this paper, we first develop a behavioral SEIRS (BSEIRS) model which is able to generate realistic simulations of COVID-19 pandemic paths. Using these simulations, we evaluate the health benefits of different lockdown policies under uncertainty regarding vaccine arrival time and effectiveness. The health benefit of a lockdown policy is measured by the additional lives and life years saved compared with a laissez-faire scenario. In particular, we focus on the real option value of lockdowns, which has been largely overlooked in the existing pandemic literature but accounts for over 70% of the total health benefit from lockdown, according to our numerical results.

Before vaccines become available, lockdowns confer a real option with uncertain exercise timing due to vaccine uncertainty. In effect, lockdowns offer susceptible individuals more waiting time for vaccines before infection, increasing the likelihood that they can be vaccinated and gain immunity without facing a high mortality risk. We quantify the real option value of lockdowns as the health benefit arising specifically from this channel.

The BSEIRS model extends the standard SEIRS framework and introduces several novelties relative to existing COVID-19 epidemiological models. First, it incorporates fear of contagion, grounded in a micro-founded theory where individuals respond to the time-varying mortality risk of the virus. Second, it explicitly models the societal learning process regarding the COVID-19 mortality rate. Third, it accounts for the possibility of reinfection, which has been largely ignored in prior work. Additionally, the model incorporates several key features of the coronavirus, including the seasonality of virus transmission, the emergence of more transmissible variants, and the uncertainty surrounding both vaccine development and lockdown policies of varying stringency. Together, these features allow the BSEIRS model to generate more accurate pandemic forecasts than standard epidemic models.

Using simulations from the BSEIRS model, we evaluate three key components of health benefits under different lockdown policies, vaccine arrival times, effectiveness, and rollout speeds:

1. Total health benefits of lockdown under vaccine uncertainty, measured by the additional lives saved compared with *laissez-faire*.
2. Option value of lockdown, capturing the health benefits achieved by providing susceptible individuals extra waiting time for vaccines before infection.
3. Health benefits from vaccination, quantified as the maximum upfront payment a government would be willing to make for access to vaccines once available.

We consider three representative lockdown strategies in our numerical exercises: *laissez-faire* (LF), intermittent lockdowns (LD) as implemented in the Netherlands, and rollover-infection lockdowns (RO), which aim to flatten the infection curve by maintaining the effective reproduction number at one. While they are not the only available strategies in reality, these strategies capture a wide range of policy approaches discussed in practice.

Our results indicate that total health benefits generally increase with lockdown stringency, as stricter measures protect more people before vaccines become available. However, these benefits are also sensitive to vaccine arrival, effectiveness, and reinfection dynamics. For less stringent lockdowns, early vaccination can paradoxically accelerate reinfections if immunity wanes quickly, potentially leading to more future cases even when a majority of the population has been vaccinated.

For any given lockdown policy, the option value constitutes a substantial share of the total health benefits associated with lockdowns. Stricter lockdowns increase the option value by providing more waiting time for vulnerable individuals before vaccines become available. The option value is also higher when vaccines arrive later or are less effective, as lockdowns play a larger role in preventing infections. Importantly, a high option value resulting from delayed or partially effective vaccination does not imply that ineffective vaccination is desirable.

The option value of lockdowns is distinct from the health benefits of vaccination. The latter, captured by the maximum upfront payment a government is willing to make for vaccine access, does not necessarily increase with earlier or more effective vaccination due to the interplay of reinfection and lockdown stringency. Rapid vaccination combined with moderate lockdowns can lead to earlier reinfections if booster shots are not administered. Conversely, under strict lockdowns, fast and efficient vaccination programs are highly effective even in the presence of potential reinfections, yielding substantial health benefits.

Overall, our findings highlight the critical importance of accounting for behavioral responses, reinfection, and vaccine uncertainty when evaluating the effectiveness of pandemic policies. By

distinguishing between the option value of lockdowns and the direct benefits of vaccination, policymakers can better design interventions that maximize health outcomes under uncertainty.

2.A Parameters of the BSEIRS Model

Seasonality The transmission of COVID-19 shows a strong seasonal trend, with cases peaking in the winter and declining during the summer. Based on the expression in Atkeson (2021), we set the seasonality of virus transmission $\psi(t)$ as

$$\psi(t) = \textit{seasonalsize} \times \cos\left(\frac{2\pi}{365}(t + \textit{seasonalposition})\right)$$

where t represents the number of days since the onset of the pandemic, $\textit{seasonalsize}$ represents the scale of seasonal fluctuations in virus transmissibility, and $\textit{seasonalposition}$ indicates the location of seasonal peaks. In Section 2.4, we set $\textit{seasonalsize} = 0.25$ and $\textit{seasonalposition} = 30$.

Hospitalization-to-Infection Ratio $\eta(t)$ and Deceased-to-Hospitalization Ratio $\nu(t)$ The hospitalization-to-infection ratio $\eta(t)$ represents the probability that an infected individual will require hospitalization, while the deceased-to-hospitalization ratio $\nu(t)$ captures the probability of death conditional on hospitalization. In the BSEIRS model, the states of infection, hospitalization, and death are denoted by I , H , and D , respectively. Then by definition, we have

$$\eta(t) = \frac{H(t)}{I(t - t_{HI})},$$

$$\nu(t) = \frac{D(t)}{H(t - t_{DH})}$$

where $t_{HI} = 1/\gamma$ is the average time to transition from state I to state H , and $t_{DH} = \frac{1}{\zeta}$ represents the average time to transition from state H to state D .

Before applying the pandemic data of infections, hospital admissions, and deaths to the above expressions, we first smooth the data using moving averages. This step accounts for reporting lags between the actual occurrence of cases and their publication date. As shown in Figure 2.A1, the daily reported data is highly volatile, which introduces noise into the computation of η and ν . To mitigate this issue, we apply 7-day moving averages, shown as solid curves in the figure.

Using the moving-average data, we compute $\eta(t)$ and $\nu(t)$, which are shown as the dashed curves in Figure 2.A2. However, these calculated values cannot be directly used in the pandemic model simulations for two main reasons. First, by definition, both $\eta(t)$ and $\nu(t)$ are probabilities and therefore must not exceed one, while the empirical ratios occasionally do. Second, these ratios reflect underlying characteristics of the coronavirus that should evolve smoothly over time, making it implausible to interpret the highly volatile trajectories observed in the raw calculations.

To solve these issues, we approximate the trajectories of $\eta(t)$ and $\nu(t)$ by smooth functions using nonlinear least square methods. Recall that t denotes the number of days since the onset

Figure 2.A1: Raw data and the moving average curves of daily infections, hospital admissions, and deceased as percentages of the total population in the Netherlands.

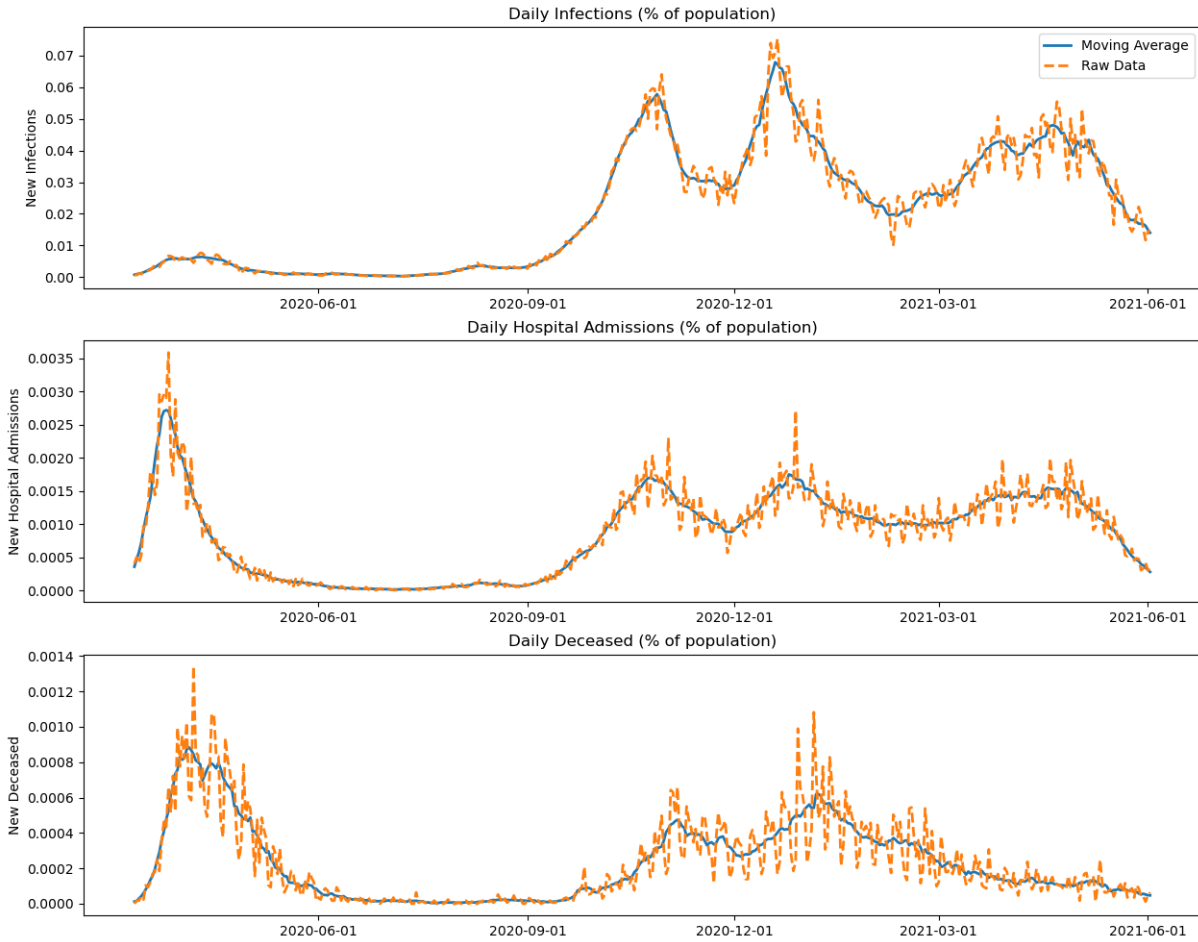
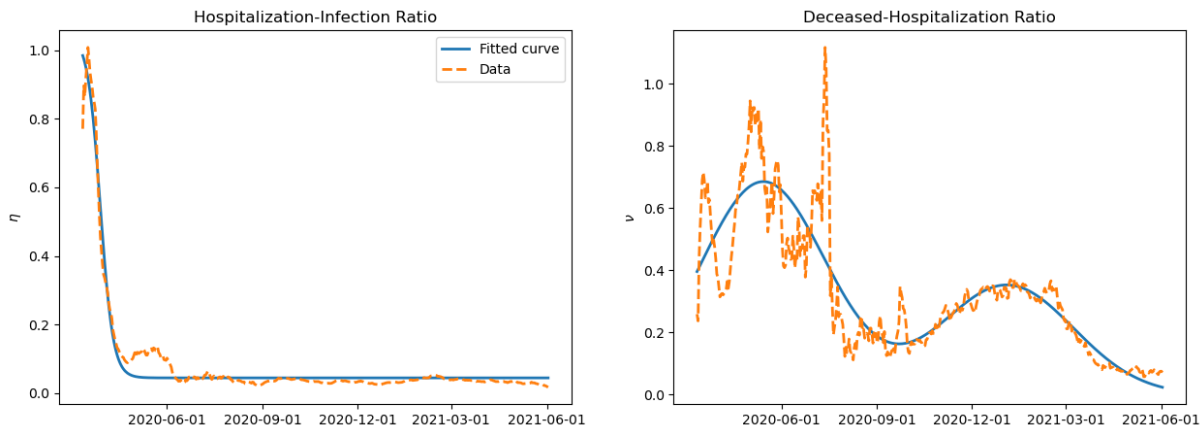


Figure 2.A2: The hospitalization-to-infection ratio η and the deceased-to-hospitalization ratio ν . The dashed curves represent values calculated from the moving average data, while the solid curves show the fitted smooth curves.



of the pandemic. For $\eta(t)$, we fit the values using a sigmoid function of form

$$\tilde{\eta}(t) = \frac{1}{1 + \exp[-k(t - x_0)]} + b$$

with the optimal values for the parameters $x_0^* = 16.91$, $k^* = -0.16$ and $b^* = 0.04$. For $v(t)$, given that its time path exhibits a bimodal pattern, we approximate its trajectory as the sum of two Gaussian functions

$$\tilde{v}(t) = s_1 \exp\left(-\frac{(t - \mu_1)^2}{2\sigma_1^2}\right) + s_2 \exp\left(-\frac{(t - \mu_2)^2}{2\sigma_2^2}\right)$$

and obtain the optimal parameter values $s_1 = 0.69$, $\mu_1 = 63.57$, $\sigma_1 = 60.67$, $s_2 = 0.35$, $\mu_2 = 297.63$, $\sigma_2 = 63.98$.

The Proportion of the Population with Fear of Contagion The proportion of susceptible people with fear of contagion $\pi(t)$ is set to increase with the belief $\theta(t)$ of the excess mortality rate. We use

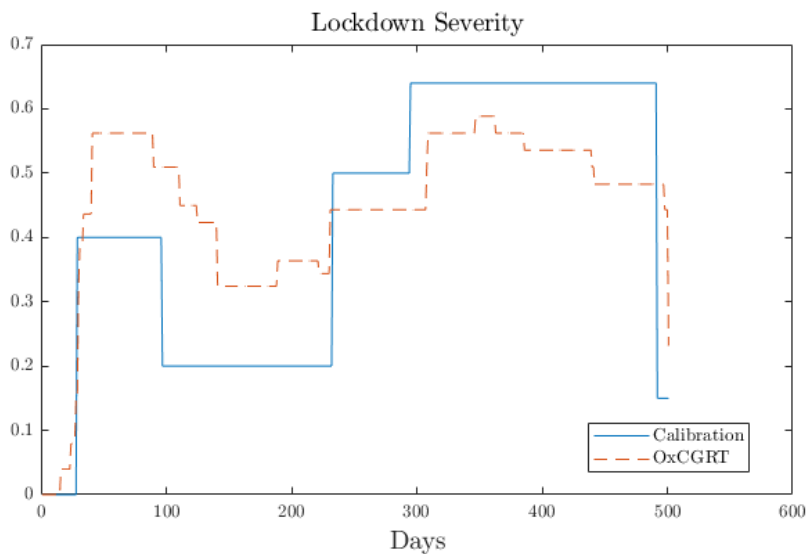
$$\pi(t) = 0.3 + 0.0275\theta(t)$$

Moreover, we let the initial belief $\theta(0)$ equal to the natural death rate δ_N . Intuitively, susceptible individuals did not anticipate that COVID-19 would significantly increase the mortality risk, and consequently there was little fear of infection during the initial stages of the pandemic.

2.B Lockdown Severity

To set the value of lockdown severity in the calibration, we compare the value in Table 2.4 with the stringency index by Oxford COVID-19 Government Response Tracker (OxCGRT) which collects government policy measures taken to tackle COVID-19. The index summarizes stringency in containment measures, economic policies, health policies, emergency investments into healthcare and vaccination policies. Given that our focus is solely on the impact of containment measures on the evolution of the pandemic, we do not use the OxCGRT data directly in our simulation. However, the comparison between in Figure 2.A3 shows that the time path of lockdown severity used in our simulation captures the overall trend and major changes of lockdown policies.

Figure 2.A3: Lockdown severity by OxCGRT stringency index and calibrated values.



2.C Alternative Models with Different Vaccine Effects

In the main analysis, we assume that vaccination reduces the likelihood of infection. However, evidence from the Dutch National Institute for Public Health and the Environment (RIVM) indicates that vaccines also significantly lower the probability of COVID-related hospitalization by approximately 95%.¹⁴ To capture this additional effect, we introduce an alternative epidemiological specification, building on the BSEIRS model in Section 2.2.5. The key modification is that the hospitalization rate is now explicitly modeled as a function of the vaccinated share of the population, denoted by M_t .

¹⁴Source: Rijksinstituut voor Volksgezondheid en Milieu (RIVM), see <https://www.rivm.nl/en/news/vaccines-very-effective-against-hospital-and-icu-admissions-also-for-delta-variant>

Formally,

$$\dot{S}_{nf}(t) = -[\beta(t)I(t) + \beta_v(t)I_v(t)]S_{nf}(t) - m_0(t) \quad (2.C.1a)$$

$$\dot{S}_f(t) = -[p\beta(t)I(t) + p\beta_v(t)I_v(t)]S_f(t) - m_f(t) \quad (2.C.1b)$$

$$\dot{S}_m(t) = -[\beta(t)I(t) + \beta_v(t)I_v(t)]S_m(t) + (1 - \alpha)(m_0(t) + m_f(t)) + \kappa R(t) \quad (2.C.1c)$$

$$\dot{E}(t) = \beta(t)I(t)S_{nf}(t) + p\beta(t)I(t)S_f(t) + \beta(t)I(t)S_m(t) - \sigma E(t) \quad (2.C.1d)$$

$$\dot{E}_v(t) = \beta_v(t)I_v(t)S_{nf}(t) + p\beta_v(t)I_v(t)S_f(t) + \beta_v(t)I_v(t)S_m(t) - \sigma E_v(t) + \bar{E}_v(t) \quad (2.C.1e)$$

$$\dot{I}(t) = \sigma E(t) - \gamma I(t) \quad (2.C.1f)$$

$$\dot{I}_v(t) = \sigma E_v(t) - \gamma I_v(t) \quad (2.C.1g)$$

$$\dot{H}(t) = \eta(\mathbf{t}, \mathbf{M}_t)\gamma(I(t) + I_v(t)) - \zeta H(t) \quad (2.C.1h)$$

$$\dot{R}(t) = (1 - \nu(t))\zeta H(t) + (1 - \eta(\mathbf{t}, \mathbf{M}_t))\gamma(I(t) + I_v(t)) + \alpha(m_0(t) + m_f(t)) - \bar{E}_v(t) - \kappa R(t) \quad (2.C.1i)$$

$$\dot{D}(t) = \nu(t)\zeta H(t) \quad (2.C.1j)$$

The hospitalization rate $\eta(t, M_t)$ is specified as a decreasing function of the vaccinated share of the population, M_t . We specify the hospitalization rate as

$$\eta(t, M_t) = \bar{\eta}(t)(1 - M_t) + (1 - \xi)\bar{\eta}(t)M_t$$

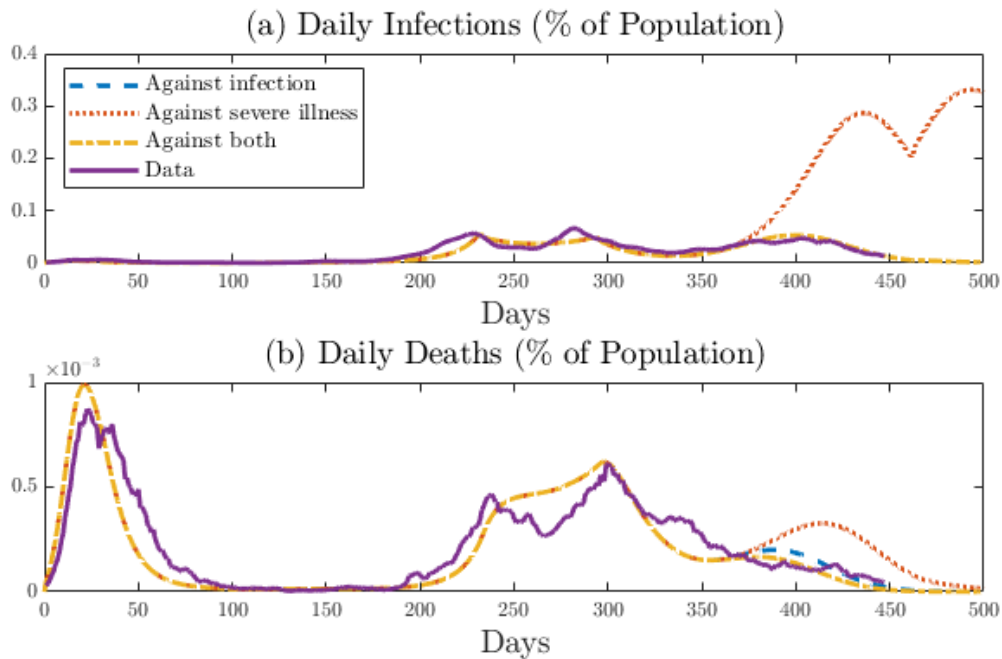
where $\bar{\eta}(t)$ is the hospitalization rate in the absence of vaccination, M_t is the vaccinated share of the population, and $\xi = 0.95$ captures the effectiveness of vaccination in preventing severe illness.

To illustrate the impact of vaccination on the pandemic dynamics, we simulate pandemic trajectories under three scenarios: vaccines reduce (i) only the probability of infection, (ii) only the probability of severe illness, or (iii) both. Consistent with earlier assumptions, we assume that vaccinations lower the probability of infection by 80% and the probability of severe illness by 95%. The vaccination rate is set at 0.4% of the population per day, in line with Dutch data. Lockdown severity is kept the same across scenarios and calibrated to match the Dutch intermittent lockdown. The simulations cover a 500-day period beginning with the onset of the pandemic.

Figure 2.A4 presents the simulated trajectories of daily infections and deaths under different assumptions about vaccine effectiveness, alongside the empirical data. The simulations suggest that if vaccines only reduce the probability of severe illness but do not prevent infection, a substantially larger number of infections would occur (red dotted line). This reflects not only the absence of protection against infection, but also weaker behavioral responses, as the lower mortality rate reduces fear of contagion. In addition, a sharp resurgence of infections emerges

following the arrival of the Delta variant around Day 450. In contrast, when vaccines also reduce infection risk, both infections and deaths remain considerably lower than in the case where vaccines provide protection solely against severe illness.

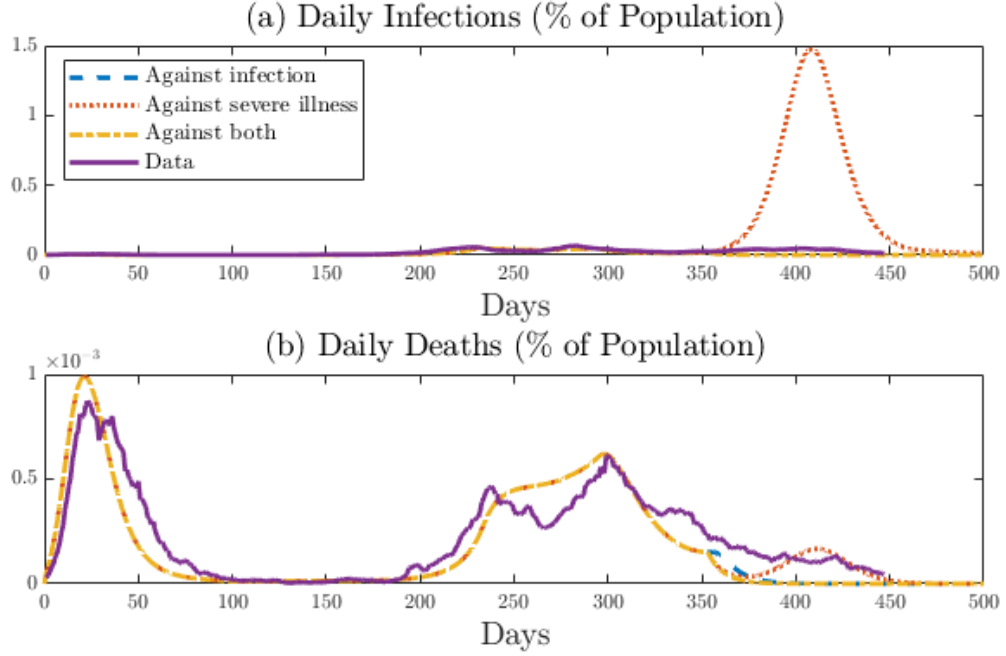
Figure 2.A4: Data and simulated daily infections and deaths when vaccination reduces infection and/or severe-illness rates. The speed of vaccine rollout is 0.4% of the population per day.



To further support the reasoning above, we simulate daily infections and deaths under the counterfactual assumption that the entire population is vaccinated instantaneously (Figure 2.A5). Comparing the simulated infection trajectories confirms the earlier result: both infection and death cases would have been higher if vaccines reduce only the probability of severe illness but not the probability of infection. Moreover, by comparing the red dotted curves in Figure 2.A4(a) and Figure 2.A5(a), we observe that when vaccines protect only against severe illness, a faster vaccine roll-out paradoxically increases infections. This occurs because the reduction in mortality lowers the perceived risk of contagion, thereby weakening behavioral responses at an earlier stage.

Under both gradual and instantaneous vaccination assumptions, our results show that daily infections and deaths are similar between the case where vaccines reduce only the infection rate and the case where vaccines reduce both infection and severe illness. In contrast, considering solely the effect of vaccination on severe illness leads to an overestimation of both infections and deaths.

Figure 2.A5: Data and simulated daily infections and deaths when vaccination reduces infection and/or severe-illness rates. Here we assume that the entire population is vaccinated within a single day.



2.D Computational Procedures for the Value Functions

Below we describe the computational procedures for evaluating the total health benefits of a lockdown policy $\{ld(t)\}_t$ under vaccine-related uncertainty, as well as the associated option value and the health benefits attributable to vaccination. The total health benefits of lockdown are defined as the difference in the value of statistical life (VSL) saved under the lockdown policy relative to a laissez-faire scenario, computed over the period from Day 1 to $T^\infty = 500$ since the outbreak of the pandemic.

Compute $V(\{ld(t)\}_t, v = 0)$

- Simulate the pandemic path using the BSEIRS model without vaccine arrival under the strategy $\{ld(t)\}_t$.
- The value generated at time t is

$$u(t|\{ld(t)\}_t, v = 0) = -\dot{D}(t|\{ld(t)\}_t, v = 0) \left[VSL - \frac{t}{365} VSLY \right]$$

where t starts from 0 and ends at T^∞ , $\dot{D}(t|\{ld(t)\}_t, v = 0)$ is the number of new deaths at t under strategy $\{ld(t)\}_t$ without vaccine. VSL and VSLY are abbreviations for Value of

Statistical Life and Value of Statistical Life per Year. Therefore $[VSL - \frac{t}{365}VSLY]$ is the value of statistical life for any one who dies at t .

- The total value under $\{ld(t)\}_t$ without vaccine arrival before T^∞ is

$$V(\{ld(t)\}_t, v = 0) = \sum_{s=0}^{T^\infty} u(s|\{ld(t)\}_t, v = 0).$$

Compute $V(\{ld(t)\}_t, v = 1)$

- Given a lockdown strategy $\{ld(t)\}_t$, vaccine arrival rate, vaccine effectiveness, and roll-out speed, simulate pandemic paths from time 0 to T^∞ using the BSEIRS model for all possible vaccine arrival dates $t_{vac} = 1, \dots, T^\infty$.
- For any vaccine arrival time t_{vac} , compute the value $u(t|\{ld(t)\}_t, t_{vac})$ generated under the strategy $(\{ld(t)\}_t, v = 1)$ at t ,

$$u(t|\{ld(t)\}_t, t_{vac}) = -\dot{D}(t|\{ld(t)\}_t, t_{vac}) \left[VSL - \frac{t}{365}VSLY \right].$$

Before the vaccine arrival ($t < t_{vac}$), the pandemic path coincides with that under the strategy $(\{ld(t)\}_t, v = 0)$, which implies $\dot{D}(t|\{ld(t)\}_t, t_{vac}) = \dot{D}(t|\{ld(t)\}_t, v = 0)$ and thus $u(t|\{ld(t)\}_t, t_{vac}) = u(t|\{ld(t)\}_t, v = 0), \forall t < t_{vac}$. Once vaccines take effect, the pandemic trajectory deviates from the counterfactual without vaccination, since vaccination reduces the number of susceptible individuals without generating additional infections and deaths. Two key characteristics determine the impact of vaccination on the pandemic path: the roll-out speed and the efficacy against infection. Consistent with Section 2.2, we assume a constant roll-out speed over time and that the vaccine is equally effective against all virus variants.

- The expected total value under $(\{ld(t)\}_t, v = 1)$ is

$$V(\{ld(t)\}_t, v = 1) = \sum_{t_{vac} \leq T^\infty} P(t_{vac}) \tilde{V}(\{ld(t)\}_t, v = 1|t_{vac}) + \mathbb{P}(t_{vac} > T^\infty)V(\{ld(t)\}_t, v = 0) \tag{2.D.1}$$

where $P(t_{vac})$ is the probability that the vaccine arrives at time t_{vac} , and $\tilde{V}(\{ld(t)\}_t, v = 1|t_{vac})$ is the value under $(\{ld(t)\}_t, v = 1)$ if vaccination starts at time t_{vac} . If vaccines arrive after T^∞ , the loss of value of statistical life in the period before T^∞ is the same as $V(\{ld(t)\}_t, v = 0)$. Given the Poisson intensity $\lambda(t)$, we have

$$P(t_{vac}) = e^{-\int_0^{t_{vac}-1} \lambda(\tau)d\tau} - e^{-\int_0^{t_{vac}} \lambda(\tau)d\tau}.$$

$\tilde{V}(\{ld(t)\}_t, v = 1|t_{vac})$ can be computed using

$$\tilde{V}(\{ld(t)\}_t, v = 1|t_{vac}) = \sum_{t=0}^{t_{vac}-1} u(t|\{ld(t)\}_t, v = 0) + \sum_{t=t_{vac}}^{T^\infty} u(t|\{ld(t)\}_t, t_{vac})$$

where $u(t|\{ld(t)\}_t, v = 0)$ and $u(t|\{ld(t)\}_t, t_{vac})$ are defined and computed in previous steps.

Chapter 3

The Social Cost of Carbon Under Climate Volatility Risk

Abstract

Weather extremes are becoming more frequent and more intense. Accordingly we calculate the social cost of carbon (SCC) under stochastic climate volatility. Using a stochastic dynamic integrated climate-economy model where representative agents are endowed with Duffie-Epstein recursive preferences, we find that climate volatility risks substantially increase the SCC both in the business-as-usual and optimal abatement policy scenario. We also show that switching to a regime with more intense disasters increases the SCC more than a switch to a regime with more frequent disasters for equal expected value.

3.1 Introduction

Recent years have seen increasing volatility of climate disasters. As the global temperature rises, extreme weather events that were once rare are becoming more frequent. Record-breaking deviations from climatological norms, such as the 2021 North American heatwaves, are occurring with rising frequency. Climate scientists and meteorologists have warned that human-induced climate change will drive both an increase in the frequency and an intensification of extreme weather events (Reidmiller et al. (2018), IPCC (2021a)). Moreover, climate disasters and the damages they cause are becoming not only more frequent but also increasingly volatile over time. Uncertainty about the timing and magnitude of increasing climate volatility has motivated climatologists to develop models for predicting unprecedented extremes (Thompson et al. (2017), Kelder et al. (2020)). However, the implications of the risk associated with such

distributional changes of climate damages have received little attention from climate economists. Current climate-economy models account only for uncertainty in climate damages themselves, typically by modeling these damages as stochastic processes with known drift and volatility. In contrast, we examine higher-order climate uncertainty – the possibility that the volatility of climate damages evolves stochastically. Specifically, we investigate how uncertainty about climate volatility affects the social cost of carbon (SCC). Our model emphasizes that climate volatility is itself stochastic, a feature that has not been addressed in existing climate economic studies.

Rising global temperature has intensified extreme weather patterns, with heatwaves, floods, and droughts occurring more frequently. Although this trend has received limited attention in the economics literature, it has been widely covered by the media and rigorously analyzed by climate scientists. The United Nations Office for Disaster Risk Reduction (UNDRR) has highlighted that climate change amplifies disaster risk by altering both the frequency and intensity of hazardous events. For example, the most severe storms are projected to occur up to twice as often under 2.5°C of warming (Bacmeister et al. (2018)); extreme daily precipitation is expected to intensify by approximately 7% for every 1°C increase in temperature (IPCC (2021a)); and the global population exposed to extreme droughts could double within the next 80 years (Pokhrel et al. (2021)).

The evidence outlined above underscores the need to study uncertainty in climate volatility. In this paper, we define climate volatility as the variability of damages arising from climate disasters. More frequent and severe weather events amplify the variability, leading to larger fluctuations in economic output and higher average losses, thereby implying a rising trajectory of climate volatility over time. Moreover, there is considerable uncertainty regarding the extent of this increase, as the future severity of climate disasters remains unknown. We refer to this phenomenon as *stochastic climate volatility*, a dimension of risk that has received little attention in the economics literature.

The SCC represents the marginal economic damages from emitting one additional unit of carbon into the atmosphere. As a measure of the negative externalities of climate change, it has been adopted by many governments to inform climate policies. In the United States, the SCC plays a central role in regulatory analysis, federal carbon tax legislation, and the development of energy efficiency standards (Rennert et al. (2022)). Standard economic theory suggests setting the optimal carbon tax equal to the SCC, although this may be an oversimplification of a complex policy problem involving global coordination and distributional concerns. These broader challenges are beyond the scope of this paper, and our focus lies in examining climate volatility risk and its implications for the SCC.

There is a substantial literature estimating the SCC under various aspects of uncertainty, including economic fluctuations and shocks to cumulative atmospheric carbon concentrations (see, for example, Cai and Lontzek (2019), Van den Bremer and Van der Ploeg (2021), Hambel

et al. (2021), Jensen et al. (2021)). However, climate economists have not yet addressed the fact that climate volatility itself is subject to uncertainty. Bansal et al. (2017) introduced endogenous volatility by assuming that both the frequency and severity of climate disasters increase once temperature reaches a tipping point, but their focus was instead on the long-run effects of temperature on consumption growth and asset prices. The lack of explicit attention to stochastic climate volatility is perhaps not surprising: the recent emergence of record-setting weather events and the nascent state of climate science on volatility prediction have limited the exploration of this issue. Nevertheless, given the irreversibility of transitioning to a high-volatility climate regime and its potentially profound welfare implications, we argue that it is important to assess this risk explicitly, despite current scientific uncertainties.

We develop a continuous-time integrated climate-economy model to compute the SCC under a stylized yet general equilibrium asset pricing framework. The economy is modeled as a pure-exchange setting: agents receive endowments over time, which cannot be stored and must be allocated between consumption and abatement. Endowment growth is subject to economic fluctuations, crises, and climate damages.

Climate conditions are characterized by the mean global surface temperature and the distribution of climate damages. Following Dietz et al. (2021a), the mean global surface temperature is assumed to increase linearly with cumulative carbon emissions. Climate damages arise solely from climate-related natural disasters. The arrival of such disasters follows a Poisson process, and the economic impact of each event is modeled as a stochastic variable. Therefore, the distribution of climate damages is characterized jointly by the arrival rate of disasters and by the distribution of their severities once a Poisson shock occurs.

To introduce stochastic climate volatility, we consider two climate regimes: the current regime and a future regime characterized by more frequent and extreme climate disasters, whose severity and timing are uncertain. Due to limited knowledge about the severity of disasters in the new regime, we analyze the model under two assumptions: (A) climate disasters occur more frequently, and (B) climate disasters become more extreme.

Given the uncertainty about the timing of the regime shift, we assume in the main analysis that the arrival of the new climate regime follows a Poisson process with an arrival rate 0.01 implying an expected arrival time of 100 years. The 100-year horizon is motivated by the first IPCC reports, is close to the atmospheric lifetimes of greenhouse gases, and avoids distortions in long-term socioeconomic scenarios (Abernethy and Jackson (2022)). In addition, we present numerical results under alternative assumptions about the arrival rate of the new climate regime in Section 3.4.3. For simplicity, the climate regime shift is regarded as a one-off, irreversible event, consistent with the irreversibility of climate change.

In the main analysis, we assume that climate volatility increases abruptly upon a regime shift. In Section 3.6, we consider an alternative specification where the long run volatility jumps

instantaneously, but actual volatility gradually adjusts to this new level over time following the regime shift. We also examine the effect of abatement policies on the SCC by comparing two policy scenarios: the business-as-usual (BAU) scenario with no emissions reduction, and an optimal abatement scenario aimed at maximizing total welfare through carbon emissions mitigation.

We find that stochastic climate volatility substantially increases risk premia and nevertheless leads to a significantly higher SCC. The climate-volatility risk premium is of the same order of magnitude as the risk premium arising from climate volatility itself. This risk premium rises with the frequency and intensity of climate disasters in the new climate regime, as well as with the arrival rate of the regime shift.

Stochastic climate volatility also affects equilibrium risk-free rates, although overall discount rates increase. It influences the SCC through two channels: (a) the discount rate of future consumption and (b) the certainty-equivalent expected value of the consumption flows being discounted. While these two channels work in opposite directions, we show unambiguously that stochastic climate volatility raises the SCC. Moreover, for a given climate severity in the new regime, the SCC under a stochastic regime shift expected to arrive in 2115 is substantially higher than the SCC under a comparable deterministic climate regime shift occurring with certainty in 2115.

Finally, we show that a shift to a climate regime with more intense but less frequent disasters induces a higher SCC than a shift to a regime with more frequent but correspondingly less intense disasters, holding the expected annual climate damages constant across both regimes.¹ Moreover, the sensitivity of the SCC to changes in the characteristics of the new regime is larger under stringent emission control than under the Business-As-Usual (BAU) scenario. For example, doubling the arrival rate of climate disasters in the new climate regime while holding intensity constant will raise the average SCC in 2025 from \$376 to \$505 per ton of carbon in the BAU scenario (an increase of 34%), but from \$385 to \$548 per ton of carbon under optimal abatement (an increase of 42%). Similarly, if climate disasters in the new regime are twice as intense for a given arrival rate, the average SCC in 2025 rises from \$376 to \$522 in the BAU scenario (up 39%) and from \$395 to \$574 per ton in optimal abatement scenario (up 45%).

We obtain similar implications under several alternative model specifications. First, we replicate our numerical exercises with endogenous rather than exogenous emissions, and find that endogenizing emissions does not qualitatively alter our results. Second, we examine the effect of smoothing the increase in climate volatility and find that it has only a modest impact on the SCC. This contributes to the broader debate on whether simplified representations of geophysical processes will understate the economic costs of climate damages (Dietz et al. (2021a)). Prior studies on climate tipping have either explicitly model the underlying geographical processes,

¹This result holds for our model and parameter specifications, but may not generalize to other settings.

yielding gradual tipping dynamics, or adopt reduced-form representations with abrupt tipping. Our framework accommodates both approaches. We show that smoothing the tipping process generates lower SCCs, since a gradual adjustment to a higher long-run volatility implies a lower volatility trajectory in the period immediately following the regime shift.

Stochastic regime shifts have been studied earlier in the more general macroeconomic literature. For example, Lettau et al. (2008) explain the persistent above-norm US aggregate stock prices by a shift to a lower macroeconomic volatility regime in the 1990s. They model the transitions between a high and a low macroeconomic volatility state as a Markov switching process. Our model has a similar structure. We assume that the transition from a low-volatility to a high-volatility regime follows a Poisson process, but we differ from Lettau et al. (2008) in that the climate regime shift is one-off and irreversible: once the stochastic regime shifts, climate volatility rises abruptly and irreversibly.

Modelling stochastic transitions among different regimes is a simplified way to analyse volatility uncertainty and can be extended to richer risk structures. The modelling of volatility risk originates from financial economics and mathematical finance, where it has been used extensively to explain asset market features. A thorough discussion of stochastic volatility models is provided in Shephard and Andersen (2009). Also, already since the early 1970s various stochastic volatility models have been used to explain empirically observed departures from Black-Scholes, such as time-varying and non-stationary volatility processes (Clark (1973), Taylor (2005), Hull and White (1987), Wiggins (1987), Barndorff-Nielsen and Shephard (2001), Eraker et al. (2003), etc.). More recent studies show that higher-order uncertainties such as the volatility of volatility and the volatility-of-volatility risk are themselves significant risk factors which affect option returns (Branger et al. (2018), Huang et al. (2019), Hu and Liu (2022), Eraker and Yang (2022), etc.). To check whether a richer risk structure of climate volatility leads to different model implications, we provide an alternative model of climate volatility risk in Section 3.6. There we assume that the climate disaster frequency follows a Cox–Ingersoll–Ross (CIR) process with its long-run value subject to a one-off irreversible Poisson jump upon the climate regime shift while the actual volatility shifts gradually towards its new long run value. Our numerical results suggest that climate volatility risk yields similar asset pricing implications under different specifications of volatility risk.

Our model of stochastic climate volatility differs from the climate tipping points discussed by many climate economists. In the current literature, climate tipping has a broad definition including nonlinear geophysical feedbacks and abrupt phase changes (Kopp et al. (2016)). Dietz et al. (2021a) provides a unified estimate of economic impacts of eight climate tipping points covered in the economic literature using a meta-analytic integrated assessment model. Tipping points considered in their paper can be broadly divided into three categories: positive feedbacks between the carbon cycle and temperature, ice shelf disintegration, and changes in large-scale

circulation. However, most economic studies represent climate tipping points in a highly stylized way. For example, Gjerde et al. (1999) models the costs of climate tipping directly as a utility loss. Lemoine and Traeger (2014) models climate tipping as abrupt irreversible shifts in system dynamics and studies the impact of uncertain climate tipping on the optimal carbon tax. They consider two types of climate tipping points: an increase in the strength of temperature feedbacks and a decrease in the ability of the earth system to remove carbon. Lontzek et al. (2015) point out that these assumptions on climate tipping are scientifically questionable. To study the impact of climate tipping on optimal policy choice, Lontzek et al. (2015) model climate tipping points as abrupt reductions in GDP. In our baseline model, stochastic climate volatility is modelled as a one-off irreversible increase in climate volatility which falls into the broad definition of climate tipping but so far has not been discussed in the literature. Like climate tipping points, climate volatility risk is not really reflected in current policy advice, presumably because its economic consequences are subject to considerable uncertainty, and relevant parameters are nearly impossible to calibrate.

Our stochastic dynamic integrated assessment model (IAM) builds on Olijslagers et al. (2022) which estimates the social cost of carbon under rare disaster risks using a high-dimensional stochastic dynamic IAM with a realistic climate model in a continuous-time framework. Our model includes rare disasters both from economic disruptions and climate change. These disasters are modelled as discrete shocks to economic outputs as in Barro (2006), Barro (2009) and Pindyck and Wang (2013). Since disaster risk can generate the high equity premia and low risk-free rates observed in the data, it is of vital importance to include disaster shocks in the model, because the SCC is essentially the expected discounted future damages from climate change. To get a clear picture of how the stochastic climate regime shift affects the social cost of carbon, we use a simplified climate model where temperature is approximately linear in cumulative carbon emissions (as in Matthews et al. (2009) and Van den Bremer and Van der Ploeg (2021)), and do not model explicitly other determinants of global warming such as atmospheric carbon decay, the earth's heat radiation, radiative forcing, and heat absorption by the ocean. In contrast, Hambel et al. (2021) models the dynamics of atmospheric carbon concentration with unexpected environmental shocks and accounts for the amount of carbon absorbed by natural sinks. Temperature follows a self-exciting process which captures the delayed climate feedback effects (IPCC (2007)) and the right-skewed distribution of future temperatures (Roe and Baker (2007)). Olijslagers and van Wijnbergen (2024) use the IPCC AR5 impulse-response model discussed in Mattauch et al. (2018). This model accounts for the nonlinear response of temperature to carbon emission. We use a simpler structure than those detailed climate models, temperature changes in our model are linear in emission flows. This simplification buys computational convenience at the expense of a slight distortion of climate dynamics.

The rest of the paper is structured as follows. Section 3.2 introduces the stochastic IAM, and Section 3.3 details the model calibration. Section 3.4 presents the numerical results under different climate regime shifts, while Section 3.5 compares outcomes under exogenous and endogenous emissions. Section 3.6 develops an alternative model of climate volatility risk and contrasts its numerical results with those in Section 3.4 under the BAU scenario. Section 3.7 concludes.

3.2 The Model

In this section, we describe the stochastic integrated climate-economy model used to estimate the SCC. Building on Olijslagers et al. (2022), the framework consists of two components: an endowment economy with a representative agent endowed with recursive preferences, and a climate system characterized by global temperature dynamics and the climate regime.

3.2.1 The Climate Model

While climate change has a broader meaning, here we focus on anthropogenic global warming due to the increasing atmospheric carbon concentration caused by fossil fuel combustion during manufacturing. Based on the climate model in Olijslagers et al. (2022), we introduce stochastic volatility to climate damages.

We assume for computational convenience that carbon emissions E are exogenous without abatement. It increases over time with economic growth, but will decline at the beginning of the next century as fossil fuel stocks are exhausted. Formally, the growth rate of emission $r_{E,t}$ is given by $r_{E,t} = e^{-\delta_E t} r_{E,0} + (1 - e^{-\delta_E t}) r_{E,\infty}$, moving from the initial value $r_{E,0}$ to its long-run level $r_{E,\infty}$ at rate δ_E . The emission dynamic is $dE_t = r_{E,t} E_t dt$, with the initial emission level E_0 . Under the emission abatement rate u_t at time t , the actual carbon emission is $\tilde{E}_t := (1 - u_t) E_t$. Since large-scale carbon capture and storage seems to be out of reach technologically, the emission control rate ranges from 0 to 100%. In Section 3.5 we will provide an alternative setup where carbon emission is a function of aggregate endowment and carbon intensity, and show that both the exogenous and the endogenous emission setups generate similar implications on how stochastic volatility affects the SCC.

The mean global surface temperature T_t increases linearly in the total carbon concentration in the atmosphere, with dynamics

$$dT_t = \chi(1 - u_t) E_t dt$$

where χ is the transient climate response to cumulative carbon emissions.

3.2.2 The Economic Model

Endowment In a continuous-time stochastic pure exchange economy, a representative agent owns an asset which pays a flow of dividends (or endowments) Y_t at time t . The endowment evolves over time

$$dY_t = \mu Y_t dt + \sigma Y_t dZ_t - J_1 Y_t dN_{1,t} - J_2 Y_t dN_{2,t}$$

where μ and σ are the growth rate and the volatility of the endowment, Z_t is a standard Brownian motion representing the diffusion economic risks. Economic disasters are introduced by the Poisson process N_1 like in Barro (2009), which is necessary to generate empirically plausible discount rates for future payoffs which is essential for the SCC calculation. The Poisson process N_1 has an arrival rate λ_1 and reduces the endowment flow by $J_1 \in (0, 1)$ upon each disaster arrival. The economic disaster size J_1 is a random variable with density $f(x) = \alpha_1(1-x)^{\alpha_1-1}$, which implies the expected economic disaster size $E J_1 = \frac{1}{\alpha_1+1}$.

Stochastic Volatility of Climate Damage Endowments are also negatively affected by climate disasters. The induced damage is a random variable J_2 , which follows the same distribution as J_1 but with a different parameter $\alpha_{2,t}$. The arrival of climate disasters follows a Poisson process N_2 with an arrival rate $\lambda_{2,t}$. Since climate disasters happen more frequently under warming, $\lambda_{2,t}$ increases in T_t . Moreover, empirical data shows that $\lambda_{2,t}$ has exhibited a pronounced increase in recent years, a trend that cannot be solely attributed to the rising temperature. Accordingly, we assume $\lambda_{2,t} := \bar{\lambda}_t T_t$, where $\bar{\lambda}_t$ represents the component capturing the effect of climate change on disaster frequency that is independent of temperature. Both the arrival rate $\lambda_{2,t}$ and the expected damage $E_t J_2 := \frac{1}{\alpha_{2,t}+1}$ (or the damage intensity parameter $\alpha_{2,t}$) jointly determine the volatility of damage from disasters.

The dynamic of $\bar{\lambda}_t$ is unknown due to limited research in this area. However, existing evidence suggests that it follows an increasing trend over time. To account for the uncertainty in $\bar{\lambda}_t$, we model a one-off irreversible Poisson jump in its value. The Poisson jump can be interpreted as a stochastic regime shift from the current climate state to a new regime characterized by higher volatility in climate damages. Formally, this irreversible regime shift is modeled as a one-off Poisson shock N_0 with arrival rate λ_0 , affecting either the disaster frequency $\lambda_{2,t}$ or expected magnitude of climate damages $E_t J_2$. Specifically, upon the realization of the regime shift, one of the following occurs:

- (A) Increased disaster frequency: The disaster frequency $\lambda_{2,t} := \bar{\lambda}_t T_t$ increases independently of temperature through an upward jump in the baseline disaster rate $\bar{\lambda}_t$ from $\bar{\lambda}^{(L)}$ to $\bar{\lambda}^{(H)}$.

- (B) Increased disaster severity: The expected size of climate damages rises from $E J_2^{(L)} := \frac{1}{\alpha_2^{(o)} + 1}$ to $E J_2^{(H)} := \frac{1}{\alpha_2^{(n)} + 1}$, corresponding to a decline in the parameter $\alpha_{2,t}$ of the damage distribution from $\alpha_2^{(o)}$ to $\alpha_2^{(n)}$.

The parameter λ_0 thus governs the stochastic timing of the transition into a high-volatility climate damage regime. Given limited knowledge about more extreme scenarios in the new climate regime at the current stage, we focus on the simple case where λ_0 is exogenously given and is independent of climate conditions.

In Section 3.4, we compare regime shifts where the frequency or the expected scale of climate disasters are respectively doubled and quadrupled, and compare the SCCs under these different climate regimes. In Section 3.6, we introduce an alternative model of climate volatility in which the increase unfolds gradually over time. This approach is motivated by the observation that tipping points in climate systems are unlikely to manifest instantaneously in real time (Dietz et al. (2021a)). Numerical results from this gradual volatility model indicate that smoothing the transition in long-run climate volatility leads to a lower time path for the SCC, as the more progressive adjustment implies a slower increase in climate volatility following the shock. For analytical tractability, we initially model climate volatility risk as a one-off stochastic jump, as outlined above. This simplification allows us to derive closed-form expressions for the pricing implications of stochastic climate volatility. Moreover, it remains consistent with the long-run shift in the distribution of climate disasters considered in the alternative model presented in Section 3.6.

Consumption and Emission Abatement The endowment Y_t cannot be stored for future expenditure and has to be spent on either consumption C_t or abatement A_t at time t . The abatement cost follows the same structure as in Nordhaus (2017) and is given by $A_t = c_{1,t} u_t^{c_2} Y_t$, where $c_{1,t}$ captures the effect of technology process on abatement cost and declines over time and $c_2 > 1$ characterizes the increase of marginal cost in the emission control rate u_t . The consumption flow is then given by

$$C_t = Y_t - A_t = (1 - c_{1,t} u_t^{c_2}) Y_t := \xi_t Y_t$$

where $\xi_t = \frac{C_t}{Y_t} = 1 - c_{1,t} u_t^{c_2}$ is the consumption-endowment ratio.

Recursive Preference We model the preferences of the representative agent by stochastic differential utility (Duffie and Epstein (1992)) which is the continuous-time version of Epstein-Zin preferences. This allows us to separately vary risk aversion γ and the elasticity of intertemporal substitution (EIS) ϵ . By separating risk aversion and EIS, such preference can generate non-trivial and empirically plausible risk premia by increasing risk aversion without compromising

the model's explanatory power on historical financial data. Moreover, the value of these preference parameters affects agents' attitude towards temporal resolution of uncertainty which in turn is critical to explain the dynamics under expected future regime shift risks. When $\gamma > \frac{1}{\epsilon}$, agents prefer an early resolution of uncertainty about future consumption. If $\gamma = \frac{1}{\epsilon}$, this boils down to the power utility and the timing of resolution of uncertainty becomes irrelevant.

Representative agents face an intertemporal trade-off between reduced consumption today due to abatement efforts and potentially lower future consumption resulting from more severe climate damages. Formally, the agents' value function is defined recursively as follows:

$$V_0 = \max_{u_t} E_0 \int_0^{\infty} f(C_t, V_t) dt$$

with $f(C, V) = \frac{\beta}{1-\frac{1}{\epsilon}} \frac{C^{1-\frac{1}{\epsilon}} - [(1-\gamma)V]^{\frac{1}{\zeta}}}{[(1-\gamma)V]^{\frac{1}{\zeta}-1}}$ as in Duffie and Epstein (1992), $\epsilon \neq 1$, $\zeta = \frac{1-\gamma}{1-\frac{1}{\epsilon}}$, and β the time discount rate. Appendix 3.A provides the numerical procedures we use to solve this optimization problem.

3.2.3 The Social Cost of Carbon

The social cost of carbon (SCC) measures the marginal cost associated with an additional unit of carbon emissions. It represents the present value of the expected future damages resulting from a marginal increase in emissions today. Formally, SCC is defined as the ratio of the marginal utility of carbon emissions to the marginal utility of consumption, enabling its expression in units of current consumption goods:

$$SCC_t = -\chi \frac{\partial V_t / \partial T_t}{f_C(C_t, V_t)} \quad (3.1)$$

where $f_C(C_t, V_t)$ is the marginal utility of consumption at time t .

3.3 Calibration

Following Johansson et al. (2012), we set the endowment growth rate at $\mu = 3\%$ and endowment volatility at $\sigma = 2.5\%$. Barro and Jin (2011) estimates that rare economic disasters arrive at rate 0.035 with size parameter $\alpha_1 = 6.5$, which generates an estimate of risk aversion γ around 4 by approximating the observed risk premium in the market. Olijslagers et al. (2022) calibrates $\epsilon = 1.5$ and $\beta = 0.025$, which, together with risk aversion $\gamma = 4.3$, yields reasonable approximations of the estimated worldwide average risk-free rate and equity risk premium during the period 1900-2010 in Dimson et al. (2011). Given that the arrival rate of climate disasters is linear in temperature, we follow Karydas and Xepapadeas (2019) who find that the arrival rate

increases by $\bar{\lambda}^{(L)} = 6\%$ if temperature rises by 1°C in the current climate regime. The mean disaster size is 1.5% which implies $\alpha_2^{(o)} = 65$ before the regime shift.

Parameters of carbon emission under BAU scenario are set to resemble the projected industrial carbon emissions in the baseline scenario in Nordhaus (2017). Taking 2015 as the starting point of our simulation, we set the initial CO_2 emission level at 35.6 gigatonnes with initial growth rate $r_{E,0} = 1.7\%$. The growth rate of carbon emission decreases over time at an annual rate 0.75% until reaching its long-run level -2% . The abatement cost function follows the same as in the RICE-2010 model (Nordhaus (2010)) with time-decreasing technology effect $c_{1,t} = 0.074e^{-0.019t}$ and cost nonlinearity $c_2 = 2.8$. The annual global mean surface temperature is approximately 0.83°C in 2015 (source: NASA) and gradually rises as cumulative carbon increases. Matthews et al. (2012) shows that the 90% confidence interval of transient climate response (TCR) to carbon emissions is between 1°C and 2.5°C per teraton of carbon. We take $\chi = 1.8^\circ\text{C}/\text{TtC}$ in the simulation as in Olijslagers et al. (2023).

Calibrating climate volatility risk is difficult for lack of time series data. Since the negative impact of climate change is going up fast over time, climate volatility in the future cannot be predicted using historical climate data. In the next section we therefore run simulations for several possible values of $\bar{\lambda}^{(H)}$ and $\alpha_2^{(n)}$ to characterize the post-shift climate regime.

3.4 The SCC and Climate Volatility Risk: Numerical Results

We numerically solve the integrated assessment model of Section 3.2 under two types of shocks to the volatility process and two assumptions about economic policy, yielding four scenarios in total. First, we distinguish between a regime shift characterized by a higher arrival rate of Poisson shocks and one characterized by larger shocks conditional on arrival, holding the arrival rate fixed. Second, we analyze both types of shocks under a Business-As-Usual (BAU) scenario and under optimal abatement.²

We analyze two types of regime shifts: (A) an increase in the frequency of climate disasters (Section 3.4.1) and (B) an increase in their intensities (Section 3.4.2). For case (A), we present numerical results for $\bar{\lambda}^{(H)}/\bar{\lambda}^{(L)} = 1, 2$ and 4 , corresponding to a baseline with no change in the arrival rate, and two cases where the rate doubles and quadruples, respectively. For case (B), we apply the same multipliers, but to the expected size of climate disasters in the new regime.

To date, research has provided limited insights into higher-order uncertainties in the climate system, particularly regarding the timing and scale of a potential future climate regime shift. In our baseline specification, we assume an arrival rate of $\lambda_0 = 0.01$, implying an expected arrival time of 100 years. This horizon is broadly consistent with the atmospheric lifetimes of

²All scenarios are solved using finite difference methods, with 2015 as the initial year and $K = 5000$ simulations. The time horizon is 500 years, with results reported up to 2100.

greenhouse gases and helps avoid distortions in long-term socioeconomic scenarios (Abernethy and Jackson (2022)). Section 3.4.3 reports numerical results for alternative values of λ_0 .

3.4.1 The New Climate Regime (A): Higher Disaster Frequency

We begin with case (A), where stochastic climate volatility arises from an increase in the frequency of climate disasters in the new regime, while their intensity remains unchanged.

Since the SCC depends both on future consumption losses from climate damages and on discount rates, its calculation naturally fits within an asset pricing framework. Within this framework, the SCC can be interpreted as the present value of an asset that delivers climate-induced reductions in consumption as “dividends” over time. Since the risk-free rate and the risk premium of this asset are key components of the consumption-based discount rate, we first examine the effects of climate volatility risk on these variables before turning to the implications for the SCC itself.

The Risk-Free Rate, Climate Risks and Climate Volatility Risk

The model without a regime shift allows for analytical solutions, as illustrated by the first three terms of Equation 3.2 which characterizes the risk-free rate r_t^f . The fourth term represents the effect of the regime shift on the risk-free rate and must be evaluated numerically (see Appendix 3.A for the derivation). Accordingly, the instantaneous risk-free rate at time t is given by

$$\begin{aligned}
 r_t^f = & \underbrace{\beta + \frac{\mu_{C,t}}{\epsilon} - \frac{\gamma}{2} \left(1 + \frac{1}{\epsilon}\right) \sigma^2}_{\text{Standard}} + \underbrace{\lambda_1 \left(\frac{\gamma - 1/\epsilon}{\alpha_1 + 1 - \gamma} - \frac{\gamma}{\alpha_1 - \gamma} \right)}_{\text{Econ. disasters}} + \underbrace{\lambda_{2,t} \left(\frac{\gamma - 1/\epsilon}{\alpha_2 + 1 - \gamma} - \frac{\gamma}{\alpha_2 - \gamma} \right)}_{\text{Clim. disasters}} \\
 & + \underbrace{\lambda_{0,t} \mathcal{J}_{f,t}}_{\text{Regime shift}} . \tag{3.2}
 \end{aligned}$$

where $\mu_{C,t}$ is the consumption growth rate (see Appendix 3.A for its explicit expression), $\lambda_{0,t} := \lambda_0 (1 - N_{0,t-})$ is the arrival rate of a new climate regime, $N_{0,t-}$ is the corresponding Poisson variable equal to 0 before and to 1 after the regime shift occurs, and $\mathcal{J}_{f,t}$ captures the effect of climate volatility risk arising from the uncertain regime shift. Equation (3.2) resembles the expression for risk-free rate presented in Olijslagers et al. (2022), with the exception of the last term $\lambda_{0,t} \mathcal{J}_{f,t}$ which specifically reflects the climate volatility risk examined in this study.

The first component of Equation (3.2) is the standard expression for the risk-free rate in the absence of disaster risks. Here, β represents the time preference rate, $\frac{\mu_{C,t}}{\epsilon}$ captures the intertemporal smoothing effect, and $-\frac{\gamma}{2} \left(1 + \frac{1}{\epsilon}\right) \sigma^2$ captures the precautionary saving effect.

The second and third component represent the impact of rare economic and climate disaster risks, respectively. Both terms depend on their associated arrival rates, λ_1 and $\lambda_{2,t}$, and the corresponding disaster intensities, α_1 and $\alpha_{2,t}$. Without loss of generality, we assume that the parameters governing the economic disaster process are time-invariant. For the parameter values chosen in Section 3.3, both the second and third terms are negative, reflecting the fact that disaster risks reduce the risk-free rate when $\epsilon > 1$. In particular, climate volatility, which is characterized by $\lambda_{2,t}$ and $\alpha_{2,t}$, also has a negative effect on the risk-free rate.

The fourth and final component captures the impact of climate volatility risk, which affects the risk-free rate through two channels: (a) the risk of a new climate regime shift increases the *expected* climate damages in the future, thereby lowering the current safe real rate, and (b) the risk of a new climate regime shift introduces an additional source of uncertainty. Both channels lead to higher prices of future goods, or equivalently, a lower risk-free rate. We refer to these two channels as the expectation effect and the risk effect of climate volatility risk.

Intuitively, the one-off stochastic regime shift can be represented as a compound Poisson process, with the jump process denoted by N_0 and the jump size determined by the climate severity in the new regime. Under mild conditions when the arrival rate and the jump size are independent, the expected value of the compound Poisson process can be decomposed into two components using Wald's equation: the jump risk (which corresponds to the risk effect) and the expected jump size (which corresponds to the expectation effect).

The expectation effect is the difference between the effects of climate disasters on r^f with and without regime shift risk (corresponding to the third term in Equation (3.2)). Formally, it can be expressed as

$$\lambda_{2,t} \left(\frac{\gamma - 1/\epsilon}{\alpha_{2,t} + 1 - \gamma} - \frac{\gamma}{\alpha_{2,t} - \gamma} \right) - \bar{\lambda}^{(L)} T_t \left(\frac{\gamma - 1/\epsilon}{\alpha_{2,0} + 1 - \gamma} - \frac{\gamma}{\alpha_{2,0} - \gamma} \right) \quad (3.3)$$

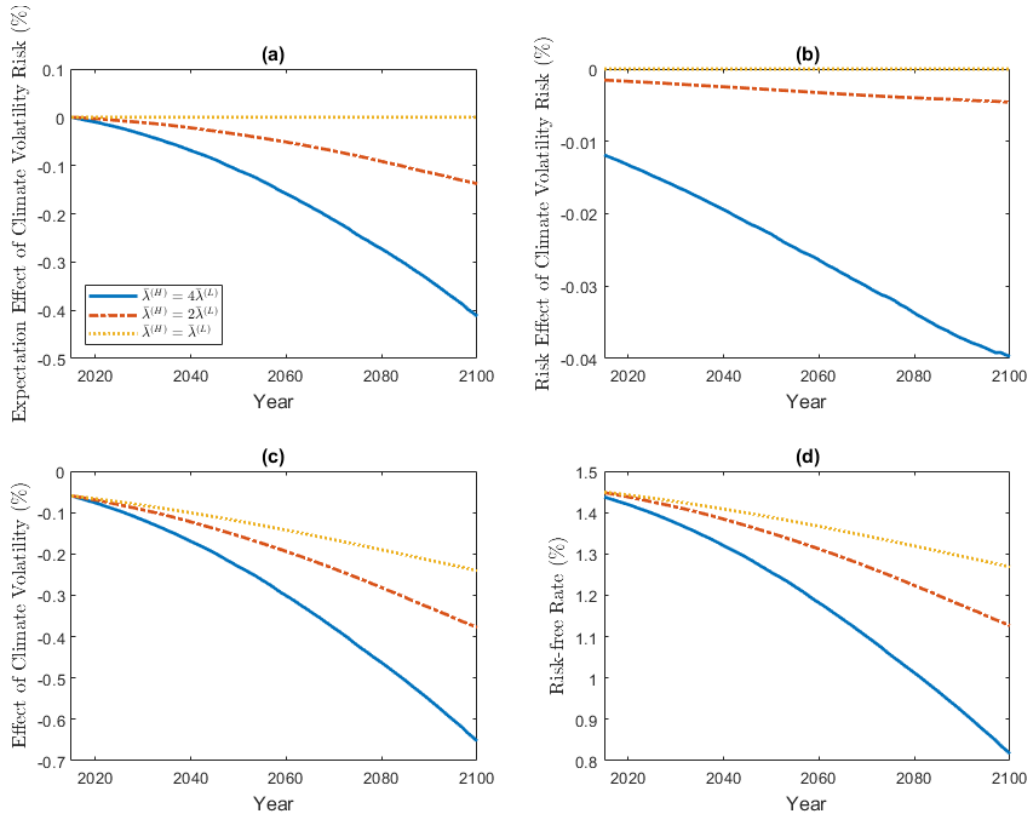
where the climate disaster frequency $\lambda_{2,t} = \bar{\lambda}_t T_t$ is the product of frequency parameter $\bar{\lambda}_t$ and temperature T_t , the first term is the same as the effect of climate disasters on r^f in Equation (3.2), and the second term is the effect of climate disasters on r^f without climate volatility risk.

Under stochastic climate volatility, the value of $\bar{\lambda}_t$ (or $\alpha_{2,t}$) jumps from its initial value $\bar{\lambda}^{(L)}$ (or $\alpha_2^{(o)}$) to $\bar{\lambda}^{(H)}$ (or $\alpha_2^{(n)}$) upon a regime shift of Type (A) (or Type (B)). The formula further shows that the impact depends on the temperature anomaly T_t in a predictable way. The magnitude of the expectation effect depends on both the frequency and intensity of climate disasters in the new climate regime. Figures 3.1 and 3.2 show the magnitudes of the expectation and risk effects under different abatement policies.

The Risk-Free Rate in the Business-As-Usual Scenario Figure 3.1 presents the decomposition of the risk-free rate in the business-as-usual scenario based on Equation (3.2). Panel (a) and

(b) show the impact of stochastic climate volatility on the risk-free rate through the expectation channel (Equation (3.3)) and the risk channel ($\lambda_{0,t}\mathcal{J}_{f,t}$), respectively. Panel (c) shows the effect of climate disaster risk on the risk-free rate, and Panel (d) shows the corresponding time paths of the risk-free rates. A comparison of Panels (a), (b), and (c) indicates that climate volatility risk influences the risk-free rate mainly via the expectation channel, with a magnitude comparable to that of climate disaster risk.

Figure 3.1: Decomposition of (average) risk-free rates in the BAU scenario under different $\bar{\lambda}^{(H)}$ in the new regime. The legends correspond to $\bar{\lambda}^{(H)} = 4\bar{\lambda}^{(L)}$, $2\bar{\lambda}^{(L)}$ and $\bar{\lambda}^{(L)}$. Panel (a) and (b) present the expectation effect (Equation (3.3)) and the risk effect (the last term in Equation (3.2)) describing the impact of stochastic climate volatility on the risk-free rate. Panel (c) shows the effect of climate disaster risk itself, and Panel (d) shows the risk-free rate over time.



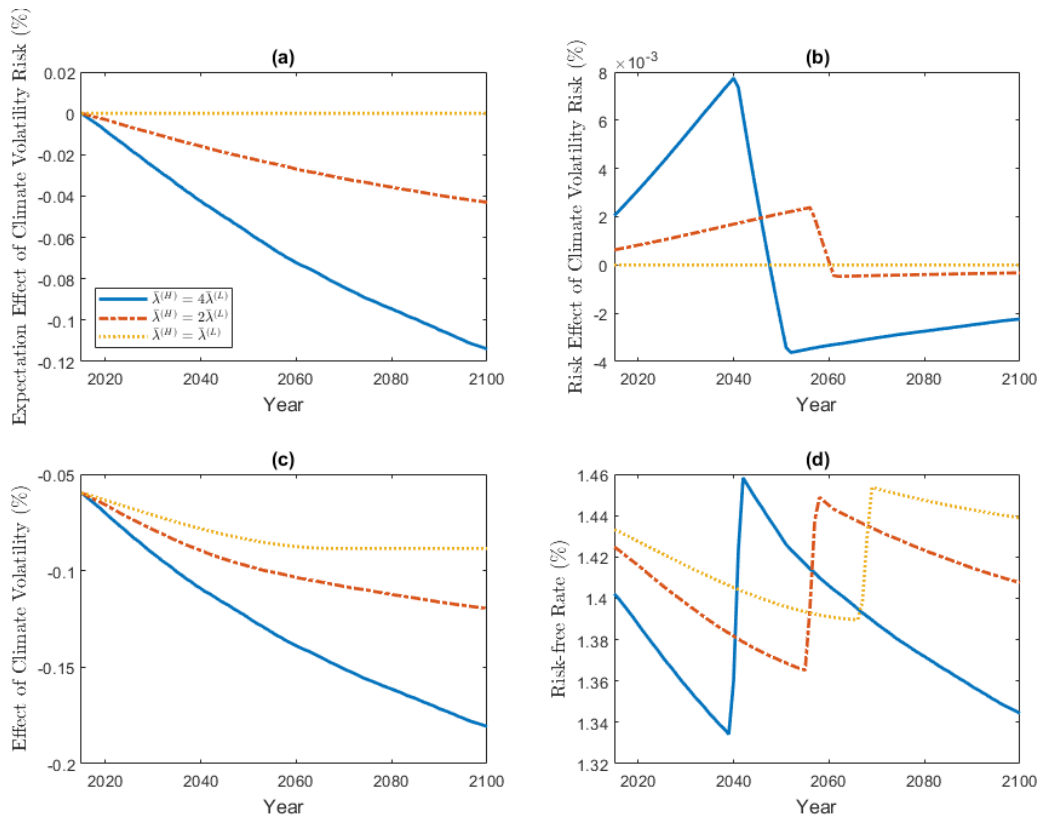
Panel (a) and (b) indicate that climate volatility risk reduces the risk-free rate through both the expectation and risk channels. The magnitude of the expectation effect increases over time and with the frequency of climate disasters. This is because both the temperature T_t and the expected value of $\bar{\lambda}_t$ increase over time, leading to a rising expected climate disaster frequency $\lambda_{2,t} = \bar{\lambda}_t T_t$. As a result, agents anticipate higher future climate disaster risks, causing the time path of the expectation channel's impact to be downward sloping.

The risk effect of climate volatility risk also declines over time, reflecting the increasing likelihood that a climate regime shift has already occurred. However, in the long run, the risk effect will converge to zero as uncertainty about climate volatility is eventually resolved.

Panel (c) shows that climate disaster risks reduce r^f , with their impact increasing over time. Since both the temperature T_t and the climate disaster frequency parameter $\bar{\lambda}_t$ increase over time, the resulting frequency of climate disasters $\lambda_{2,t}$ also increases. Higher expected future disaster frequency leads to greater anticipated damages, thereby intensifying the precautionary saving effect (i.e., increasing the scarcity of future goods) and resulting in lower risk-free rates.

The Risk-Free Rate Under Optimal Abatement We next repeat the numerical exercise under optimal abatement. In this scenario, the average risk-free rate and its decomposition are presented in Figure 3.2. Panel (a) and (b) show the effects of climate volatility risk through the expectation and the risk channels, respectively; Panel (c) illustrates the effect of climate disaster risks, and Panel (d) shows the time path of the risk-free rate under different climate disaster frequencies in the new climate regime.

Figure 3.2: Decomposition of (average) risk-free rates under optimal abatement policies. The legends correspond to $\bar{\lambda}^{(H)} = 4\bar{\lambda}^{(L)}$, $2\bar{\lambda}^{(L)}$, and $\bar{\lambda}^{(L)}$. Panel (a) and (b) present the expectation effect (Expression (3.3)) and the risk effect (i.e. the last term in Equation (3.2)) of stochastic climate volatility on the risk-free rate. Panel (c) shows the effect of climate disaster risk, and Panel (d) shows the risk-free rate over time.



Compared with the business-as-usual scenario, both climate disaster risk and climate volatility risk have a smaller impact on the risk-free rate under optimal abatement. This is because temperature rises more slowly under abatement, making extreme weather events less likely to happen.

A comparison of Panels (a), (b), and (c) indicates that climate volatility risk continues to significantly influence the risk-free rate. Its effect occurs largely through the expectation channel (Panel (a)), although the risk channel (Panel (b)) remains non-negligible. Notably, the risk effect is positive until the emission control rate reaches 100%, after which it declines below zero. Intuitively, once abatement reaches its maximum, future emissions cannot be further reduced, which intensifies the precautionary saving effect and results in a sharp decline in the risk effect shown in Panel (b). Over time, as uncertainty about the climate regime shift resolves, the risk effect will gradually converge to zero. However, this convergence occurs well beyond the time horizon displayed in the figures.

Panel (d) shows that under any assumption of climate disaster frequency in the new regime, the risk-free rate declines in both the short and long run as climate conditions deteriorate due to global warming and increasingly frequent disasters. In the medium run, however, the risk-free rate exhibits a sharp upward jump when the emission control rate reaches its maximum of 100%. Since abatement costs stop increasing afterwards, consumption growth is no longer constrained by increasing abatement costs. Consequently, the precautionary saving effect weakens, leading to the observed increase in the risk-free rate.

The Risk Premium

In Appendix 3.A, we show that the risk premium is given by

$$\begin{aligned}
 r_{p,t} = & \underbrace{\gamma\sigma^2}_{\text{Standard}} + \lambda_1 \underbrace{\left[\frac{-1}{\alpha_1 + 1} + \frac{\gamma}{\alpha_1 - \gamma} + \frac{1 - \gamma}{\alpha_1 + 1 - \gamma} \right]}_{\text{Econ. disasters}} + \lambda_{2,t} \underbrace{\left[\frac{-1}{\alpha_2 + 1} + \frac{\gamma}{\alpha_2 - \gamma} + \frac{1 - \gamma}{\alpha_2 + 1 - \gamma} \right]}_{\text{Clim. disasters}} \\
 & + \underbrace{\lambda_{0,t} \mathcal{J}_{rp,t}}_{\text{Regime shift}} \tag{3.4}
 \end{aligned}$$

which again can be decomposed into four parts. The first component, $\gamma\sigma^2$, represents the standard constant relative risk aversion (CRRA) risk premium arising from diffusive risk in the endowment process. The second and the third terms capture the risk compensations for rare economic and climate disasters, both of which are positive. The fourth term reflects the compensation for climate volatility risk associated with the uncertain one-off regime shift, where $\lambda_{0,t}$ is the arrival rate of a new regime and $\mathcal{J}_{rp,t}$ is the instantaneous effect of the regime shift on

r_p . As shown in Appendix 3.A, $J_{rp,t}$ does not admit an analytical expression and is therefore computed numerically.

Similar to the discussion of the risk-free rate in Section 3.4.1, the effect of climate volatility risk on risk premia can be decomposed into two components: the expectation effect and the risk effect. The expectation effect comes from an increase in the expected future climate damages under volatility risk and is formally given by

$$\lambda_{2,t} \left[\frac{-1}{\alpha_{2,t} + 1} + \frac{\gamma}{\alpha_{2,t} - \gamma} + \frac{1 - \gamma}{\alpha_{2,t} + 1 - \gamma} \right] - \bar{\lambda}^{(L)} T_t \left[\frac{-1}{\alpha_2^{(o)} + 1} + \frac{\gamma}{\alpha_2^{(o)} - \gamma} + \frac{1 - \gamma}{\alpha_2^{(o)} + 1 - \gamma} \right] \quad (3.5)$$

which is the difference between the third term in Equation (3.4) and its counterpart when the climate disaster frequency does not change in the new regime. The risk effect is captured by the last term $\lambda_{0,t} \mathcal{J}_{rp,t}$ in Equation (3.4), which measures how much climate volatility risk affects the risk premium. Figure 3.3 and 3.4 show the relative size of these two components.

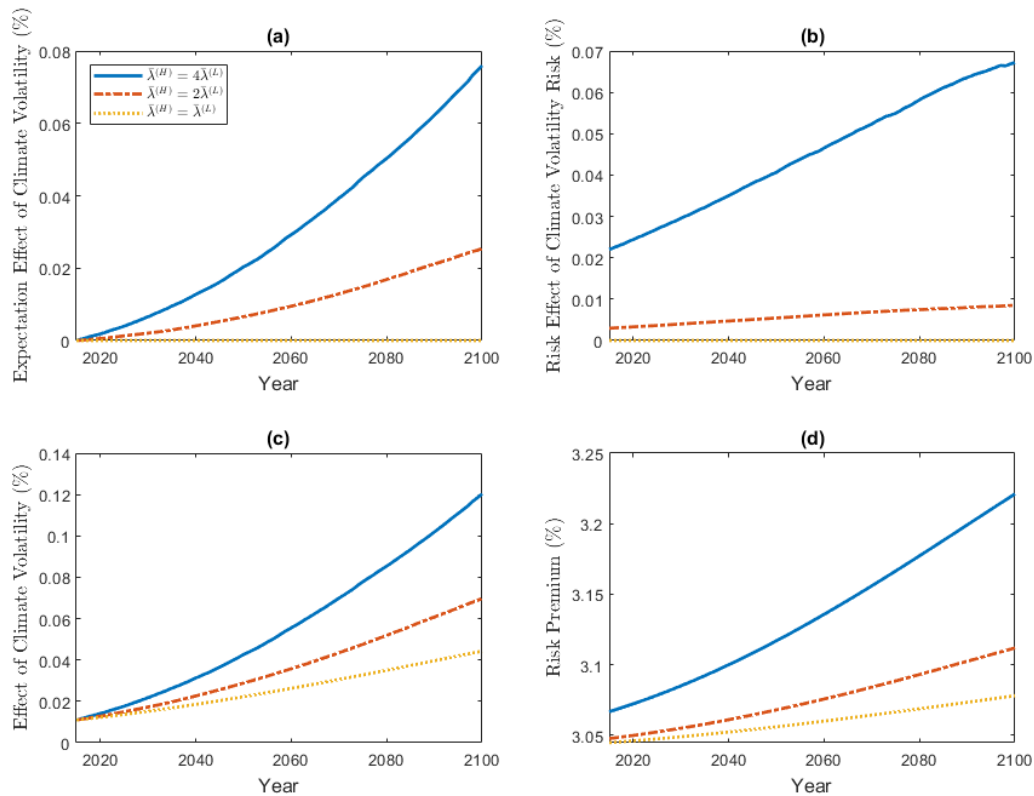
The Risk Premia in the Business-As-Usual Scenario Figure 3.3 shows the impact of climate disaster risks and volatility risks on the risk premium in the business-as-usual (BAU) scenario. Panel (a) and (b) show the expectation and risk effects of climate volatility risk, respectively. Panel (c) shows the contribution of climate disaster risk, and Panel (d) shows the time paths of the risk premium. A comparison of Panels (a), (b), and (c) indicates that the effects of climate disasters, the expectation effect, and the risk effect of climate volatility risk are positive and of comparable magnitude. This finding implies that climate volatility risk is as significant as climate disasters themselves in determining risk premia.

The climate disaster effect (Panel (c)) and the expectation effect of climate volatility risk (Panel (a)) both increase over time, reflecting the irreversibility of global warming, which leads to more frequent climate disasters. In addition, a positive shock to disaster frequency associated with a regime shift further worsens climate conditions. Anticipating more frequent future disasters, agents demand higher risk compensation.

The risk effect of stochastic climate volatility (Panel (b)) increases with disaster frequency, because a new regime with more frequent disasters poses larger threats to economic growth and thus raises the required risk premium. In addition, the risk effect of climate volatility risk on risk premia increases over time under the possibility of a positive shock to climate volatility. However, far beyond the displayed time horizon, the risk effect converges to zero as the uncertainty regarding a regime shift is gradually resolved.

The Risk Premia Under Optimal Abatement Figure 3.4 shows the impact of climate disasters and volatility risks on the risk premium under optimal abatement. Panel (a) and (b) show the

Figure 3.3: Decomposition of risk premia in the BAU scenario under different $\bar{\lambda}^{(H)}$ in the new regime. The legends correspond to $\bar{\lambda}^{(H)} = 4\bar{\lambda}^{(L)}$, $2\bar{\lambda}^{(L)}$, and $\bar{\lambda}^{(L)}$. Panel (a) and (b) present the expectation effect (Expression (3.5)) and the risk effect (the last term in Equation (3.4)) of stochastic climate volatility on risk premia. Panel (c) shows the effect of climate disaster risk, and Panel (d) shows the risk premia over time.

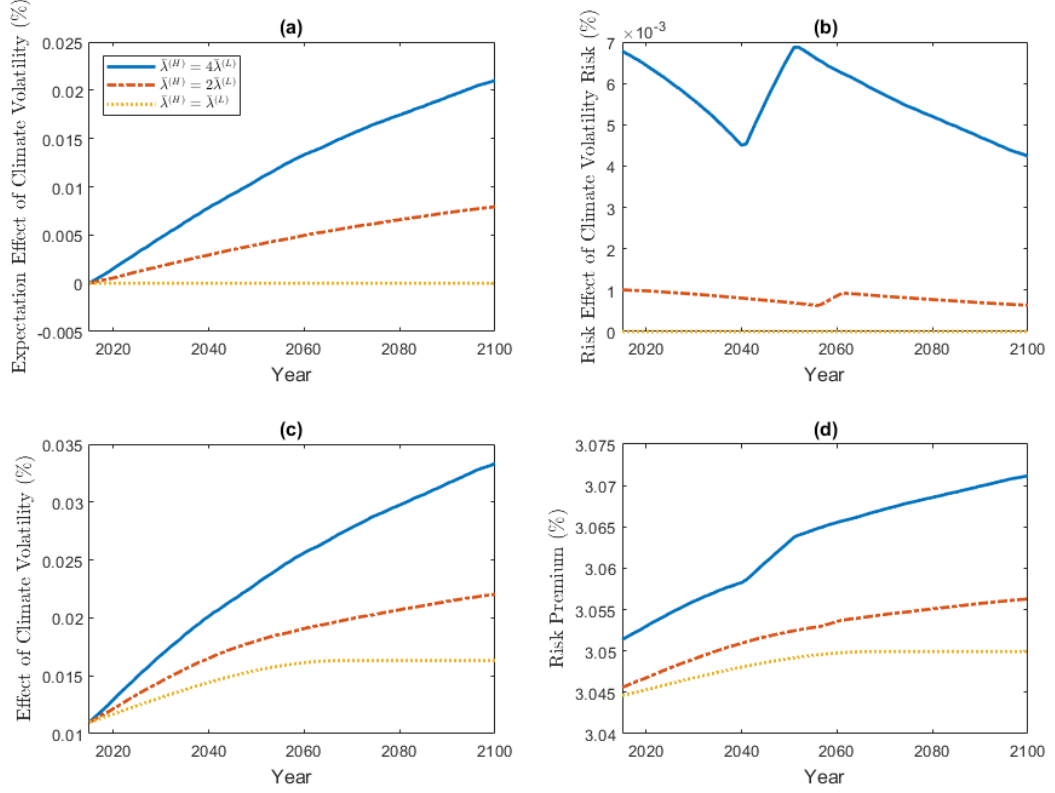


expectation and the risk effects of climate volatility risk, respectively. Panel (c) shows the effect of climate disaster risk, and Panel (d) plots the time paths of the risk premium.

Compared with the BAU scenario, the effects of both climate volatility risk and climate disasters on the risk premium are smaller under optimal abatement, reflecting the mitigating effect of stringent abatement policies. Nevertheless, the magnitudes of these effects remain comparable, indicating that climate volatility risk is as important as climate disasters in determining risk premia, regardless of the stringency of abatement policies.

Panel (a), (b) and (c) in Figure 3.4 imply that both climate disaster risk and volatility risk increase the risk compensation required by agents, as deteriorating climate conditions pose larger threat to economic growth. In Panel (b), the short-run and long-run risk effects of volatility risk decline over time as uncertainty about climate volatility resolves over time. The sharp increase in the middle of the period occurs when the emission control rate reaches its maximum of 100%. Beyond this point, abatement rate cannot increase, so future severe climate conditions cannot be

Figure 3.4: Decomposition of risk premia in the optimal abatement policy scenario under different $\bar{\lambda}^{(H)}$ in the new regime. The legends correspond to $\bar{\lambda}^{(H)} = 4\bar{\lambda}^{(L)}$, $2\bar{\lambda}^{(L)}$, and $\bar{\lambda}^{(L)}$. Panel (a) and (b) present the expectation effect (Expression (3.5)) and the risk effect (the last term in Equation (3.4)) of stochastic climate volatility on the risk premium. Panel (c) shows the effect of climate disaster risk, and Panel (d) shows the time paths of the risk premium.



further mitigated, resulting in a sharp rise in the risk compensation required by agents. This is reflected as the sudden increase in Panel (b).

Panel (d) shows that the risk premium exhibits little variation across different assumptions about climate conditions in the new regime. This arises because stringent emission control effectively slows global warming and delays the adverse economic impacts of climate change. Therefore, agents require less compensation for climate risks than in the BAU scenario shown in Figure 3.3.

The Stochastic Discount Factor

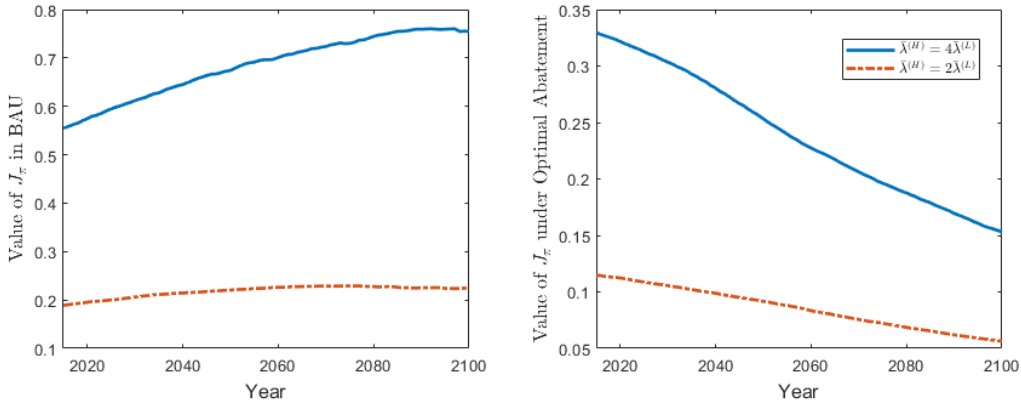
The dynamics of the stochastic discount factor π_t are essential for understanding the sources and consequences of risks in our model. Using Ito's lemma, we show in Appendix 3.A that

$$\frac{d\pi_t}{\pi_{t-}} = \mu_{\pi,t} dt - \gamma \sigma dZ_t + [(1 - J_1)^{-\gamma} - 1] dN_{1,t} + [(1 - J_2)^{-\gamma} - 1] dN_{2,t} + \mathcal{J}_{\pi,t} dN_{0,t}$$

where $\mu_{\pi,t} = -r_t^f - \lambda_1 \frac{\gamma}{\alpha_1 - \gamma} - \lambda_{2,t} \frac{\gamma}{\alpha_2 - \gamma} - \lambda_{0,t} \mathcal{J}_{\pi,t}$.

The stochastic discount factor (SDF) prices diffusive risks in the economy (dZ_t), disaster risks from both the economy (N_1) and the climate (N_2), and the risk associated with climate regime shifts (N_0). The price of economic diffusive risk is given by $\gamma\sigma$ and is positive. The sensitivity of the SDF to economic and climate disasters is captured by $[(1 - J_1)^{-\gamma} - 1]$ and $[(1 - J_2)^{-\gamma} - 1]$, respectively, both of which take positive values. The term $\mathcal{J}_{\pi,t}$ captures the exposure to regime shift risk, which is positive under both policy scenarios, as shown in Figure 3.5. Consistent with intuition, this exposure is higher in the absence of climate mitigation or under greater future climate volatility.

Figure 3.5: Exposure to the climate regime shift risk $\mathcal{J}_{\pi,t}$ under BAU (left) and optimal abatement (right). The legends correspond to $\bar{\lambda}^{(H)} = 4\bar{\lambda}^{(L)}$ and $2\bar{\lambda}^{(L)}$.



The SCC and Stochastic Climate Volatility

We now pull everything together and examine how climate volatility risk affects the SCC under different abatement policies. To explain the underlying mechanisms, we first rewrite the SCC at time 0 using the following expression derived in Appendix 3.A:

$$SCC_0 \approx \underbrace{\int_0^\infty \left(\int_0^t \chi \frac{\partial \lambda_{2,s}}{\partial T_0} \frac{1}{\alpha_2 + 1 - \gamma} ds \right)}_{(i)} \underbrace{E_0 C_t \cdot \exp \left(- \int_0^t r_s^{(CDR)} ds \right)}_{(ii)} dt \quad (3.6)$$

which is an integral of the product of two terms, (i) and (ii), from the initial time 0 to infinity. Since Equation (3.6) is challenging to evaluate numerically, we use Equation (3.1) to compute the SCC in practice. Nevertheless, Equation (3.6) provides an intuitive decomposition which will be analyzed next. This decomposition facilitates our analysis and helps identify the channels through which the climate volatility risk affects the SCC.

Term (i) captures the marginal welfare loss resulting from an incremental increase in current carbon emissions. An additional unit of carbon emitted to the atmosphere accelerates global warming, and subsequently raises the frequency of climate disasters $\lambda_{2,s}$. The marginal increase in the disaster arrival rate $\lambda_{2,s}$ with one extra unit of carbon emission today is given by $\chi \frac{\partial \lambda_{2,s}}{\partial T_0}$, which jumps from $\chi \bar{\lambda}^{(L)}$ to $\chi \bar{\lambda}^{(H)}$ upon a regime shift. The certainty equivalent of damage from a single climate disaster is measured by $\frac{1}{\alpha_2+1-\gamma}$, which remains constant under the assumption of a Type (A) regime shift, since the expected damage does not vary over time. Since the intensity of climate disasters is defined as a fraction of consumption, the integral in Term (i) is scaled by the expected consumption $E_0 C_t$.

We show in Appendix 3.A that the expected consumption flow $E_0 C_t$ can be written as

$$E_0 C_t = C_0 \exp \left\{ \int_0^t \left[\mu_{C,s} - \frac{\lambda_1}{\alpha_1 + 1} - \frac{\lambda_{2,s}}{\alpha_2 + 1} + \lambda_{0,s} \left(\frac{\xi_s}{\xi_{s-}} - 1 \right) \right] ds \right\} \quad (3.7)$$

where μ_C is the consumption growth rate, with a detailed expression provided in Appendix 3.A. It is equal to the endowment growth rate μ plus a correction term for the abatement cost. The last term in the integrand, $\frac{\xi_s}{\xi_{s-}} - 1$, is the percentage change in the consumption-endowment ratio ξ upon the arrival of a new climate regime at time s .

Equation (3.7) shows that $E_0 C_t$ is influenced by climate volatility risk through three terms in the integrand: $\mu_{C,s}$, $-\frac{\lambda_{2,s}}{\alpha_2+1}$, and $\lambda_{0,s} \left(\frac{\xi_s}{\xi_{s-}} - 1 \right)$. The term $-\frac{\lambda_{2,s}}{\alpha_2+1}$ reflects the expectation effect of climate volatility risk through $\lambda_{2,s}$. It captures the fact that future consumption is expected to grow more slowly under higher anticipated climate damages in the new regime.

The remaining two terms, $\mu_{C,s}$ and $\lambda_{0,s} \left(\frac{\xi_s}{\xi_{s-}} - 1 \right)$, capture the risk effect of volatility risk on expected consumption growth. Intuitively, consumption growth depends on the emission control rate u and hence the consumption-endowment ratio ξ . Upon a climate regime shift, the consumption growth rate jumps because both u and ξ change discontinuously. This is because the regime shift induces a sudden increase in climate disaster frequency, leading to a discontinuous rise in the marginal damage from carbon emissions. Since the optimal emission control rate equates the marginal abatement cost with the marginal damage, both the emission control rate and the consumption–endowment ratio ξ adjust discontinuously when the regime shift occurs.

In the BAU scenario, consumption equals endowment and Equation (3.7) boils down to

$$E_0 C_t = C_0 \exp \left[\int_0^t \left(\mu - \frac{\lambda_1}{\alpha_1 + 1} - \frac{\lambda_{2,t}}{\alpha_2 + 1} \right) dt \right] \quad (3.8)$$

which implies that climate volatility risk affects $E_0 C_t$ only through the expectation channel. In the absence of abatement, the consumption growth rate is not directly affected by the regime shift jump described in Equation (3.7).

Term (ii) represents the discount factor for climate damages captured by Term (i), where $r_s^{(CDR)}$ is the consumption growth-adjusted discount rate. As shown in Appendix 3.A,

$$r_t^{(CDR)} = r_t^f + r_{p,t} + r_{J,t}. \quad (3.9)$$

where r_t^f is the risk-free rate, $r_{p,t}$ is the risk premium, and $r_{J,t}$ is an additional component arising from the risk effect of stochastic climate volatility, which distinguishes it from the consumption discount rate in Olijslagers et al. (2022).

The value of $r^{(CDR)}$ depends on the preference parameters γ and ϵ . To illustrate their influence, we consider the BAU scenario without disaster risks and without abatement. In this case, the consumption growth rate $\mu_{C,t}$ equals the endowment growth rate μ , so the risk-free rate becomes

$$r_t^f = \beta + \frac{\mu}{\epsilon} - \frac{\gamma}{2} \left(1 + \frac{1}{\epsilon} \right) \sigma^2,$$

the risk premia equals $\gamma\sigma^2$, and $r_J \equiv 0$. Summing these components and subtracting μ yields the growth-adjusted discount rate

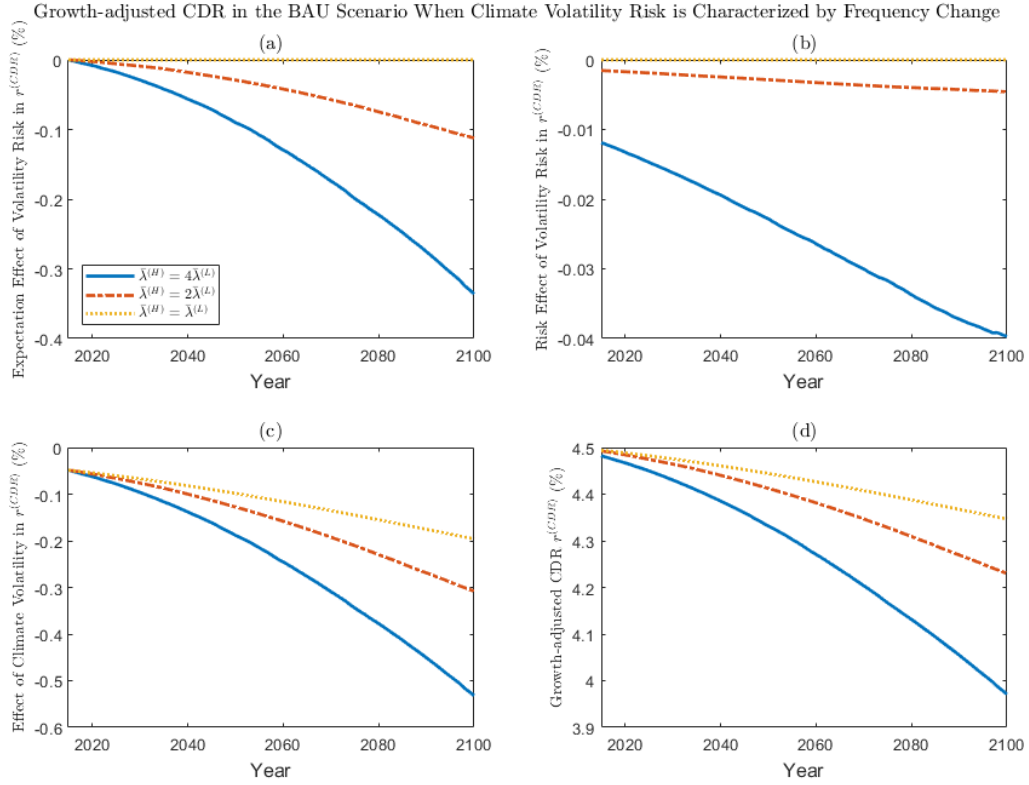
$$\beta + \left(\frac{1}{\epsilon} - 1 \right) \left(\mu - \frac{1}{2} \gamma \sigma^2 \right),$$

which increases with risk aversion γ when $\epsilon > 1$ and decreases with γ if $\epsilon < 1$. Intuitively, higher γ reduces the risk-free rate but raises the risk premium, so its net effect on the growth-adjusted discount rate depends on the relative importance of these two components, which is determined by ϵ . When ϵ is small, the precautionary saving effect dominates, and the risk-free rate effect drives the discount rate. When ϵ is large, the risk premium plays a more significant role than precautionary saving in determining the discount rate.

The SCC in the Business-As-Usual Scenario Before analyzing the SCC in the BAU scenario, we first examine the time paths of the growth-adjusted consumption discount rate $r^{(CDR)}$ and the growth rate of expected consumption given in Equation (3.7). Since neither them can be evaluated analytically, we present numerical results from our simulations to show the effects of climate volatility risk on each component.

Figure 3.6 shows the expectation effect (Panel (a)) and the risk effect (Panel (b)) of stochastic climate volatility, the effect of climate disaster risk on the growth-adjusted consumption discount rate $r^{(CDR)}$ (Panel (c)), and the time paths of $r^{(CDR)}$ (Panel (d)) in the BAU scenario. Because $r^{(CDR)}$ is the sum of the risk-free rate r^f , the risk premium r_p , and the additional term r_J , the expectation effect shown in Panel (a) corresponds to the sum of the relevant components in r^f and r_p , which can be formally computed as the sum of Equations (3.3) and (3.5). Likewise, the risk effect of stochastic climate volatility shown in Panel (b) is given by $\lambda_{0,t} \mathcal{J}_{f,t} + \lambda_{0,t} \mathcal{J}_{r_p,t} + r_J$.

Figure 3.6: The expectation effect (Panel (a)) and the risk effect (Panel (b)) of stochastic climate volatility, the effect of climate disaster risk (Panel (c)) in the growth-adjusted consumption discount rate $r^{(CDR)}$, and the time paths of $r^{(CDR)}$ (Panel (d)) under BAU. The legends correspond to $\bar{\lambda}^{(H)} = 4\bar{\lambda}^{(L)}$, $2\bar{\lambda}^{(L)}$, and $\bar{\lambda}^{(L)}$.



Negative values in Panel (a), (b) and (c) imply that both climate disaster risk and stochastic climate volatility reduce the growth-adjusted consumption discount rate $r^{(CDR)}$, which increases the SCC. The negative impact of stochastic climate volatility increases over time since rising temperatures raise the frequency of climate disasters and the likelihood of a new climate regime. A comparison of Panels (a) and (b) shows that the expectation effect dominates the risk effect in determining the growth-adjusted consumption discount rate. Panel (d) illustrates that, as a result of the climate risk effects captured in Panels (a)–(c), the growth-adjusted consumption discount rate declines over time.

Figure 3.7 shows the expected consumption growth over time in the BAU scenario, which is the integrand in Equation (3.8). Consistent with the analytical expression, expected future consumption growth is influenced by climate volatility risk only through the expectation channel, as captured by the increasing climate disaster frequency $\lambda_{2,t}$. If climate volatility risk does not exist and the frequency parameter remains time invariant, expected consumption growth still declines over time but at a slower pace, reflecting the gradual rise in the probability of climate disasters due to global warming.

Figure 3.7: The expected consumption growth rate in the business-as-usual scenario when $\bar{\lambda}^{(H)} = 4\bar{\lambda}^{(L)}$, $2\bar{\lambda}^{(L)}$, and $\bar{\lambda}^{(L)}$.

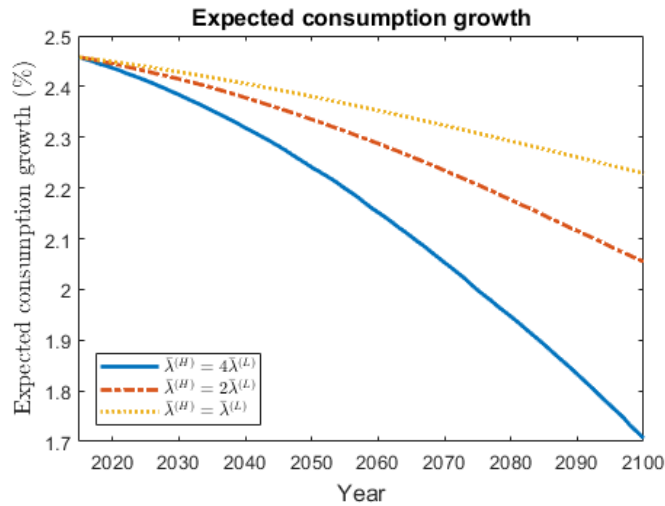


Figure 3.8 presents the average SCC and mean global surface temperature from 2015 to 2100. Since total carbon emissions are exogenously determined and independent of the magnitude of climate damages in the BAU scenario, temperature trajectories are deterministic and identical across different assumptions regarding the disaster frequency in the new climate regime, as shown in the right panel. Without abatement, the mean global surface temperature is projected to rise to 3.35°C by the end of this century.

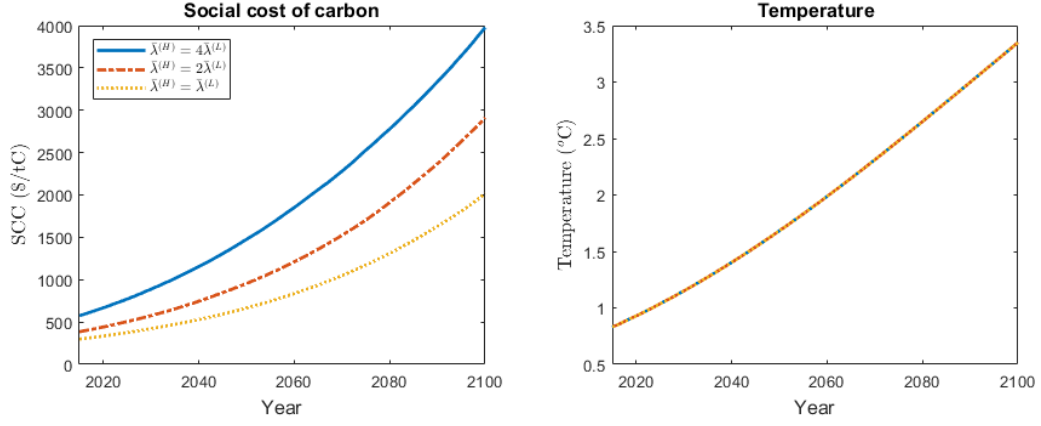
The left panel of Figure 3.8 shows the time paths of the SCC. At time 0, the initial SCC rises to \$385.06 and \$574.41 per ton of carbon if climate disasters are expected to occur two and four times as frequently in the new climate regime, respectively, compared with \$298.05 per ton of carbon when the regime shift is not considered.³

As Equation (3.6) implies, the SCC is substantially affected by climate volatility risk through both the certainty equivalent of climate disasters and the growth-adjusted consumption discount rate. When climate disasters are expected to occur more frequently in the new regime, the certainty equivalent of climate disasters increases and the growth-adjusted consumption discount rate decrease, resulting in a higher SCC.

As shown in Equation (3.6), stochastic climate volatility affects the certainty equivalent of climate disasters through the expectation channel, and affects the growth-adjusted consumption discount rate through both the expectation and risk channels. We next separate the effects of these channels on SCC and examine their interaction with preference parameters.

³Compared with Olijslagers et al. (2022), our initial SCC estimates are higher because their climate model incorporates atmospheric carbon decay and a concave radiative forcing function, both of which slow the impact of carbon emissions on global warming. By contrast, our model ignores such delays, leading to faster warming and more frequent or intense climate damages.

Figure 3.8: Social cost of carbon (US dollar per ton of carbon, or $\$/tC$) and mean global surface temperature ($^{\circ}C$) in the business-as-usual (BAU) scenario from 2015 to 2100, when climate disaster frequency in the new regime rises to $4\bar{\lambda}^{(L)}$, $2\bar{\lambda}^{(L)}$, or remains unchanged.



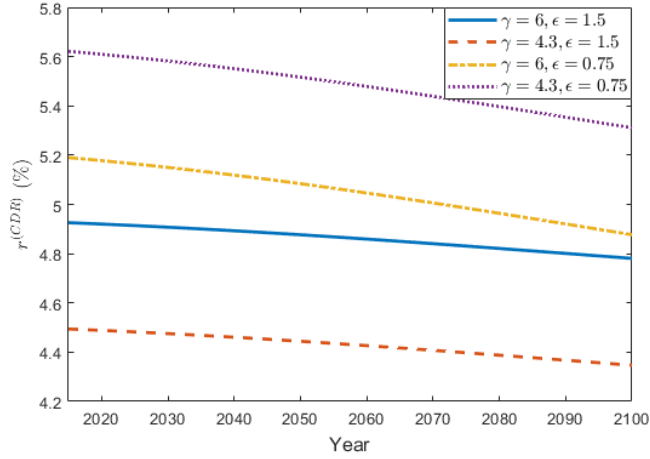
To quantify the impact of these two channels, we calculate the SCC under two different assumptions regarding the regime shift: (a) it arrives as a Poisson process with rate $\lambda_0 = 0.01$, implying an expected arrival time of 100 years, and (b) it arrives deterministically in the 100th year. Table 3.1 reports the numerical results under the assumption that climate disaster frequency doubles in the new regime (i.e. $\bar{\lambda}^{(H)} = 2\bar{\lambda}^{(L)}$). Since the SCC under deterministic regime shift captures the expectation effect of stochastic climate volatility but is not exposed to volatility risk, the difference between the values in Column (a) and (b) measures how much stochastic climate volatility affects the SCC through the risk channel. The certainty equivalent component of the SCC is identical under both types of regime shift, while volatility risk reduces the growth-adjusted consumption discount rate, resulting in higher SCCs when the regime shift is stochastic.

Table 3.1: The business-as-usual social cost of carbon ($\$/tC$) in Year 2025 as a function of risk aversion γ , EIS ϵ with and without the risk effect of climate volatility. The parameter set $(\gamma, \epsilon) = (4.3, 1.5)$ is the calibrated values in Section 3.3. Here we assume that climate disaster frequency doubles ($\bar{\lambda}^{(H)} = 2\bar{\lambda}^{(L)}$) but its size remains unchanged in the new climate regime.

γ	ϵ	(a) Stochastic regime shift	(b) Deterministic regime shift
6	1.5	359.23	268.17
4.3	1.5	504.68	377.02
6	0.75	360.07	242.49
4.3	0.75	243.37	172.76

As shown in Table 3.1, the risk channel of stochastic climate volatility leads to significant increases in the SCC across all combinations of preference parameters γ and ϵ . Higher risk aversion raises the certainty equivalent of climate disasters, but its effect on the growth-adjusted consumption discount rate $r^{(CDR)}$ and SCC depends on the value of ϵ . To see this, Figure

Figure 3.9: Growth-adjusted consumption discount rate under different risk aversion γ and EIS ϵ when regime shift is deterministic and $\bar{\lambda}^{(H)} = 2\bar{\lambda}^{(L)}$.



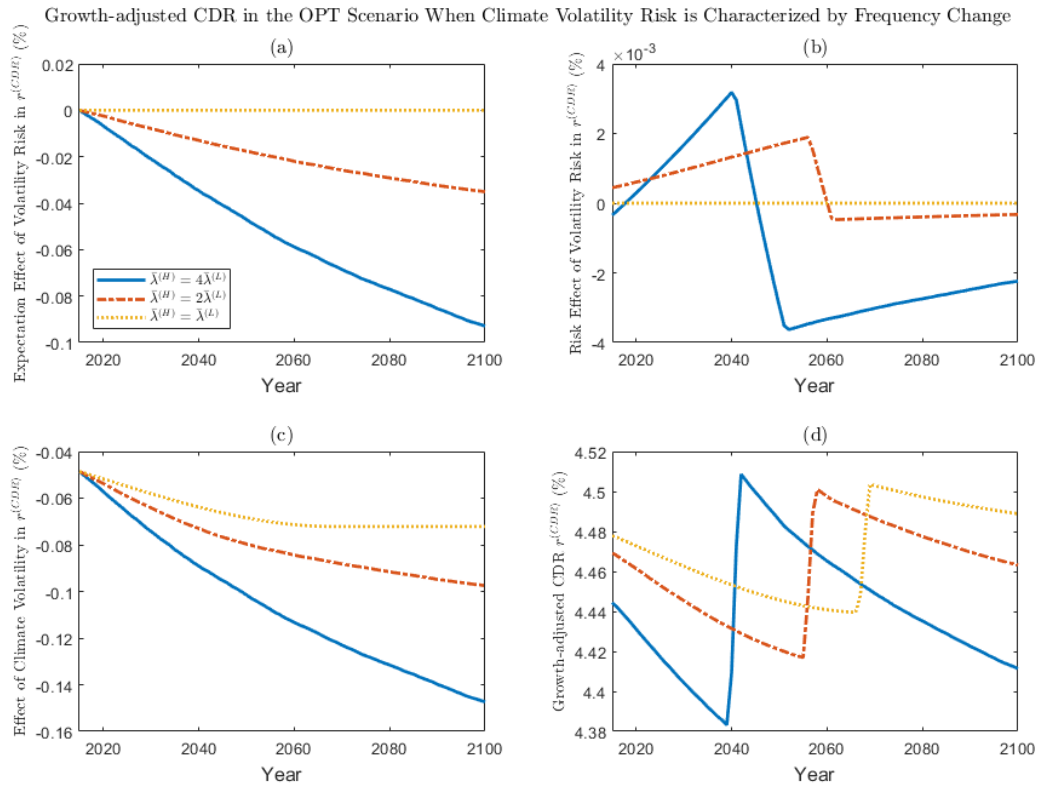
3.9 presents the time paths of $r^{(CDR)}$ under different combinations of preference parameters, assuming a deterministic regime shift. When $\epsilon > 1$, the growth-adjusted consumption discount rate $r^{(CDR)}$ increases with higher risk aversion γ , whereas it decreases with γ when $\epsilon < 1$. Table 3.1 shows that the SCC declines with increasing risk aversion for $\epsilon > 1$, but rises with risk aversion when $\epsilon < 1$. This implies that the discount effect dominates the certainty equivalent effect, consistent with the findings of Cai and Lontzek (2019) and Olijslagers and van Wijnbergen (2024).

The SCC Under Optimal Abatement We now study the effect of climate volatility risk on the SCC under optimal abatement policies. As before, we first check the dynamics of growth-adjusted consumption discount rates $r^{(CDR)}$ and the growth rate of expected consumption, since both play an important role in determining the SCC. We do this numerically, AS analytical solution is not possible.

The growth-adjusted consumption discount rate $r^{(CDR)}$ and its climate risk components under optimal abatement is shown in Figure 3.10. Panel (a) and (b) show the expectation effect and the risk effect of stochastic climate volatility on $r^{(CDR)}$, both of which are smaller than those in the BAU scenario because abatement mitigates the impact of climate volatility risk. The expectation effect shown in Panel (a) is negative and its magnitude increases over time due to the rising probability of climate disasters. The risk effect in Panel (b) initially increases over time as the probability of climate disasters rises, and gradually converges to zero in the long run as uncertainty about climate volatility is resolved. Consistent with Figure 3.2 and Figure 3.4, it exhibits a sharp decline in the medium run when the emission control rate reaches its maximum. Compared with the BAU scenario, the growth-adjusted consumption discount rate in Panel (d) remains relatively stable over time. It experiences an upward jump in the medium

run, coinciding with the point at which emission control reaches its maximum, a pattern also observed in the time paths of the risk-free rate (Figure 3.2) and risk premia (Figure 3.4).

Figure 3.10: The expectation effect (Panel (a)), the risk effect (Panel (b)) of stochastic climate volatility, the effect of climate disaster (Panel (c)) on growth-adjusted consumption discount rate, and the time paths of the discount rate (Panel (d)) under optimal abatement policies (OPT). In the new regime, climate disaster frequency rises to $4\bar{\lambda}^{(L)}$, $2\bar{\lambda}^{(L)}$, or remains unchanged.

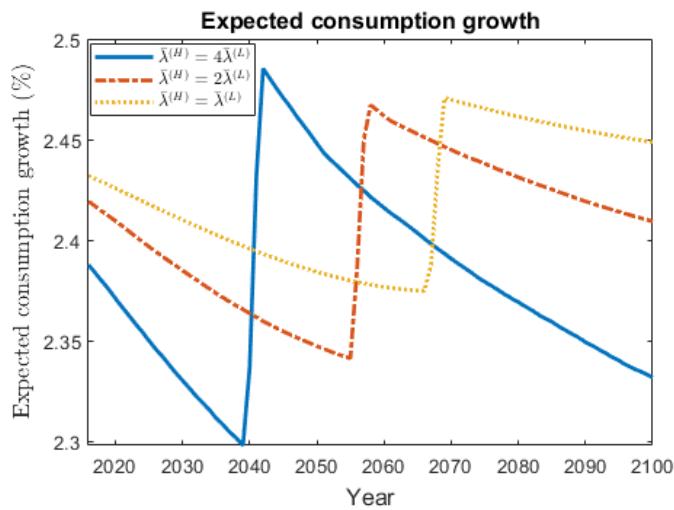


A comparison of Figure 3.11 with the corresponding BAU scenario in Figure 3.7 indicates that expected consumption growth is substantially less affected under optimal abatement. Although abatement costs reduce the endowment in each period, they substantially mitigate future climate damages by slowing the rise in temperature, thereby preserving consumption growth relative to the BAU scenario.

The expected consumption growth rate experiences an upward jump midway through the century when the emission control rate u reaches its maximum of 100%. As the marginal damage of carbon emissions rises over time, the optimal emission control rate increases correspondingly. Since we do not incorporate the possibility of carbon capture, the emission control rate ceases to increase after reaching 100% and remains at this maximum level thereafter (see Figure 3.12). Because expected consumption growth depends on both the anticipated endowment growth rate and the growth rate of abatement costs, the sudden stop of abatement cost growth results in a discrete upward jump in the expected consumption growth rate.

In the short run, the decline in expected consumption growth reflects both anticipated climate damages under regime shift risk and the more stringent emission controls over time. In the long run, once abatement reaches its maximum of 100%, the consumption growth rate is expected to decline again. However, this decline is now driven solely by the increasing *expected* damages from climate disasters to the aggregate endowment and consumption under regime shift risk.

Figure 3.11: Expected consumption growth rate under optimal abatement policies when $\bar{\lambda}^{(H)} = 4\bar{\lambda}^{(L)}$, $2\bar{\lambda}^{(L)}$ and $\bar{\lambda}^{(L)}$.

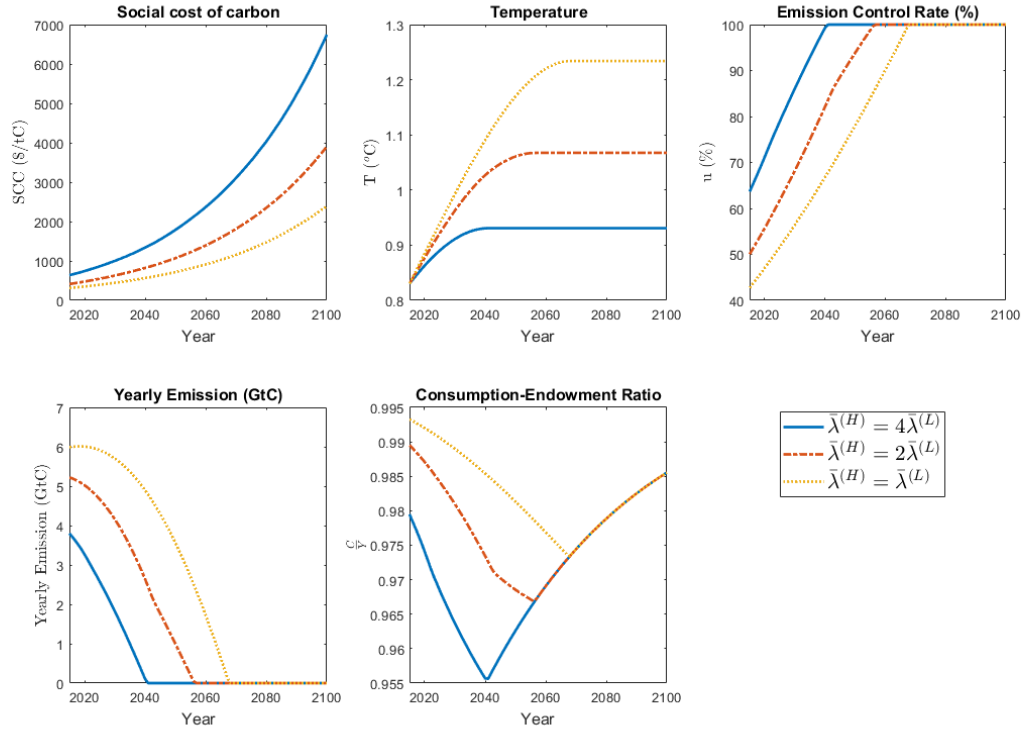


We also find that a larger value of $\bar{\lambda}^{(H)}$ results in lower *expected* consumption growth in both the short and long run. This is because the frequency of climate disasters in the new climate regime $\lambda_{2,t} = \bar{\lambda}^{(H)}T_t$ increases with $\bar{\lambda}^{(H)}$. Although higher disaster risk induces stronger abatement efforts, which in turn lower long-run temperature T , this mitigation effect is insufficient to offset the increase in $\bar{\lambda}^{(H)}$. As shown in Figure 3.12, under optimal abatement, doubling the disaster frequency parameter (i.e., $\bar{\lambda}^{(H)} = 2\bar{\lambda}^{(L)}$) reduces long-run temperature by only about 16%. Therefore, more severe climate conditions in the new regime lead to slower expected consumption growth even under optimal abatement.

Figure 3.12 presents the time paths of the SCC, mean global surface temperature, emission control rate, annual carbon emissions, and the consumption-endowment ratio under optimal abatement policies. Under all assumptions on $\bar{\lambda}^{(H)}$, the SCC increases over time since it is proportional to consumption which grows over time. Moreover, the SCC is larger when climate disasters are expected to be more frequent in the new regime: lower discount rates and higher certainty equivalent of climate damages under volatile climate conditions both contribute to a higher SCC. Specifically, when climate disasters are expected to occur twice and four times as frequently in the new regime, the initial SCC rises to \$413.64 and \$637.94 per ton of carbon, respectively, compared with \$311.06 per ton of carbon in the absence of a climate regime shift.

3.4 The SCC and Climate Volatility Risk: Numerical Results

Figure 3.12: Social cost of carbon, mean global surface temperature, emission control rate, yearly carbon emissions and consumption-endowment ratio from Year 2015 to 2100 under optimal abatement, when $\bar{\lambda}^{(H)} = 4\bar{\lambda}^{(L)}$, $2\bar{\lambda}^{(L)}$ and $\bar{\lambda}^{(L)}$.



The dynamics of emission control, annual carbon emissions, temperature, and the consumption-endowment ratio vary across different values of $\bar{\lambda}^{(H)}$. More stringent emission controls under higher $\bar{\lambda}^{(H)}$ reduce annual emissions and slow the rise in temperature T . Meanwhile, since the climate disaster frequency is given by $\lambda_{2,t} := \bar{\lambda}_t T_t$, temperature T directly affects the marginal damage of carbon emissions and thus the stringency of emission control. Initially, temperatures are the same under different values of $\bar{\lambda}^{(H)}$, but stricter emission controls under higher $\bar{\lambda}^{(H)}$ slow the increase in T , partially mitigating the effect of $\bar{\lambda}^{(H)}$ on disaster frequency $\lambda_{2,t}$. However, as shown in Figure 3.12, stricter emission controls under both $\bar{\lambda}^{(H)} = 2\bar{\lambda}^{(L)}$ and $\bar{\lambda}^{(H)} = 4\bar{\lambda}^{(L)}$ yield less than a 20% reduction in the long-run temperature relative to the baseline case where $\bar{\lambda}^{(H)} = \bar{\lambda}^{(L)}$. This implies that the mitigating effect of slower temperature growth is insufficient to offset the direct impact of higher $\bar{\lambda}^{(H)}$. Therefore, a higher $\bar{\lambda}^{(H)}$ leads to larger marginal damages from emissions and stricter emission control. In particular, without climate volatility risk, the optimal abatement rate in 2015 is slightly above 40%. With more frequent disasters in the new regime, the optimal emission control rate increases and reaches 100% earlier, and remain at this maximum level thereafter. As technological progress lowers marginal abatement costs, the consumption-endowment ratio increases in the long run.

Compared with the BAU scenario, the SCC is larger under optimal abatement policy. This reflects the joint impact of the certainty equivalent of climate damages and discounting effects, as described in Equation (3.6). On the one hand, emission abatement slows global warming, so future aggregate endowment and consumption are less affected by climate damages, which increases the certainty equivalent component (Term (i) in Equation (3.6)). On the other hand, the discount rate under optimal abatement (Figure 3.10) is higher than in the BAU scenario (Figure 3.6). Intuitively, when future consumption is better protected from climate damages under stringent abatement, the discount factor declines, or equivalently, the discount rate rises. Since the SCC is higher under optimal abatement despite this stronger discounting effect, we conclude that the certainty equivalent effect dominates.

Finally, we find that there is considerable uncertainty about the SCC in the future under both policies, because the endowment process is stochastic and the climate regime shift is uncertain. Table 3.2(a) reports the means and standard deviations of the SCC in the BAU scenario for 2025, 2050 and 2100. In all cases, both the mean and the standard deviation increase over time. This is consistent with the fact that the SCC is a geometric Brownian motion (GBM) because it depends on aggregate endowment which itself follows a GBM process (Shephard and Andersen (2009)). In the optimal abatement scenario, there is also substantial uncertainty, as shown in Table 3.2(b). Compared with BAU, both the mean and the standard deviation are larger under the same assumptions about the new climate regime. This is due to the different impact of the certainty equivalent effects and the discount effect of climate volatility risk on SCC. Under optimal abatement, the certainty equivalent effect is larger but the discount effect is weaker than in the BAU case. The higher SCC under optimal abatement implies that the certainty equivalent effect dominates the discount effect.

Table 3.2: Means and standard deviations of SCC (\$/tC) in Year 2025, 2050 and 2100 from Monte Carlo simulations.

New Regime	Year	(a) Business as usual		(b) Optimal abatement	
		Mean	Standard Deviation	Mean	Standard Deviation
$\frac{\bar{\lambda}^{(H)}}{\bar{\lambda}^{(L)}} = 1$	2025	375.79	49.12	395.19	51.89
	2050	666.22	166.46	717.51	177.09
	2100	2013.39	804.42	2393.98	942.04
$\frac{\bar{\lambda}^{(H)}}{\bar{\lambda}^{(L)}} = 2$	2025	504.68	87.11	548.38	100.82
	2050	955.47	281.33	1070.20	323.57
	2100	2911.38	1208.18	3900.78	1666.68
$\frac{\bar{\lambda}^{(H)}}{\bar{\lambda}^{(L)}} = 4$	2025	770.80	164.00	863.49	204.97
	2050	1475.99	457.98	1788.28	666.13
	2100	3976.36	1679.76	6741.11	3120.43

3.4.2 The New Climate Regime (B): Higher Disaster Intensity

We now introduce climate volatility risk by assuming that in the new climate regime, climate disasters become more severe rather than more frequent. Specifically, upon the regime shift, the expected damages from a single extreme weather event increases immediately to $E J_2^{(H)}$ from the current value $E J_2^{(L)}$. We refer to this setting as Regime (B). To compare the numerical results under different types of climate volatility risk, we scale the post-shift expected damage size by the same multipliers, considering $\frac{E J_2^{(H)}}{E J_2^{(L)}} = 2$ and 4.⁴ We first analyze the BAU scenario, and then contrast the results with those under the optimal abatement policy.

Business-As-Usual Scenario We begin with the BAU scenario, under exogenous emissions and assuming the stochastic shock structure of Regime (B). In Section 3.5, we extend the analysis to endogenous and hence stochastic emissions.

Without abatement and with deterministic emissions, the emission path is the same under all possible values of the expected disaster size $E J_2^{(H)}$ in the new regime. Consequently, in the BAU scenario with non-stochastic emissions, the temperature path T is also identical across all assumptions on $E J_2^{(H)}$.⁵ Therefore, expected annual climate damages remain the same after a regime shift of either type, as long as $\frac{E J_2^{(H)}}{E J_2^{(L)}}$ in Regime (B) equals $\frac{\bar{\lambda}^{(H)}}{\bar{\lambda}^{(L)}}$ in Regime (A). However, we will show that the resulting SCC differs in the two regimes, even though expected damages are identical.

We first isolate the effect through the consumption discount rate (CDR), recall the analytical expression for the SCC (Equation (3.6)). Figure 3.13 shows the growth-adjusted consumption discount rate $r^{(CDR)}$ and its components associated with climate disaster risk and climate volatility risk in the BAU scenario. Panel (a) and (b) show the expectation and the risk effects of stochastic climate volatility on $r^{(CDR)}$, respectively. Panel (c) shows the effect of climate disasters on $r^{(CDR)}$. Panel (d) plots the time paths of $r^{(CDR)}$ under different assumptions regarding the disaster intensity $E J_2^{(H)}$ in the new regime.

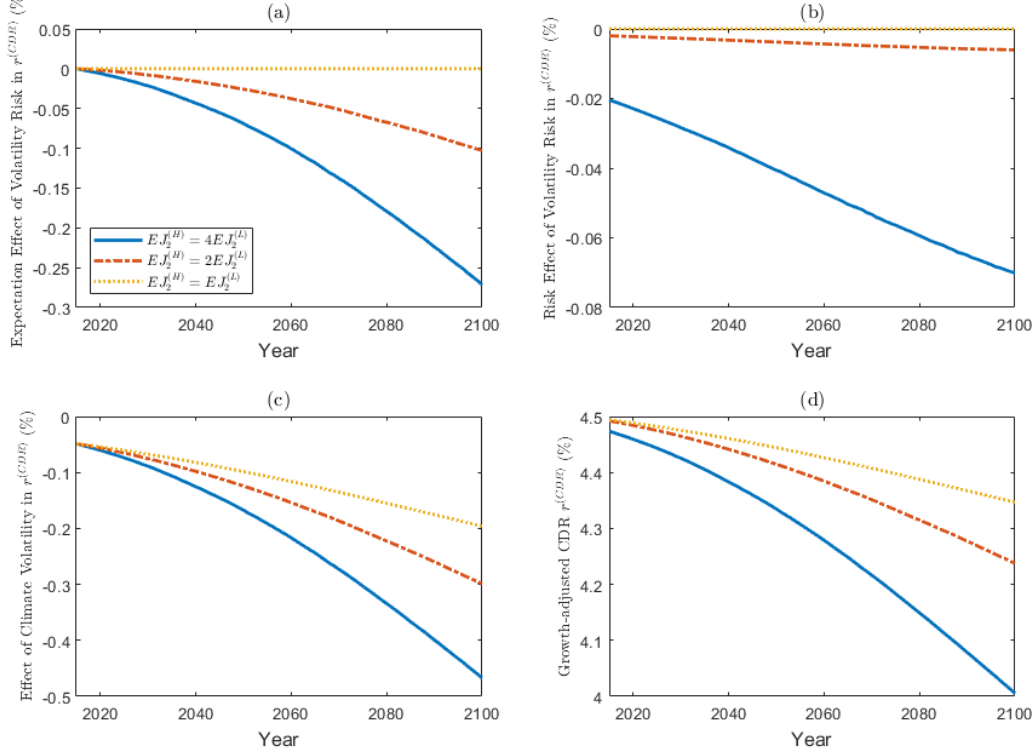
The magnitudes in all these panels do not differ much from those in Figure 3.6 for Regime (A) in the BAU scenario. Negative values in Panel (a), (b) and (c) imply that both climate disaster risk and climate volatility risk reduce the growth-adjusted consumption discount rate $r^{(CDR)}$. A lower CDR obviously implies a higher consumption discount factor, which in turn raises the SCC by reducing the discount rate of future damages. The expectation effect of climate volatility risk (Panel (a)) and the effect of climate disaster risk (Panel (c)) are of comparable magnitude and both dominate the risk effect of climate volatility risk (Panel (b)).

⁴The implications of Regime (B) for risk-free rates and risk premia are shown in Appendix 3.B.

⁵This equivalence does not hold under optimal abatement since abatement responds to both the type and the magnitude of shocks. Because carbon concentration depends on $(1 - u_t)E_t$, endogenous abatement generates distinct emissions and temperature trajectories.

Figure 3.13: The expectation effect of climate volatility risk (Panel (a)), the risk effect of climate volatility risk (Panel (b)) and the effect of climate disaster risk (Panel (c)) on the growth-adjusted consumption discount rate $r^{(CDR)}$, as well as the time paths of $r^{(CDR)}$ (Panel (d)) in the BAU scenario. The expected intensity of one climate disaster in the new regime rises to $4EJ_2^{(L)}$, $2EJ_2^{(L)}$, or remains unchanged.

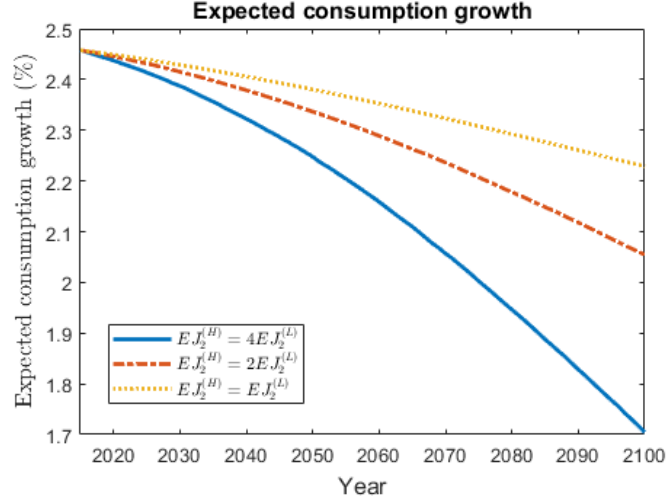
Growth-adjusted CDR in the BAU Scenario When Climate Volatility Risk is Characterized by Intensity Change



Next, we examine the certainty equivalent effect on the SCC, which consists of two parts according to Equation (3.6): the expected future consumption flow $E_0 C_t$ and the marginal increase in the certainty equivalent of climate damages to $E_0 C_t$ from one additional unit of emissions today. Figure 3.14 shows the growth rate of expected consumption $E_0 C_t$ in Regime (B) (see Equation (3.8) for the analytical expression). As climate damages intensify with global warming, expected consumption growth declines over time. Moreover, a higher disaster intensity $E J_2^{(H)}$ in the new regime generate an even sharper decline in expected consumption growth, since more severe climate disasters hinder the economic growth to a larger extent. A comparison with Figure 3.7 implies that the dynamic response of expected consumption growth is nearly the same under Regime (A) and Regime (B).

However, the marginal increase in the certainty equivalent component of climate damages on expected consumption at time t , given by $\int_0^t \chi \frac{\partial \lambda_{2,s}}{\partial T_0} \frac{1}{\alpha_{2,s} + 1 - \gamma} ds$, is larger in Regime (B) than Regime (A), even when the *expected* climate damages are the same in both new regimes (i.e. when the multipliers on disaster frequency and intensity are equal). This result follows from the concavity of utility under risk aversion. When climate disasters become more intense,

Figure 3.14: Expected consumption growth in the BAU scenario when the expected size of one climate disaster in the new regime rises to $4EJ_2^{(L)}$, $2EJ_2^{(L)}$, or remains unchanged.



the certainty equivalent of the marginal increase in climate damage is larger, even though the expected climate damages are the same under both regimes.

As a numerical example, consider the regime shift arrives at the same date τ under both regimes when the multiplier is 2. Then

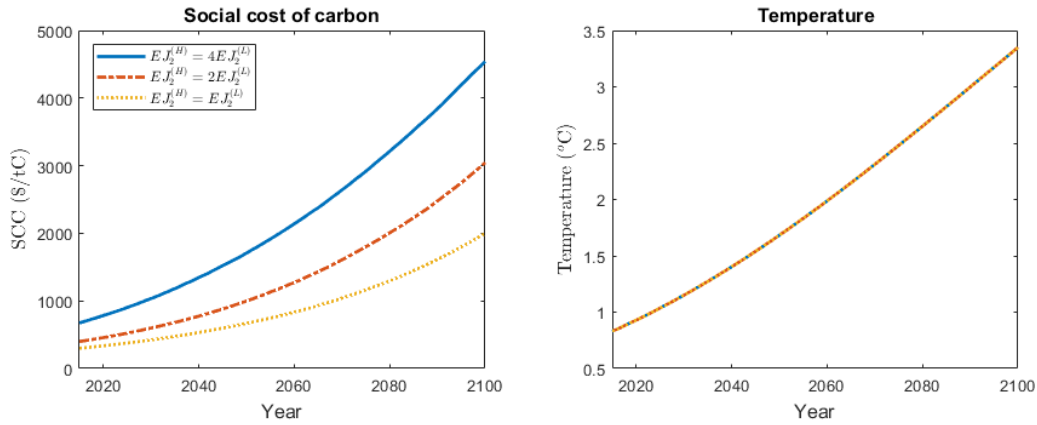
$$\begin{aligned}
 CE_t(B) &= \left(\int_0^\tau \chi \bar{\lambda}^{(L)} \frac{1}{\alpha_2^{(o)} + 1 - \gamma} ds + \int_\tau^t \chi \bar{\lambda}^{(L)} \frac{1}{\alpha_2^{(n)} + 1 - \gamma} ds \right) E_0 C_t \\
 &> \left(\int_0^\tau \chi \bar{\lambda}^{(L)} \frac{1}{\alpha_2^{(o)} + 1 - \gamma} ds + 2 \int_\tau^t \chi \bar{\lambda}^{(L)} \frac{1}{\alpha_2^{(o)} + 1 - \gamma} ds \right) E_0 C_t \\
 &= \left(\int_0^t \chi \frac{\partial \lambda_{2,s}}{\partial T_0} \frac{1}{\alpha_{2,s} + 1 - \gamma} ds \right) E_0 C_t = CE_t(A)
 \end{aligned}$$

where $CE_t(A)$ and $CE_t(B)$ are the certainty equivalent term at time t in Equation (3.6) under regime (A) and (B), respectively. The inequality arises because the disaster intensity in the new regime $EJ_2^{(H)} := \frac{1}{\alpha_2^{(n)} + 1}$ is twice the current disaster intensity $EJ_2^{(L)} := \frac{1}{\alpha_2^{(o)} + 1}$. Consequently, for $\gamma > 0$, we have $\frac{1}{\alpha_2^{(n)} + 1 - \gamma} > 2 \cdot \frac{1}{\alpha_2^{(o)} + 1 - \gamma}$.

Finally, we consider the dynamics of the SCC. Figure 3.15 shows the time paths of the SCC and temperature in the BAU scenario under Regime (B). As previously noted, temperature evolves identically across all assumptions on $EJ_2^{(H)}$ under deterministic emissions. However, the SCC is larger when shocks follow Regime (B). While the growth-adjusted discount rates are similar under both regimes, the certainty equivalent effect of climate damages in Regime (B) is greater than in Regime (A). Specifically, the initial SCC equals \$298.05 per ton of carbon

without climate volatility risk, rises to \$398.88 per ton of carbon when the intensity of one climate disaster doubles, and reaches \$673.73 per ton when the disaster multiplier is four.

Figure 3.15: SCC (\$/tC) and mean global surface temperature ($^{\circ}\text{C}$) in the BAU scenario from 2015 to 2100. The expected size of one climate disaster in the new regime rises to $4EJ_2^{(L)}$, $2EJ_2^{(L)}$, or remains unchanged.



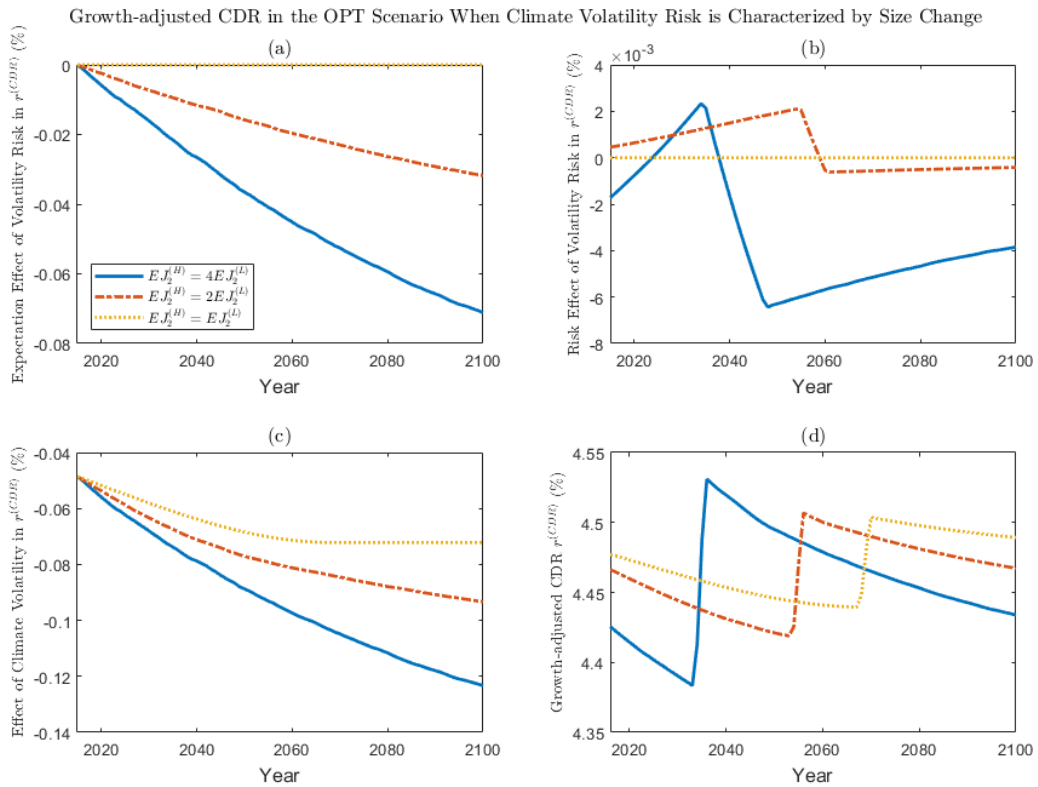
Optimal Abatement Policy We next examine the SCC under optimal abatement policy, focusing on how climate volatility risk influences the SCC through both the discount effect and the certainty equivalent effect.

As before, in Figure 3.16, we decompose the growth-adjusted consumption discount rate $r^{(CDR)}$ into the expectation effect (Panel (a)), the risk effect (Panel (b)), and a risk effect attributable specifically to volatility risk rather than to volatility itself (Panel (c)). Panel (d) shows the combined impact of climate disasters on $r^{(CDR)}$ under optimal abatement. Comparing the plots with the corresponding BAU scenario (3.15) indicates that the magnitudes of climate risk effects in Panel (a), (b) and (c), as well as the time path of the growth-adjusted consumption discount rates, are similar to those under Regime (A). However, relative to the BAU scenario, both the expectation effect and the risk effect of stochastic climate volatility are smaller under optimal abatement. This reflects the mitigating effect of emission control, which weakens the impact of climate volatility risk on the consumption discount factor.

We next examine the certainty equivalent effect on the SCC (Equation (3.6)), which consists of two components: the expected future consumption $E_0 C_t$ and the marginal increase in the certainty equivalent of climate damages on $E_0 C_t$ from one extra unit of emissions today. Figure 3.17 presents the growth rate of expected future consumption $E_0 C_t$ under optimal abatement in Regime (B), which closely resembles Figure 3.11 for Regime (A). In the short run, expected consumption growth declines over time due to increasing climate damages and more stringent emission control. In the medium run, it increases discontinuously when the emission control rate u reaches its maximum of 100% and remains at this level afterwards. This upward jump

3.4 The SCC and Climate Volatility Risk: Numerical Results

Figure 3.16: The effect of climate volatility risk on growth-adjusted consumption discount rate through the expectation channel (Panel (a)) and the risk channel (Panel (b)), the effect of climate disaster risk (Panel (c)), and the discount rate (Panel (d)) under optimal abatement policy. In the new climate regime, the expected damage size of one climate disaster increases to $4EJ_2^{(L)}$, $2EJ_2^{(L)}$, or remains unchanged in the new regime.

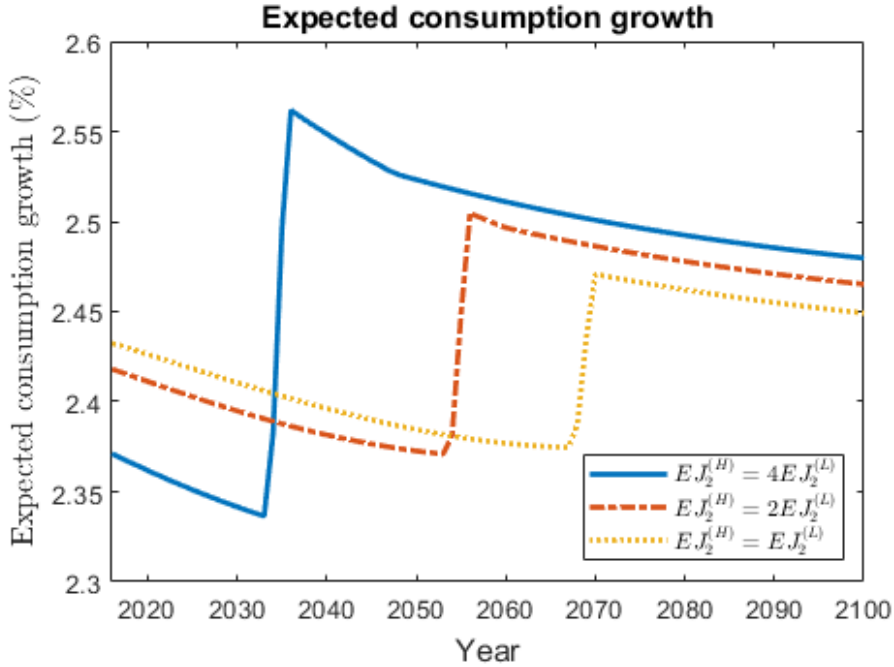


occurs because expected consumption growth reflects the combined growth of endowment and abatement costs. When the growth of abatement costs stops, the contribution from abatement growth also stops, resulting in a discrete increase in consumption growth.

Under optimal abatement, expected consumption growth is less sensitive to climate change than in the BAU scenario. While abatement consumes a fraction of the endowment in each period, it significantly mitigates the adverse effects of climate disasters on consumption, resulting in higher long-run endowment and consumption growth.

Figure 3.18 presents the time paths of the SCC, mean global surface temperature, emission control rate, annual carbon emissions, and consumption-endowment ratio under optimal abatement policies in Regime (B). As in Regime (A), the SCC rises over time, as it is proportional to consumption which increases over time. Moreover, higher disaster intensity in the new regime leads to a larger SCC due to lower discount rates and a higher certainty equivalent of climate damages. Specifically, when the average intensity of climate disasters is doubled and quadrupled

Figure 3.17: Expected consumption growth rate under optimal abatement if the expected damage size of one climate disaster increases to $6EJ_2^{(L)}$, $4EJ_2^{(L)}$, $2EJ_2^{(L)}$, or remains unchanged in the new regime.



in the new regime, the initial SCC rises to \$429.71 and \$762.70 per ton of carbon, respectively, compared with \$311.06 per ton of carbon when climate volatility risk is not considered.

The dynamics of emission control, annual emissions, temperature, and the consumption-endowment ratio vary with the assumed disaster intensity $EJ_2^{(H)}$ in the new regime. Larger $EJ_2^{(H)}$ induces stricter emission control, which reduces the consumption-endowment ratio, lowers annual emissions, and slows the increase in temperature.

Comparing Regime (B) with Regime (A) (in Figure 3.12), we find that emission control is stricter under Regime (B). This is because the certainty equivalent of climate damage increases more under Regime (B) than (A), as discussed earlier in this section. More stringent emission control accounts for the lower consumption-endowment ratio, faster reduction in annual emissions, and slower temperature increase under Regime (B).

For completeness, we provide the means and standard deviations of the SCC under both policy scenarios in Table 3.3. In both cases, the mean and standard deviation of the SCC increase over time. Comparison with Table 3.2 indicates that a new climate regime characterized by more intense disasters raises the SCC more than a regime with more frequent disasters, holding the expected damage value constant.

Figure 3.18: Social cost of carbon, mean global surface temperature, emission control rate, yearly carbon emissions and consumption-endowment ratio from Year 2015 to 2100 under optimal abatement in Regime (B) of climate volatility risk, where the expected size of one climate disaster in the new regime rises to $4EJ_2^{(L)}$, $2EJ_2^{(L)}$, or remains unchanged.

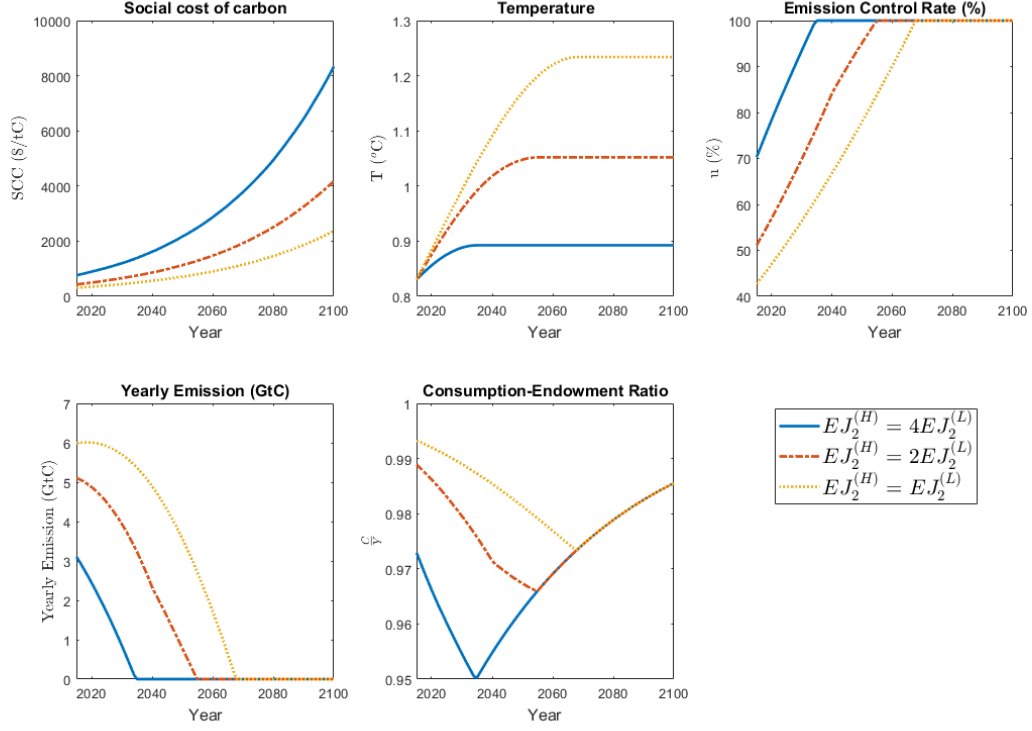


Table 3.3: Means and standard deviations of SCC (\$/tC) in Year 2025, 2050 and 2100 when climate disasters become more intense in the new regime.

New Regime	Year	(a) Business as usual		(b) Optimal abatement	
		Mean	Standard Deviation	Mean	Standard Deviation
$\frac{EJ_2^{(H)}}{EJ_2^{(L)}} = 1$	2025	375.79	49.12	395.19	51.89
	2050	666.22	166.46	717.51	177.09
	2100	2013.39	804.42	2393.98	942.04
$\frac{EJ_2^{(H)}}{EJ_2^{(L)}} = 2$	2025	521.70	93.18	573.66	109.66
	2050	997.56	300.53	1130.65	357.51
	2100	3043.94	1276.30	4176.99	1804.32
$\frac{EJ_2^{(H)}}{EJ_2^{(L)}} = 4$	2025	901.94	196.30	1036.46	260.80
	2050	1706.84	540.31	2168.28	840.28
	2100	4542.63	2009.69	8332.87	4026.95

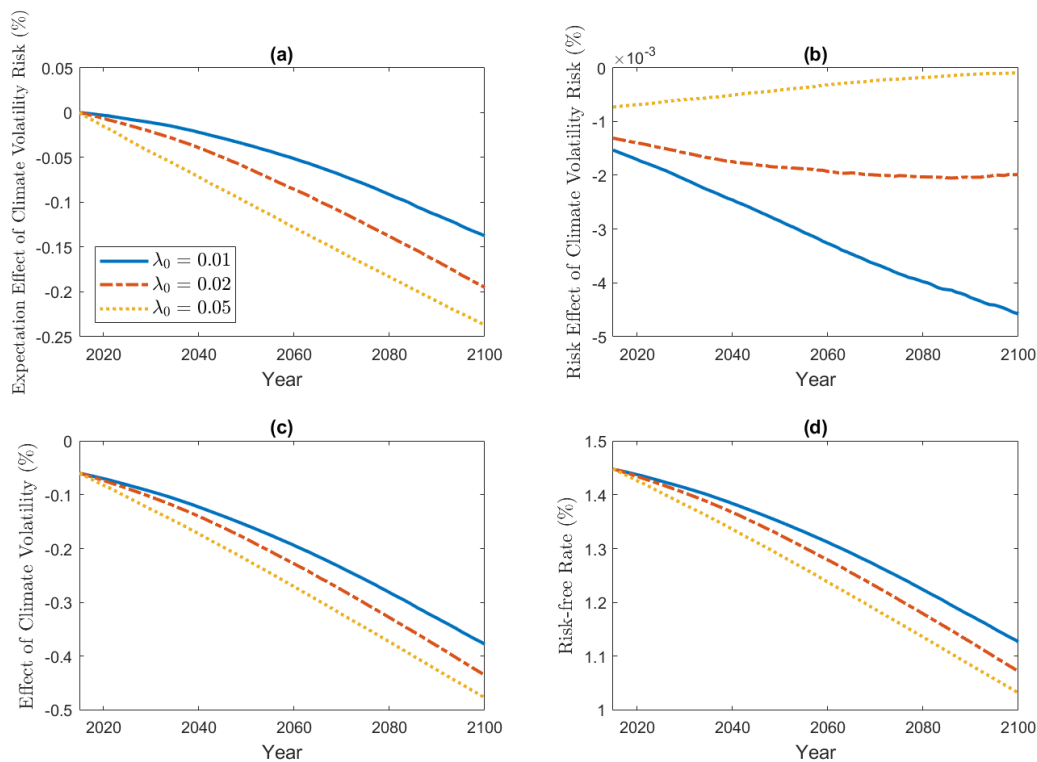
3.4.3 Arrival Rates of Climate Regime Shift

Given the absence of time-series data and reliable models of climate volatility risk, calibrating the arrival rate of a new climate regime, λ_0 , is inherently challenging. In the analysis above, we

set $\lambda_0 = 0.01$, implying an expected arrival time of 100 years, consistent with the horizon used in the first IPCC reports. In this section, we explore alternative values of λ_0 (0.01, 0.02, and 0.05) under the BAU scenario, assuming that the disaster frequency parameter in the new regime doubles (i.e., $\bar{\lambda}^{(H)} = 2\bar{\lambda}^{(L)}$). We then examine how different values of λ_0 affect the risk-free rate, the risk premium, and the SCC.

Risk-Free Rate Figure 3.19 shows the risk-free rate and its decomposition under $\lambda_0 = 0.01$, 0.02, and 0.05. Panel (a) and (b) show the expectation effect and the risk effect of the stochastic climate volatility on risk-free rates. Panel (c) isolates the contribution of climate disasters, and Panel (d) plots the time paths of the risk-free rate.

Figure 3.19: Decomposition of (average) risk-free rates in the BAU scenario under $\lambda_0 = 0.01, 0.02,$ and 0.05 , where $\bar{\lambda}^{(H)} = 2\bar{\lambda}^{(L)}$. Panel (a) and (b) present the expectation effect (Expression (3.3)) and the risk effect (i.e. the last term in Equation (3.2)) of stochastic climate volatility on the risk-free rate. Panel (c) shows the effect of climate disaster risk, and Panel (d) shows the risk-free rate over time.



Panel (a) - (c) show that both climate disaster risk and climate volatility risk contribute to lowering the risk-free rate, with magnitudes that increase under higher values of λ_0 . This reflects that an earlier arrival of the new climate regime (i.e., a higher risk of climate regime shift) exposes the economy to greater climate risks. The magnitudes of the expected effect of climate volatility risk (Panel (a)) and the disaster risk (Panel (c)) both increase over time, as rising temperatures induce more frequent climate damages and larger expected climate damages

under stochastic regime. While the expectation effect of volatility risk and the disaster risk effect are of comparable size, the risk effect of volatility risk (Panel (b)) is much smaller.

Panel (b) shows that the risk effect of climate volatility is non-monotonic over time. When λ_0 is high, the uncertainty about the regime shift is expected to be resolved sooner, so the risk effect converges to zero earlier. In contrast, when λ_0 is smaller, the resolution of this uncertainty is delayed, leading the magnitude of the risk effect to increase over a longer time horizon before eventually converging to zero. Since the risk effect is relatively small, the risk-free rate in Panel (d) is mainly shaped by the expectation effect of climate volatility risk and by climate disaster risk, resulting in a downward-sloping time path.

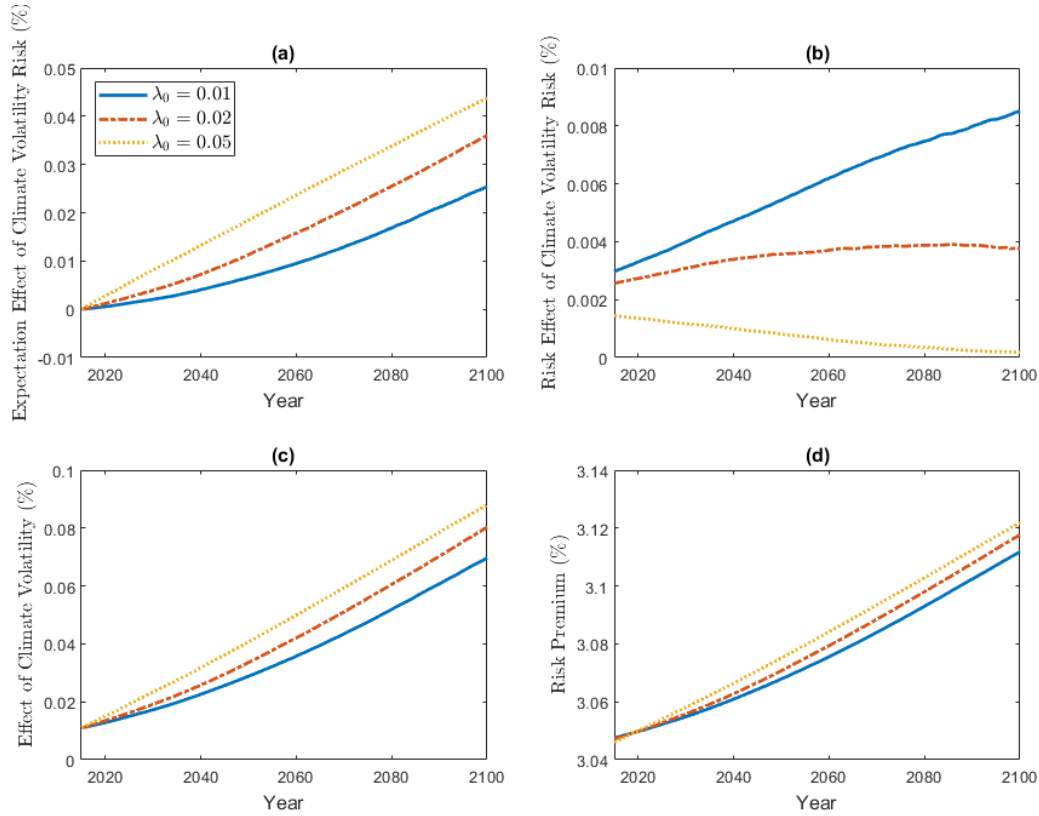
Risk Premium Figure 3.20 shows the risk premia and its climate-related components in the BAU scenario. Panel (a) and (b) present the expectation effect and the risk effect of climate volatility risk, respectively. Panel (c) the contribution of climate disaster risk, and Panel (d) plots the resulting time paths of risk premia. All these three components of climate risk have positive effects on the risk premium. The expectation effect (Panel (a)) and the disaster effect (Panel (c)) are of comparable magnitude, whereas the risk effect of climate volatility is relatively smaller

Panel (a) and (c) indicate that both the expectation effect and the disaster effect increase in λ_0 , as agents demand higher compensation when a regime with more frequent extreme weather is expected to arrive sooner. The risk effect of stochastic climate volatility, shown in Panel (b), converges to zero in the long run once uncertainty about the regime shift is resolved. In the short run, a smaller λ_0 implies a later arrival of the new regime, resulting in a larger impact on risk premia that persists and converges only further into the future.

Social Cost of Carbon Before turning to the SCC, we first present the time paths of the growth-adjusted consumption discount rate $r^{(CDR)}$ and the growth rate of expected consumption defined in Equation (3.7). Since neither can be evaluated analytically, we report numerical results from simulations to illustrate the role of climate volatility risk.

Figure 3.21 shows the expectation effect (Panel (a)) and the risk effect (Panel (b)) of stochastic climate volatility, the effect of climate disaster risk on $r^{(CDR)}$ (Panel (c)), and the time path of $r^{(CDR)}$ itself (Panel (d)). Negative values in Panel (a) - (c) indicate that both climate disaster risk and stochastic climate volatility reduce the growth-adjusted consumption discount rate $r^{(CDR)}$, thereby raising the SCC. The magnitudes of the climate disaster effect and the expectation effect of climate volatility risk increase over time due to the irreversible global warming and the threat of a more severe future regime, and they are larger for higher λ_0 , reflecting earlier exposure to volatility shocks. The risk effect in Panel (b) is relatively small and converges to zero more quickly under larger λ_0 , as uncertainty is resolved earlier. Hence, the downward-sloping paths

Figure 3.20: Decomposition of risk premia in the BAU scenario under $\lambda_0 = 0.01, 0.02, \text{ and } 0.05$, where $\bar{\lambda}^{(H)} = 2\bar{\lambda}^{(L)}$. Panel (a) and (b) present the expectation effect (Expression (3.5)) and the risk effect (the last term in Equation (3.4)) of stochastic climate volatility on risk premia. Panel (c) shows the effect of climate disaster risk, and Panel (d) shows the risk premia over time.



of $r^{(CDR)}$ in Panel (d) are primarily driven by the disaster effect and the expectation effect of volatility risk.

Figure 3.22 shows the time path of expected consumption growth. As indicated by Equation (3.8), climate volatility risk affects expected growth only through the expectation channel. For all values of λ_0 , the expected consumption growth rate declines over time due to worsening climate conditions. Higher λ_0 corresponds to an earlier arrival of a regime with more frequent disasters, which slows the growth of aggregate endowments and consumption, yielding a lower trajectory of expected consumption growth.

Figure 3.23 presents the average SCC and mean global surface temperature from 2015 to 2100 in the BAU scenario under different arrival rates of a new climate regime. Since carbon emissions are exogenous and independent of climate damages in this scenario, temperature evolution is deterministic and identical across all values of λ_0 , as shown in the right panel. that the SCC is slightly higher for larger λ_0 , although the differences remain modest. This is because in the short run, an earlier expected arrival of severe climate conditions (higher λ_0) increases welfare losses and raises the SCC. Over the long term, however, as uncertainty about the regime

3.4 The SCC and Climate Volatility Risk: Numerical Results

Figure 3.21: The expectation effect (Panel (a)) and the risk effect (Panel (b)) of stochastic climate volatility, the effect of climate disaster risk (Panel (c)) in the growth-adjusted consumption discount rate $r^{(CDR)}$, and the time paths of $r^{(CDR)}$ (Panel (d)) in the BAU scenario under $\lambda_0 = 0.01, 0.02,$ and 0.05 , where $\bar{\lambda}^{(H)} = 2\bar{\lambda}^{(L)}$.

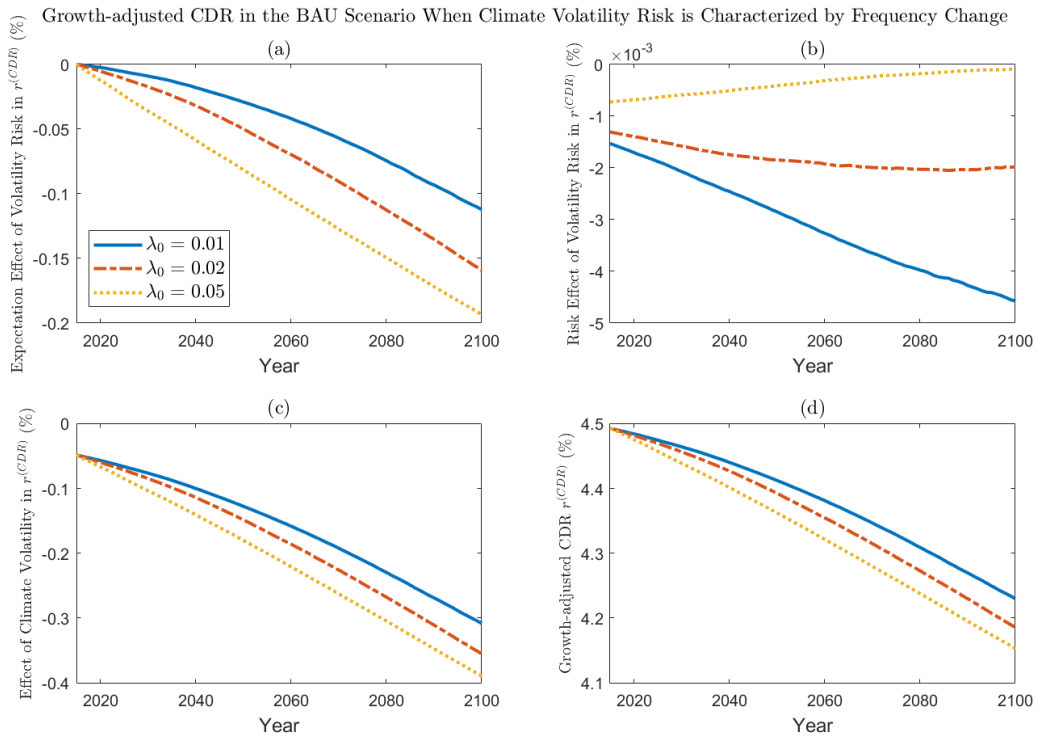
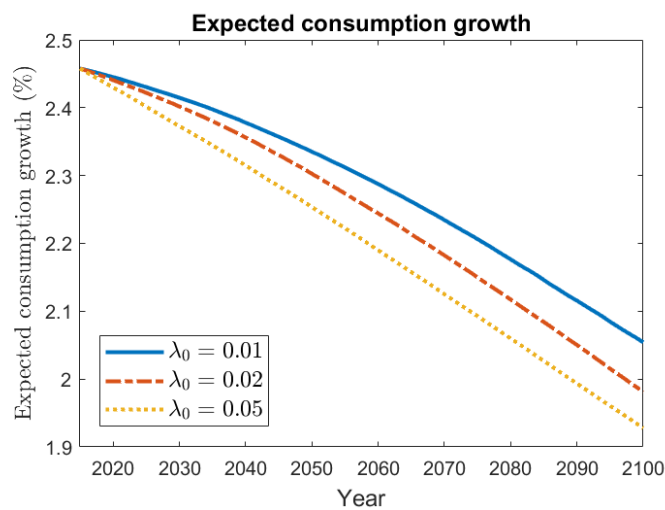
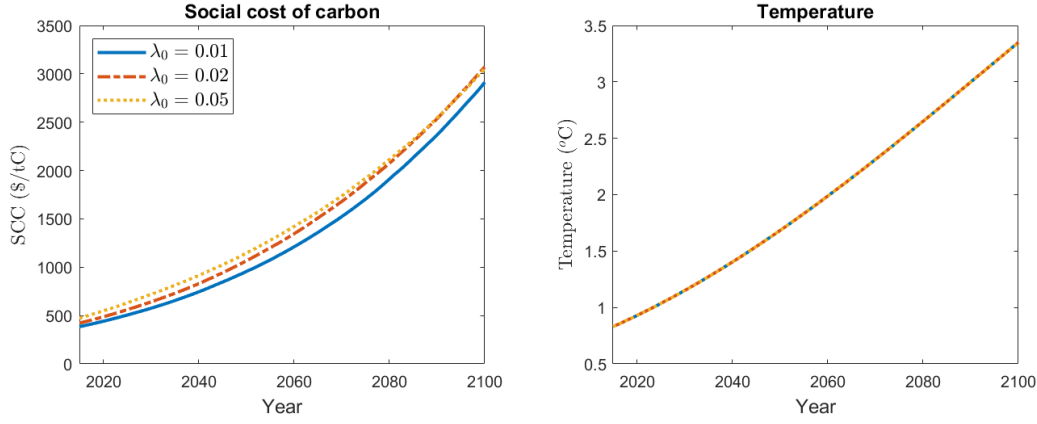


Figure 3.22: Expected consumption growth rate in the BAU scenario under $\lambda_0 = 0.01, 0.02,$ and 0.05 , where $\bar{\lambda}^{(H)} = 2\bar{\lambda}^{(L)}$.



shift is resolved, the timing of arrival becomes less important relative to the long-run climate conditions of the new regime.

Figure 3.23: Social cost of carbon (US dollar per ton of carbon, or \$/tC) and mean global surface temperature ($^{\circ}\text{C}$) in the business-as-usual (BAU) scenario from 2015 to 2100 under $\lambda_0 = 0.01, 0.02,$ and 0.05 , where $\bar{\lambda}^{(H)} = 2\bar{\lambda}^{(L)}$.



3.5 Endogenous Carbon Emissions

For analytical convenience, we have so far assumed that BAU carbon emissions are exogenous and deterministic, which rise initially over time but eventually decline due to fossil fuel depletion and the adoption of renewable energy. This simplification allowed us to largely decompose the SCC analytically (see Equation (3.6)) and to examine the climate risk impact of each component separately. However, in reality, emissions are linked to economic output and are therefore stochastic. To assess the implications of this simplification, we repeat much of the analysis with emissions modeled as a stochastic process tied to the output dynamics.

We now model emissions E_t as

$$E_t = \psi_t Y_t$$

where Y_t is the endowment process that captures the intensity of economic activity at t , and ψ_t is the carbon intensity, i.e., the amount of carbon emitted per unit of GDP. The carbon intensity is calibrated so that *expected* emissions closely match those in the exogenous baseline scenario, as in Olijslagers et al. (2022). We assume that ψ_t declines over time due to technological improvements in production and the widespread adoption of renewable energy:

$$d\psi_t = -\delta_t \psi_t dt$$

where δ_t increases over time and follows the dynamic

$$d(\delta_t - \delta_\infty) = -\alpha_\psi (\delta_t - \delta_\infty) dt, \quad \alpha_\psi > 0$$

with initial value δ_0 and long-run value δ_∞ , or equivalently, $\delta_t = \delta_\infty + e^{-\alpha t}(\delta_0 - \delta_\infty)$. Initially, carbon intensity declines at a rate lower than economic growth, so rising endowments drive up emissions. In the long run, carbon intensity declines at a rate δ_∞ exceeding the economic growth rate, causing emissions to eventually fall and converge to zero. We set $\delta_0 = -0.5\%$, $\delta_\infty = -6.5\%$ and $\alpha = 0.25\%$. Unlike the exogenous emission scenario, carbon emissions are now stochastic because they are linked to the volatile output process. This introduces an additional source of risk, making the scenario more realistic, but it also precludes analytical expressions for the SCC. Therefore, we present only numerical results.

3.5.1 Endogenous Emissions and Changing Disaster Frequency

Table 3.4 reports the numerical results assuming that the frequency of climate disasters doubles in the new regime (i.e. $\lambda^{(H)} = 2\lambda^{(L)}$) under endogenous carbon emissions. As in Table 3.1, we calculate the SCC under two assumptions on the climate regime shift: Column (a) assumes a Poisson arrival with rate $\lambda_0 = 0.01$ (implying an expected arrival in 100 years), while Column (b) assumes the regime shift occurs deterministically in 2115 (100 years from the 2015 simulation start). We also report SCC values for different preference parameters, γ and ϵ .

Table 3.4: The business-as-usual social cost of carbon (\$/tC) in Year 2025 as a function of risk aversion γ , EIS ϵ with and without the risk effect of climate volatility. Assume that in the new regime climate disaster frequency doubles ($\lambda^{(H)} = 2\lambda^{(L)}$) but its size remains unchanged. Carbon emission is a function of aggregate endowment and carbon intensity.

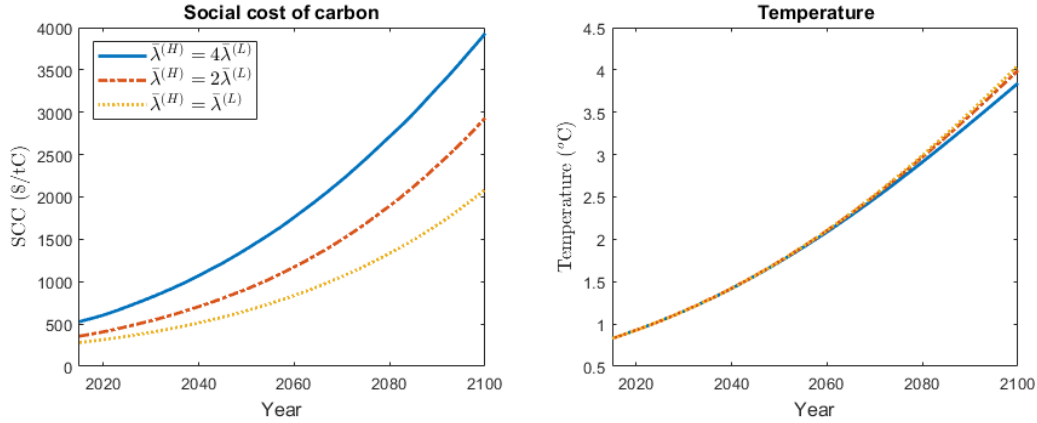
γ	ϵ	(a) Stochastic regime shift	(b) Deterministic regime shift
6	1.5	345.18	256.82
4.3	1.5	439.65	347.77
6	0.75	347.71	237.83
4.3	0.75	232.16	171.51

As in the exogenous emissions setup shown in Table 3.1, the SCC is significantly higher in Column (a) than in Column (b) for the same preference parameters, implying that the stochasticity of climate volatility substantially increases the SCC and cannot be ignored in its assessment. We also observe the same patterns across different values of γ and ϵ as in Table 3.1, which can be interpreted similarly.

Linking carbon emissions to aggregate endowment introduces an additional source of stochasticity in the extended model. As expected for risk-averse agents, incorporating endogenous emissions amplifies the risk effect of stochastic climate volatility on the social cost of carbon.

Figure 3.24 and 3.25 show the time path of the SCC and temperature T under the BAU and the optimal abatement scenarios, accounting for endogenous and therefore stochastic emissions. In

Figure 3.24: Social cost of carbon (US dollar per ton of carbon, or \$/tC) and mean global surface temperature ($^{\circ}\text{C}$) in the business-as-usual (BAU) scenario when carbon emission is endogenous. The frequency of climate disasters in the new regime rises to $4\bar{\lambda}^{(L)}$, $2\bar{\lambda}^{(L)}$, or remains unchanged.

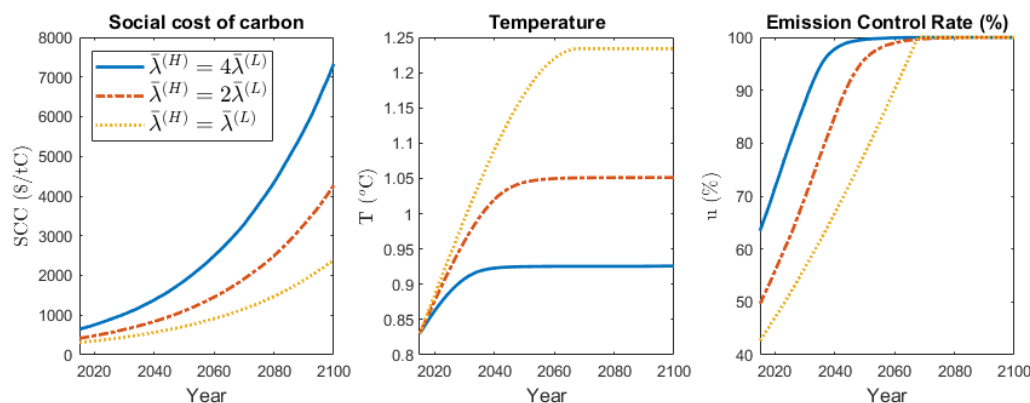


the BAU scenario, the dynamics of temperature differ across specifications of climate volatility risk, unlike in the exogenous emissions case. This is because emissions are now linked to aggregate endowment, which is affected by higher climate disaster arrival rates.

An increase in $\bar{\lambda}^{(H)}$ reduces temperature T because higher $\bar{\lambda}^{(H)}$ generates larger economic losses, which lower future endowments, reduce emissions, and slow the increase in temperature. The effect of $\bar{\lambda}^{(H)}$ on the SCC comes from two channels. First, an increase in $\bar{\lambda}^{(H)}$ increases the Expected Loss effect as we just discussed (see Term (i) in Equation (3.6)), raising the SCC. Second, reduced aggregate endowments and consumption under a higher $\bar{\lambda}^{(H)}$ increase the price of future goods, or equivalently, the stochastic discount factor (SDF) / lower growth-adjusted Consumption Discount Rate (CDR), which also increases the SCC. Figure 3.24 demonstrates the positive impact of a higher $\bar{\lambda}^{(H)}$ on the SCC numerically.

Under optimal abatement, the SCC, temperature, and emission control rate follow similar pattern to those in the exogenous emission setup shown in Figure 3.12. Higher $\bar{\lambda}^{(H)}$ increases the expected marginal damage from climate disasters, prompting more stringent optimal emission control, and consequently lower future temperatures. A higher climate disaster frequency increases the SCC through two channels: a larger certainty-equivalent effect (Term (i) in Equation (3.6)) and a lower discount rate (Term (ii) in Equation (3.6)). Specifically, a higher $\bar{\lambda}^{(H)}$ increases the certainty equivalent of climate damages, while aggregate endowment and consumption decline in a world with more frequent climate disasters. Lower future consumption implies a higher stochastic discount factor and a lower discount rate. These effects together result in higher SCC values.

Figure 3.25: Social cost of carbon, mean global surface temperature, emission control rate, yearly carbon emissions and consumption-endowment ratio from Year 2015 to 2100 under optimal abatement, where carbon emission is endogenous. The frequency of climate disasters in the new regime rises to $4\bar{\lambda}^{(L)}$, $2\bar{\lambda}^{(L)}$, or remains unchanged.



3.5.2 Endogenous Emissions and Changing Disaster Intensity

Next, we present the SCC, temperature, and emission control rates in Figure 3.26 and 3.27 under both scenarios for a Type (B) climate regime shift, where the climate disaster intensity increases in the new regime but the disaster frequency remains unchanged.

In the BAU scenario, the SCC increases with higher climate disaster intensity $EJ_2^{(H)}$, even though temperature is lower under more intense disasters. As in the higher frequency scenarios (see Figure 3.24), this occurs because larger disasters reduce output and emissions, which in turn slightly dampens the increase in T .

The effect of disaster intensity on the SCC also depends on the expected loss and the discount rate channels. First, higher $EJ_2^{(H)}$ leads to larger future economic losses in the future. Second, greater climate damages reduce aggregate consumption, raising the stochastic discount factor (or equivalently lowering the discount rate), which further increases the SCC.

Figure 3.27 shows the SCC, temperature, and emission control rate under optimal abatement. Their dynamics mirror those in Figure 3.12 for the exogenous emissions case. When climate disasters become more intense in the new climate regime, expected marginal damages from climate disasters rise, leading to stricter emission controls, lower emissions, and a slower temperature increase over time. The SCC rises with disaster intensity. As in Section 3.4.2, larger $EJ_2^{(H)}$ increases expected losses, so the certainty equivalent effect of climate volatility risk increases. Moreover, higher abatement reduces the portion of the endowment available for consumption, and lower aggregate endowment and consumption due to higher climate damages and abatement costs raise the stochastic discount factor, or equivalently, lower the discount rate. Both the larger certainty equivalent effect and lower discount rate lead to higher SCC values.

Figure 3.26: Social cost of carbon (US dollar per ton of carbon, or $\$/tC$) and mean global surface temperature ($^{\circ}C$) in the business-as-usual scenario when carbon emission is endogenous. The expected size of one climate disaster in the new regime rises to $4EJ_2^{(L)}$, $2EJ_2^{(L)}$, or remains unchanged.

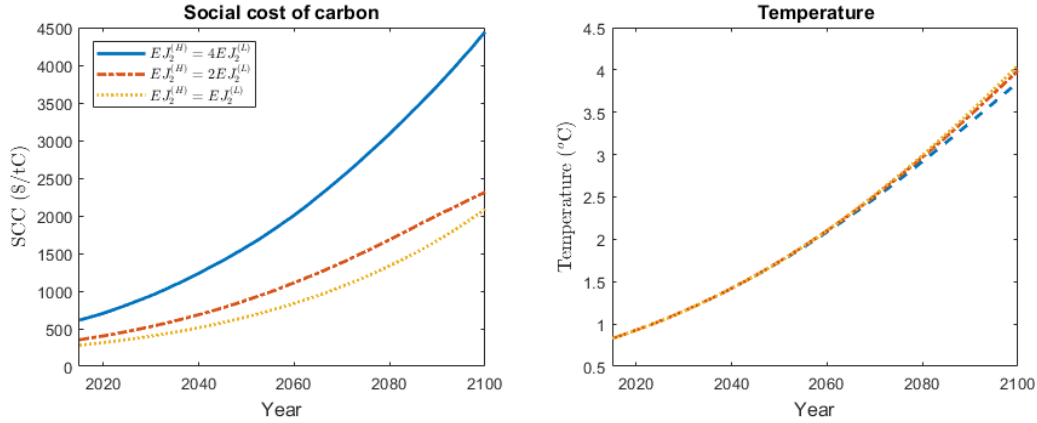
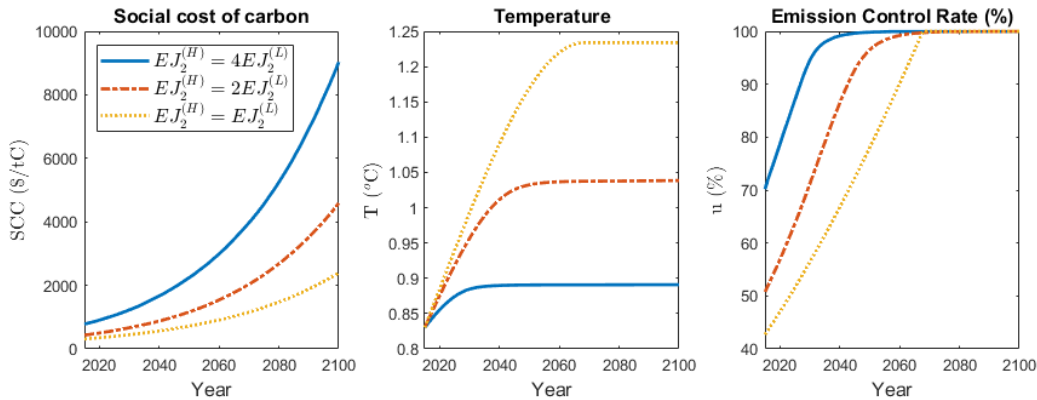


Figure 3.27: Social cost of carbon, mean global surface temperature, emission control rate, yearly carbon emissions and consumption-endowment ratio from Year 2015 to 2100 under optimal abatement when carbon emission is endogenous. The expected size of one climate disaster in the new regime rises to $4EJ_2^{(L)}$, $2EJ_2^{(L)}$, or remains unchanged.



3.6 An alternative Model of Climate Volatility Risk: Gradually Unfolding Tipping Points

Tipping points are central in the climate literature, as discussed in Section 3.1. In particular, Dietz et al. (2021a) and Lontzek et al. (2015) argue that what appears as an instantaneous jump on a geographical timescale unfolds more gradually on conventional timescales (see also Lenton and Ciscar (2013)). Motivated by this, we propose an alternative model of climate volatility risk: instead of an immediate increase upon a regime shift, climate volatility follows a Cox–Ingersoll–Ross (CIR) process (Eraker and Yang, 2022), with its long-run value subject to a one-off jump and volatility gradually rising to this level after the regime shift. This approach is more realistic than the baseline model, because actual jumps in the climate system occur

gradually over time. We find that this alternative model of climate volatility risk yields similar asset pricing implications, suggesting that gradual regime shifts have little effect on the SCC, which is dominated by the long-run impact of the new regime.

All parameters are as in Section 3.2, except that the climate disaster frequency parameter $\bar{\lambda}_t$ now follows a Cox–Ingersoll–Ross (CIR) process, where its long-run value is subject to a one-off irreversible Poisson jump (i.e., a climate regime shift) N_0 occurring at rate λ_0 . Formally,

$$d\bar{\lambda}_t = \theta \left(\bar{\bar{\lambda}}_t - \bar{\lambda}_t \right) dt + \sigma_\lambda \sqrt{\bar{\lambda}_t} dZ_{\lambda,t},$$

$$\bar{\bar{\lambda}}_t = (1 - N_{0,t}) \bar{\lambda}^{(L)} + N_{0,t} \bar{\lambda}^{(H)}$$

where $\bar{\bar{\lambda}}_t$ is the long-run value of $\bar{\lambda}_t$ which jumps from $\bar{\lambda}^{(L)}$ to $\bar{\lambda}^{(H)}$ upon the regime shift, θ is the mean-reversion speed, $\sigma_\lambda \sqrt{\bar{\lambda}_t}$ is the standard deviation and Z_λ is a Brownian motion independent of the economic fluctuation risk Z . We impose the Feller condition (Feller (1951))

$$2\theta \bar{\bar{\lambda}}_t \geq \sigma_\lambda^2$$

to ensure $\bar{\lambda}_t > 0$.

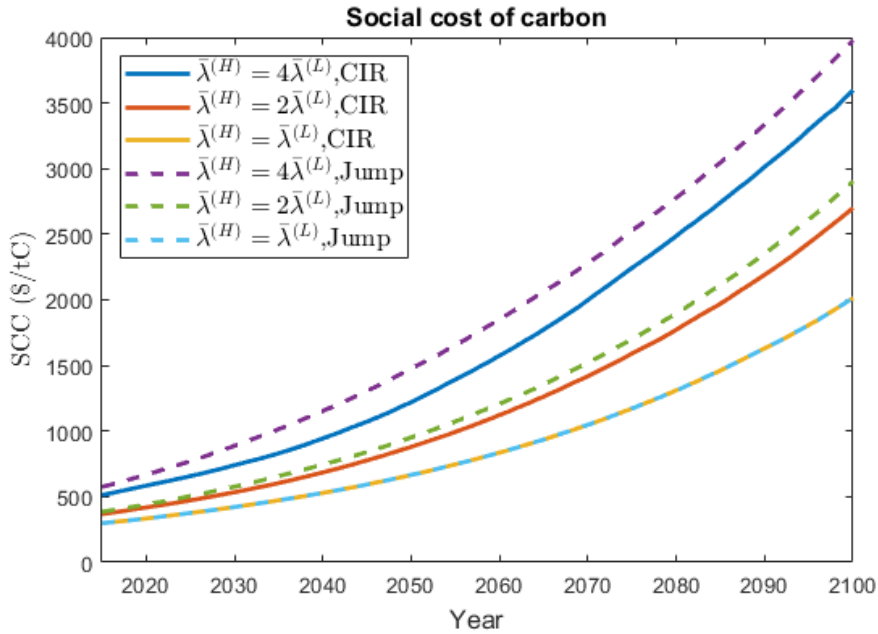
To assess whether different risk structures of climate volatility affect the SCC, we compare the time paths of the SCC under the CIR model and the baseline one-off jump model in Figure 3.28, assuming a BAU scenario with exogenous carbon emissions. Similar results are expected for the stochastic emissions case analyzed in Section 3.5.

In our simulation, we use the same values of $\bar{\lambda}^{(L)}$ and $\bar{\lambda}^{(H)}$ as before. For illustrative purposes, we set the speed of volatility increase to $\theta = 0.1$, so that climate volatility reaches the new level within approximately 10 years. To facilitate comparison with the baseline model, we set $\sigma_\lambda = 0$, ensuring that SCCs are unaffected by the Brownian stochasticity of $\bar{\lambda}_t$ in the CIR process.

Figure 3.28 shows that for the same long-run value of $\bar{\lambda}_t$ in the new climate regime, the SCC is larger in the one-off jump model than in the CIR model. In other words, the SCC is higher when climate volatility rises more quickly after a regime shift. This is intuitive: a more gradual adjustment to a positive shock in the long-run volatility results in a lower volatility path over time, reducing the SCC.

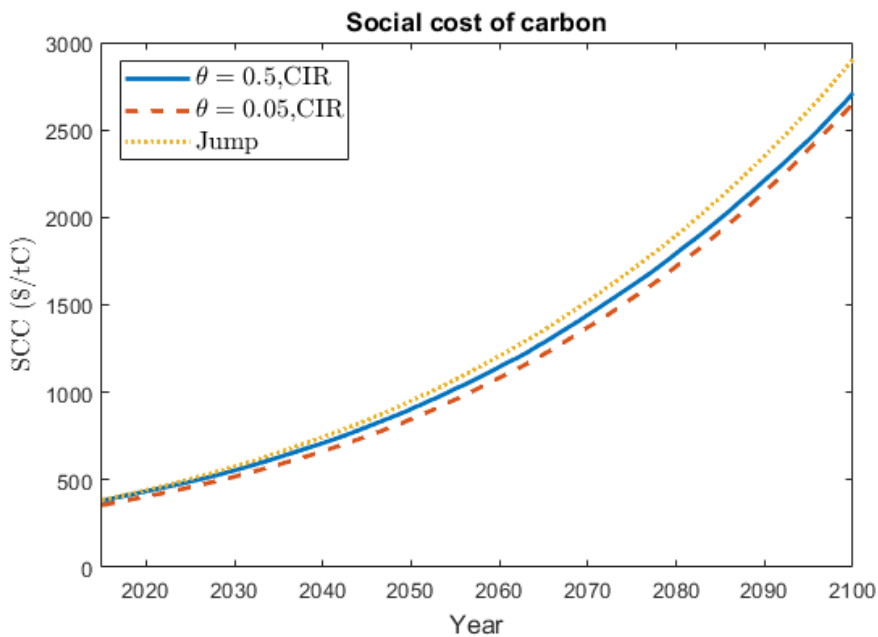
Figure 3.29 shows how the speed of climate volatility increase, θ , affects the SCC. We assume that the climate disaster frequency parameter is doubled in the new regime, $\bar{\lambda}^{(H)} = 2\bar{\lambda}^{(L)}$, and compare SCCs for $\theta = 0.05$ and $\theta = 0.5$ in the CIR model, alongside the baseline scenario with an immediate volatility jump. Consistent with the intuition above, a slower adjustment of volatility leads to a lower SCC, although differences across θ are relatively small. When θ is larger, climate disaster frequency increases more rapidly to its new long-run level, generating

Figure 3.28: Social costs of carbon in the BAU scenario when $\bar{\lambda}_t$ follows an CIR process (“CIR”) and when $\bar{\lambda}_t$ is subject to a one-off Poisson jump (“Jump”), where $\theta = 0.1$ and $\sigma_\lambda = 0$.



larger marginal damages from carbon emissions and higher long-run SCCs. Differences in SCCs at the beginning of the simulation are negligible, because climate volatility only increases once the regime shift uncertainty is resolved, and future damages under different θ are discounted back to the present value.

Figure 3.29: Social costs of carbon in the BAU scenario when $\bar{\lambda}_t$ either jumps immediately (“Jump”) or follows an CIR process (“CIR”) under $\sigma_\lambda = 0$ and different speed θ .



3.7 Conclusion

In this paper, we focus on stochastic climate volatility, a second-order uncertainty in the climate system that has so far received little attention in the climate economic literature. We show that under plausible calibrations, the impact of volatility risk on the SCC is far from negligible. This is particularly relevant since climate scientists have argued that global warming may trigger irreversible and potentially permanent increases in climate volatility as part of a transition to a new climate risk regime, possibly in the near future. However, the timing and severity of such a shift remain uncertain, implying that climate volatility itself should be considered as a stochastic process. This introduces a new source of climate risk that materially affects the SCC.

Using a dynamic stochastic integrated climate-economic model with representative agents endowed with Duffie-Epstein recursive preferences, we examine how stochastic climate volatility affects the SCC under different abatement policies. We model climate volatility risk as an irreversible, one-off jump in climate volatility arriving as a Poisson process, and test the robustness of our results using an alternative specification in which volatility rises gradually to its long-run level following the Poisson shock. This more realistic assumption does not materially alter our conclusions.

First, we find that climate volatility risk is as important as the climate volatility itself in terms of its impact on the Social Cost of Carbon (SCC), risk premia, and risk-free rates. Climate volatility risk increases equilibrium risk premia on the same scale as climate volatility, yet also leads to a higher SCC. The increase in expected losses following climate volatility shocks more than offsets the effect of higher risk premia.

Second, the stochasticity of climate volatility substantially increases the SCC, underscoring the need to explicitly incorporate it into climate-economy models. Comparing to a deterministic scenario with a known, scheduled volatility shock, we find that both the certainty equivalent of climate damages and the stochastic discount factor are smaller without climate volatility risk. Ignoring stochasticity therefore leads to underestimation of the SCC.

Third, increases in the frequency and intensity of climate disasters affect the SCC differently. Both types of shocks raise the SCC, but the marginal impact differs. For equal expected climate damage, the effect on the stochastic discount factor is similar, while the certainty-equivalent effect increases proportionally under higher disaster frequency but more than proportionally under higher disaster intensity. Consequently, a regime with more intense disasters produces a higher SCC than a regime with more frequent disasters, even for equal expected damages, due to risk aversion.

Fourth, endogenizing carbon emissions by linking them to the output process introduces additional stochasticity but does not qualitatively change our results. While stochastic emissions

increase the SCC, the overall patterns remain consistent with the exogenous emissions setup. The exogenous emission model allows for analytical expressions, which help interpret the numerical results. When calibrated to match expected emissions, both specifications produce similar impacts on temperature, climate change, asset pricing, and the SCC.

Fifth, smoothing the increase in climate volatility leads to lower time paths of the SCC but does not qualitatively change the conclusions. Gradual adjustment of volatility slows the rise in the SCC, but does not lead to different implications regarding the effect of climate volatility risk on the SCC.

Finally, since shocks to climate volatility are largely yet to occur, there is a lack of time-series data to calibrate stochastic volatility. This uncertainty makes the impact of volatility risk a natural candidate for a multiple-prior or ambiguity-averse framework as proposed by Chen and Epstein (2002) and Klibanoff et al. (2005), an issue we intend to take up in future work.

3.A Solution to the Optimization Problem and SCC

We describe details on solving the optimization problem of the representative agent in Section 4.2, where climate volatility risk is modeled by a stochastic arrival of a new regime in which climate disasters happen more frequently (Type (A)). Then we provide analytical expression of SCC. Under the other type of climate volatility risk (Type (B)), optimization problems can be solved analogously so we will not provide the details.

The following steps follow Tsai and Wachter (2015) and Olijslagers et al. (2022). Let V_t be the total welfare which is a function of time t and state variables $(Y_t, T_t, \bar{\lambda}_t)$ with dynamics

$$\begin{aligned} dY_t &= \mu Y_t dt + \sigma Y_t dZ_t - J_1 Y_t dN_{1,t} - J_2 Y_t dN_{2,t}, \\ dT_t &= \chi(1 - u_t) E_t dt, \\ d\bar{\lambda}_t &= (\bar{\lambda}^{(H)} - \bar{\lambda}^{(L)}) dN_{0,t} \end{aligned}$$

Then the Hamilton–Jacobi–Bellman (HJB) equation is given by

$$\begin{aligned} 0 = \max_{u_t} \left\{ & f(C_t, V_t) + \frac{\partial V}{\partial t} + \mu Y_t V_Y + \mu_{T,t} V_T + \frac{1}{2} \sigma^2 Y_t^2 V_{YY} \right. \\ & + \lambda_1 \mathbb{E} [V((1 - J_1)Y_{t-}, T_t, \bar{\lambda}_t, t) - V(Y_{t-}, T_t, \bar{\lambda}_t, t)] \\ & + \lambda_{2,t} \mathbb{E} [V((1 - J_2)Y_{t-}, T_t, \bar{\lambda}_t, t) - V(Y_{t-}, T_t, \bar{\lambda}_t, t)] \\ & \left. + \lambda_0(1 - N_{0,t-}) \mathbb{E} [V(Y_t, T_t, \bar{\lambda}^{(H)}, t) - V(Y_t, T_t, \bar{\lambda}^{(L)}, t-)] \right\} \end{aligned}$$

where $\mu_{T,t} = \chi(1 - u_t) E_t$, $\lambda_{2,t} = \bar{\lambda}_t T_t$, V_X and V_{XX} are the first- and second-order partial derivatives of variable X .

Tsai and Wachter (2015) showed that under this model setup, the conjecture $V = g(T, \bar{\lambda}_t, t) \frac{Y^{1-\gamma}}{1-\gamma}$ can be used to reduce the dimensionality of the state space and simplify the numerical procedure. Define $\xi_t := \frac{C_t}{Y_t}$ as the consumption-endowment ratio, then the flow utility can be rewritten as

$$f(C, V) = \beta \zeta \left(g^{-\frac{1}{\zeta}} \xi^{1-\frac{1}{\zeta}} - 1 \right) V$$

The HJB equation can then be rewritten as

$$\begin{aligned} 0 = \min_{u_t} \left\{ & \left[\beta \zeta \left(g_{t-}^{-\frac{1}{\zeta}} \xi_{t-}^{1-\frac{1}{\zeta}} - 1 \right) + (1 - \gamma) \left(\mu - \frac{1}{2} \gamma \sigma^2 - \frac{\lambda_1}{\alpha_1 + 1 - \gamma} - \frac{\bar{\lambda}_t T_t}{\alpha_2 + 1 - \gamma} \right) \right] g_{t-} \right. \\ & \left. + \frac{\partial g}{\partial t} + \mu_{T,t} g_T + \lambda_0 (1 - N_{0,t-}) (g_t - g_{t-}) \right\} \end{aligned} \quad (3.A.1)$$

where $g_t = g(T_t, \bar{\lambda}_t, t)$ and $g_{t-} = g(T_t, \bar{\lambda}_{t-}, t)$. If the one-off jump N_0 does not happen at t , then we have $g_t = g_{t-}$. Equation 3.A.1 is a minimization problem because $\gamma > 1$.

The optimal abatement policy u_t^* satisfies the first order condition

$$\beta(1 - \gamma)g_t^{1-1/\zeta} \xi_t^{-1/\epsilon} \frac{\partial \xi_t}{\partial u_t} - \chi E_t g_T = 0.$$

Stochastic Discount Factor To solve for the carbon price, we start with the stochastic discount factor which is given by $\pi_t = \exp \left[\int_0^t f_V(C_s, V_s) ds \right] f_C(C_t, V_t)$ (Duffie and Epstein (1992)). Taking derivatives of $f(C, V)$ with respect to C and V , we get $f_C(C, V) = \frac{\beta C^{-1/\epsilon}}{[(1-\gamma)V]^{1/\zeta-1}}$ and $f_V(C, V) = \beta \zeta \left[\left(1 - \frac{1}{\zeta}\right) ((1-\gamma)V)^{-1/\zeta} C^{1-1/\epsilon} - 1 \right]$. Plugging $C_t = \xi_t Y_t$ and the conjecture $V_t = g_t \frac{Y_t^{1-\gamma}}{1-\gamma}$ into the derivatives above yields

$$f_C(C_t, V_t) = \beta g_t^{1-1/\zeta} \xi_t^{-1/\epsilon} Y_t^{-\gamma}, \quad f_V(C_t, V_t) = \beta \zeta \left[\left(1 - \frac{1}{\zeta}\right) g_t^{-1/\zeta} \xi_t^{1-1/\epsilon} - 1 \right].$$

Substituting $f_C(C, V)$ and $f_V(C, V)$ into the expression of stochastic discount factor π and using Ito's formula, we obtain the stochastic differential equation of π

$$\begin{aligned} \frac{d\pi_t}{\pi_{t-}} = & \beta \zeta \left[\left(1 - \frac{1}{\zeta}\right) g_{t-}^{-1/\zeta} \xi_{t-}^{1-1/\epsilon} - 1 \right] dt + \frac{dY_t^{-\gamma}}{Y_{t-}^{-\gamma}} + \frac{dg_t^{1-1/\zeta}}{g_{t-}^{1-1/\zeta}} + \frac{d\xi_t^{-1/\epsilon}}{\xi_{t-}^{-1/\epsilon}} + \frac{dY_t^{-\gamma} dg_t^{1-1/\zeta}}{Y_{t-}^{-\gamma} g_{t-}^{1-1/\zeta}} \\ & + \frac{dY_t^{-\gamma} d\xi_t^{-1/\epsilon}}{Y_{t-}^{-\gamma} g_{t-}^{1-1/\zeta}} + \frac{dg_t^{1-1/\zeta} d\xi_t^{-1/\epsilon}}{g_{t-}^{1-1/\zeta} \xi_{t-}^{-1/\epsilon}} \end{aligned}$$

where

$$\begin{aligned} \frac{dY_t^{-\gamma}}{Y_{t-}^{-\gamma}} &= -\gamma \left(\mu - \frac{1}{2} (1 + \gamma) \sigma^2 \right) dt - \gamma \sigma dZ_t + [(1 - J_1)^{-\gamma} - 1] dN_{1,t} + [(1 - J_2)^{-\gamma} - 1] dN_{2,t} \\ \frac{dg_t^{1-1/\zeta}}{g_{t-}^{1-1/\zeta}} &= \left(1 - \frac{1}{\zeta}\right) \left(\frac{\partial g_t / \partial t}{g_{t-}} + \frac{g_T}{g_{t-}} \mu_T \right) dt + \left(\frac{g_t^{1-1/\zeta}}{g_{t-}^{1-1/\zeta}} - 1 \right) dN_{0,t} \\ \frac{d\xi_t^{-1/\epsilon}}{\xi_{t-}^{-1/\epsilon}} &= \left(-\frac{1}{\epsilon}\right) \left(\frac{\partial \xi_t / \partial t}{\xi_{t-}} + \frac{\xi_T}{\xi_{t-}} \mu_T \right) dt + \left(\frac{\xi_t^{-1/\epsilon}}{\xi_{t-}^{-1/\epsilon}} - 1 \right) dN_{0,t}. \end{aligned}$$

Plugging in yields

$$\begin{aligned} \frac{d\pi_t}{\pi_{t-}} = & \left\{ \beta\zeta \left[\left(1 - \frac{1}{\zeta}\right) g_{t-}^{-1/\zeta} \xi_{t-}^{1-1/\epsilon} - 1 \right] - \gamma \left(\mu - \frac{1}{2}(1+\gamma)\sigma^2 \right) + \left(1 - \frac{1}{\zeta}\right) \left(\frac{\partial g_t/\partial t}{g_{t-}} + \frac{g_T}{g_{t-}} \mu_T \right) \right. \\ & \left. + \left(-\frac{1}{\epsilon} \right) \left(\frac{\partial \xi_t/\partial t}{\xi_{t-}} + \frac{\xi_T}{\xi_{t-}} \mu_T \right) \right\} dt - \gamma\sigma dZ_t + [(1 - J_1)^{-\gamma} - 1] dN_{1,t} + [(1 - J_2)^{-\gamma} - 1] dN_{2,t} \\ & + \left[\left(\frac{g_t^{1-\frac{1}{\zeta}}}{g_{t-}^{1-\frac{1}{\zeta}}} - 1 \right) + \left(\frac{\xi_t^{-\frac{1}{\epsilon}}}{\xi_{t-}^{-\frac{1}{\epsilon}}} - 1 \right) + \left(\frac{g_t^{1-\frac{1}{\zeta}}}{g_{t-}^{1-\frac{1}{\zeta}}} - 1 \right) \left(\frac{\xi_t^{-\frac{1}{\epsilon}}}{\xi_{t-}^{-\frac{1}{\epsilon}}} - 1 \right) \right] dN_{0,t}, \end{aligned}$$

or

$$\frac{d\pi_t}{\pi_{t-}} = \mu_{\pi,t} dt - \gamma\sigma dZ_t + [(1 - J_1)^{-\gamma} - 1] dN_{1,t} + [(1 - J_2)^{-\gamma} - 1] dN_{2,t} + \mathcal{J}_{\pi,t} dN_{0,t}, \quad (3.A.2)$$

where

$$\begin{aligned} \mu_{\pi,t} = & \beta\zeta \left[\left(1 - \frac{1}{\zeta}\right) g_{t-}^{-1/\zeta} \xi_{t-}^{1-1/\epsilon} - 1 \right] - \gamma \left(\mu - \frac{1}{2}(1+\gamma)\sigma^2 \right) + \left(1 - \frac{1}{\zeta}\right) \left(\frac{\partial g_t/\partial t}{g_{t-}} + \frac{g_T}{g_{t-}} \mu_T \right) \\ & - \frac{1}{\epsilon} \left(\frac{\partial \xi_t/\partial t}{\xi_{t-}} + \frac{\xi_T}{\xi_{t-}} \mu_T \right), \end{aligned}$$

and

$$\mathcal{J}_{\pi,t} := \left(\frac{g_t^{1-\frac{1}{\zeta}}}{g_{t-}^{1-\frac{1}{\zeta}}} - 1 \right) + \left(\frac{\xi_t^{-\frac{1}{\epsilon}}}{\xi_{t-}^{-\frac{1}{\epsilon}}} - 1 \right) + \left(\frac{g_t^{1-\frac{1}{\zeta}}}{g_{t-}^{1-\frac{1}{\zeta}}} - 1 \right) \left(\frac{\xi_t^{-\frac{1}{\epsilon}}}{\xi_{t-}^{-\frac{1}{\epsilon}}} - 1 \right).$$

Equation (3.A.2) implies that the stochastic discount factor captures the exposure to economic diffusive risk dZ , economic disaster risk dN_1 , climate disaster risk dN_2 and the climate volatility risk dN_0 .

Risk-Free Rate Consider a risk-free bond B_t with return r_t^f . Let $\mu_{\pi,t}$ be the drift term in the stochastic differential equation of π at time t . Under no-arbitrage condition, $\pi_t B_t$ is a martingale, which implies

$$r_t^f = -\mu_{\pi,t} - \lambda_1 \frac{\gamma}{\alpha_1 - \gamma} - \bar{\lambda}_t T_t \frac{\gamma}{\alpha_2 - \gamma} - \lambda_0 (1 - N_{0,t-}) \mathcal{J}_{\pi,t}.$$

Note that the HJB equation (3.A.1) implies

$$\begin{aligned} \frac{\partial g_t / \partial t}{g_{t-}} + \mu_{T,t-} \frac{g_T}{g_{t-}} = & -\beta \zeta \left(g_{t-}^{-1/\zeta} \xi_{t-}^{1-1/\epsilon} - 1 \right) - (1-\gamma) \left(\mu - \frac{\gamma}{2} \sigma^2 - \frac{\lambda_1}{\alpha_1 + 1 - \gamma} - \frac{\bar{\lambda}_t T_t}{\alpha_2 + 1 - \gamma} \right) \\ & - \lambda_0 (1 - N_{0,t-}) \left(\frac{g_t}{g_{t-}} - 1 \right) \end{aligned}$$

Substituting the expression of $\frac{\partial g_t / \partial t}{g_{t-}} + \mu_{T,t-} \frac{g_T}{g_{t-}}$ above into $\mu_{\pi,t}$ yields the risk-free interest rate

$$\begin{aligned} r_t^f = & \beta + \frac{\mu + \mu_{\xi,t}}{\epsilon} - \frac{\gamma}{2} \left(1 + \frac{1}{\epsilon} \right) \sigma^2 + \lambda_1 \left(\frac{\gamma - 1/\epsilon}{\alpha_1 + 1 - \gamma} - \frac{\gamma}{\alpha_1 - \gamma} \right) + \bar{\lambda}_t T_t \left(\frac{\gamma - 1/\epsilon}{\alpha_2 + 1 - \gamma} - \frac{\gamma}{\alpha_2 - \gamma} \right) \\ & + \lambda_0 (1 - N_{0,t-}) \left[\left(1 - \frac{1}{\zeta} \right) \left(\frac{g_t}{g_{t-}} - 1 \right) - \mathcal{J}_{\pi,t} \right]. \end{aligned}$$

where $\mu_{\xi} = \frac{\partial \xi_t / \partial t}{\xi_{t-}} + \frac{\xi_T}{\xi_{t-}} \mu_T$. Note that the dynamic of consumption process C_t is given by

$$\begin{aligned} \frac{dC_t}{C_{t-}} = \frac{d(\xi_t Y_t)}{\xi_{t-} Y_{t-}} = & \frac{d\xi_t}{\xi_t} + \frac{dY_t}{Y_{t-}} + \frac{d\xi_t dY_t}{\xi_t Y_{t-}} \\ = & \mu_{C,t} dt + \sigma dZ_t - J_1 dN_{1,t} - J_2 dN_{2,t} + \left(\frac{\xi_t}{\xi_{t-}} - 1 \right) dN_{0,t} \end{aligned} \quad (3.A.3)$$

where $\mu_{C,t} = \mu + \mu_{\xi,t}$. Therefore the risk-free rate is equivalent to

$$\begin{aligned} r_t^f = & \beta + \frac{\mu_{C,t}}{\epsilon} - \frac{\gamma}{2} \left(1 + \frac{1}{\epsilon} \right) \sigma^2 + \lambda_1 \left(\frac{\gamma - 1/\epsilon}{\alpha_1 + 1 - \gamma} - \frac{\gamma}{\alpha_1 - \gamma} \right) + \bar{\lambda}_t T_t \left(\frac{\gamma - 1/\epsilon}{\alpha_2 + 1 - \gamma} - \frac{\gamma}{\alpha_2 - \gamma} \right) \\ & + \lambda_0 (1 - N_{0,t-}) \mathcal{J}_{f,t} \end{aligned}$$

where

$$\mathcal{J}_{f,t} = \left(1 - \frac{1}{\zeta} \right) \left(\frac{g_t}{g_{t-}} - 1 \right) - \mathcal{J}_{\pi,t}.$$

Risk Premium Consider an asset which pays continuous dividends equal to the consumption C_t , then its ex-dividend price S_t also measures the total wealth of the agent. The risk premium is given by the difference between the asset return and the risk-free rate r_t^f .

Let $\kappa_t := \frac{C_t}{S_t}$ be the consumption-wealth ratio (or price-dividend ratio). Given that $f_C = V_S$ under optimal condition (Tsai and Wachter (2015)) and $V_S = \kappa_t V_C$ (chain rule), we have $\kappa_t = \frac{f_C}{V_C} = \beta g_t^{-1/\zeta} \xi_t^{1-1/\epsilon}$ and thus the ex-dividend price of the asset is $S_t = \frac{C_t}{\kappa_t} = \beta^{-1} g_t^{1/\zeta} \xi_t^{1/\epsilon} Y_t$. Using

Ito's lemma, we have

$$\frac{dS_t}{S_{t-}} = \frac{dY_t}{Y_{t-}} + \frac{dg_t^{\frac{1}{\zeta}}}{g_{t-}^{\frac{1}{\zeta}}} + \frac{d\xi_t^{\frac{1}{\epsilon}}}{\xi_{t-}^{\frac{1}{\epsilon}}} + \frac{dY_t dg_t^{1/\zeta}}{Y_{t-} g_{t-}^{1/\zeta}} + \frac{dY_t d\xi_t^{1/\epsilon}}{Y_{t-} \xi_{t-}^{1/\epsilon}} + \frac{dg_t^{1/\zeta} d\xi_t^{1/\epsilon}}{g_{t-}^{1/\zeta} \xi_{t-}^{1/\epsilon}}$$

where $\frac{dY_t}{Y_{t-}} = \mu dt + \sigma dZ_t - J_1 dN_{1,t} - J_2 dN_{2,t}$ is given, and by Ito's formula

$$\begin{aligned} \frac{dg_t^{1/\zeta}}{g_{t-}^{1/\zeta}} &= \frac{1}{\zeta} \mu_{g,t} dt + \left(\frac{g_t^{1/\zeta}}{g_{t-}^{1/\zeta}} - 1 \right) dN_{0,t}, \\ \frac{d\xi_t^{1/\epsilon}}{\xi_{t-}^{1/\epsilon}} &= \frac{1}{\epsilon} \mu_{\xi,t} dt + \left(\frac{\xi_t^{1/\epsilon}}{\xi_{t-}^{1/\epsilon}} - 1 \right) dN_{0,t} \end{aligned}$$

where $\mu_{g,t} = \frac{\partial g_t / \partial t}{g_{t-}} + \frac{g_T}{g_{t-}} \mu_T$ and $\mu_{\xi,t} = \frac{\partial \xi_t / \partial t}{\xi_{t-}} + \frac{\xi_T}{\xi_{t-}} \mu_T$. Then we can derive the dynamic of the cum-dividend price S_t^d

$$\frac{dS_t^d}{S_{t-}} = \frac{dS_t}{S_{t-}} + \kappa_t dt = \mu_{S,t} dt + \sigma dZ_t - J_1 dN_{1,t} - J_2 dN_{2,t} + \mathcal{J}_{S,t} dN_{0,t}$$

where

$$\begin{aligned} \mu_{S,t-} &= \beta + \frac{\mu_{C,t}}{\epsilon} + \frac{1}{2} \gamma \sigma^2 \left(1 - \frac{1}{\epsilon} \right) + \lambda_1 \frac{1 - 1/\epsilon}{\alpha_1 + 1 - \gamma} + \bar{\lambda}_t T_t \frac{1 - 1/\epsilon}{\alpha_2 + 1 - \gamma} - \lambda_0 (1 - N_{0,t-}) \frac{1}{\zeta} \left(\frac{g_t}{g_{t-}} - 1 \right), \\ \mathcal{J}_{S,t} &= \left(\frac{g_t^{1/\zeta}}{g_{t-}^{1/\zeta}} - 1 \right) + \left(\frac{\xi_t^{1/\epsilon}}{\xi_{t-}^{1/\epsilon}} - 1 \right) + \left(\frac{g_t^{1/\zeta}}{g_{t-}^{1/\zeta}} - 1 \right) \left(\frac{\xi_t^{1/\epsilon}}{\xi_{t-}^{1/\epsilon}} - 1 \right). \end{aligned}$$

Therefore the risk premium r_p is given by

$$\begin{aligned} r_{p,t} &= \mu_{S,t} - r_t^f - \lambda_1 \mathbf{E} J_1 - \bar{\lambda}_t T_t \mathbf{E} J_2 + \lambda_0 (1 - N_{0,t-}) \mathcal{J}_{S,t} \\ &= \gamma \sigma^2 + \lambda_1 \left[\frac{-1}{\alpha_1 + 1} + \frac{\gamma}{\alpha_1 - \gamma} + \frac{1 - \gamma}{\alpha_1 + 1 - \gamma} \right] + \bar{\lambda}_t T_t \left[\frac{-1}{\alpha_2 + 1} + \frac{\gamma}{\alpha_2 - \gamma} + \frac{1 - \gamma}{\alpha_2 + 1 - \gamma} \right] \\ &\quad + \lambda_0 (1 - N_{0,t-}) \left[-\frac{1}{\zeta} \left(\frac{g_t}{g_{t-}} - 1 \right) - \mathcal{J}_{f,t} + \mathcal{J}_{S,t} \right] \\ &= \gamma \sigma^2 + \lambda_1 \left[\frac{-1}{\alpha_1 + 1} + \frac{\gamma}{\alpha_1 - \gamma} + \frac{1 - \gamma}{\alpha_1 + 1 - \gamma} \right] + \bar{\lambda}_t T_t \left[\frac{-1}{\alpha_2 + 1} + \frac{\gamma}{\alpha_2 - \gamma} + \frac{1 - \gamma}{\alpha_2 + 1 - \gamma} \right] \\ &\quad + \lambda_0 (1 - N_{0,t-}) \left[\mathcal{J}_{S,t} + \mathcal{J}_{\pi,t} - \left(\frac{g_t}{g_{t-}} - 1 \right) \right] \end{aligned}$$

SCC By definition, the social cost of carbon at time 0 is

$$SCC_0 = -\chi \frac{\partial V_0 / \partial T_0}{f_C(C_0, V_0)} = -\frac{\chi Y_0}{\beta(1-\gamma) g_0^{1-\frac{1}{\zeta}} \xi_0^{-\frac{1}{\epsilon}}} g_{T,0} = -\frac{\chi C_0}{1-1/\epsilon} \frac{\partial(\kappa_0^{-1})}{\partial T_0} - \chi S_0 \frac{\partial \xi_0 / \partial T_0}{\xi_0} \quad (3.A.4)$$

where $\kappa_0^{-1} = \frac{S_0}{C_0}$ by definition, and the last line comes from the substitution $g_0 = \beta^\zeta \xi^{1-\gamma} \kappa_0^{-\zeta}$. The second term in Equation (3.A.4) measures the effect of abatement on carbon price. The first term can be further expanded as follows. Note that the initial asset price S_0 is the sum of all future consumption flows discounted back to time 0, i.e. $S_0 = \int_0^\infty E\left(\frac{\pi_s C_s}{\pi_0}\right) ds$, where $E\left(\frac{\pi_t C_t}{\pi_0}\right)$ is the time-0 value of time- t consumption C_t . Applying Ito's lemma on $\pi_t C_t$, we have

$$\begin{aligned} \frac{d(\pi_t C_t)}{\pi_t C_t} = & \left[\mu_{C,t} - r_t^f - \lambda_1 \frac{\gamma}{\alpha_1 - \gamma} - \bar{\lambda}_t T_t \frac{\gamma}{\alpha_2 - \gamma} - \lambda_0 (1 - N_{0,t-}) \mathcal{J}_{\pi,t} - \gamma \sigma^2 \right] dt \\ & + (1 - \gamma) \sigma dZ_t + [(1 - J_1)^{1-\gamma} - 1] dN_{1,t} + [(1 - J_2)^{1-\gamma} - 1] dN_{2,t} \\ & + \left[\mathcal{J}_{\pi,t} + \left(\frac{\xi_t}{\xi_{t-}} - 1 \right) + \left(\frac{\xi_t}{\xi_{t-}} - 1 \right) \mathcal{J}_{\pi,t} \right] dN_{0,t} \end{aligned}$$

which implies

$$\begin{aligned} E_0 \frac{\pi_t C_t}{\pi_0 C_0} = & \exp \left\{ \int_0^t \left[\mu_{C,s} - r_s^f - \frac{\lambda_1 \gamma}{\alpha_1 - \gamma} - \frac{\bar{\lambda}_s T_s \gamma}{\alpha_2 - \gamma} - \gamma \sigma^2 + \lambda_1 \frac{\gamma - 1}{\alpha_1 + 1 - \gamma} + \bar{\lambda}_s T_s \frac{\gamma - 1}{\alpha_2 + 1 - \gamma} \right. \right. \\ & \left. \left. + \lambda_0 (1 - N_{0,s-}) \left(\left(\frac{\xi_s}{\xi_{s-}} - 1 \right) + \left(\frac{\xi_s}{\xi_{s-}} - 1 \right) \mathcal{J}_{\pi,s} \right) \right] ds \right\} \\ = & \exp \left\{ - \int_0^t \left[r_s^f + r_{p,s} - \lambda_0 (1 - N_{0,s-}) \left(\frac{\xi_s}{\xi_{s-}} \mathcal{J}_{\pi,s} + \mathcal{J}_{S,s} - \left(\frac{g_s}{g_{s-}} - 1 \right) \right) \right. \right. \\ & \left. \left. - \left(\mu_{C,s} - \frac{\lambda_1}{\alpha_1 + 1} - \frac{\bar{\lambda}_s T_s}{\alpha_2 + 1} + \lambda_0 (1 - N_{0,s-}) \left(\frac{\xi_s}{\xi_{s-}} - 1 \right) \right) \right] ds \right\}. \end{aligned}$$

Given that $E_0 C_t = C_0 \exp \left\{ \int_0^t \left[\mu_{C,s} - \frac{\lambda_1}{\alpha_1 + 1} - \frac{\bar{\lambda}_s T_s}{\alpha_2 + 1} + \lambda_0 (1 - N_{0,s-}) \left(\frac{\xi_s}{\xi_{s-}} - 1 \right) \right] ds \right\}$ from Equation (3.A.3), we can rewrite $E_0 \frac{\pi_t C_t}{\pi_0 C_0}$ as

$$E_0 \frac{\pi_t C_t}{\pi_0 C_0} = \exp \left\{ - \int_0^t \left[r_s^f + r_{p,s} + r_{J,s} \right] ds \right\} \frac{E_0 C_t}{C_0}$$

where

$$\begin{aligned} r_{J,s} &= -\lambda_0 (1 - N_{0,s-}) \left(\frac{\xi_s}{\xi_{s-}} \mathcal{J}_{\pi,s} + \mathcal{J}_{S,s} - \left(\frac{g_s}{g_{s-}} - 1 \right) \right) \\ &= -\lambda_0 (1 - N_{0,s-}) \left(\frac{g_t^{1-1/\zeta}}{g_{t-}^{1-1/\zeta}} - \frac{\xi_t^{1/\epsilon}}{\xi_{t-}^{1/\epsilon}} \right) \left(\frac{\xi_t^{1-1/\epsilon}}{\xi_{t-}^{1-1/\epsilon}} - \frac{g_t^{1/\zeta}}{g_{t-}^{1/\zeta}} \right) \end{aligned}$$

The numerical value of $r_{J,s}$ is much smaller than r^f and r_p because both $\frac{g_t^{1-1/\zeta}}{g_{t-}^{1-1/\zeta}} - \frac{\xi_t^{1/\epsilon}}{\xi_{t-}^{1/\epsilon}}$ and $\frac{\xi_t^{1-1/\epsilon}}{\xi_{t-}^{1-1/\epsilon}} - \frac{g_t^{1/\zeta}}{g_{t-}^{1/\zeta}}$ are approximately zero. The rate $r^f + r_p + r_J$ at which future consumption flows are discounted is called the (consumption) growth-adjusted consumption discount rate.

The inverse of consumption-wealth ratio is given by

$$\kappa_0^{-1} = \frac{S_0}{C_0} = \int_0^\infty \mathbb{E} \left(\frac{\pi_t C_t}{\pi_0 C_0} \right) dt = \int_0^\infty \exp \left[- \int_0^t (r_s^f + r_{p,s} + r_{J,s}) ds \right] \frac{\mathbb{E}_0 C_t}{C_0} dt \quad (3.A.5)$$

Substituting Equation (3.A.5) into the first term in Equation (3.A.4) yields

$$\begin{aligned} & - \frac{\chi C_0}{1-1/\epsilon} \frac{\partial(\kappa_0^{-1})}{\partial T_0} = - \frac{\chi}{1-1/\epsilon} \int_0^\infty \frac{\partial}{\partial T_0} \left\{ \exp \left[- \int_0^t (r_s^f + r_{p,s} + r_{J,s}) ds \right] \mathbb{E}_0 C_t \right\} dt \\ & = \frac{\chi}{1-1/\epsilon} \int_0^\infty \left\{ \int_0^t \frac{\partial}{\partial T_0} \left[r_s^f + r_{p,s} + r_{J,s} - \left(\mu_{C,s} - \frac{\lambda_1}{\alpha_1 + 1} - \frac{\bar{\lambda}_s T_s}{\alpha_2 + 1} \right. \right. \right. \\ & \quad \left. \left. \left. + \lambda_0 (1 - N_{0,s-}) \left(\frac{\xi_s}{\xi_{s-}} - 1 \right) \right) \right] ds \right\} \exp \left[- \int_0^t (r_s^f + r_{p,s} + r_{J,s}) ds \right] \mathbb{E}_0 C_t dt \\ & = \frac{\chi}{1-1/\epsilon} \int_0^\infty \left\{ \int_0^t \left[\frac{\partial \lambda_{2,s}}{\partial T_0} \left(\frac{1-1/\epsilon}{\alpha_2 + 1 - \gamma} \right) \right] ds \right\} \cdot \exp \left[- \int_0^t (r_s^f + r_{p,s} + r_{J,s}) ds \right] \mathbb{E}_0 C_t dt \\ & = \int_0^\infty \left\{ \int_0^t \chi \left(\frac{1}{\alpha_2 + 1 - \gamma} \right) \frac{\partial \lambda_{2,s}}{\partial T_0} ds \right\} \cdot \exp \left[- \int_0^t (r_s^f + r_{p,s} + r_{J,s}) ds \right] \mathbb{E}_0 C_t dt \quad (3.A.6) \end{aligned}$$

3.B Numerical Results for the New Climate Regime (B)

Below we provide the numerical results for the risk-free rate and the risk premium in Regime (B), as a supplementary analysis for Section 3.4.2.

We consider the case, where under climate volatility risk, the intensity of climate disasters increases while their frequency remains unchanged, referred to as Regime (B). Since the SCC can be interpreted as the current price of an asset which pays the climate-induced future losses in consumption as a “dividend” in each period, its calculation naturally fits within the standard asset pricing framework. Based on the analytical framework in Section 3.4, we provide numerical results for the key components of the consumption discount rate, the risk-free rate, and the risk premium. We consider three scenarios for disaster intensity in the new regime: $E J_2^{(H)} = 4 E J_2^{(L)}$, $2 E J_2^{(L)}$, and $E J_2^{(L)}$.

3.B.1 Risk-Free Rate

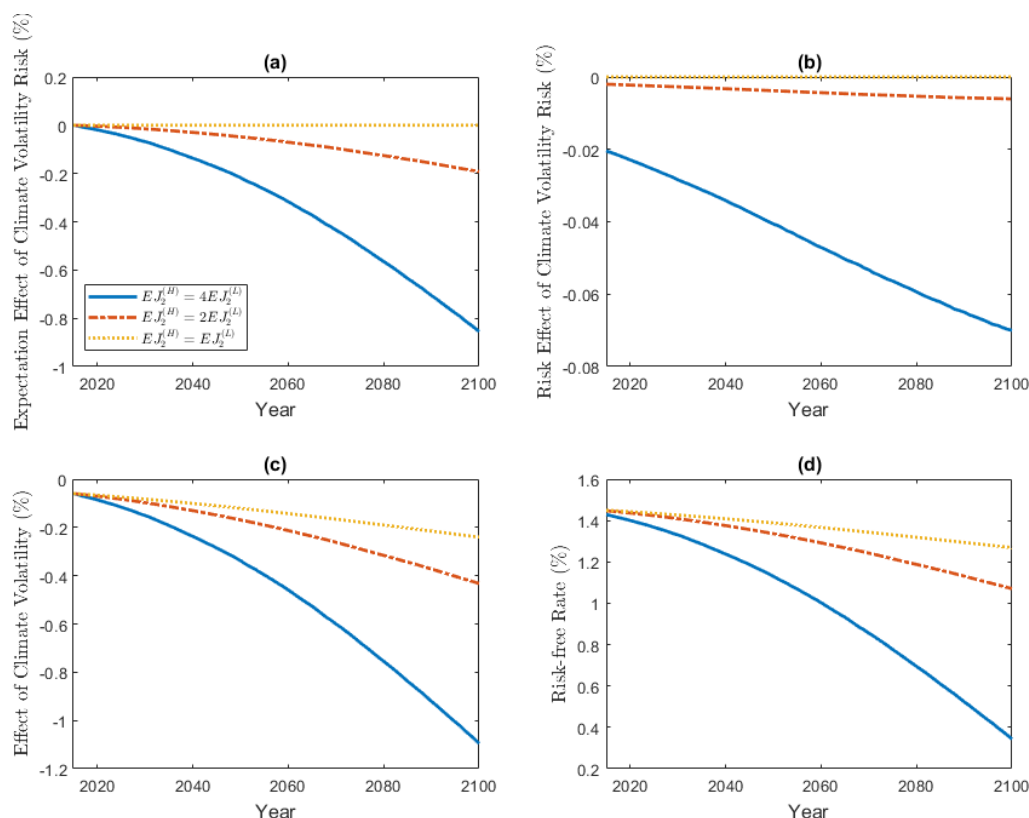
The Risk-Free Rate in the Business-As-Usual Scenario Figure 3.A1 shows the decomposition of risk-free rates in the BAU scenario, based on Equation (3.2). Panel (a) and (b) show the expectation effect and the risk effect of the stochastic climate volatility on the risk-free rate, Panel (c) shows the effect of climate disasters, and Panel (d) plots the time paths of the risk-free rate itself.

Both climate disaster risk and climate volatility risk reduce the risk-free rate, as can be seen in Panel (a), (b) and (c). Their magnitudes increase with higher disaster intensity $E J_2^{(H)}$, reflecting greater exposure to climate risks. Besides, the sizes of all effects increase over time, because rising temperature leads to more frequent climate damages, and the expected climate damage rises as the probability of a climate volatility shock occurring in the future increases. The expectation effect of climate volatility risk and the climate disaster effect are of similar magnitude, while the risk effect is considerably smaller. Consequently, the risk-free rate exhibits a downward-sloping trajectory over time due to the cumulative negative impact of both types of climate risks. Compared with Regime (A) in the BAU scenario, all effects in Panels (a), (b), and (c) are larger under Regime (B), resulting in lower time paths of the risk-free rate.

The Risk-Free Rate Under Optimal Abatement Figure 3.A2 shows the average risk-free rate and its decomposition under optimal abatement policies. Panel (a) and (b) measure the effects of climate volatility risk through the expectation and the risk channels, Panel (c) shows the effect of climate disaster risks, and Panel (d) shows the time path of the risk-free rate under different climate disaster intensities in the new climate regime.

Compared with the BAU scenario, both climate disaster risk and climate volatility risk have a smaller impact on the risk-free rate, because emission control slows the rise in temperature and

Figure 3.A1: Decomposition of (average) risk-free rates in the BAU scenario under climate volatility risk (B). The expected size of one climate disaster in the new regime rises to $4EJ_2^{(L)}$, $2EJ_2^{(L)}$, or remains unchanged. Panel (a) and (b) show the expectation effect and the risk effect of the stochastic climate volatility on risk-free rates, Panel (c) shows the effect of climate disasters on the risk-free rate, and Panel (d) plots the time paths of the risk-free rate itself.

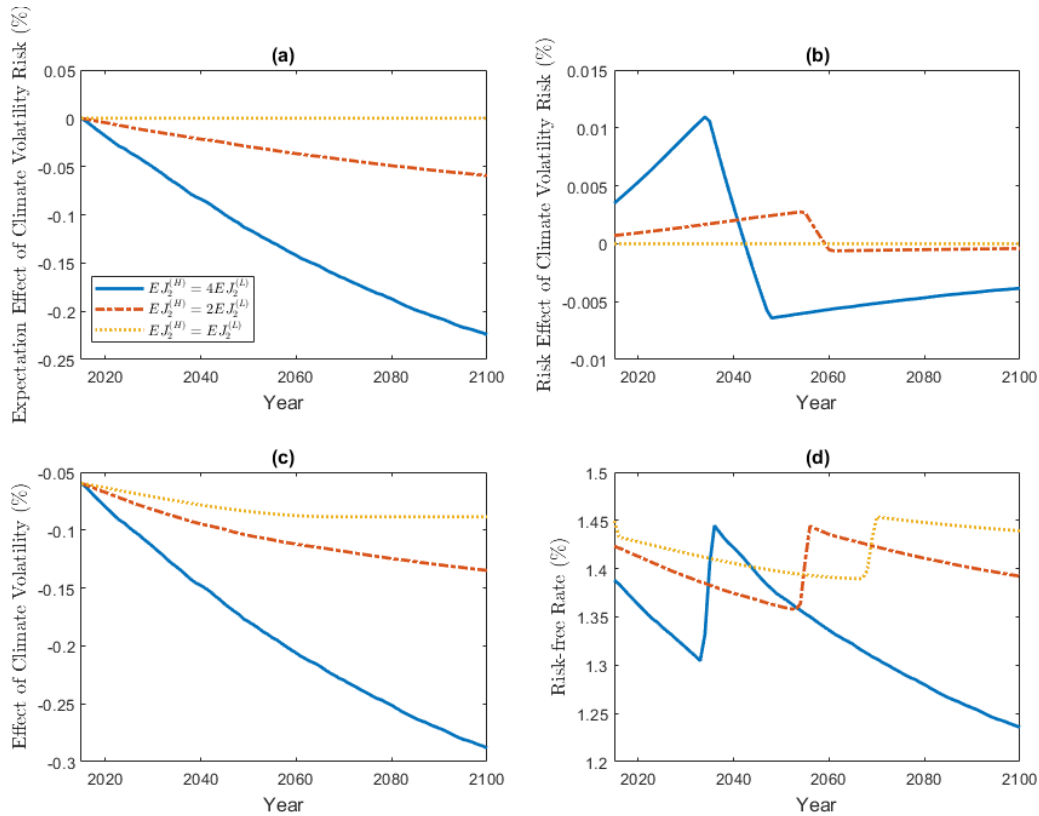


thus reduces the likelihood of extreme weather events. Climate volatility risk plays a significant role. As shown in Panels (a) and (b), its influence on the risk-free rate operates primarily through the expectation channel. The risk effect of climate volatility risk is initially positive, prior to the emission control rate reaching its maximum of 100%, but turns negative thereafter. Over time, as climate volatility risk gradually resolves, its effect in Panel (b) converges toward zero, though this occurs beyond the time horizon shown in the figures.

3.B.2 Risk Premium

The Risk Premia in the BAU Scenario Figure 3.A3 shows the risk premia and its climate-related components in the BAU under Regime (B). Panel (a) and (b) shows the expectation effect and the risk effect of climate volatility risk, respectively. Panel (c) shows the effect of climate disaster risk, and Panel (d) shows the time paths of risk premia.

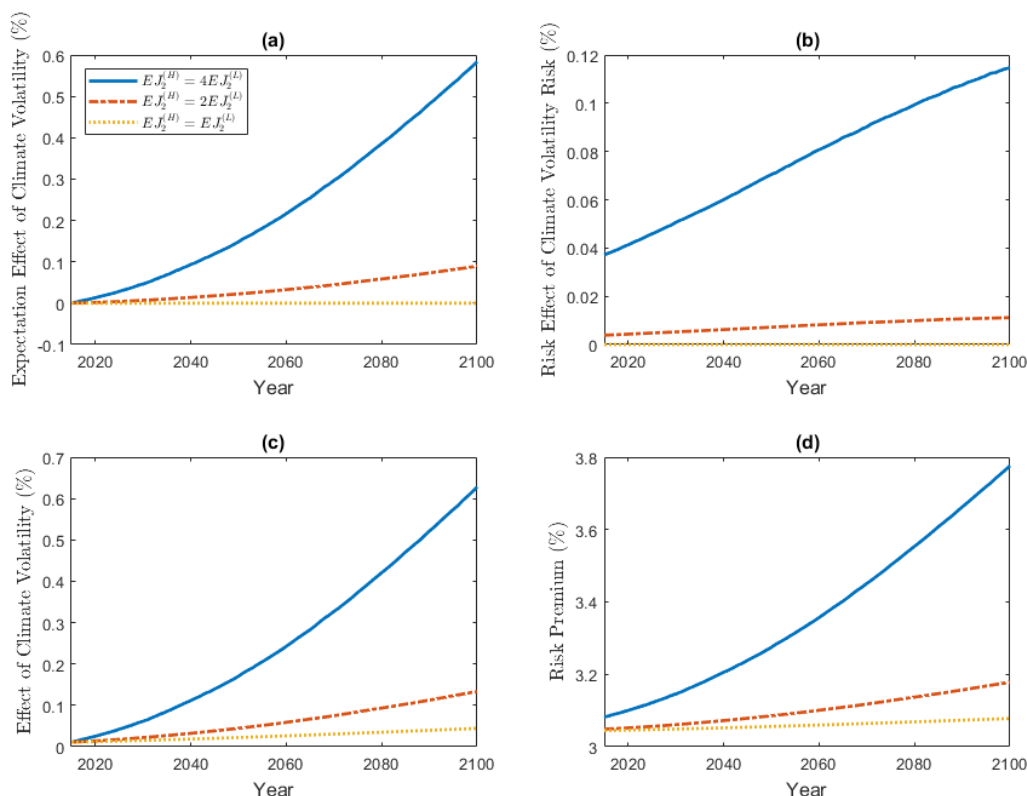
Figure 3.A2: Decomposition of risk-free rates under optimal abatement policies under climate volatility risk (B). The expected size of one climate disaster in the new regime rises to $4EJ_2^{(L)}$, $2EJ_2^{(L)}$, or remains unchanged. Panel (a) and (b) show the expectation effect and the risk effect of the stochastic climate volatility on risk-free rates, Panel (c) shows the effect of climate disasters on the risk-free rate, and Panel (d) plots the time paths of the risk-free rate itself.



Compared with the BAU scenario under Regime (A) (Figure 3.3), Regime (B) results in higher compensation for both climate disaster risk and climate volatility risk, as shown in Panels (a), (b), and (c). The expectation effect, risk effect, and climate disaster effect contribute to the risk premia at similar orders of magnitude, consistent with the main conclusion of this paper: climate volatility risk is as important as climate volatility itself in determining the discount rate and the SCC.

The effects of climate disasters and the expectation effect of volatility risk increase over time, reflecting the fact that the intensity of climate disasters rises and higher temperatures lead to more frequent future disasters. Anticipating more severe natural disasters, agents demand higher risk compensation. The risk effect of stochastic climate volatility also rises with disaster intensity, since a new regime with more severe disasters poses larger threats to economic growth and therefore increases the required risk compensation. As the uncertainty associated with climate volatility gradually resolves over time, the risk effect in Panel (b) converges to zero. However, this occurs beyond the time horizon displayed in the figures.

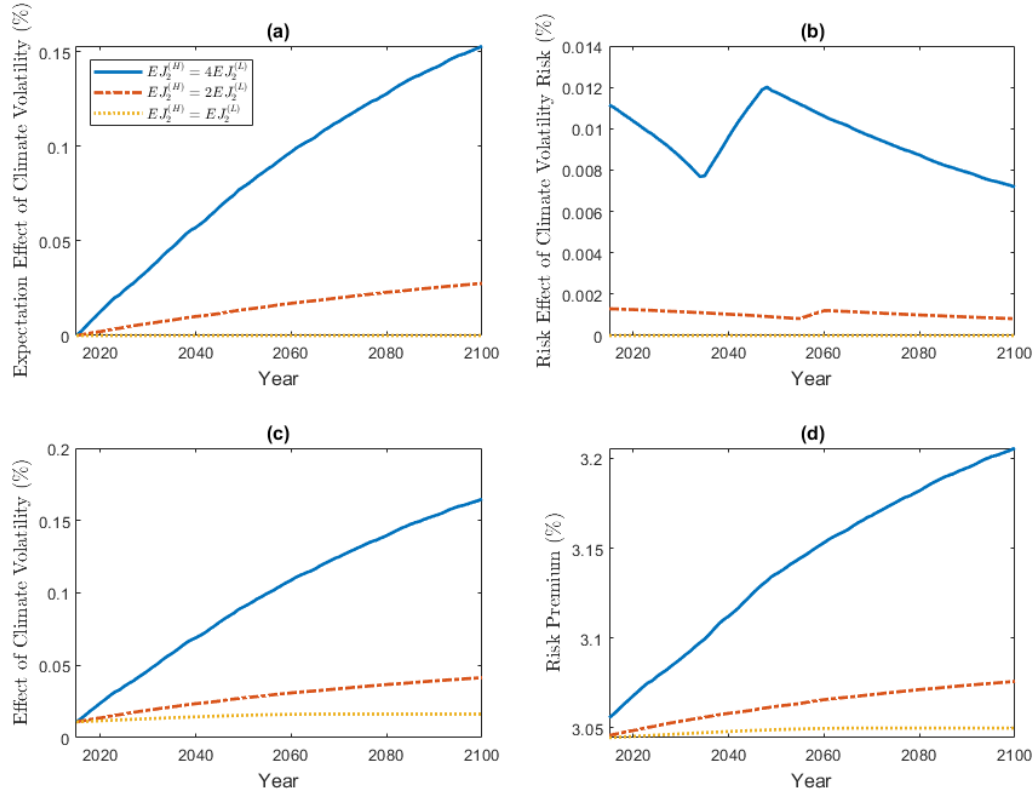
Figure 3.A3: Decomposition of risk premia in the BAU scenario under climate volatility risk of Type (B). The expected size of one climate disaster in the new regime rises to $4EJ_2^{(L)}$, $2EJ_2^{(L)}$, or remains unchanged. Panel (a) and (b) shows the expectation effect and the risk effect of climate volatility risk, respectively. Panel (c) shows how much the risk premium is affected by climate disaster risk, and Panel (d) shows the time paths of risk premia.



The Risk Premia Under Optimal Abatement Figure 3.A4 shows the risk premium and its decomposition under optimal abatement. Panel (a) and (b) show the expectation effect and the risk effect of climate volatility risk, respectively. Panel (c) shows the effect of climate disaster risk on risk premia, and Panel (d) plots the risk premia over time. The impacts of climate volatility risk and climate disasters are smaller under optimal abatement than in the BAU scenario because stringent abatement mitigates the progression of climate change. However, their sizes are of the same order. This implies that climate volatility risk is as important as climate volatility itself when calculating risk premia and the SCC, regardless of abatement policy stringency.

Panel (a), (b), and (c) imply that both climate disaster risk and climate volatility risk increase with $EJ_2^{(H)}$. As the new climate regime poses a greater threat to economic conditions, agents require higher compensation for climate risks. In Panel (b), the initial and long-run effects of climate volatility risk through the risk channel decline over time as uncertainties about climate volatility gradually resolve. The upward jumps observed mid-century correspond to the kink point in the emission control rate. Panel (d) shows that risk premia exhibit little variation across

Figure 3.A4: Decomposition of risk premia in the optimal abatement policy scenario under climate volatility risk of Type (B). The expected size of one climate disaster in the new regime rises to $4EJ_2^{(L)}$, $2EJ_2^{(L)}$, or remains unchanged. Panel (a) and (b) show the expectation effect and the risk effect of climate volatility risk, respectively. Panel (c) shows the effect of climate disaster risk on risk premia, and Panel (d) plots the risk premia over time



different assumptions about the climate conditions in the new regime, reflecting the effectiveness of emission control in slowing global warming and delaying the adverse economic impacts of climate change.

Chapter 4

Carbon Price and Tipping Risk: the Case of the Greenland Ice Sheet and Thawing Permafrost

Abstract

We analyze the impact of tipping points in the Greenland Ice Sheet (GIS) and permafrost, along with their interactions, on the Social Cost of Carbon (SCC), optimal emission abatement strategies, global temperature, and climate damage to global GDP. By integrating reduced-form models of both tipping points into a stochastic dynamic integrated climate-economy model, we find that both tipping points can significantly alter future climate trajectories in the absence of effective emission abatement policies. In the short term, permafrost thaw significantly increases climate damages and SCC estimates, primarily through methane emissions. While the melting of the GIS alone does not substantially raise the SCC, its effects are notably exacerbated when combined with permafrost thaw. Under stringent emission abatement policies, both future climate damages and the SCC are expected to be substantially reduced. Policy analyses accounting for permafrost thaw tend to favor more stringent abatement measures compared to those considering only GIS melting.

4.1 Introduction

Recent scientific and economic studies on climate change have increasingly highlighted concerns over the potential impacts of climate tipping elements. These tipping elements are components in the climate system that can undergo significant qualitative changes when key parameters surpass critical thresholds (commonly referred to as climate tipping points) under

climate change. Once a tipping point is crossed, the subsequent change in climate dynamics will have profound implications for the economic consequences of climate change. Moreover, there are complex interactions between tipping elements through various physical mechanisms in the climate system. As a result, the crossing of one tipping point can influence the dynamics of other tipping elements. Given the substantial and often irreversible consequence of climate tipping, recent economic literature has sought to incorporate these tipping points into climate-economy integrated assessment models. However, the majority of these models represent climate tipping points as abrupt shifts in climate variables, without accounting for the interactive dynamics between tipping elements. In addition, these simplified models tend to overlook the different mechanisms through which tipping points impact the economy, potentially leading to biased recommendations on climate policies.

In this paper, we account for the heterogeneity of climate tipping points by considering their distinct impacts on future climate and economic conditions, while explicitly modeling the interactive dynamics between multiple types of tipping elements. By incorporating the dynamics of two specific tipping elements into a stochastic integrated assessment model, our objective is to analyze how the interaction between these climate tipping points influences future climate projections, the Social Cost of Carbon (SCC), and the optimal emission abatement policy in the near term. Specifically, we focus on two critical tipping points: the disintegration of the Greenland Ice Sheet (GIS) and the thawing of permafrost, instead of all possible tipping points within the climate system. Compared with other global-scale climate tipping points, these two are highly likely to be triggered in the near future and are irreversible within the human timescale, making them particularly relevant for policy considerations. Furthermore, there is more robust scientific evidence on their triggering mechanisms, thereby allowing for more certainty about their consequences for both the climate and the global economy (Hope and Schaefer (2016), Nordhaus (2019), Wang et al. (2023)).

Another reason for focusing on these two tipping points is that their underlying mechanisms are better understood compared with other tipping elements. Since research on climate tipping points is still in progress, there remains significant uncertainty about the threshold conditions that could trigger different types of tipping points as well as their potential consequences. Although more tipping points may be crossed in the coming centuries, there is currently a lack of models capable of accurately determining how much warming is required to trigger them. Therefore, we restrict our attention to the GIS and permafrost at this stage. By incorporating only these two tipping elements into the model, we are able to provide a more precise assessment of how tipping elements interact and quantify the impacts of both individual tipping points and their interactions.

The SCC is an important indicator of the stringency of current climate policies, and measures how much damages are added by carbon emissions. It provides a useful way to understand the

impact of climate tipping on social welfare and climate policy, and is therefore a main focus of this paper. Since human emission of greenhouse gases is the key driver of climate change (IPCC (2021a)), one of the most effective way to decelerate warming is emission abatement. Policies can be made to reduce the consumption of dirty energies and optimize the efficiency of production across the whole economy. However, emission abatement is costly, therefore creating a trade-off for policy makers between investing in greater abatement efforts to achieve a cooler planet in the future and prioritizing the consumption today which leads to a warmer climate. This trade-off reflects the tension between immediate economic welfare and long-run climate stability, since increased abatement spending reduces current consumption but mitigates future climate risks. To capture this trade-off in the decision-making process, we use stochastic differential utility (Duffie and Epstein (1992)) to characterize the preference of representative agents in the economy. It is the continuous-time version of Epstein-Zin preferences, which allows us to separate risk aversion parameter and the elasticity of intertemporal substitution in order to better match the macroeconomic data.

We use a continuous-time Dynamic Stochastic Integrated assessment model of Climate and the Economy (DSICE) to generate climate and policy implications under the risk of multiple climate tipping points. Rather than the DICE model which tackles uncertainties by focusing on the uncertainty of key parameters, we model the stochastic dynamics in both the climate and the economic systems as in Cai and Lontzek (2019). This allows us to evaluate different climate change policies and generates significantly different economic implications from the DICE model. Building on the standard framework of the DSICE models in the current literature, we incorporate reduced-form models to represent the disintegration of the Greenland Ice Sheet (GIS) and the thawing of permafrost. In these reduced-form models, we abstract from the detailed geophysical mechanisms underlying each tipping element and instead establish a direct relationship between the key parameters of the tipping system and the global climate system. This simplification of the geophysical processes enables us to analyze the interaction between tipping elements while maintaining analytical tractability for deriving optimal climate policies within a stochastic dynamic model framework. This approach allows for a balance between capturing the essential tipping dynamics and ensuring the model's feasibility for policy analysis.

To analyze the impact of climate mitigation in the context of climate tipping, we examine two policy scenarios in our numerical exercise. The first scenario is the Business-As-Usual (BAU) scenario, where no climate mitigation policy is imposed on the economy. The second scenario involves the implementation of an optimal abatement policy. In this case, the social planner chooses the optimal rate of carbon emission control for each year to maximize total social welfare over an infinite time horizon. By comparing the numerical results from both policy scenarios, we can quantify the extent to which emission abatement can effectively combat climate change in the presence of tipping risks.

Our findings indicate that the melting GIS and thawing permafrost can substantially impact future economic and climate variables. This underscores the importance of distinguishing between different types of climate tipping points in economic analyses, as well as the mechanisms through which these tipping points influence the economy. Both tipping points would result in global GDP losses, albeit through different channels. We identify two key channels through which climate change induces economic damage: the direct impact of global warming as characterized by Nordhaus's damage function (Nordhaus (1992)), and the economic repercussions of rising sea levels due to the melting ice sheet.

Since the GIS melts gradually, its contribution to sea-level rise remains limited even if the tipping point is crossed by the end of the next century. Consequently, the GIS alone is projected to reduce global GDP by less than 0.03% by 2100, irrespective of abatement policy. In contrast, thawing permafrost releases large amounts of greenhouse gases with high warming potential, which substantially accelerates global warming. Rising temperature not only increases the frequency of extreme weather events but also intensifies the melting of the GIS. By 2100, permafrost thaw is projected to contribute an additional 1°C of warming, which nearly doubles GIS melt. Consequently, its economic impact arises through both the temperature and sea-level rise channels, making it larger than the damages from GIS melting alone. Relative to a scenario without tipping elements, accounting for permafrost thaw increases projected global GDP losses in 2100 by approximately 1% in the BAU scenario and 0.7% under optimal abatement. When both tipping elements are incorporated into the model, the higher damages from climate change are driven primarily by the warming effects of permafrost thaw.

The SCC rises over time with increasing climate damages under global warming, and is further elevated by the presence of tipping elements. In 2100, GIS melting alone raises the SCC by only 1% relative to the no-tipping scenario, whereas permafrost thaw increases it by 14%, reflecting its much larger economic impact. This discrepancy arises because the volume of melted GIS over the next century remains limited, while permafrost thaw significantly amplifies global warming and the associated GDP losses. When both tipping elements are included, their positive correlation reinforces their adverse effects, jointly magnifying climate damages. As a result, the SCC rises by 31% by 2100 when accounting for both GIS melting and permafrost thaw.

The adverse impacts of climate tipping points and their interactions can be substantially mitigated under the optimal abatement policy. Although carbon emission from permafrost cannot be directly abated, reducing anthropogenic carbon emissions slows global warming, which lowers damages from extreme weather events and decelerating the tipping of both the GIS and permafrost. Consequently, the SCC is markedly lower under optimal abatement than in the BAU scenario. Across all tipping scenarios, the optimal abatement rate increases over time and converges to 100% within roughly a century. Permafrost thaw substantially increases

the optimal abatement rate, since stricter emission controls are required to offset its additional warming effects. In contrast, GIS melting has negligible influence on abatement policy, because it does not directly affect carbon emissions.

We further examine the dynamics of individual tipping elements, focusing on methane emissions from thawing permafrost. Although methane accounts for only 2% of total permafrost carbon emissions, it contributes roughly 0.7°C of additional warming and 0.55% of global annual GDP loss by 2100. This disproportionate effect reflects its stronger radiative forcing relative to carbon dioxide, which induces greater warming per unit of carbon emission. Given methane's high warming potential and short atmospheric lifetime, its role is particularly relevant for short-term economic assessments. Our findings highlight the importance of incorporating methane emissions from multiple sources into future economic analyses, alongside carbon dioxide.

Finally, we compare the economic implications of alternative GIS dynamics. Climate science identifies three commonly discussed scenarios, each reflecting a distinct equilibrium relationship between GIS volume and temperature. The first assumes a hysteretic system, where exceeding a critical temperature threshold triggers an abrupt and irreversible shift of GIS volume, capturing the key characteristic of a tipping point. The second and third scenarios assume reversibility of GIS volume, with either linear or nonlinear equilibrium responses to temperature. Our results show that these different GIS dynamics yield similar SCC estimates, economic outcomes, and climate projections over the next century, with large divergences only emerging in the long term. This is largely because the model parameters are calibrated to recent climate data, which constrains short-term differences, and the gradual unfolding of GIS tipping even in the hysteretic case.

Literature Review The DSICE model builds on Olijslagers et al. (2023), Olijslagers and van Wijnbergen (2024). The economic block is a pure exchange economy model with Barro-type rare disasters (Barro (2006), Barro (2009)). Including rare disaster risk improves the model's ability to match the observed high equity premia and low risk-free rates, which is important for SCC estimation, since the SCC reflects the expected discounted future climate damages. The climate block models global mean surface temperature as a linear function of cumulative carbon emissions (as in Matthews et al. (2009), Van den Bremer and Van der Ploeg (2021)), and uses reduced-form representations for the GIS tipping (Nordhaus (2019)) and permafrost thaw (Kessler (2017)). Other climate dynamics, such as atmospheric carbon decay and Earth's heat radiation, are excluded to simplify the climate model and enhance computational tractability.

The economic consequences of climate tipping points have drawn growing attention from researchers and policymakers, though approaches differ across climate science and economics. Climate scientists define tipping elements as components of the Earth system that respond nonlinearly once critical thresholds are crossed (McKay et al. (2022)). They have studied

numerous candidate tipping elements that are likely to be triggered both in the near- and long-term, and provided detailed descriptions of their geophysical mechanisms and consequences (Wang et al. (2023)). Predictions of tipping points rely on large-scale climate models and scenario analysis, and the predictability of each tipping point varies. Recent literature has examined the climate and economic implications of multiple tipping points (Klose et al. (2020), Wang et al. (2023)), highlighting that the likelihood and impact of one tipping point may depend on the triggering of others. Lenton et al. (2019) argues that cascading tipping points are already observable, and emphasizes the urgency of immediate climate action due to their potentially irreversible impacts.

Economists analyze climate tipping points using a different approach, often defining them as abrupt and irreversible shifts in climate conditions induced by global warming. In economic models, climate tipping points are typically modeled in highly stylized forms, such as sudden increases in temperature sensitivity to carbon emissions (Lemoine and Traeger (2014)) or exogenous percentage declines in GDP (Cai et al. (2016)). While such simplifications enhance tractability, they abstract from the underlying geographical processes and interactions between climate and economic systems, potentially leading to oversimplified results.

Much of the climate economics literature analyzes tipping risk in general terms without distinguish between specific tipping elements. In practice, however, different climate tipping points affect the Earth system and thus the economy through different mechanisms. For example, thawing permafrost releases large amounts of greenhouse gases, accelerating global warming; melting of Greenland and Antarctic ice sheet raises sea levels, increasing coastal flooding risk while also weakening the ice-albedo effect and amplifying warming; and Amazon rainforest dieback can transform the region into a carbon source, threaten biodiversity, and disrupt local agriculture. Neglecting the heterogeneity of climate tipping points can yield misleading policy implications. Moreover, the mechanisms underlying some tipping points remains uncertain, and it is unclear whether global warming accelerates the process of tipping. Examples include the potential collapse of Atlantic Meridional Overturning Circulation (AMOC), boreal forest ecosystem shifts, and disruption of tropical seasonal monsoons. Given these uncertainties and policy constraints, it is reasonable to focus only on a subset of temperature-driven tipping points for the time being.

A further limitation of the current economic literature is the limited attention to interactions between climate tipping points. There are only a few studies that incorporate multiple tipping points into economic models. Indeed, doing so often requires more state variables and increases the computational complexity. Cai et al. (2016) integrates the interactions between five candidate climate tipping elements into the DICE model using a Markov transition matrix, with hazard rates postulated from expert opinions. They find that accounting for such interactions increases the SCC and encourages stronger emission reductions. Different from this paper, they abstract

from the tipping process and model climate tipping as a discrete GDP loss, while omits impacts on the Earth system such as global temperature dynamics. Lemoine and Traeger (2016) examines the impact of multiple tipping points on optimal policy making. However, they adopt a broader definition of tipping points, treating them as systemic social, economic, and climate shifts rather than specific geophysical tipping elements. In contrast, this paper adopts the definition of tipping points from climate science, and uses reduced-form models for the dynamics of each tipping element. These models are linked through common climate parameters, which allows us to analyze the interactions between tipping points.

A more recent paper Dietz et al. (2021a) studies the economic impact of eight interacting climate tipping points using a meta-analytic integrated assessment model, and find that climate tipping points jointly increase the SCC by around 25%. While we build on their model structure for tipping elements, our approach differs in three key aspects. First, we focus only on tipping points with global impact, thereby excluding those with primarily regional impact and heterogeneous nation-level damages. Second, our analysis emphasizes near-term effect of climate tipping, as policymakers are particularly concerned with tipping elements that may be triggered within decades rather than centuries or millennia. This justifies excluding long-horizon tipping points and facilitates their integration into a dynamic stochastic model of the global economy, which better fits the macroeconomic data and yields more policy-relevant insights. Third, we analyze how tipping risks and their interactions influence the emission abatement policy, which is not addressed in Dietz et al. (2021a). By solving the representative agents' intertemporal optimization problem, we find optimal abatement strategies under different tipping scenarios. Our results show that accounting for climate tipping points and their interactions significantly alters the policy response.

The global-scale tipping points discussed in Dietz et al. (2021a) can be categorized into two groups based on their underlying mechanisms: those driven by positive carbon-temperature feedback and those associated with sea-level rise from melting ice sheet. As a first step, we choose permafrost thawing and Greenland ice sheet disintegration from both categories to show how different types of tipping elements interact.

Permafrost carbon release is one of the most frequently discussed tipping elements in the climate literature. Permafrost refers to soil, sediment, and rock that remain frozen for several consecutive years. At low temperatures, organic matter decomposes slowly and accumulates in the frozen earth, resulting in a permafrost carbon stock that far exceeds the cumulative atmospheric carbon (Olefeldt et al. (2016), Schuur et al. (2018)). In recent decades, rising permafrost temperature under global warming has accelerated thawing of organic matter and carbon emissions (Biskaborn et al. (2019)), which motivates extensive research on its climatic consequences. Meanwhile, economic research has examined the macroeconomic impact of permafrost carbon. Hope and Schaefer (2016) is the first to quantify these impacts. By

incorporating additional permafrost carbon emissions from four IPCC scenarios (Nakicenovic (2000)) into the PAGE09 integrated assessment model (Hope (2011)), they show that carbon emissions from thawing permafrost substantially increase the net present value of the climate damages, underscoring the urgency of mitigation. In a more recent work, Kessler (2017) developed a model of the permafrost carbon feedback and integrates it into the DICE model. Their results indicate that neglecting the permafrost carbon feedback when setting industrial emission standard can raise the global mean surface temperature by up to 2°C in the early next century.

Another tipping element that requires urgent attention is the Greenland Ice Sheet (GIS). Continued warming could trigger rapid melting over the coming centuries, driving multi-meter sea-level rise and threatening the development of coastal areas (Box et al. (2022)). Moreover, GIS ice loss is irreversible on human timescales, implying long-lasting impacts (Gregory et al. (2020)). To assess its the economic implications, Nordhaus (2019) integrate a reduced-form GIS model into the DICE-2016R2 model. Consistent with our analysis, they find that GIS disintegration adds little to the SCC under alternative discount rates and GIS dynamics.

The remainder of the paper is organized as follows. Section 4.2 introduces the DSICE model, which combines a stochastic endowment economy with disaster risks and a climate block with tipping elements. Section 4.3 provides more details on the functional forms of key parameters and the model calibration. Numerical results are presented and analyzed in Section 4.4. Section 4.5 concludes.

4.2 Model

We develop a continuous-time integrated assessment model to analyze the effects of climate tipping elements on both climate dynamics and the economy. In particular, we focus on two widely studied tipping points: Greenland Ice Sheet (GIS) melting and permafrost thaw. They are of particular interest due to their relatively high near-term likelihood and their long-lasting consequences. Both tipping elements interact with the global climate system, influencing global mean surface temperature and thereby human welfare and economic output. The economic environment is modeled as an endowment economy, where representative agents with recursive preferences maximize their lifetime welfare by choosing climate actions such as carbon emission abatement, in response to potential climate-related damages from global warming.

The Thawing Permafrost Permafrost is the perennially frozen ground remaining at or below 0°C for at least two consecutive years. As temperature rises, permafrost thaws and the frozen organic matter it contains decomposes, releasing carbon dioxide (CO₂) and methane (CH₄) in addition to anthropogenic carbon emissions. These permafrost carbon emissions amplify

global warming, which further accelerates thawing – a process known as the Permafrost Carbon Feedback (PCF). Because the warming induced by permafrost carbon emissions is irreversible on human timescales, it is a critical consideration for climate policy analysis.

To model permafrost carbon release under global warming, we use the two-phase model from Kessler (2017). As the name implies, the permafrost carbon emission model consists of two phases. In the first phase, rising temperature drives permafrost degradation. In the second phase, carbon emissions from newly thawed permafrost are quantified. This approach captures two key features of the PCF. First, there is a time lag between temperature increases and permafrost carbon release, implying that emissions will have long-lasting effects on global temperatures for centuries. Second, although thawing permafrost may enhance regional plant growth and potentially mitigate some warming effects, it is expected to contribute positively to global warming overall.

In the first phase, we model the relative size of the remaining permafrost with respect to a reference time t_0 , when the size of the permafrost area remains stable at temperature T_{t_0} . As temperature rises, permafrost area declines, releasing extra carbon from the newly thawed ground. Let PF_t be the fraction of permafrost remaining at time t relative to time t_0 . Following Kessler (2017), PF_t decreases at rate $\beta_{PF} > 0$ with temperature increases:

$$PF_t = PF_{t_0} - \beta_{PF}(T_t - T_{t_0})$$

where $T_t - T_{t_0}$ is the cumulative temperature change, and $PF_{t_0} = 1$ by definition.

We assume that carbon is uniformly distributed in the permafrost area, so changes in carbon storage in the permafrost are proportional to changes in permafrost area. Formally, let $C_{PF,t}$ be the amount of carbon in the newly thawed permafrost at time t , and \bar{C}_{PF} be the total permafrost carbon at the reference time t_0 . Then

$$\frac{C_{PF,t}dt}{\bar{C}_{PF}} = -dPF_t = \beta_{PF}dT_t$$

In the second phase of the model, we quantify permafrost carbon emissions at each time t , which occur in the form of carbon dioxide (CO₂) and methane (CH₄). Although only around 2% of carbon released from permafrost is methane (Kessler (2017)), its impact on global warming is substantial. Methane accounts for roughly 30% of observed warming since the pre-industrial period (McArthur (2021)). Although it has a shorter atmospheric lifetime than CO₂, it absorbs more energy when staying in the atmosphere and thus has more aggressive impacts on global warming. For this reason, it is essential to account for the radiative forcing from methane when assessing the near-term climate impact of thawing permafrost.

We decompose the carbon stock $C_{PF,t}$ in the thawed permafrost at time t into two pools: an unstable pool where carbon is gradually released into the atmosphere, and a passive (or stable)

pool where carbon stays in the thawed permafrost and does not contribute to emissions. We assume that the share of permafrost carbon in each pool is constant over time, with $p = 40\%$ in the stable pool and $1 - p = 60\%$ in the unstable pool. Therefore, only 60% of the thawed permafrost carbon is emitted to the atmosphere, and the remaining 40% stays.

The decomposition of permafrost organic matter is gradual, so carbon emissions at time t comes not only from the newly thawed permafrost but also from permafrost thawed in earlier periods. The release rate depends on both the amount of thawed permafrost and the time elapsed since thawing. We assume that the carbon released from the thawed permafrost follows an exponential decay process at rate τ . Then the instantaneous permafrost carbon emission $E_{PF,t}$ is given by

$$E_{PF,t} = (1 - p) \int_{t_0}^t \frac{1}{\tau} e^{-\frac{t-s}{\tau}} C_{PF,s} ds$$

which is the aggregate carbon emissions from all previously thawed permafrost in the unstable pool.

The dynamics of $E_{PF,t}$ satisfy the differential equation

$$dE_{PF,t} = \frac{1}{\tau} [-E_{PF,t} + (1 - p)\bar{C}_{PF}\beta_{PF}\mu_{T,t}] dt$$

where $\mu_{T,t}$ is the drift of temperature T at time t .

Finally, we distinguish between emissions in the form of CO₂ and CH₄. Empirical evidence suggests that $q = 98\%$ of released permafrost carbon is emitted as CO₂, and $1 - q = 2\%$ as CH₄ (Kessler (2017)). Let $E_{PF,t}^{CO_2}$ and $E_{PF,t}^{CH_4}$ be the emission flows in the form of carbon dioxide and methane, respectively. Then we have

$$\begin{aligned} E_{PF,t}^{CO_2} &= qE_{PF,t}, \\ E_{PF,t}^{CH_4} &= (1 - q)E_{PF,t}. \end{aligned}$$

Greenland Ice Sheet (GIS) Melting Recent climate research suggests that mass loss from the Greenland Ice Sheet (GIS) will substantially contribute to sea level rise under continued global warming. Over the past four decades, the rate of sea-level rise has accelerated due to polar ice melt. The loss of ice from the GIS is irreversible on human timescales and is expected to account for the majority of long-term sea-level rise. The Fifth Assessment Report of the Intergovernmental Panel on Climate Change (IPCC) indicates that the temperature threshold for the complete disintegration of the GIS lies between 1°C to 4°C of warming, a range that is highly likely to be reached by the late 21st century according to the temperature projections under most Representative Concentration Pathway (RCP) scenarios. The total collapse of the GIS would

raise global sea levels by more than 7 meters, posing severe threat to human settlements and industries in coastal areas around the world.

The ongoing GIS melting reduces ice cover, which weakens the albedo effect and amplifies warming. However, we exclude this mechanism from our analysis for two reasons. First, the loss of ice from melting is largely offset by the increased precipitation (which adds ice volume) at higher temperatures, resulting in a negligible net effect on albedo (Nordhaus (2019)). Second, although climate studies suggest that reduced ice albedo could induce an abrupt temperature increase of up to 10°C under small perturbations in carbon emissions (Ashwin and von der Heydt (2020)), such dynamics are primarily relevant to transitions between glacial and interglacial periods, and thus lie beyond the scope of this paper. Moreover, Armstrong McKay et al. (2022) estimates that the GIS disintegration would raise global temperatures by only up to 0.13°C in the coming millennia. Given its relatively small impact on near-term temperature dynamics, we exclude the ice albedo effect and the associated temperature tipping from our analysis, and focus instead on the economic consequences of GIS melting through sea-level rise.

We use the volume of the GIS to describe its tipping state, and model the dependence of volume changes on temperature. Let $v_t \in [0, 1]$ be the ratio of GIS volume at t to its pre-industrial level. Following Nordhaus (2019), the dynamics of v_t are given by

$$dv_t = \beta_{GIS} \text{sgn}(T_t - T^*(v_t)) (T_t - T^*(v_t))^2 v_t^{0.2} dt$$

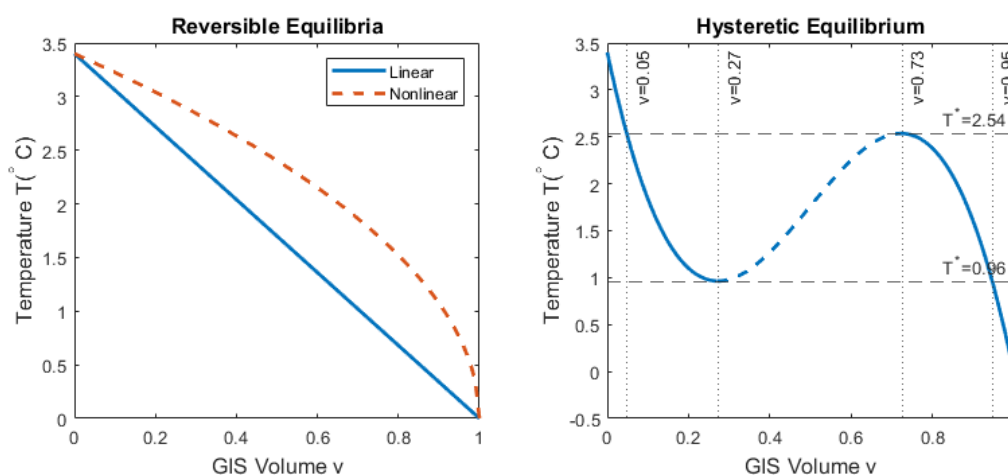
where β_{GIS} is the melting speed, and $T^*(v_t)$ is the equilibrium temperature associated with volume v_t . If the actual temperature T_t is higher than the equilibrium temperature (i.e. $\text{sgn}(T_t - T^*(v_t)) = 1$), the ice sheet melts ($dv_t/dt < 0$), whereas if $\text{sgn}(T_t - T^*(v_t)) = -1$, it rebuilds ($dv_t/dt > 0$). Since our model abstracts from carbon sequestration, atmospheric carbon concentration and temperature do not decline over the horizon considered. Therefore, the possibility of ice sheet restoration at lower temperatures is irrelevant for the economic analysis in this paper and is excluded.

The equilibrium temperature $T^*(v)$ is the threshold temperature at which the GIS volume v remains stable. Climate research highlights two possible forms of this equilibrium relationships: reversible and irreversible. In a reversible system, the GIS volume declines as temperature rises but can fully regain once temperatures fall back. In contrast, an irreversible system exhibits path dependence. Global warming can induce qualitative shifts such that once ice sheets have melted, they cannot return to their initial state even if temperatures subsequently decline. Evidence from climate studies (Ridley et al. (2010), Robinson et al. (2012)) suggests that the Greenland system is best described as irreversible, in particular, a hysteretic system. In a hysteretic system, partial regain of the ice sheet is possible, but it requires a significantly lower temperature than the threshold triggering the initial melting.

The explicit functional forms of $T^*(v)$ for different equilibrium specifications are provided in Section 4.3. Here we show these equilibrium relationships graphically in Figure 4.1. The solid line and dashed line on the left correspond to two reversible cases. In the linear specification (solid), the GIS volume changes proportionally with the equilibrium temperature. In the nonlinear case (dashed), the GIS volume declines faster at the initial stage of temperature rise. In both reversible systems, there is a unique GIS volume associated with each equilibrium temperature, and the GIS volume fully recovers to its previous level in equilibrium once the temperature returns.

The right panel of Figure 4.1 shows the equilibrium relationship in a hysteretic system, which effectively captures the qualitative shifts in the climate dynamics associated with GIS melting and thus aligns with the broad discussion of climate tipping. In this case, multiple equilibrium volumes may coexist at the same temperature. Specifically, the equilibrium GIS volume is unique when temperature is above 2.54°C or below 0.96°C , but within this range three equilibrium volume levels exist. Among all these equilibrium GIS volumes, two (on the solid curve) are stable, while the third (on the dashed curve) is unstable. A small perturbation of temperature near a stable equilibrium leads the GIS volume to return to its original state. However, a perturbation near the unstable equilibrium induces divergence toward a different stable equilibrium, representing the irreversible characteristic of climate tipping.

Figure 4.1: Equilibrium relationships between temperature and the GIS volume. The left panel shows two reversible equilibrium relationships (linear and nonlinear) between temperature and the GIS volume. The right panel shows the irreversible equilibrium relationship between temperature and the GIS volume in a hysteretic system. When temperature is between 0.96°C and 2.54°C , it corresponds to three equilibria, with two of them stable (on the solid curve) and one unstable (on the dashed curve).

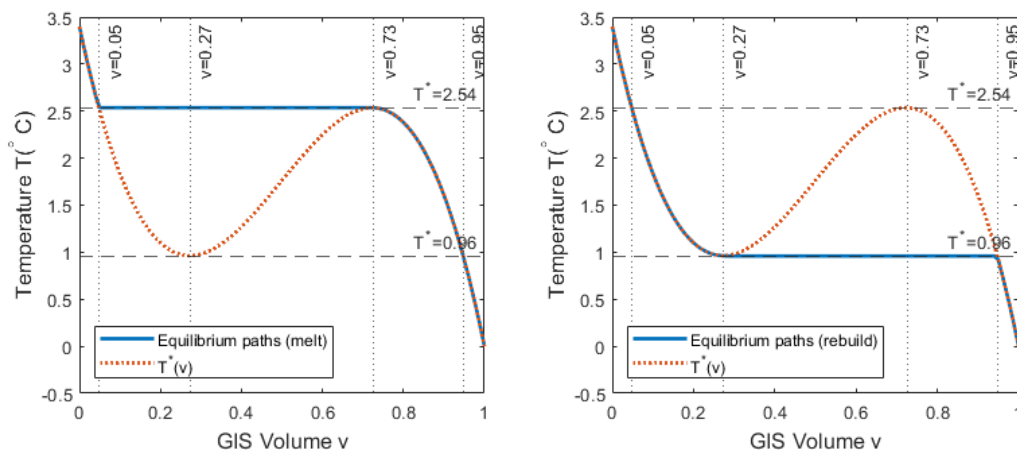


To illustrate the link between hysteretic equilibria and climate tipping, Figure 4.2 shows the equilibrium paths of temperature and ice volume during both melting and rebuilding processes of the GIS. Starting from full volume (100%), the equilibrium GIS volume declines gradually as temperature rises, following the solid curve in the left panel. Before temperature reaches 2.54°C ,

the equilibrium GIS volume declines gradually, leading to gradual melting. However, once the temperature exceeds this threshold, the equilibrium volume collapses abruptly to 5%. This discontinuous shift illustrates the tipping point: the GIS disintegrates rapidly to a near-complete loss of volume beyond 2.54°C .

Similarly, the right panel shows the equilibrium path during the GIS rebuilding. If temperature declines from 3.4°C but remains above 0.96°C , the equilibrium GIS volume will increase gradually from 0% to 27%, which is substantially lower than the 95% volume during the melting process at the same temperature. This indicates that once the tipping point is triggered, temperature must be reduced to a much lower level for the ice sheet to recover. In practice, GIS rebuilding is slow and influenced by other climate factors. Therefore, the actual GIS volume may lag behind the equilibrium level, even if the temperature falls below 0.96°C .

Figure 4.2: Equilibrium paths of temperature and GIS volume during melting and rebuilding processes of the GIS. The left panel illustrates melting under rising temperatures, which is the primary focus of this paper. The right panel depicts rebuilding under declining temperatures, which is less relevant to the subsequent analysis.



Temperature The global mean surface temperature T increases with carbon emissions, as increased atmospheric carbon enhances the greenhouse effect. Economic agents can slow global warming by reducing carbon emissions, though at a cost. The temporal evolution of temperature T depends on both greenhouse gas emissions and emission abatement. Carbon emissions arise from anthropogenic activities and the decay of organic matters in the thawing permafrost. In contrast, GIS melting does not directly contribute additional carbon to the atmosphere.

Let E_t be the anthropogenic carbon emissions at time t , all in the form of CO_2 . As before, we let $E_{PF,t}$ be the total permafrost carbon emissions at t , which can be decomposed into emissions

of CO₂ and CH₄. Specifically, we define

$$\begin{aligned} E_{PF,t}^{CO_2} &:= qE_{PF,t}, \\ E_{PF,t}^{CH_4} &:= (1 - q)E_{PF,t} \end{aligned}$$

where q is the fraction of permafrost carbon emitted as carbon dioxide, and the remaining share $1 - q$ is released as methane.

Carbon dioxide and methane differ substantially in their global warming potential (GWP). The IPCC Sixth Assessment Report (IPCC (2021b)) highlights that the warming impact of one ton of CH₄ is equivalent to that of more than 80 tons of CO₂ over a 20-year horizon, but only 28 to 36 tons of CO₂ over 100 years, reflecting a much shorter atmospheric lifetime of methane. Given the different warming potentials of CO₂ and CH₄, we model their contributions to temperature change separately. Let T^{CO_2} be the temperature increase due to carbon dioxide, and T^{CH_4} be the increase attributable to methane. The global mean surface temperature relative to pre-industrial levels is then given by

$$T = T^{CO_2} + T^{CH_4}.$$

Following Dietz et al. (2021b), we assume that temperature responds linearly to cumulative CO₂ emissions. The temperature dynamics are given by

$$dT_t^{CO_2} = \chi[(1 - u_t)E_t + E_{PF,t}^{CO_2}]dt$$

where χ is the transient climate response to cumulative carbon emissions which measures the sensitivity of temperature to CO₂ emissions, and $u_t \in [0, 1]$ is the abatement rate of anthropogenic emissions. Common abatement measures include improvements in energy efficiency, shifts to renewable energy sources, and adoption of low-carbon technologies. While these measures reduce anthropogenic emissions, they cannot mitigate emissions from thawing permafrost. Given current technological constraints, we assume that CO₂ emissions from permafrost cannot be abated.

Anthropogenic carbon emissions E_t are entirely in the form of CO₂ and are proportional to economic output Y_t . Defining the carbon intensity ψ_t as emissions per unit of output, we have $E_t = \psi_t Y_t$. The time path of ψ_t is calibrated to match the baseline emission scenario in Nordhaus (2017).

To model the warming impact of methane, we use a reduced-form temperature model derived from the Budyko-Ghil-Sellers energy balance model (Budyko (1969)). Radiative forcing increases as atmospheric methane accumulates, thereby accelerating global warming. We use the simplified expression for methane-induced radiative forcing provided by the IPCC (Stocker

(2014)). Let $F_t^{CH_4}$ be the radiative forcing at time t due to atmospheric methane:

$$F_t^{CH_4} = \alpha_{CH_4} \left(\sqrt{M_{CH_4,t}} - \sqrt{\bar{M}_{CH_4}} \right) - (f(M_{CH_4,t}, M_{N_2O}) - f(\bar{M}_{CH_4}, M_{N_2O})) \quad (4.1)$$

where $\alpha_{CH_4} > 0$, \bar{M}_{CH_4} is the atmospheric methane concentration in the pre-industrial period, and $M_{CH_4,t}$ is its level at t relative to \bar{M}_{CH_4} .

The atmospheric methane concentration evolves as

$$dM_{CH_4,t} = \left(E_{PF,t}^{CH_4} \cdot Conv - \delta_{CH_4} M_{CH_4,t} \right) dt$$

where $E_{PF,t}^{CH_4}$ is the carbon from permafrost methane emissions at time t , $Conv$ converts from carbon (in GtC) to methane (in ppb), and δ_{CH_4} is the atmospheric decay rate of methane.

Equation (4.1) further shows that radiative forcing from methane depends not only on methane concentration but also on atmospheric nitrous oxide (N_2O). This is due to the overlap of their infrared absorption bands (Hoover et al. (1967), Byrom and Shine (2022)). We capture this effect through the function f ,

$$f(M_{CH_4}, M_{N_2O}) = 0.47 \log \left(1 + 2.01 \times 10^{-5} (M_{CH_4} M_{N_2O})^{0.75} + 5.31 \times 10^{-15} (M_{CH_4} M_{N_2O})^{1.52} \right)$$

which M_{N_2O} is the baseline atmospheric concentration of nitrous oxide.

The temperature change due to methane emissions is modeled as

$$dT_t^{CH_4} = \frac{1}{\tau_{CH_4}} \left(F_t^{CH_4} - bT_t^{CH_4} \right) dt$$

where τ_{CH_4} is the heat capacity of the Earth's surface, and its inverse measures the sensitivity of temperature to radiative forcing. The parameter $b > 0$ captures the strength of outgoing long-wave radiation, which increases with temperature and thus partially offsets the warming effect of radiative forcing. Since the above expression focuses only on methane, the second term on the right-hand side can be interpreted as the portion of outgoing long-wave radiation specifically counteracting methane-induced warming. We then aggregate the warming effect of both CO_2 and CH_4 to characterize the dynamics of global mean surface temperature:

$$dT_t = dT_t^{CO_2} + dT_t^{CH_4}.$$

The Economy We model a continuous-time stochastic pure exchange economy to derive analytical results while maintaining tractability. The model structure follows Olijslagers et al. (2023). The endowment evolves as a jump-diffusion process subject to long-run growth and

fluctuations, rare economic crises, and climate-related damages:

$$dY_t = \mu Y_t dt + \sigma Y_t dW_t - J Y_t dN_t$$

where μ is the baseline economic growth rate absent GIS tipping. The GIS volume v_t declines with melting, contributing to sea-level rise and associated output losses. The term $\sigma Y_t dW_t$ represents stochastic fluctuations of the endowment, with σ denoting endowment volatility and W_t a standard Brownian motion. The last term, $J Y_t dN_t$, captures the impact of rare economic crises, which is modeled as a Poisson process N_t with constant intensity λ . Each crisis reduces output by a random fraction $J \in (0, 1)$. We characterize the distribution of J by $X := 1 - J$ with density $f(x) = \alpha x^{\alpha-1}$, implying that the expected disaster size is $EJ = \frac{1}{\alpha+1}$. Incorporating rare economic disasters into the endowment dynamics is important, since it yields empirically plausible discount rates for the future (Barro (2009)), which is a key variable in climate economic analysis.

Consumption by representative agents differs from endowment for two main reasons. First, emission abatement entails costs, meaning that part of the endowment will be diverted to mitigation efforts. Second, output is subject to climate damages from both global warming and sea level rise. Global warming reduces agricultural and industrial productivity, generating proportional GDP losses (Nordhaus (1992)). In addition, sea level rise from GIS melting increases flood risk, imposing substantial economic damages, especially in coastal regions.

Let $r_{SLR}(v_t)$ be the percentage loss of economic output due to sea-level rise when the remaining GIS volume is v_t , and $D(T_t, \omega_t) > 0$ be the damage ratio from global warming at temperature T_t , where ω_t captures stochastic variation (discussed in detail in Section 4.3). The remaining endowment Y'_t after accounting for climate damages is then given by

$$Y'_t = \frac{1 - r_{SLR}(v_t)}{1 + D(T_t, \omega_t)} Y_t.$$

In this pure exchange economy, the remaining endowment after accounting for climate damages cannot be stored and must be allocated between emission abatement and consumption. Let $A(u_t)$ be the share of the endowment spent on emission abatement at control rate u_t . Consumption at t is then given by

$$C_t = (1 - A(u_t)) Y'_t = \frac{(1 - A(u_t))(1 - r_{SLR}(v_t))}{1 + D(T_t, \omega_t)} Y_t.$$

The abatement cost $A(u_t)$ increases with u_t and can be viewed as an investment in a greener future. Therefore, agents face a trade-off between lower consumption today to mitigate future climate damages and higher current consumption at the expense of greater climate risks in the long run.

The preference of representative agents is modeled using Stochastic Differential Utility (SDU) (Duffie and Epstein (1992)), which is a continuous-time version of Epstein-Zin preferences. It allows for a separation between the risk aversion parameter γ and the elasticity of intertemporal substitution (EIS) ϵ , generating empirically plausible risk premia by increasing risk aversion without compromising the model's fit to historical financial data. Formally, the value function at time t is defined recursively as

$$V_t = \max_{\{u_s: s \geq t\}} E_t \int_t^\infty f(C_s, V_s) ds \quad (4.2)$$

with

$$f(C, V) = \frac{\beta}{1 - \frac{1}{\epsilon}} \frac{C^{1 - \frac{1}{\epsilon}} - [(1 - \gamma)V]^{\frac{1}{\zeta}}}{[(1 - \gamma)V]^{\frac{1}{\zeta} - 1}}$$

where $\epsilon \neq 1$, $\zeta = \frac{1 - \gamma}{1 - \frac{1}{\epsilon}}$, and β is the time discount rate.

Social Cost of Carbon (SCC) The SCC measures the monetary value of the marginal welfare loss from an additional unit of carbon emission. In other words, it is the present value of the economic damages caused by a marginal increase in carbon emissions today. Formally, the SCC at time t is given by

$$SCC_t = \frac{-\chi \cdot dV_t/dT_t}{f_C(C_t, V_t)} \quad (4.3)$$

where $f_C(C_t, V_t)$ is the marginal utility of consumption. The numerator in Equation (4.3) captures the marginal utility loss associated with an incremental carbon emission, and the denominator scales this loss in units of consumption goods. Appendix 4.A provides further details on the numerical computation of the SCC.

4.3 Calibration

In this section, we present the parameter values used in the integrated assessment model for both the climate and economic blocks. A comprehensive summary of all parameters is provided in Appendix 4.B.

The Climate Model The model simulations begin in 2023, when the annual global mean surface temperature is approximately $T_0 = 1^\circ\text{C}$ above the pre-industrial level and is expected to rise with cumulative carbon emissions. For simplicity, we attribute this 1°C increase entirely to anthropogenic carbon dioxide, i.e., $T_0^{CO_2} = 1^\circ\text{C}$ and $T_0^{CH_4} = 0^\circ\text{C}$. The transient climate response

to cumulative carbon emissions from CO₂ is set at $\chi = 0.0018^\circ\text{C}$ per gigatonne of carbon (GtC), following Van den Bremer and Van der Ploeg (2021).

To quantify the warming impact of CH₄, we set the radiative forcing parameter to $\alpha_{CH_4} = 0.036$, following Dietz et al. (2021a). The atmospheric methane concentration was $\bar{M}_{CH_4} = 722$ ppb in pre-industrial times, and 1920 ppb in 2023. Therefore, the initial methane concentration relative to pre-industrial levels is given by $M_{CH_4,0} = 1920 - \bar{M}_{CH_4} = 1198$ ppb. The atmospheric nitrous oxide concentration in 2023 is $M_{N_2O} = 337$ ppb. These greenhouse gas concentrations are obtained from the US National Oceanic and Atmospheric Administration (NOAA) Global Monitoring Laboratory¹.

The atmospheric lifetime of methane is approximately 12.4 years (IPCC (2007)), which corresponds to a decay rate of $\delta_{CH_4} \approx 8\%$. For the Earth's surface heat capacity, we use $\tau_{CH_4} = 7.35$ as in Dietz et al. (2021a). The parameter b is calibrated to 0.5 so that methane emissions contribute an additional 0.64°C of warming in the BAU scenario by 2300, consistent with the temperature projections in Kessler (2017).

To quantify anthropogenic carbon emissions, we assume that the carbon emission intensity ψ_t declines over time as renewable energy use increases and production processes become more efficient. Formally, the evolution of ψ_t is given by

$$d\psi_t = -\delta_t\psi_t dt$$

where the time-varying decline rate δ_t evolves according to

$$d(\delta_t - \delta_\infty) = -\alpha_\psi(\delta_t - \delta_\infty)dt,$$

or equivalently,

$$\delta_t = \delta_\infty + e^{-\alpha_\psi t}(\delta_0 - \delta_\infty)$$

with $\alpha_\psi > 0$, initial value δ_0 , and long-run value δ_∞ .

Under this specification, the carbon intensity ψ_t initially declines at a rate smaller than the economic growth rate, so the near-term emissions rise with endowment growth. In the long run, ψ_t declines at a rate δ_∞ that exceeds the economic growth, which results in a gradual reduction in carbon emissions that eventually converges to zero. We set $\delta_0 = -0.5\%$, $\delta_\infty = -6.5\%$, and $\alpha_\psi = 0.25\%$ so that the projected carbon emissions matches the baseline emission scenario in Nordhaus (2017).

The parameter values for thawing permafrost are based on Kessler (2017). The coefficient β_{PF} , which represents the sensitivity of permafrost area to temperature increases, is estimated at 0.172 using pooled ordinary least squares (OLS) on existing projections of future permafrost

¹See <https://gml.noaa.gov/ccgg/>

thaw. The total permafrost carbon stock is set at $\bar{C}_{PF} = 1035$ GtC. The proportion of carbon in the passive (or stable) pool remains constant at $p = 0.4$, while the remaining 60% in the unstable pool will be eventually released. Of the carbon released from thawed permafrost, $q = 98\%$ is emitted as CO₂ and $1 - q = 2\%$ as CH₄. The decay rate of carbon from thawed permafrost is set as $\tau = 70$ years.

Only anthropogenic carbon emissions can be abated. The abatement cost function is

$$A_t = c_{1,t} u_t^{c_2}$$

where $c_{1,t}$ reflects the impact of technological progress on abatement costs and declines over time, $c_2 > 1$ characterizes the increasing marginal cost associated with emission control rate u_t (Nordhaus (2017)). The time-varying coefficient $c_{1,t}$ is given by

$$c_{1,t} = 0.074 e^{-0.019t}$$

which reflects lower abatement costs in the future due to improved technology. The convexity parameter of abatement costs, c_2 , is set to 2.6.

Following Nordhaus (2019) and Dietz et al. (2021a), we set the coefficient of ice melting speed at $\beta_{GIS} = -0.0000106$. We use the specification from Nordhaus (2019) to describe the three types of equilibria between temperature and GIS volume. For the hysteretic equilibrium, we assume a cubic functional form:

$$T^*(v_t) = -34.5833v_t^3 + 51.625v_t^2 - 20.4417v_t + 3.4.$$

where $v_t \in [0, 1]$ represents the remaining percentage of ice sheet volume relative to the pre-industrial period. In a reversible system, we consider both linear and non-linear relationships between temperature and GIS volume. In the linear case,

$$T^*(v_t) = 3.4(1 - v_t)$$

which implies that the GIS volume decreases proportionally as temperature rises. During the pre-industrial period, the ice volume $v = 1$ and the corresponding equilibrium temperature is 0°C. As temperature rises to 3.4°C, the GIS melts completely in equilibrium. In the nonlinear reversible case,

$$T^*(v_t) = 3.4(1 - v_t)^{0.5}$$

where the equilibrium temperature increases more rapidly during the early phase of ice melting, capturing the higher sensitivity of the ice sheet to initial temperature rises.

The Economic Model The initial endowment level is set at 105 trillion US dollars, which corresponds to the global GDP in 2023. Following the OECD Economic Outlook (OECD (2023)), we assume an endowment growth rate of $\mu = 3.0\%$ and endowment volatility $\sigma = 2.5\%$.

Economic disasters N are modeled as a Poisson process with a rate of 0.035, and the disaster size J follows a Pareto distribution with parameter $\alpha = 10.5$ (Barro and Jin (2011)). Based on these disaster parameters, the risk aversion parameter is approximately $\gamma = 4$ to match the observed market risk premia. With this risk aversion, we set the elasticity of intertemporal substitution to $\epsilon = 1.5$ and the time discount rate to $\beta = 0.025$, to provide a reasonable approximation of the historical global average risk-free rate and equity risk premium from 1900 to 2010 (Dimson et al. (2011)).

Climate change affects the economy through two main channels. First, rising temperature reduces capital stock and labor productivity. This direct damage is proportional to GDP and is modeled using the damage function D as in Van den Bremer and Van der Ploeg (2021):

$$D_t = T_t^{1+\theta_T} \omega_t^{1+\theta_\omega}$$

where T_t is the global mean surface temperature and ω_t is a stochastic factor capturing the sensitivity of climate damages to temperature. The parameters θ_T and θ_ω represent the convexity of temperature effects and the skewness of the stochastic damage factor, respectively. The stochastic term ω_t evolves according to a mean-reverting process:

$$d\omega_t = \nu(\bar{\omega} - \omega_t)dt + \sigma_t^{(\omega)} dW_t^{(\omega)},$$

where $\bar{\omega}$ is the long-run mean and ν is the mean-reversion rate. The volatility $\sigma_t^{(\omega)}$ declines over time as uncertainty about climate damages resolves:

$$\sigma_t^{(\omega)} = \max\left(\left(1 - \frac{t}{\bar{t}}\right) \sigma_0^{(\omega)}, 0\right).$$

Here, $\sigma_0^{(\omega)}$ is the initial volatility at time $t = 0$, and \bar{t} is the time horizon over which uncertainty gradually disappears. To ensure that ω_t is non-negative, we impose a lower bound of 0 for ω_t in numerical simulations.

The second channel of climate damage arises from sea-level rise caused by the melting of the GIS. To calibrate the economic impact of sea-level rise, we follow Nordhaus (2019) which estimates that a one-meter rise in sea level leads to a 1% reduction in annual global output, with economic losses assumed to be linear in sea-level rise. Given that the total volume of the GIS is 2.85 million km³ and that the GIS loss of 280 km³ over the past two decades has contributed 0.7 mm to sea-level rise, we infer that a 1% reduction in GIS volume results in an annual global output of 0.0713%. This aligns with Nordhaus (2019) which estimates that the

complete disintegration of the GIS would reduce annual global output by approximately 7%. Accordingly, the output loss in year t due to sea-level rise is given by

$$r_{SLR,t} = r_{SLR}(v_t) = 0.000713(100v_0 - 100v_t) = 0.0713(v_0 - v_t)$$

where v_0 is the GIS volume in the pre-industrial period, v_t is the GIS volume at time t , and the economic output loss increases linearly with the percentage reduction in GIS volume.

4.4 Numerical Results

We numerically solve the integrated assessment model in Section 4.2 using the stochastic grid method (Jain and Oosterlee (2012), Olijslagers (2021)). To examine the impact of climate tipping points and their interactions on climate and economic policies, we compare the simulation results under different assumptions regarding climate tipping. Furthermore, we analyze the outcomes under two different policy scenarios: one without any emission abatement and the other with optimal emission abatement.

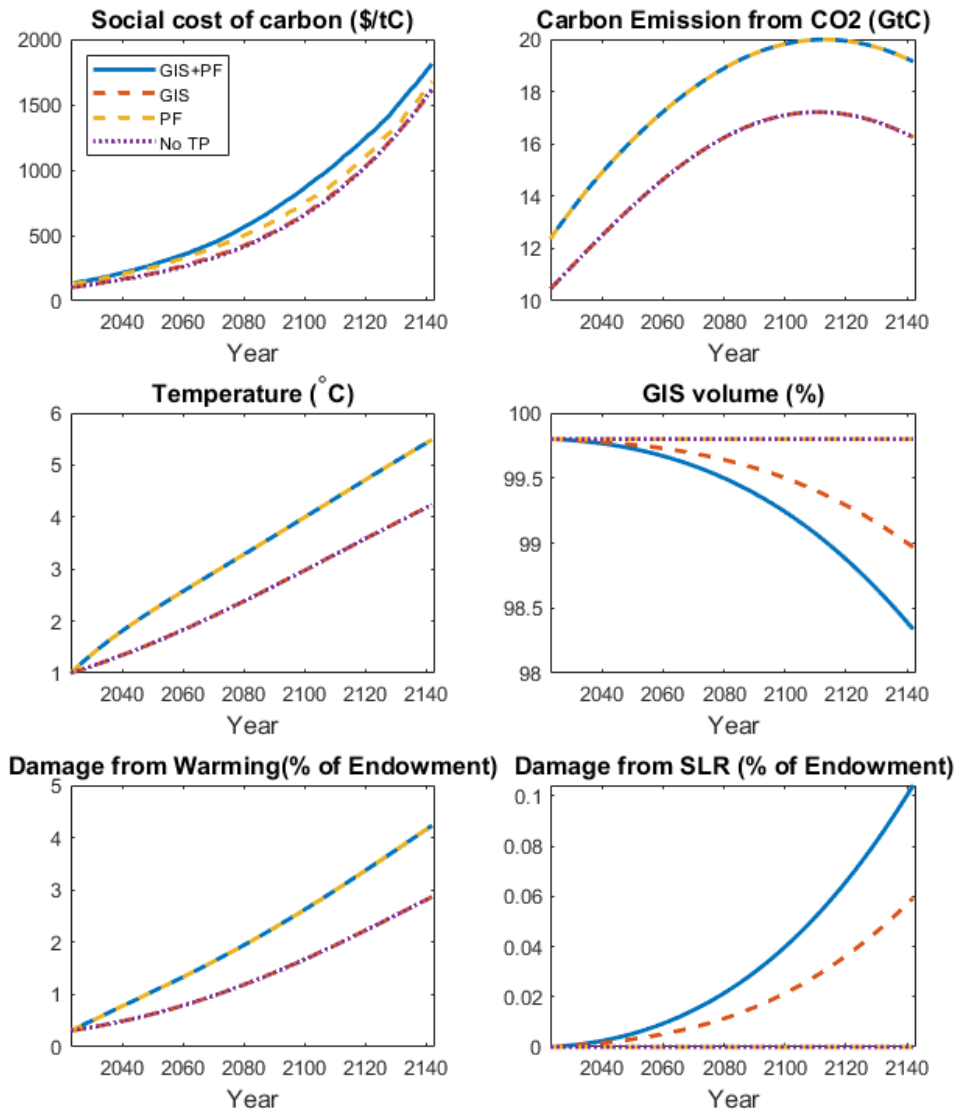
4.4.1 The Business-As-Usual scenario

We begin by presenting numerical results that illustrate the effects of climate tipping points on the SCC, as well as on key climate and economic variables over the next century. Figure 4.3 shows the trajectories of the SCC, annual carbon emissions from CO₂, global mean surface temperature, the remaining GIS volume, and climate damages from both temperature increases and sea-level rise in the BAU scenario, spanning from 2023 to the mid-22nd century. We examine four climate tipping scenarios: (i) Both GIS melting and permafrost thawing (GIS+PF); (ii) GIS melting only (GIS); (iii) Permafrost thawing only (PF); and (iv) A baseline scenario with no tipping points considered (No TP).

We first examine how climate tipping affects the projections of key climate variables. In terms of carbon emissions, we find that annual CO₂ emissions across all tipping scenarios initially increase over time, peaking in the early 22nd century, and then begin to decline. This decline is mainly driven by reductions in anthropogenic emissions as production processes become greener and more energy-efficient over time. Since the melting of the GIS does not directly influence the carbon cycle, the projections of carbon emissions and temperature are identical in scenarios (i) and (iii), as well as in scenarios (ii) and (iv). Differences in total emission paths arise solely from permafrost carbon emissions.

Compared with the baseline scenario in which no tipping points are considered, thawing permafrost releases approximately 2 gigatons of carbon annually since the early 21st century, mainly in the form of carbon dioxide. As global temperatures continue to rise, additional

Figure 4.3: The trajectories of the SCC, annual carbon emissions from CO₂, temperature, remaining GIS volume, and annual climate damage (as a percentage of global annual GDP) from both warming and sea-level rise (SLR) over the next century in the BAU scenario.



permafrost thaws, causing carbon emissions from permafrost to increase over time. These additional emissions from thawing permafrost constitute a significant share of total annual carbon emissions, and consequently accelerate global warming. By 2100, the temperature in both the baseline and GIS-only scenarios is projected to reach 3°C. When permafrost thawing is incorporated, the additional carbon emissions are expected to increase the temperature by approximately 0.3°C, as reflected in the temperature trajectories for scenarios that include permafrost carbon release.

The volume of the GIS remains constant over time in both the baseline and the permafrost-thawing-only scenarios. However, when the melting GIS is considered, its volume declines more rapidly if permafrost carbon emissions are included. The accelerated decline is driven by additional carbon emissions from thawing permafrost, which raise temperatures and in turn enhance ice melt. The gap in GIS volume between the GIS+PF scenario (solid blue line) and the GIS-only scenario (red dashed line) widens over time, from 0.03% in 2050 to 0.26% in 2100. In both scenarios involving the GIS, the rate of melting increases over time, even though temperature increases approximately linearly. This underscores the nonlinear nature of climate tipping: as temperatures continue to rise over the coming centuries, the rate of ice loss is expected to accelerate further. Once a critical temperature threshold is exceeded, a qualitative shift occurs in the GIS dynamics, which marks a tipping point and can ultimately lead to the complete disintegration of the GIS.

The annual endowment remains relatively stable across all tipping scenarios, since production technology is not directly affected by climate conditions. However, incorporating tipping points into economic analyses leads to significantly different projections of climate-induced economic losses, and therefore affect the predictions of future consumption. The bottom two panels of Figure 4.3 show that damages from both global warming and sea-level rise increase over time. Rising temperature amplify the frequency and intensity of extreme weather events, which threatens economic growth and human health, and thereby causing larger GDP losses. Furthermore, the nonlinear acceleration of ice melting with higher temperatures explains the convexity of damages associated with sea-level rise.

Table 4.1 summarizes climate damages across the four tipping scenarios. In the baseline and permafrost-thawing-only cases, climate damages arise solely from higher temperatures, and therefore increase steadily over time with global warming. Without tipping points, climate change is projected to reduce global GDP by 0.63% in 2050 and 1.67% in 2100. Incorporating permafrost thawing raises these losses to 1.06% and 2.62%, respectively.

Melting of the GIS amplifies climate damages primarily through the additional flooding risk associated with sea-level rise. In the GIS-only scenario, total climate damages are projected to reach 1.69% of annual global GDP in 2100, which is just 0.02% higher than in the no-tipping scenario. This additional damage in the GIS-only case is entirely attributed to sea-level rise, since warming-induced damages are identical in both scenarios. A similar pattern holds when comparing the PF-only and GIS+PF scenarios, but total economic losses are higher in the GIS+PF scenario because sea-level rise contributes an additional 0.04% of global GDP loss by 2100.

The SCC rises over time in all tipping scenarios, reflecting the increasing economic damages associated with global warming. Moreover, higher climate tipping risk substantially raises both current and future SCC estimates. Intuitively, climate tipping elements accelerate warming

Table 4.1: SCC (USD per ton of carbon, or \$/tC) and annual climate damages (percentage of global GDP) from rising temperatures and sea-level rise in 2025, 2050 and 2100 in the BAU scenario. Damages from temperature increases (*T*) and sea-level rise (*SLR*) are reported separately.

Tipping	Year	Business as usual			
		SCC (\$/tC)	Damage (<i>T</i>)	Damage (<i>SLR</i>)	Total climate damage
No tipping	2025	108	0.33%	0	0.33%
	2050	207	0.63%	0	0.63%
	2100	656	1.67%	0	1.67%
GIS only	2025	109	0.33%	0.0001%	0.33%
	2050	210	0.63%	0.0031%	0.63%
	2100	664	1.67%	0.0214%	1.69%
PF only	2025	132	0.36%	0	0.36%
	2050	256	1.06%	0	1.06%
	2100	747	2.62%	0	2.62%
GIS+PF	2025	141	0.36%	0.0001%	0.36%
	2050	276	1.06%	0.0053%	1.11%
	2100	861	2.62%	0.0399%	2.66%

and introduce additional sources of damage such as sea-level rise, thereby corresponding to higher carbon prices. As shown in Table 4.1, accounting for GIS tipping increases the SCC only slightly, from \$108 to \$109 per ton of carbon in 2025, and from \$656 to \$664 in 2100. In contrast, permafrost thawing has a more pronounced effect, which increases the SCC by 22% in 2025 and 24% in 2100. When both tipping points are incorporated, the SCC is the highest of all tipping scenarios, since permafrost carbon feedback accelerates GIS melting and amplifies climate damages. These differences highlight that capturing the dynamics of individual climate subsystems is crucial for accurate economic assessment, and modeling climate tipping as an abrupt system-wide shift is insufficient.

4.4.2 Optimal Abatement

We now illustrate how the risk of climate tipping influences the SCC, optimal abatement strategies, and the projections of key economic and climate variables over the next century. By simulating future climate and economic dynamics under the same tipping scenarios as in the BAU case, we emphasize the importance of emission abatement in mitigating climate damages in the long term. The corresponding numerical results are shown in Figure 4.4 and Table 4.2.

Comparing Figure 4.3 and Figure 4.4, we find that emission abatement substantially reduces future temperature increases, climate damages, and the rate of GIS melting. The optimal abatement rate rises over time and differs across tipping scenarios. Both permafrost thawing and GIS melting increase the optimal abatement rate, since tipping elements introduce irreversible

shifts to the climate system. Consequently, more stringent emission controls are required to mitigate tipping risks. Consistent with this rationale, the most stringent abatement occurs when both tipping elements are considered jointly (GIS+PF).

Accounting for thawing permafrost substantially increases the stringency of abatement policies, while the impact of GIS melting on the optimal abatement rate is relatively small. This difference arises because GIS dynamics do not directly affect the carbon cycle, and their economic impacts remain relatively limited in the coming centuries. In contrast, additional carbon emissions from permafrost accounts for a significant share of total annual emissions and cannot be effectively abated. These extra carbon emissions accumulate in the atmosphere, effectively shrinking the carbon budget available for anthropogenic activities. As a result, abatement efforts must be more stringent to offset part of this effect. As shown in Table 4.2, incorporating the impact of thawing permafrost raises the optimal abatement rate by 8.4% in 2025 and 15% in 2100, while accounting for GIS alone increases the optimal abatement rate by only 0.5% in 2025 and 0.4% in 2100. Comparing the third and last rows in Table 4.2, we observe that the effect of GIS melting is amplified when combining with thawing permafrost, raising the abatement rate by 2.2% in 2025 and 4.7% in 2100. This highlights that interactions among multiple tipping points can materially alter policy implications, underscoring the need to explicitly account for such interactions in economic analyses.

Table 4.2: SCC (USD per ton of carbon, or \$/tC), annual climate damages (as a percentage of global annual GDP) from rising temperature and sea-level rise, and the optimal abatement rates in 2025, 2050 and 2100 in the optimal abatement scenario. Damages from temperature increases (T) and sea-level rise (SLR) are reported separately.

Tipping	Year	Optimal abatement				
		SCC	Damage (T)	Damage (SLR)	Total climate damage	Abatement
No tipping	2025	18	0.33%	0	0.33%	5.5%
	2050	115	0.59%	0	0.59%	20.3%
	2100	507	1.12%	0	1.12%	65.9%
GIS only	2025	20	0.33%	0.0001%	0.33%	6.0%
	2050	113	0.59%	0.0030%	0.60%	21.0%
	2100	511	1.13%	0.0163%	1.15%	66.3%
PF only	2025	82	0.36%	0	0.36%	13.9%
	2050	181	0.96%	0	0.97%	27.4%
	2100	696	1.73%	0	1.79%	80.0%
GIS+PF	2025	104	0.36%	0.0001%	0.36%	16.1%
	2050	239	0.96%	0.0049%	0.97%	32.7%
	2100	706	1.74%	0.0296%	1.77%	80.0%

The annual carbon emissions are substantially reduced under optimal abatement policies in all tipping scenarios. Compared with the BAU scenario, emissions rise more slowly in the coming

decades and are expected to decline to zero over the next centuries. In the absence of permafrost thaw, annual carbon emissions are lower in the coming decades despite less stringent abatement requirements. In contrast, when thawing permafrost is accounted for, the additional carbon emissions from permafrost cannot be abated, which necessitates stricter emission controls to offset its effects. By 2100, total CO₂ emissions are projected to converge to roughly the same level across all scenarios. However, because permafrost thaw continues to release carbon into the atmosphere independently of abatement policy, total carbon emissions do not fully decline to zero even at 100% abatement. Nevertheless, stringent abatement measures remain effective in slowing global warming, and thus weakens the intensity of the permafrost carbon feedback, leading to gradually lower permafrost-related emissions in the coming centuries.

As in the BAU scenario, temperature increases approximately linearly with cumulative carbon emissions. However, under optimal abatement policies, lower emissions lead to a slower rise in temperature across all tipping scenarios. Although anthropogenic CO₂ emissions are similar across scenarios, accounting for thawing permafrost generates a clear divergence in temperature trajectories, mainly due to the additional warming effect of permafrost methane. By 2100, methane released from thawed permafrost is projected to contribute roughly 0.7°C of additional warming.

In the absence of permafrost carbon emissions, temperatures rise more gradually and stabilize once anthropogenic emissions decline to zero. By the end of the century, global temperature is expected to reach about 2.3°C in both the baseline and GIS-only scenarios, compared to nearly 3°C in the other two scenarios that incorporate permafrost thawing. Since permafrost carbon emissions cannot be abated, temperature in the PF and the GIS+PF scenarios continues to rise even if anthropogenic emissions are fully abated, although at a lower pace.

For tipping scenarios that include GIS melting, the projected decline in ice sheet volume is about 0.2% by 2100, which is only half of the reduction estimated in the BAU scenario. This highlights the important role of mitigation in slowing down nonlinear ice sheet responses to warming.

Comparing climate damages in the BAU (Table 4.1) and optimal abatement scenarios (Table 4.2), we find that emission abatement substantially reduces projected economic losses from climate change across all tipping scenarios. In the absence of tipping points, damages fall from 1.67% of global GDP in 2100 under BAU to 1.12% with optimal abatement. In the permafrost-only scenario, damages decline from 2.62% to 1.79%, while in the GIS-only case they fall from 1.69% to 1.15%. When both tipping elements are present, damages are reduced from 2.66% to 1.77%. These results highlight the effectiveness of emission abatement in mitigating climate damages through both the temperature and sea-level rise channels.

The SCC is projected to rise over time following economic growth and more severe climate conditions. Incorporating tipping points further increases SCC estimates, since passing climate

tipping points can trigger more severe and irreversible climate damages. However, optimal emission abatement slows global warming, leading to substantially lower SCC estimates compared to the BAU scenario. A comparison of Table 4.1 and Table 4.2 shows that without tipping risks, the SCC in 2100 would be 23% lower under optimal abatement than in the BAU scenario. When both GIS and permafrost thawing risks are considered, the SCC in the optimal abatement scenario is 18% lower than in the BAU scenario by 2100. Similarly, SCC in 2100 decreases by 23% in the GIS-only scenario and 7% in the permafrost-only scenario.

The impact of emission abatement on the SCC is more pronounced in the presence of GIS melting than with thawing permafrost. This is because GIS melting increases the SCC mainly through rising sea levels. Since carbon emissions directly affect warming and thus the rate of ice melting, abatement is effective in limiting temperature rise and reducing sea-level-related damages. However, abatement measures cannot mitigate the additional emissions from thawing permafrost, so its impact on the SCC is relatively weaker. Overall, although climate damages are expected to grow over time even under optimal emission control, abatement policies remain effective in mitigating future climate damages. Nevertheless, given the varying effectiveness of abatement across different tipping scenarios, additional policy measures are essential to address the escalating risks associated with climate tipping.

In summary, our results highlight that accounting for climate tipping elements and their interactions is crucial in economic analyses. Ignoring the risks associated with climate tipping points can lead to a substantial underestimation of the SCC and the mitigation efforts required today to prevent severe long-term damages to society.

4.4.3 The Warming Effect of Permafrost Methane

Although methane constitutes only about 2% of total permafrost carbon emissions, its warming potential far exceeds that of carbon dioxide. In this subsection, we quantify the impact of permafrost methane on future projections of climate and economic variables, as well as the SCC, across different tipping scenarios. In particular, we focus on scenarios that include thawing permafrost, namely, the PF and GIS+PF scenarios, under the assumption of no emission abatement policies.

Figure 4.5 shows the simulation results from 2023 to 2123 across four scenarios: (i) Both tipping points (GIS melting and permafrost thawing) are considered, with permafrost carbon emitted as both CO₂ and CH₄; (ii) Both tipping points are considered, with permafrost carbon emitted only as CO₂; (iii) Thawing permafrost is the only tipping element, with permafrost carbon emitted as both CO₂ and CH₄; and (iv) Thawing permafrost is the only tipping element, with permafrost carbon emitted only as CO₂. In scenarios (ii) and (iv), we account only for 98% of permafrost carbon emissions in the form of CO₂ and ignore the remaining 2% methane.

Therefore, any differences in the trajectories across scenarios are solely from the presence of permafrost methane.

Since the melting of the GIS does not directly affect global temperature, the warming effect of permafrost methane is independent of the state of the GIS. Consequently, the economic damages from rising temperature are unaffected by GIS conditions. Temperature projections can be substantially underestimated if permafrost methane is ignored. As shown in Figure 4.5, permafrost methane contributes nearly 0.7°C to global warming by 2100.

As methane accumulates in the atmosphere, radiative forcing increases, which accelerates temperature rise. Higher temperatures enhance the thawing process of permafrost, and as a result amplifies the permafrost carbon feedback effect, leading to more emissions of both methane and carbon dioxide. The divergence in CO_2 emission trajectories reflects this feedback, with additional permafrost carbon dioxide emissions amounting to 0.65 GtC in 2050 and 0.5 GtC in 2100. The direct damages from warming, as measured by the Nordhaus-type damage function, increase from 1.67% to 2.21% of global GDP in 2100 after accounting for permafrost methane emissions.

The melting of the GIS is projected to accelerate in the coming decades when the warming effect of permafrost methane is considered. By the end of this century, the additional warming from permafrost methane increases the cumulative GIS loss by roughly 30%, rising from 0.35% to 0.56% of the total GIS volume. Since damages from sea-level rise are assumed to increase linearly with GIS volume losses, accounting for permafrost methane translates directly into a proportional increase in GDP losses associated with rising sea levels.

From this analysis, we conclude that permafrost methane can substantially change the projections of future economic and climate outcomes, although it accounts for only 2% of total permafrost carbon emissions. Due to its significantly higher warming potential compared to carbon dioxide and its shorter atmospheric lifetime, the greenhouse effect of methane evolves differently from that of CO_2 . Therefore, it is important to distinguish between these gases in economic analyses and climate modeling.

4.4.4 The Tipping of GIS Under Different Equilibria

As discussed in Section 4.2, there are multiple approaches for modeling the dynamics of the GIS, and considerable uncertainty exists regarding which one best captures its actual evolution. The simplest model assumes that the GIS system is entirely reversible, so that the GIS volume declines as temperature rises and regains as temperature falls. In this case, the equilibrium relationship between GIS volume and temperature can be either linear or non-linear, as shown in the left panel of Figure 4.1. A more realistic approach accounts for multiple equilibrium states of temperature and GIS volume, as shown in the right panel of Figure 4.1. In this model, once

temperature exceeds a critical threshold, even a small perturbation in temperature can trigger a qualitatively different long-run equilibrium for both temperature and GIS volume, reflecting a tipping point within the GIS system. In this section, we investigate how different equilibrium specifications for temperature and GIS volume affect projections of the SCC, temperature, and associated climate damages to GDP.

We first examine scenarios where the melting GIS is the only tipping element. Figure 4.6 shows the SCC, temperature, the remaining GIS volume, and annual climate damages over the next 150 years under different equilibrium relationships for the GIS. The differences across these scenarios are minimal, which implies that the choice of GIS dynamics has a negligible effect on near-term climate conditions and economic output. This outcome arises because GIS melting does not directly affect global warming. Therefore, projections of future temperature and the associated climate damages remain the same across all equilibrium models.

The remaining GIS volume deviates only slightly across different GIS dynamics. This is primarily due to two reasons. First, the equilibrium temperature T^* is estimated using the same set of climate data across all GIS dynamics, so the resulting projections in the short term are nearly identical. Second, our analysis focuses on a 100-year horizon, which is short compared to the timescale required for complete GIS disintegration that is estimated to span centuries to millennia (Armstrong McKay et al. (2022)).

Although temperatures are projected to exceed the tipping threshold of 2.54°C by 2100 (Figure 4.1), the GIS will undergo a gradual melting process instead of an abrupt change in volume. This is because both the actual temperature T and the equilibrium temperature T^* increase gradually over time, resulting in a correspondingly gradual decline in GIS volume.

This finding contrasts with much of the existing economic literature, which climate tipping is often modeled as an abrupt transition. By explicitly modeling the dynamics of climate tipping elements, we show that the effects of climate tipping manifest only gradually over time. Although qualitative shifts in the climate system occur relatively quickly on a geological timescale, they unfold over a protracted duration from a human perspective.

We observe similar results when considering both tipping points. Specifically, incorporating the impacts of thawing permafrost does not substantially change future projections across different GIS dynamics. Figure 4.7 shows the SCC, temperature, remaining GIS volume, and annual climate damage over the coming 150 years when both GIS melting and permafrost thawing are considered. As before, altering the equilibrium relationship between GIS volume and temperature yields minimal differences in the estimated SCC and future climate variables.

Thawing permafrost contributes roughly an additional 1°C to the temperature by 2150 and slightly reduces GIS volume, but its impact on climate and economic conditions remains relatively modest within a short time horizon. Although temperatures are projected to exceed the threshold for GIS tipping by 2100 in the hysteretic case, the consequence of tipping are not

immediately reflected in the climate and economic states. Nevertheless, a qualitative change in the climate system occurs after crossing the temperature threshold, and the negative impacts of tipping are expected to manifest gradually over centuries or millennia.

Figure 4.4: Projections of the SCC (USD per ton of carbon), optimal abatement rates, total carbon emissions, global mean surface temperature, the remaining GIS volume, and annual climate damages (as a percentage of global GDP) from both warming and sea-level rise (SLR) over the next century under optimal emission abatement policy.

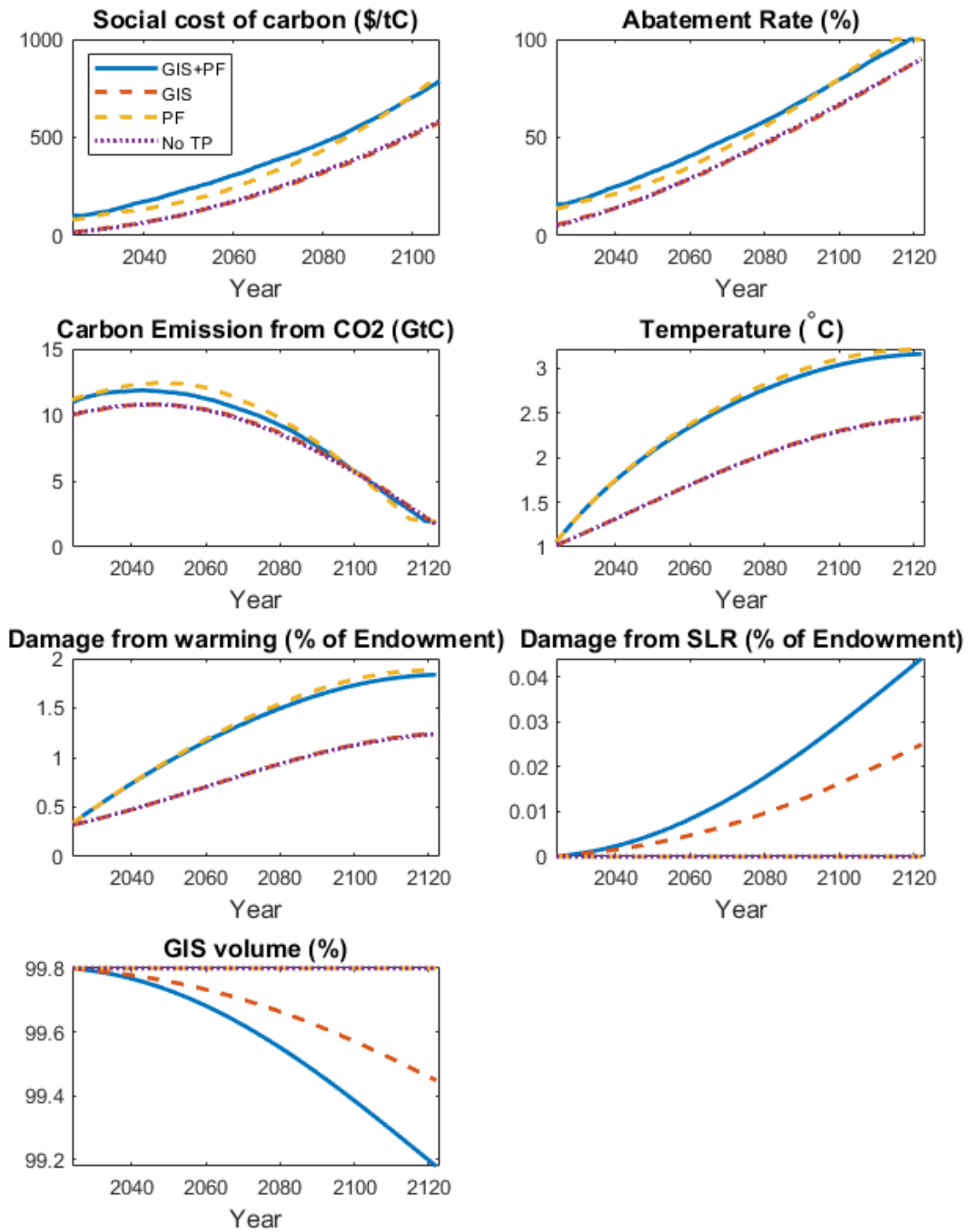


Figure 4.5: Time paths of the SCC, carbon emissions from CO₂, temperature, remaining GIS volume, and climate damage from both warming and sea-level rise (SLR) in the next 100 years with and without considering permafrost methane. Four scenarios: (i) Both tipping points (GIS melting and permafrost thawing) are considered, with permafrost carbon emitted in the forms of CO₂ and CH₄; (ii) Both tipping points are considered, with permafrost carbon emitted only in the form of CO₂; (iii) Thawing permafrost is the only tipping element, with permafrost carbon emitted in the forms of CO₂ and CH₄; and (iv) Thawing permafrost is the only tipping element, with permafrost carbon emitted only in the form of CO₂.

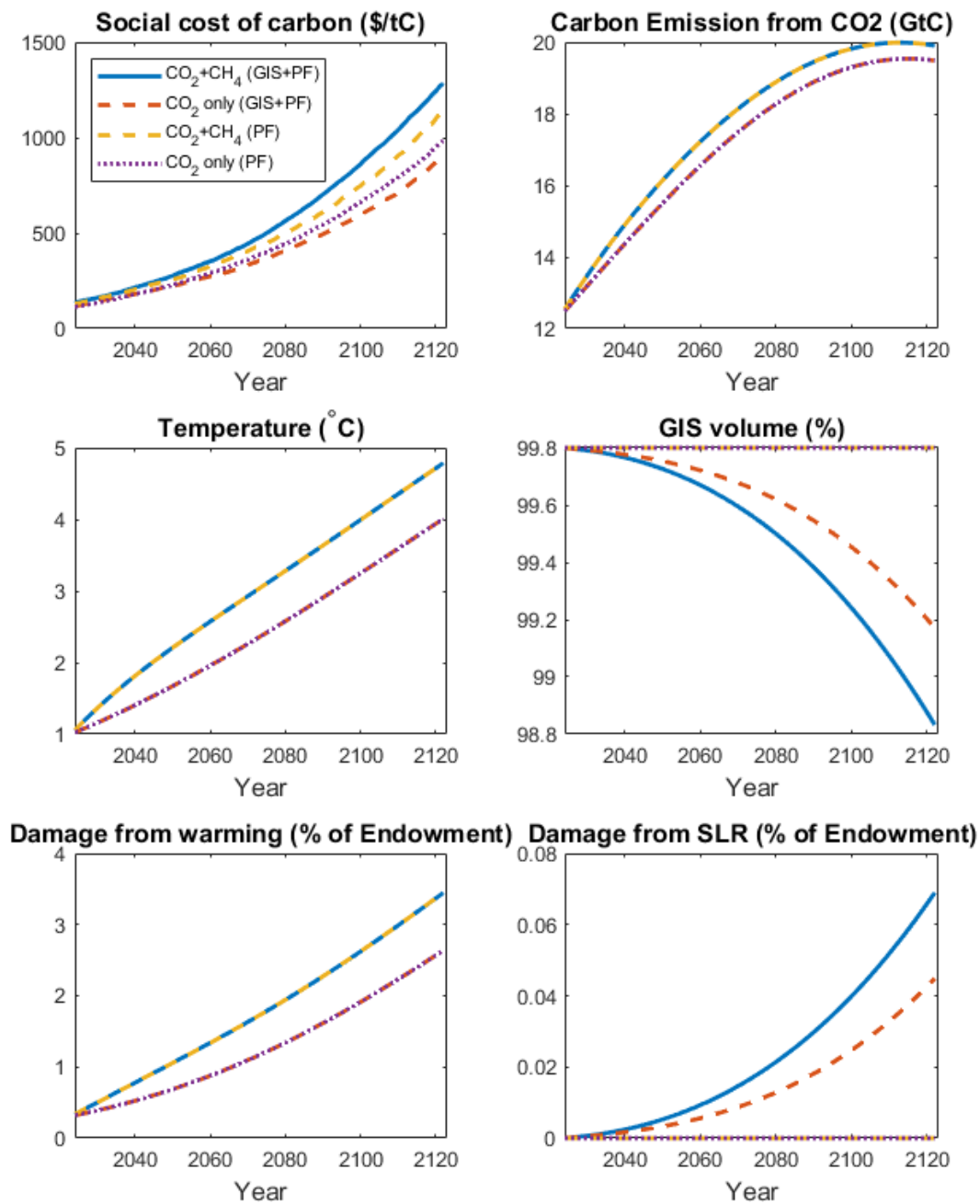


Figure 4.6: The SCC, temperature, the remaining GIS volume, and annual climate damages over the coming 150 years when the melting GIS is the only tipping point. Three types of GIS equilibria are considered: hysteretic (irreversible), linear (reversible) and nonlinear (reversible).

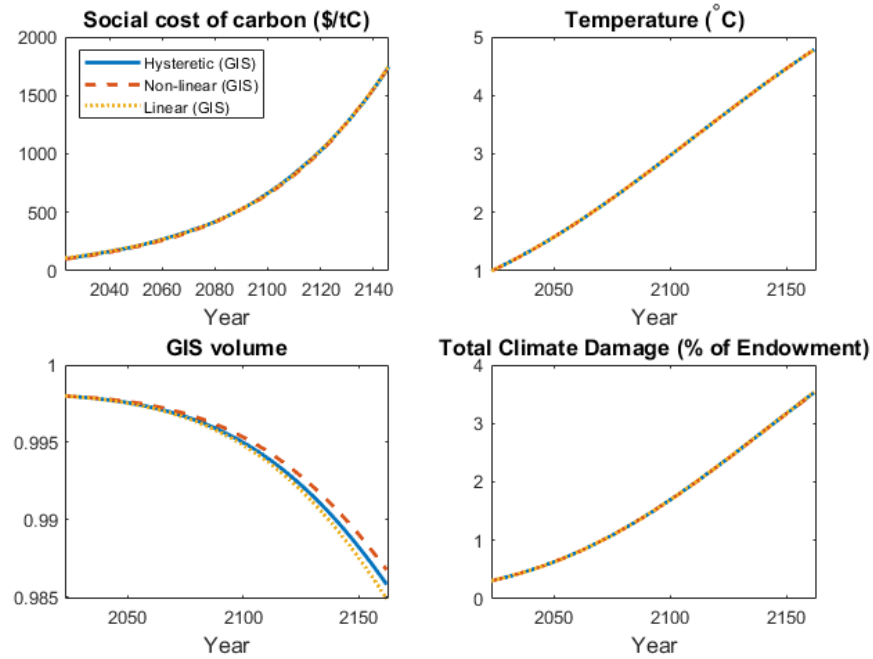
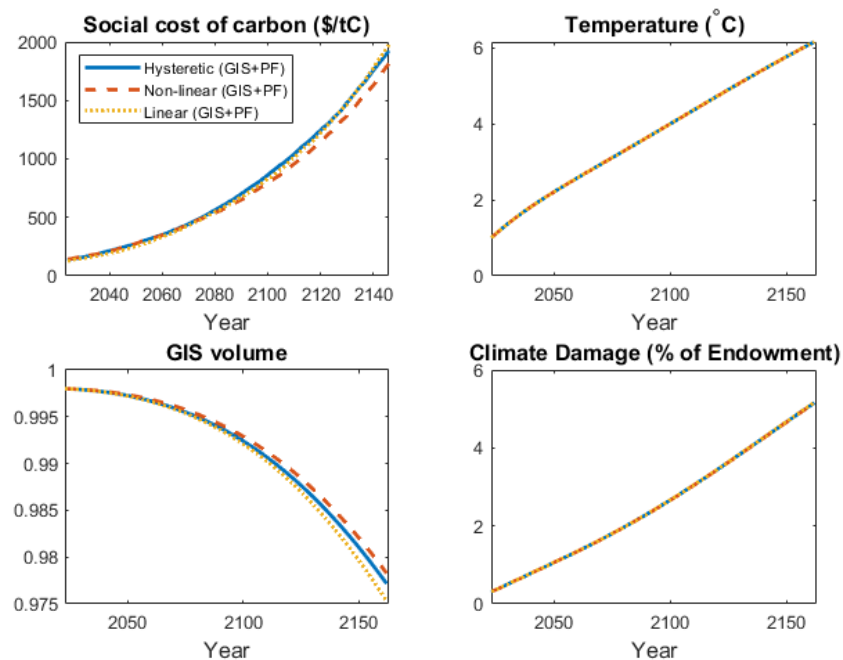


Figure 4.7: The SCC, temperature, remaining GIS volume, and annual climate damage over the coming 150 years when both GIS and permafrost thawing are considered. Three different types of equilibria of temperature and GIS volume are considered: hysteretic (irreversible), linear (reversible) and nonlinear (reversible). The graphical interpretations of these GIS dynamics are shown in Figure 4.1.



4.5 Conclusion

This paper analyzes how tipping points in the Greenland Ice Sheet (GIS) and permafrost thawing affect the social cost of carbon (SCC), optimal abatement policies, and projections of future climate and economic conditions. As global warming intensifies, the probability of triggering climate tipping points rises, and interactions between geophysical subsystems can substantially shape climate policy. Therefore, it is crucial to account for the risks associated with tipping points in economic analyses, especially those likely to be triggered in the near term.

We focus on two tipping points of immediate policy relevance: the Greenland Ice Sheet (GIS) melting and permafrost thawing. GIS disintegration accelerates sea-level rise, threatening coastal regions with severe economic damages. Thawing permafrost releases large quantities of carbon, mainly in the form of CO₂ and CH₄, accelerating global warming and reinforcing the permafrost-temperature feedback loop. Both tipping processes amplify climate risks and pose significant threats to economic development.

To assess these dynamics, we develop a continuous-time dynamic stochastic integrated climate-economic (DSICE) model with reduced-form representations of climate tipping elements to study how tipping points. Unlike most existing economic models which treat climate tipping as abrupt shifts in parameters, our framework explicitly models the dynamics of tipping elements, enabling the quantification of individual tipping risk and their interactive effects.

Our findings show that climate tipping points significantly alter the SCC and climate–economic projections in the absence of abatement (BAU). Rising temperatures from permafrost carbon emissions accelerate GIS melting, amplifying sea-level rise and the associated damages. While GIS tipping unfolds gradually over time and has limited near-term impact on GDP, permafrost thawing accelerates global warming, raising the SCC more substantially. Importantly, the interaction between the two tipping elements further amplifies climate risks.

Optimal abatement policies substantially mitigate these effects. As climate damages rise with temperature, the optimal abatement policy becomes more stringent to effectively curb the long-run climate risks. Emission reductions limit global warming, delay climate tipping, and lower both SCC and climate damages relative to BAU. The impact of permafrost thawing on optimal policy is particularly pronounced, since it necessitates larger cuts in anthropogenic emissions to offset additional permafrost carbon emissions. In contrast, GIS dynamics have negligible influence on optimal abatement, since GIS melting does not directly increase the atmospheric carbon.

Our sensitivity analyses highlight two insights. First, methane from permafrost has a disproportionate effect due to its higher warming potential than carbon dioxide. Although only 2% of permafrost carbon is released as methane, excluding it would lead to a 0.7°C underestimation of global warming by 2100, underscoring the need to account for methane in climate economic

analyses. Since atmospheric methane also arises from other major sources such as livestock and fossil fuel use, it is essential to incorporate methane explicitly into future climate economic studies. Second, alternative specifications of GIS dynamics, including irreversible tipping, produce little difference in near-term outcomes. Since GIS tipping manifests only gradually, its consequences are muted within a century even if the tipping threshold is exceeded.

Finally, our analysis is limited to two temperature-driven tipping points that are likely to become relevant in the near future. Over longer time horizons, other tipping elements such as the Atlantic Meridional Overturning Circulation (AMOC) may interact with temperature in different ways, potentially altering the dynamics we describe. Nevertheless, our framework provides a tractable and flexible approach for analyzing tipping dynamics and climate policy in a stochastic setting. Future work can extend this model to incorporate additional tipping processes, enabling more comprehensive evaluation of climate risks and optimal mitigation strategies.

4.A The Hamilton-Jacobi-Bellman (HJB) Equation of the Optimization Problem and SCC

In this section we provide the mathematical induction of the Hamilton-Jacobi-Bellman (HJB) equation of the optimization problem (4.2) in Section 4.2, and then a more explicit analytical expression of the SCC.

Let V_t be the value function at time t or the total social welfare from time t on. It is a function of time t and state variables $(Y, T^{CO_2}, T^{CH_4}, M_{CH_4}, E_{PF}, v, \omega)$. We know from Section 4.2 that the dynamics of the state variables $(Y, T^{CO_2}, T^{CH_4}, M_{CH_4}, E_{PF}, v, \omega)$ are

$$\begin{aligned}
dY_t &= \mu Y_t dt + \sigma Y_t dZ_t - JY_t dN_t, \\
dT_t^{CO_2} &= \chi((1 - u_t)E_t + E_{PF,t}^{CO_2}) dt, \\
dT_t^{CH_4} &= \frac{1}{\tau_{CH_4}} (F_t^{CH_4} - bT_t^{CH_4}) dt, \\
dM_{CH_4,t} &= (E_{PF,t}^{CH_4} \cdot Conv - \delta_{CH_4} M_{CH_4,t}) dt, \\
dE_{PF,t} &= \frac{1}{\tau} \left[-E_{PF,t} + (1 - p)\bar{C}_{PF}\beta_{PF} \left(\chi((1 - u_t)E_t + E_{PF,t}^{CO_2}) + \frac{1}{\tau_{CH_4}} (F_t^{CH_4} - bT_t^{CH_4}) \right) \right] dt, \\
dv_t &= -\beta_{GIS} \text{sgn}(T_t - T^*(v_t)) (T_t - T^*(v_t))^2 v_t^{0.2} dt, \\
d\omega_t &= \nu(\bar{\omega} - \omega_t) dt + \sigma_t^{(\omega)} dW_t^{(\omega)}.
\end{aligned}$$

where we use $\mu_{X,t}$ to denote the drift of variable X at time t . Then the Hamilton–Jacobi–Bellman (HJB) equation of the representative agents' optimization problem can be written as

$$\begin{aligned}
0 = \max_{u_t} & \left\{ f(C_t, V_t) + \frac{\partial V}{\partial t} + \mu_{Y,t} Y_t V_Y + \mu_{T^{CO_2},t} V_{T^{CO_2}} + \mu_{T^{CH_4},t} V_{T^{CH_4}} + \mu_{M_{CH_4},t} V_{M_{CH_4}} \right. \\
& + \mu_{E_{PF},t} V_{E_{PF}} + \mu_{v,t} V_v + \mu_{\omega,t} V_\omega + \frac{1}{2} \sigma^2 Y_t^2 V_{YY} + \frac{1}{2} \sigma_t^{(\omega)2} V_{\omega\omega} \\
& + \lambda E \left[V \left((1 - J)Y_{t-}, T_t^{CO_2}, T_t^{CH_4}, M_{CH_4,t}, E_{PF,t}, v_t, \omega_t, t \right) \right. \\
& \left. \left. - V(Y_{t-}, T_t^{CO_2}, T_t^{CH_4}, M_{CH_4,t}, E_{PF,t}, v_t, \omega_t, t-) \right) \right] \left. \right\}
\end{aligned}$$

where Y_{t-} is the endowment immediately before an economic crisis happens at t , V_X and V_{XX} are the first- and second-order partial derivatives of the state variable X respectively. For notational simplicity we omit the time subscripts for these partial derivatives.

The optimal abatement policy u_t^* satisfies the first order condition

$$\left. \frac{\partial f(C_t, V_t)}{\partial u_t} \right|_{u_t=u_t^*} - \chi E_t \left(V_{T^{CO_2}} + \frac{1}{\tau} (1 - p) C_{PF} \beta_{PF} V_{E_{PF}} \right) = 0. \quad (4.A.1)$$

Let $\xi_t := \frac{C_t}{Y_t}$ be the consumption-endowment ratio at time t . Then $\xi_t = \frac{(1-r_{SLR}(v_t))(1-A(u_t))}{1+D_t}$ and the partial derivative of the flow utility $f(C, V)$ with respect to the abatement rate u is

$$\frac{\partial f}{\partial u} = \frac{\beta \xi^{-1/\epsilon} Y^{1-1/\epsilon}}{[(1-\gamma)V]^{1/\zeta-1}} \frac{\partial \xi}{\partial u}$$

Plugging into the first order condition (4.A.1) yields

$$\frac{\beta \left(\frac{1-A(u_t^*)}{1+D(T_t, \omega_t)} \right)^{-1/\epsilon} Y^{1-1/\epsilon}}{[(1-\gamma)V_t]^{1/\zeta-1}} \frac{-A'(u_t^*)}{1+D(T_t, \omega_t)} \chi E_t \left(V_{T^{CO_2}} + \frac{1}{\tau} (1-p) C_{PF} \beta_{PF} V_{E_{PF}} \right) = 0.$$

4.B Summary of Model Parameters

All parameter values in the integrated assessment model are summarized in Table 4.A1.

Table 4.A1: Summary of parameter values

Parameters	Values	Explanation
$T_0^{CO_2}$	1	Initial temperature due to CO ₂ emissions (°C, 2023)
$T_0^{CH_4}$	0	Initial temperature due to CH ₄ emissions (°C, 2023)
χ	0.0018	Transient climate response to cumulative emissions (°C/GtC)
E_0	10.03	Initial carbon emission from CO ₂ in 2023 (GtC)
δ_0	-0.5%	The declining rate of carbon intensity at time 0
δ_∞	-6.5%	The declining rate of carbon intensity in the long run
α_ψ	0.25%	The changing rate of δ_t
\bar{M}_{CH_4}	722	Pre-industrial atmospheric methane level (ppb)
$M_{CH_4,0}$	1198	Initial atmospheric methane level (in year 2023, ppb)
$M_{N_2O,0}$	337	Initial atmospheric N ₂ O level (in year 2023, ppb)
α_{CH_4}	0.036	Radiative forcing parameter due to atmospheric methane
δ_{CH_4}	0.08	Decay rate of atmospheric methane
τ_{CH_4}	7.35	Heat capacity of the earth's surface
b	0.5	Outgoing longwave radiation parameter for methane
θ_T	0.56	Convexity of the climate damage function
θ_ω	2.7	Skewness of stochastic shocks ω to climate damage
ν	0.2	Mean-reversion rate of the stochastic shock ω
ω_0	0.21	Initial value of the stochastic shock ω
$\bar{\omega}$	0.21	Long-run value of the stochastic shock ω
σ_{ω_0}	0.05	Initial volatility of ω
\bar{t}_ω	10 ¹⁰	Time for the resolution of climate damage uncertainty
β_{GIS}	-0.0000106	The coefficient of ice melting speed
β_{PF}	0.172	The speed of permafrost thawing as temperature rises
\bar{C}_{PF}	1035	Total amount of permafrost carbon (GtC)
p	0.4	The proportion of thawed permafrost in the passive pool
q	0.98	The proportion of permafrost carbon released as CO ₂
τ	70	Decay rate of carbon released from thawed permafrost
v_0	0.945	Initial GIS volume

Bibliography

- ABERNETHY, S. AND R. B. JACKSON (2022): “Global temperature goals should determine the time horizons for greenhouse gas emission metrics,” *Environmental Research Letters*, 17, 024019.
- ACEMOGLU, D., V. CHERNOZHUKOV, I. WERNING, AND M. D. WHINSTON (2021): “Optimal targeted lockdowns in a multigroup SIR model,” *American Economic Review: Insights*, 3, 487–502.
- ARMSTRONG MCKAY, D. I., A. STAAL, J. F. ABRAMS, R. WINKELMANN, B. SAKSCHEWSKI, S. LORIANI, I. FETZER, S. E. CORNELL, J. ROCKSTRÖM, AND T. M. LENTON (2022): “Exceeding 1.5 C global warming could trigger multiple climate tipping points,” *Science*, 377, eabn7950.
- ARON, J. L. AND I. B. SCHWARTZ (1984): “Seasonality and period-doubling bifurcations in an epidemic model,” *Journal of theoretical biology*, 110, 665–679.
- ASHWIN, P. AND A. S. VON DER HEYDT (2020): “Extreme sensitivity and climate tipping points,” *Journal of Statistical Physics*, 179, 1531–1552.
- ATKESON, A. (2021): “A Parsimonious Behavioral SEIR Model of the 2020 COVID Epidemic in the United States and the United Kingdom,” Tech. rep., National Bureau of Economic Research.
- AVERY, C., W. BOSSERT, A. CLARK, G. ELLISON, AND S. F. ELLISON (2020): “An economist’s guide to epidemiology models of infectious disease,” *Journal of Economic Perspectives*, 34, 79–104.
- BACMEISTER, J. T., K. A. REED, C. HANNAY, P. LAWRENCE, S. BATES, J. E. TRUESDALE, N. ROSEN-BLOOM, AND M. LEVY (2018): “Projected changes in tropical cyclone activity under future warming scenarios using a high-resolution climate model,” *Climatic Change*, 146, 547–560.
- BANSAL, R., M. OCHOA, AND D. KIKU (2017): “Climate change and growth risks,” Tech. rep., National Bureau of Economic Research.

- BARNDORFF-NIELSEN, O. E. AND N. SHEPHARD (2001): “Non-Gaussian Ornstein–Uhlenbeck-based models and some of their uses in financial economics,” *Journal of the Royal Statistical Society: Series B (Statistical Methodology)*, 63, 167–241.
- BARRO, R. J. (2006): “Rare disasters and asset markets in the twentieth century,” *The Quarterly Journal of Economics*, 121, 823–866.
- (2009): “Rare disasters, asset prices, and welfare costs,” *American Economic Review*, 99, 243–264.
- BARRO, R. J. AND T. JIN (2011): “On the size distribution of macroeconomic disasters,” *Econometrica*, 79, 1567–1589.
- BISKABORN, B. K., S. L. SMITH, J. NOETZLI, H. MATTHES, G. VIEIRA, D. A. STRELETSKIY, P. SCHOENEICH, V. E. ROMANOVSKY, A. G. LEWKOWICZ, A. ABRAMOV, ET AL. (2019): “Permafrost is warming at a global scale,” *Nature communications*, 10, 264.
- BOX, J. E., A. HUBBARD, D. B. BAHR, W. T. COLGAN, X. FETTWEIS, K. D. MANKOFF, A. WEHRLÉ, B. NOËL, M. R. VAN DEN BROEKE, B. WOUTERS, ET AL. (2022): “Greenland ice sheet climate disequilibrium and committed sea-level rise,” *Nature Climate Change*, 12, 808–813.
- BRANGER, N., H. HÜLSBUSCH, AND A. KRAFTSCHIK (2018): “The volatility-of-volatility term structure,” in *Paris December 2017 Finance Meeting EUROFIDAI-AFFI*.
- BUDYKO, M. I. (1969): “The effect of solar radiation variations on the climate of the Earth,” *tellus*, 21, 611–619.
- BYROM, R. E. AND K. P. SHINE (2022): “Methane’s solar radiative forcing,” *Geophysical Research Letters*, 49, e2022GL098270.
- CAI, Y., T. M. LENTON, AND T. S. LONTZEK (2016): “Risk of multiple interacting tipping points should encourage rapid CO2 emission reduction,” *Nature Climate Change*, 6, 520–525.
- CAI, Y. AND T. S. LONTZEK (2019): “The social cost of carbon with economic and climate risks,” *Journal of Political Economy*, 127, 2684–2734.
- CHEN, Z. AND L. EPSTEIN (2002): “Ambiguity, risk, and asset returns in continuous time,” *Econometrica*, 70, 1403–1443.
- CLARK, P. K. (1973): “A subordinated stochastic process model with finite variance for speculative prices,” *Econometrica: journal of the Econometric Society*, 135–155.

- DAVIES, N. G., S. ABBOTT, R. C. BARNARD, C. I. JARVIS, A. J. KUCHARSKI, J. D. MUNDAY, C. A. PEARSON, T. W. RUSSELL, D. C. TULLY, A. D. WASHBURNE, ET AL. (2021): “Estimated transmissibility and impact of SARS-CoV-2 lineage B. 1.1. 7 in England,” *Science*, 372, eabg3055.
- DIETZ, S., J. RISING, T. STOERK, AND G. WAGNER (2021a): “Economic impacts of tipping points in the climate system,” *Proceedings of the National Academy of Sciences*, 118, e2103081118.
- DIETZ, S., F. VAN DER PLOEG, A. REZAI, AND F. VENMANS (2021b): “Are economists getting climate dynamics right and does it matter?” *Journal of the Association of Environmental and Resource Economists*, 8, 895–921.
- DIMSON, E., P. MARSH, AND M. STAUNTON (2011): “Equity premia around the world,” *Available at SSRN 1940165*.
- DIXIT, A. K. AND R. S. PINDYCK (1994): *Investment under uncertainty*, Princeton university press.
- DOLGIN, E. ET AL. (2021): “COVID vaccine immunity is waning-how much does that matter,” *Nature*, 597, 606–607.
- DORIA-ROSE, N., M. S. SUTHAR, M. MAKOWSKI, S. O’CONNELL, A. B. McDERMOTT, B. FLACH, J. E. LEDGERWOOD, J. R. MASCOLA, B. S. GRAHAM, B. C. LIN, ET AL. (2021): “Antibody persistence through 6 months after the second dose of mRNA-1273 vaccine for Covid-19,” *New England Journal of Medicine*, 384, 2259–2261.
- DUFFIE, D. AND L. G. EPSTEIN (1992): “Stochastic differential utility,” *Econometrica: Journal of the Econometric Society*, 353–394.
- DYER, O. (2021): “Covid-19: Countries are learning what others paid for vaccines,” *BMJ: British Medical Journal (Online)*, 372.
- EPSTEIN, J. M., E. HATNA, AND J. CRODELLE (2021): “Coupled Contagion: A Two-Fears Epidemic Model,” *arXiv preprint arXiv:2102.11045*.
- ERAKER, B., M. JOHANNES, AND N. POLSON (2003): “The impact of jumps in volatility and returns,” *The Journal of Finance*, 58, 1269–1300.
- ERAKER, B. AND A. YANG (2022): “The Price of Higher Order Catastrophe Insurance: The Case of VIX Options,” *The Journal of Finance*, 77, 3289–3337.
- FELLER, W. (1951): “Two singular diffusion problems,” *Annals of mathematics*, 173–182.

- GJERDE, J., S. GREPPERUD, AND S. KVERNDOKK (1999): “Optimal climate policy under the possibility of a catastrophe,” *Resource and energy economics*, 21, 289–317.
- GOOLSBEE, A. AND C. SYVERSON (2021): “Fear, lockdown, and diversion: Comparing drivers of pandemic economic decline 2020,” *Journal of public economics*, 193, 104311.
- GREENWOOD, P. E. AND L. F. GORDILLO (2009): “Stochastic epidemic modeling,” in *Mathematical and statistical estimation approaches in epidemiology*, Springer, 31–52.
- GREGORY, J. M., S. E. GEORGE, AND R. S. SMITH (2020): “Large and irreversible future decline of the Greenland ice sheet,” *The Cryosphere*, 14, 4299–4322.
- HAMBEL, C., H. KRAFT, AND E. SCHWARTZ (2021): “Optimal carbon abatement in a stochastic equilibrium model with climate change,” *European Economic Review*, 132, 103642.
- HE, S., Y. PENG, AND K. SUN (2020): “SEIR modeling of the COVID-19 and its dynamics,” *Nonlinear dynamics*, 101, 1667–1680.
- HOOVER, G. M., C. E. HATHAWAY, AND D. WILLIAMS (1967): “Infrared absorption by overlapping bands of atmospheric gases,” *Applied Optics*, 6, 481–487.
- HOPE, C. (2011): “The PAGE09 integrated assessment model: A technical description,” *Cambridge Judge Business School Working Paper*, 4.
- HOPE, C. AND K. SCHAEFER (2016): “Economic impacts of carbon dioxide and methane released from thawing permafrost,” *Nature Climate Change*, 6, 56–59.
- HU, G. AND Y. LIU (2022): “The Pricing of Volatility and Jump Risks in the Cross-Section of Index Option Returns,” *Journal of Financial and Quantitative Analysis*, 57, 2385–2411.
- HUANG, D., C. SCHLAG, I. SHALIASTOVICH, AND J. THIMME (2019): “Volatility-of-volatility risk,” *Journal of Financial and Quantitative Analysis*, 54, 2423–2452.
- HULL, J. AND A. WHITE (1987): “The pricing of options on assets with stochastic volatilities,” *The journal of finance*, 42, 281–300.
- IPCC (2007): “The physical science basis. Contribution of working group I to the fourth assessment report of the Intergovernmental Panel on Climate Change,” *Cambridge University Press, Cambridge, United Kingdom and New York, NY, USA*, 996, 113–119.
- (2021a): *Climate Change 2021: The Physical Science Basis. Contribution of Working Group I to the Sixth Assessment Report of the Intergovernmental Panel on Climate Change*, vol. In Press, Cambridge, United Kingdom and New York, NY, USA: Cambridge University Press.

- (2021b): *Climate Change 2021: The Physical Science Basis. Contribution of Working Group I to the Sixth Assessment Report of the Intergovernmental Panel on Climate Change*, vol. In Press, Cambridge, United Kingdom and New York, NY, USA: Cambridge University Press.
- JAIN, S. AND C. W. OOSTERLEE (2012): “Pricing high-dimensional Bermudan options using the stochastic grid method,” *International Journal of Computer Mathematics*, 89, 1186–1211.
- JENSEN, S., C. P. TRAEGER, AND C. TRÄGER (2021): “Pricing climate risk,” Tech. rep., CESifo Working Paper.
- JOHANSSON, Å., Y. GUILLEMETTE, F. MURTIN, D. TURNER, G. NICOLETTI, C. DE LA MAISON-NEUVE, G. BOUSQUET, AND F. SPINELLI (2012): “Looking to 2060: Long-term global growth prospects: A going for growth report,” .
- KAPLAN, G., B. MOLL, AND G. L. VIOLANTE (2020): “The great lockdown and the big stimulus: Tracing the pandemic possibility frontier for the US,” Tech. rep., National Bureau of Economic Research.
- KARYDAS, C. AND A. XEPAPADEAS (2019): “Pricing climate change risks: CAPM with rare disasters and stochastic probabilities,” *CER-ETH Working Paper Series Working Paper*, 19, 311.
- KELDER, T., M. MÜLLER, L. SLATER, T. MARJORIBANKS, R. WILBY, C. PRUDHOMME, P. BOHLINGER, L. FERRANTI, AND T. NIPEN (2020): “Using UNSEEN trends to detect decadal changes in 100-year precipitation extremes,” *npj Climate and Atmospheric Science*, 3, 47.
- KERMACK, W. O. AND A. G. MCKENDRICK (1927): “A contribution to the mathematical theory of epidemics,” *Proceedings of the royal society of london. Series A, Containing papers of a mathematical and physical character*, 115, 700–721.
- KESSLER, L. (2017): “Estimating the economic impact of the permafrost carbon feedback,” *Climate Change Economics*, 8, 1750008.
- KLIBANOFF, P., M. MARINACCI, AND S. MUKERJI (2005): “A smooth model of decision making under ambiguity,” *Econometrica*, 73, 1849–1892.
- KLOSE, A. K., V. KARLE, R. WINKELMANN, AND J. F. DONGES (2020): “Emergence of cascading dynamics in interacting tipping elements of ecology and climate,” *Royal Society open science*, 7, 200599.
- KNIESNER, T. J., W. K. VISCUSI, C. WOOCK, AND J. P. ZILIAK (2012): “The value of a statistical life: Evidence from panel data,” *Review of Economics and Statistics*, 94, 74–87.

- KNIGHT, F. H. (1921): *Risk, uncertainty and profit*, vol. 31, Houghton Mifflin.
- KOPP, R. E., R. L. SHWOM, G. WAGNER, AND J. YUAN (2016): “Tipping elements and climate–economic shocks: Pathways toward integrated assessment,” *Earth’s Future*, 4, 346–372.
- LEMOINE, D. AND C. TRAEGER (2014): “Watch your step: optimal policy in a tipping climate,” *American Economic Journal: Economic Policy*, 6, 137–166.
- LEMOINE, D. AND C. P. TRAEGER (2016): “Economics of tipping the climate dominoes,” *Nature Climate Change*, 6, 514–519.
- LENTON, T. AND J. CISCAR (2013): “Integrating tipping points into climate impact assessments,” *Climate Change*, 585–597.
- LENTON, T. M., J. ROCKSTRÖM, O. GAFFNEY, S. RAHMSTORF, K. RICHARDSON, W. STEFFEN, AND H. J. SCHELLNHUBER (2019): “Climate tipping points—too risky to bet against,” .
- LETTAU, M., S. C. LUDVIGSON, AND J. A. WACHTER (2008): “The declining equity premium: What role does macroeconomic risk play?” *The Review of Financial Studies*, 21, 1653–1687.
- LIU, Y., A. A. GAYLE, A. WILDER-SMITH, AND J. ROCKLÖV (2020): “The reproductive number of COVID-19 is higher compared to SARS coronavirus,” *Journal of travel medicine*.
- LIU, Y. AND J. ROCKLÖV (2021): “The reproductive number of the Delta variant of SARS-CoV-2 is far higher compared to the ancestral SARS-CoV-2 virus,” *Journal of travel medicine*.
- LONTZEK, T. S., Y. CAI, K. L. JUDD, AND T. M. LENTON (2015): “Stochastic integrated assessment of climate tipping points indicates the need for strict climate policy,” *Nature Climate Change*, 5, 441–444.
- LÓPEZ, L. AND X. RODO (2021): “A modified SEIR model to predict the COVID-19 outbreak in Spain and Italy: simulating control scenarios and multi-scale epidemics,” *Results in Physics*, 21, 103746.
- MATTAUCH, L., R. MILLAR, R. VAN DER PLOEG, A. REZAI, A. SCHULTES, F. VENMANS, N. BAUER, S. DIETZ, O. EDENHOFER, N. FARRELL, ET AL. (2018): “Steering the climate system: an extended comment,” Tech. rep., CESifo Working Paper.
- MATTHEWS, H. D., N. P. GILLETT, P. A. STOTT, AND K. ZICKFELD (2009): “The proportionality of global warming to cumulative carbon emissions,” *Nature*, 459, 829–832.
- MATTHEWS, H. D., S. SOLOMON, AND R. PIERREHUMBERT (2012): “Cumulative carbon as a policy framework for achieving climate stabilization,” *Philosophical Transactions of the Royal Society A: Mathematical, Physical and Engineering Sciences*, 370, 4365–4379.

- McARTHUR, J.-A. (2021): “Methane emissions are driving climate change. Here’s how to reduce them,” *United Nations Environment Programme*. August, 20, 2021.
- McCALLUM, H., N. BARLOW, AND J. HONE (2001): “How should pathogen transmission be modelled?” *Trends in ecology & evolution*, 16, 295–300.
- McKAY, D. A., A. STAAL, J. F. ABRAMS, R. WINKELMANN, B. SAKSCHEWSKI, S. LORIANI, I. FETZER, S. E. CORNELL, J. ROCKSTRÖM, AND T. M. LENTON (2022): “Updated assessment suggests > 1.5° C global warming could trigger multiple climate tipping points,” *Authorea Preprints*.
- NAKICENOVIC, N. (2000): “Special report on emissions scenarios. Special Report on Emissions Scenarios, Edited by Nebojsa Nakicenovic and Robert Swart,” *ISBN*, 521804930, 612.
- NORDHAUS, W. (2019): “Economics of the disintegration of the Greenland ice sheet,” *Proceedings of the National Academy of Sciences*, 116, 12261–12269.
- NORDHAUS, W. D. (1992): “The ‘DICE’ Model: Background and Structure of a Dynamic Integrated Climate-Economy Model of the Economics of Global Warming,” Cowles Foundation Discussion Papers 1009, Cowles Foundation for Research in Economics, Yale University.
- (2010): “Economic aspects of global warming in a post-Copenhagen environment,” *Proceedings of the National Academy of Sciences*, 107, 11721–11726.
- (2017): “Revisiting the social cost of carbon,” *Proceedings of the National Academy of Sciences*, 114, 1518–1523.
- OECD (2023): *OECD Economic Outlook, Volume 2023 Issue 2*.
- OLEFELDT, D., S. GOSWAMI, G. GROSSE, D. HAYES, G. HUGELIUS, P. KUHR, A. D. MCGUIRE, V. ROMANOVSKY, A. B. K. SANNEL, E. SCHUUR, ET AL. (2016): “Circumpolar distribution and carbon storage of thermokarst landscapes,” *Nature communications*, 7, 13043.
- OLIJSLAGERS, S. (2021): “Solution methods for DSGE models in continuous time: application to a climate-economy model,” .
- OLIJSLAGERS, S., F. VAN DER PLOEG, AND S. VAN WIJNBERGEN (2023): “On current and future carbon prices in a risky world,” *Journal of Economic Dynamics and Control*, 146, 104569.
- OLIJSLAGERS, S. AND S. VAN WIJNBERGEN (2024): “Discounting the Future: On Climate Change, Ambiguity Aversion and Epstein–Zin Preferences,” *Environmental and Resource Economics*, 1–48.

Bibliography

- OLIJSLAGERS, S. ET AL. (2022): *The economics of climate change: On the role of risk and preferences*.
- PERRA, N., D. BALCAN, B. GONÇALVES, AND A. VESPIGNANI (2011): “Towards a characterization of behavior-disease models,” *PloS one*, 6, e23084.
- PINDYCK, R. S. (2013): “Climate change policy: what do the models tell us?” *Journal of Economic Literature*, 51, 860–72.
- PINDYCK, R. S. AND N. WANG (2013): “The economic and policy consequences of catastrophes,” *American Economic Journal: Economic Policy*, 5, 306–339.
- POKHREL, Y., F. FEFELANI, Y. SATOH, J. BOULANGE, P. BUREK, A. GÄDEKE, D. GERTEN, S. N. GOSLING, M. GRILLAKIS, L. GUDMUNDSSON, ET AL. (2021): “Global terrestrial water storage and drought severity under climate change,” *Nature Climate Change*, 11, 226–233.
- PRILLAMAN, M. (2022): “One coronavirus infection wards off another—but only if it’s a similar variant,” .
- RAHMAN, S., M. M. RAHMAN, M. MIAH, M. N. BEGUM, M. SARMIN, M. MAHFUZ, M. E. HOSSAIN, M. Z. RAHMAN, M. J. CHISTI, T. AHMED, ET AL. (2022): “COVID-19 reinfections among naturally infected and vaccinated individuals,” *Scientific reports*, 12, 1–10.
- REIDMILLER, D., C. W. AVERY, D. R. EASTERLING, K. E. KUNKEL, K. LEWIS, T. K. MAYCOCK, AND B. C. STEWART (2018): “Fourth national climate assessment,” *Volume II: Impacts, Risks, and Adaptation in the United States*, 440.
- RENNERT, K., F. ERRICKSON, B. C. PREST, L. RENNELS, R. G. NEWELL, W. PIZER, C. KINGDON, J. WINGENROTH, R. COOKE, B. PARTHUM, ET AL. (2022): “Comprehensive evidence implies a higher social cost of CO₂,” *Nature*, 610, 687–692.
- RIDLEY, J., J. M. GREGORY, P. HUYBRECHTS, AND J. LOWE (2010): “Thresholds for irreversible decline of the Greenland ice sheet,” *Climate Dynamics*, 35, 1049–1057.
- ROBINSON, A., R. CALOV, AND A. GANOPOLSKI (2012): “Multistability and critical thresholds of the Greenland ice sheet,” *Nature Climate Change*, 2, 429–432.
- ROE, G. H. AND M. B. BAKER (2007): “Why is climate sensitivity so unpredictable?” *Science*, 318, 629–632.
- SCHUUR, T., A. D. MCGUIRE, V. E. ROMANOVSKY, C. SCHADEL, AND M. MACK (2018): “Arctic and boreal carbon,” *Review of the Draft Second State of the Carbon Cycle Report (SOCCR2)*.

-
- SHEPHARD, N. AND T. G. ANDERSEN (2009): “Stochastic volatility: origins and overview,” in *Handbook of financial time series*, Springer, 233–254.
- STOCKER, T. (2014): *Climate change 2013: the physical science basis: Working Group I contribution to the Fifth assessment report of the Intergovernmental Panel on Climate Change*, Cambridge university press.
- TAYLOR, S. J. (2005): “Financial returns modelled by the product of two stochastic processes study of the daily sugar prices 1961–75,” *Stochastic Volatility: Selected Readings*, N. Shephard, ed., Oxford University Press, New York, 60–82.
- THOMPSON, V., N. J. DUNSTONE, A. A. SCAIFE, D. M. SMITH, J. M. SLINGO, S. BROWN, AND S. E. BELCHER (2017): “High risk of unprecedented UK rainfall in the current climate,” *Nature communications*, 8, 107.
- TSAI, J. AND J. A. WACHTER (2015): “Disaster risk and its implications for asset pricing,” *Annual Review of Financial Economics*, 7, 219–252.
- VAN DEN BREMER, T. S. AND F. VAN DER PLOEG (2021): “The risk-adjusted carbon price,” *American Economic Review*, 111, 2782–2810.
- VAN WIJNBERGEN, S. (2022): “Lockdowns as options,” *Economics Letters*, 214, 110420.
- WANG, S., A. FOSTER, E. A. LENZ, J. D. KESSLER, J. C. STROEVE, L. O. ANDERSON, M. TURETSKY, R. BETTS, S. ZOU, W. LIU, ET AL. (2023): “Mechanisms and impacts of Earth system tipping elements,” *Reviews of Geophysics*, 61, e2021RG000757.
- WIGGINS, J. B. (1987): “Option values under stochastic volatility: Theory and empirical estimates,” *Journal of financial economics*, 19, 351–372.

Summary

This dissertation demonstrates how stochastic modeling can be applied to economic and policy analysis, emphasizing its crucial role in addressing uncertainty. Predicting future economic conditions is particularly challenging when irreversible events such as the COVID-19 pandemic and global warming are expected to leave long-lasting impacts on humanity. In the presence of significant uncertainty, stochastic dynamic models provide a natural and powerful framework for generating more reliable projections and informing policy decisions.

The focus of this work is on measurable uncertainty (risk) in the contexts of public health and climate economics, leaving the study of unmeasurable uncertainty (ambiguity) for future research. As first distinguished by Knight (1921), risk arises when the probabilities of different outcomes can be quantified, and ambiguity refers to situations where such probabilities are unknown. While most of the current literature in epidemiology and climate economics focuses on risk, there is growing awareness of the importance of ambiguity in policymaking. For instance, Olijslagers and van Wijnbergen (2024) studies the social cost of carbon under ambiguity aversion.

In the domain of public health, we use stochastic models to analyze policy responses to COVID-19, particularly under uncertainty regarding the timing and effectiveness of vaccines. We develop a behavioral epidemiological model (BSEIRS) that incorporates the stochastic arrival of vaccines and several underexplored aspects of virus transmission. Our simulations show that stricter lockdown measures create a “real option” for individuals to benefit from vaccination before infection, thereby reducing mortality. This real option value constitutes a substantial share of the health benefits from lockdowns and offers a new framework for communicating the rationale for such policies to the public.

In climate economics, we address two major sources of uncertainty. The first concerns stochastic climate volatility, which refers to the fact that the volatility of climate damages evolves stochastically over time. Using a Dynamic Stochastic Integrated model of Climate and Economy (DSICE), we incorporate this feature and endogenize the discount rate, addressing key critiques of static integrated assessment models by Pindyck (2013). Our results indicate that stochastic climate volatility substantially increases the SCC, both in the business-as-usual and optimal abatement scenarios. Meanwhile, it also increases the stochastic discount factor

and certainty equivalent of climate damages. Incorporating the stochastic volatility of climate damages influences both carbon pricing and optimal abatement policy.

The second climate issue we examine is the economic consequences of climate tipping points. Climate tipping points are defined as irreversible, large-scale shifts in climate systems with long-lasting effects. We integrate two climate tipping elements – the Greenland Ice Sheet (GIS) and thawing permafrost – into a Dynamic Stochastic Integrated model of Climate and Economy (DSICE) framework. Our analysis shows that both tipping points influence long-run economic output, although through different mechanisms and magnitudes. This indicates the need to account for multiple, interacting climate tipping points in economic research and carefully differentiate among them in policy design.

Overall, this dissertation demonstrates how stochastic dynamic modeling enhances the analysis of public health and climate policies by explicitly incorporating risk and uncertainty. The results provide new insights in pandemic management and the economic significance of climate change.

Nederlandse Samenvatting

(Summary in Dutch)

Deze dissertatie laat zien hoe stochastische modellen kunnen worden toegepast in economische en beleidsanalyse, en benadrukt haar cruciale rol bij het omgaan met onzekerheid. Het voorspellen van toekomstige economische omstandigheden is bijzonder uitdagend wanneer onomkeerbare gebeurtenissen, zoals de COVID-19-pandemie en de opwarming van de aarde, naar verwachting langdurige gevolgen zullen hebben voor de mensheid. In aanwezigheid van aanzienlijke onzekerheid bieden stochastische dynamische modellen een natuurlijk en krachtig raamwerk om betrouwbaardere projecties te genereren en beleidsbeslissingen te ondersteunen.

De focus van dit werk ligt op meetbare onzekerheid (risico) in de context van volksgezondheid en klimaat economie, waarbij de studie van niet-meetbare onzekerheid (ambiguïteit) wordt overgelaten aan toekomstig onderzoek. Zoals voor het eerst onderscheiden door Knight (1921), ontstaat risico wanneer de waarschijnlijkheden van verschillende uitkomsten kunnen worden gekwantificeerd, terwijl ambiguïteit verwijst naar situaties waarin dergelijke waarschijnlijkheden onbekend zijn. Hoewel het grootste deel van de huidige literatuur in de epidemiologie en klimaat economie zich richt op risico, groeit het besef dat ambiguïteit een belangrijke rol speelt in beleidsvorming. Zo bestudeert Olijslagers and van Wijnbergen (2024) de sociale kosten van koolstof onder ambiguïteitsaversie.

Op het gebied van volksgezondheid gebruiken wij stochastische modellen om beleidsreacties op COVID-19 te analyseren, met name onder onzekerheid over de timing en effectiviteit van vaccins. Wij ontwikkelen een gedragsmatig epidemiologisch model (BSEIRS) dat de stochastische aankomst van vaccins en verschillende onderbelichte aspecten van virusoverdracht incorporeert. Onze simulaties tonen aan dat strengere lockdownmaatregelen een “reële optie” creëren voor individuen om te profiteren van vaccinatie vóór infectie, wat leidt tot een lagere sterfte. Deze reële optiewaarde vormt een substantieel deel van de gezondheidsbaten van lockdowns en biedt een nieuw kader om de rationale van dergelijk beleid aan het publiek te communiceren.

In de klimaat economie behandelen wij twee belangrijke bronnen van onzekerheid. De eerste betreft stochastische klimaatvolatiliteit, wat verwijst naar het feit dat de volatiliteit van klimaatschade zich stochastisch ontwikkelt in de tijd. Met behulp van een Dynamic Stochastic

Integrated model of Climate and Economy (DSICE) incorporeren wij dit kenmerk en endogeniseren wij de discontovoet, waarmee wij ingaan op belangrijke kritiekpunten op statische geïntegreerde beoordelingsmodellen van Pindyck (2013). Onze resultaten tonen aan dat stochastische klimaatvolatiliteit de sociale kosten van koolstof (SCC) aanzienlijk verhoogt, zowel in het business-as-usual-scenario als onder optimale mitigatie. Tegelijkertijd verhoogt zij ook de stochastische disconteringsfactor en het certainty equivalent van klimaatschade. Het meenemen van stochastische volatiliteit van klimaatschade heeft daarmee invloed op zowel koolstofbeprijzing als optimaal mitigatiebeleid.

Het tweede klimaatthema dat wij onderzoeken betreft de economische gevolgen van klimaat tipping-points. Klimaat tipping-points worden gedefinieerd als onomkeerbare, grootschalige verschuivingen in klimaatsystemen met langdurige effecten. Wij integreren twee klimaat tipping elementen — de Groenlandse Ijs Sheet (GIS) en ontdooiende permafrost — in een DSICE-raamwerk. Onze analyse laat zien dat beide tipping-points de langetermijneconomische output beïnvloeden, zij het via verschillende mechanismen en met verschillende omvang. Dit onderstreept de noodzaak om meerdere, interacterende klimaat tipping-points in economisch onderzoek mee te nemen en deze zorgvuldig van elkaar te onderscheiden bij het ontwerpen van beleid.

Al met al laat deze dissertatie zien hoe stochastische dynamische modellen de analyse van beleid op het gebied van volksgezondheid en klimaat verbetert door risico en onzekerheid expliciet te integreren. De resultaten bieden nieuwe inzichten in pandemiemanagement en in de economische betekenis van klimaatverandering.

The Tinbergen Institute is the Institute for Economic Research, which was founded in 1987 by the Faculties of Economics and Econometrics of the Erasmus University Rotterdam, University of Amsterdam and Vrije Universiteit Amsterdam. The Institute is named after the late Professor Jan Tinbergen, Dutch Nobel Prize laureate in economics in 1969. The Tinbergen Institute is located in Amsterdam and Rotterdam. For a full list of PhD theses that appeared in the series we refer to <https://www.tinbergen.nl/list-of-phd-theses>. The following books recently appeared in the Tinbergen Institute Research Series:

840. Q. WIERSMA, *Dynamic Models for Multi-Dimensional Time Series*
841. R. SILVESTRINI, *On the Importance of Firm Heterogeneity, Business Dynamism, and Market Power Dynamics in the Macroeconomy*
842. E.S.R. DIJK, *Innovative Start-Ups and Competition Policy – How to Reign in Big*
843. T.D. SCHENK, *Essays in Causal Inference with Panel Data*
844. S. TYROS, *Workers' Skills and (green) Technology Adoption*
845. C.J. GRASER, *Mechanisms for the Evolution of Prosociality*
846. K. IOANNIDIS, *On the role of information in strategic and individual decision making*
847. G.M. MIYAZATO SZINI, *Advances in Panel and Network Econometrics*
848. L.V. VOOIS, *Empirical studies of health-related expectations and behaviors*
849. M.A. RÖSCH, *Multinational Firms and Local Workers*
850. E.S. MIHAYLOV, *Essays on Routine-Biased Technical Change, Job Tasks and Wages*
851. M. MAVUS KÜTÜK, *Essays on Currency Crash Risk, Carry Trade Returns, and Sovereign Bond Yields*
852. V. MOGHANI, *Essays on Health and Labor Economics*
853. T. VAN DER ZWAN, *Policy, Pricing and Prediction: Investigating Shock Dynamics, Equity Risk and Machine Learning*
854. S.H.P. WÖHRMÜLLER, *Essays in Macroeconomics with Household Heterogeneity*
855. P.A. OPSCHOOR, *On Asymmetries and Heterogeneities in Economic Modelling and Forecasting*
856. P.R. BOSE, *From Preferences to Policy: Essays in Political Economy*
857. J. KLOOSTER, *Robust Inference in Instrumental Variable Models*
858. K.E.A. HANEMAAIJER, *Widening the Divide: Barriers for Marginalised Groups in Education and Justice*
859. I. CUSTODIO JOÃO, *Dynamic Clustering Methods in Panel Data*
860. K.A. WACKER, *Analyses of Policies and Innovation in Banking*
861. S.J.D. VAN ALTEN, *Genetics, Human Capital Formation and the Intergenerational Transmission of Socioeconomic Status*
862. M. BASTIAANS, *Public Policies, Labor Market Shocks and Inequality*

863. M. MUSUMECI, *Three Essays on the Economics of Science and the Economics of Education: The Role of Barriers to Success in Academia and in School*
864. J.J.M. VAN SPRONSEN, *Sovereign Debt Markets and Resilience in a Heterogenous Union on the Interaction of European Economic and National Fiscal Policies*
865. A.B. HIRMAS, *Seeing Differently, Doing Differently: Essays on Visual Attention and Individual Decision-Making*
866. K.H.L. SOMMER, *Environmental Policy in Open Economies: Differences in Policy Stringency and the Effects on Leakage and Pollution Havens*
867. M. ARTEMOVA, *Studies in Observation-Driven Time Series Models: Theory, Methods, and Applications*
868. Y. LI, *Micro Studies on Self-Employment, Housing and Pensions*
869. S.J. DEN NIJS, *Investing in a Green Economy: Firm Perspectives and Spatial Economic Implications*
870. L. BREMER, *Technological Progress in the Transition to a Sustainable Economy*
871. D. MININA, *Essays on Expectation Formation and Learning*
872. J. ILCIUKAS, *Fertility and Family*
873. A. KURZ, *Competitiveness in the Green Transition*
874. A. TITTON, *Economic Consequences of Environmental Catastrophes*
875. D.A. CANDIA RIQUELME, *Assessing Innovative Transport Technologies and Policies: A Spatial General-Equilibrium Analysis*
876. M. HAASBROEK, *Trade and Industrial Policy in Emerging Economies*
877. Y. VAN DER STRATEN, *Financing Adaptation and the Green Transition: Climate Risk, Housing, and Capital Markets*
878. N.M.T. NGUYEN, *Market Concentration, Institutional Demand, and Risk Factors in Asset Pricing*
879. N.J. STEGEHUIS, *Beyond the Surface: Advancing Structural Models for Richer Causal Insights*
880. L.M. TIMM, *Migrants and Multinationals: Essays on the Local Effects of Globalization*
881. R. NUNES TEIXEIRA, *Changing Contexts, Shifting Norms & Shaping Behaviors: Insights from Behavioral Economics*
882. G. MINGOLI, *Modeling Explosive Dynamics in Time Series: Theory and Applications*
883. J. KORPERSHOEK, *Essays in Political Economy: The Press, Petitions and Political Campaigns*
884. D.R. GONZALEZ JIMENEZ, *Setting (and Mapping) Expectations: Essays on the Measurement of Beliefs, Learning Through Experience and Decision Making under Uncertainty*
885. M. JURGIEL, *The Rate of Collateral Reuse Within the Financial System*

886. I.L. SARU, *Econometric Analyses of Financial Markets: Essays on Market Microstructure*
887. Y. ZHONG, *Working under Pressure*
888. H. DENG, *Advanced Methods in Personalization for Marketing Decisions*